# Investigations on Uniformity, Radiation Resistance and Calibration of ZEUS Calorimeter Components at HERA

DISSERTATION

zur Erlangung des Doktorgrades
des Fachbereichs Physik
der Universität Hamburg

vorgelegt von

Ilja Bohnet
aus Berlin

Hamburg
Oktober 1999

| | |
|---|---|
| **Gutachter der Dissertation:** | Prof. Dr. K. Wick<br>Prof. Dr. R. Klanner |
| **Gutachter der Disputation:** | Prof. Dr. K. Wick<br>Prof. Dr. W. Scobel |
| **Datum der Disputation:** | 1999 |
| **Sprecher des Fachbereiches Physik und Vorsitzender des Promotionsausschusses:** | Prof. Dr. F. W. Büßer |

## Abstract:

The ZEUS detector at HERA has to provide highly reliable and precise measurements of $ep$ final states for a period of more than fifteen years. One of the main components of the ZEUS detector is the high resolution sampling calorimeter. It consists of alternating layers of depleted uranium and plastic scintillator tiles which are read out by wavelength shifting light guides and photomultipliers. The ZEUS experiment requires a precise measurement of particle energies from $ep$ scattering and a calibration at the level of 1%. As a consequence the required stability over several years, especially concerning the ageing and the radiation resistance of scintillators, wavelength shifters and light guides is therefore of fundamental importance.
This thesis describes theoretical and experimental aspects of calorimetry, especially with respect to the calibration, uniformity and radiation resistance of the plastic scintillators and wavelength shifters. Several methods and techniques for measuring the reliability of the optical components have been developed and applied to the demands of ZEUS. The most important experimental basis in this thesis is the $^{60}$Co monitor system. It is an off-line system based on scans of a moving $^{60}$Co source on the investigated calorimeter section. An analytical approach has been developed for the description of light propagation through radiation damaged optical materials such as scintillators and wavelength shifters. Testbeam measurements at DESY in connection with $^{60}$Co measurements have been performed using an irradiated ZEUS electromagnetic test calorimeter. These measurements investigated both the influence of irradiation of the optical components on calorimetry and the sensivity of the $^{60}$Co monitor system. As a matter of fact for the ZEUS uranium calorimeter there is no worsening expected due to the accumulated dose of some Gy, which has been confirmed by annual controls with the $^{60}$Co monitor system. Although small ageing effects of the scintillators are found, indeed the consequences on the energy calibration can be neglected. But the scintillators of a small calorimeter component close to the HERA beams, the beam pipe calorimeter, have been radiation damaged. The correlation between optical damage and performance has been studied and the effects on linearity are determined. A water damage of a certain cooling system influenced some optical components of the ZEUS calorimeter. $^{60}$Co scans were performed with the aim to study the influence of the water damage on the longitudinal uniformity of the calorimeter response. Strong recovery effects were observed. The measured non-uniformities were used to estimate the influence on the energy calibration.

## Zusammenfassung:

Das ZEUS Experiment besteht aus einem komplexen Teilchen-Detektor, der zur Messung von Teilchenkollisionen am weltweit ersten *ep* Beschleuniger HERA in Hamburg eingesetzt wird. Eine der Hauptkomponenten des ZEUS-Detektors ist das hochauflösende Stichprobenkalorimeter, das aus abwechselnden Lagen von Uran- und Szintillator-Platten besteht und von Wellenlängenschiebern und Photoröhren ausgelesen wird. Das ZEUS Experiment erfordert eine möglichst genaue Energiemessung und benötigt hierbei eine optimale Linearität und Uniformität. Die Stabilität, insbesondere die Strahlenresistenz der Szintillatoren und Wellenlängenschieber ist deshalb von fundamentaler Bedeutung, auch bezüglich der Detektor-Laufzeit von mehr als fünfzehn Jahren.
Diese Dissertation beschreibt theoretische und experimentelle Grundlagen der Kalorimetrie in Hinblick auf Strahlenschäden von Plastik-Szintillatoren und Wellenlängenschiebern. Ein Algorithmus wurde entwickelt zur Beschreibung der Lichtausbreitung in quaderförmigen Lichtleitern mit inhomogenen Strahlenschaden, der die Übertragung der physikalischen Kenntnisse aus Messungen an kleinen bestrahlten Proben auf realistische Dimensionen optischer Komponenten eines Kalorimeters erlaubt. Ausgehend von den Ansprüchen von ZEUS in Hinblick auf Strahlenresistenz und Uniformität der optischen Komponenten wurden Methoden und Techniken zur Qualtitätskontrolle entwickelt und auf das Kalorimeter angewendet, insbesondere auf der Grundlage eines mobilen $^{60}$Co-Präparates. Teststrahlmessungen am DESY in Verbindung mit Messungen mit dem $^{60}$Co-Kontroll-System wurden an einem strahlengeschädigten Testkalorimeter durchgeführt. Diese dienten der Untersuchung des Einflusses der strahlengeschädigten optischen Komponenten auf die Kalorimetrie und ihrer Nachweismöglichkeiten durch das $^{60}$Co-Kontroll-System. Für das ZEUS Uran-Kalorimeter ist bei den bisher akkumulierten Strahlendosen kein signifikanter Strahlenschäden zu erwarten. Dies hat sich bestätigt bei jährlichen Untersuchungen durch das $^{60}$Co-Kontroll-System. Hierbei sind Alterungseffekte der Szintillatoren gemessen worden, allerdings können die Konsequenzen auf die Kalibration vernachlässigt werden. Dagegen wurden die optischen Komponenten einer kleinen Kalorimeter-Komponente nahe am HERA-Strahlrohr strahlengeschädigt. Die Korrelation zwischen optischen Schaden und der Kalorimeterantwort dieser Komponente wurde studiert und die Effekte auf die Linearität wurden abgeschätzt. Ein Wasserschaden eines Kühlungssystems beeinträchtigte einige optische Komponenten des ZEUS-Kalorimeters. $^{60}$Co Untersuchungen wurden durchgeführt mit dem Ziel, den Einfluß des Wasserschadens auf die longitudinale Uniformität der Kalorimeterantwort zu bestimmen. Große Ausheilungseffekte wurden beobachtet. Die gemessenen Inhomogenitäten wurden benutzt, um den Einfluß des Wasserschadens auf die Energiemessung von Elektronen zu ermitteln.

# Contents


**1 Introduction** **1**

**2 HERA** **5**
2.1 Historical review . . . . . 5
2.2 The electron-proton collider . . . . . 6
2.3 Physics at HERA . . . . . 7

**3 The ZEUS detector** **11**
3.1 Overview . . . . . 11
3.2 Calorimetry at ZEUS . . . . . 12
3.3 Running conditions . . . . . 14

**4 Theoretical aspects** **17**
4.1 Passage of radiation through matter . . . . . 17
4.1.1 Electromagnetic and hadronic showers . . . . . 19
4.1.2 Calorimetry . . . . . 20
4.2 Principle of the ZEUS calorimeter . . . . . 21
4.3 The optical components of the ZEUS calorimeter . . . . . 22
4.4 Calculation of light propagation . . . . . 26
4.5 Simulation of electromagnetic showers . . . . . 31

**5 Experimental aspects** **33**
5.1 The $^{60}$Co monitor system . . . . . 33
5.1.1 The $^{60}$Co signal response . . . . . 34
5.1.2 The optical parameters . . . . . 36
5.1.3 Model of unfolding . . . . . 37
5.1.4 The $^{60}$Co measurement system . . . . . 39
5.2 Investigations on individual samples . . . . . 43
5.2.1 Scanning bench . . . . . 43
5.2.2 Excitation sources . . . . . 44
5.3 Dosimetry . . . . . 45

**6 Testbeam measurements and $^{60}$Co scans** **47**
6.1 Description of the test calorimeter . . . . . 47
6.2 The testbeam set-up and beam generation . . . . . 49
6.3 Results of $^{60}$Co measurements . . . . . 51
6.4 Linearity tests . . . . . 55
6.5 Uniformity tests . . . . . 59

6.6 Conclusions . . . . . 60

**7 Uniformity measurements on the ZEUS calorimeter 63**
7.1 Measurement performance . . . . . 63
7.2 Strategy of analysis . . . . . 65
7.3 Investigation on radiation damage effects . . . . . 67
7.3.1 Results of investigations on the FCAL . . . . . 68
7.3.2 Results of investigations on the RCAL . . . . . 69
7.3.3 Harp scans . . . . . 72
7.4 Investigations on ageing effects . . . . . 73
7.4.1 Outside scans on the FCAL module 12 bottom . . . . . 75
7.4.2 Inside scans on the FCAL module 17 . . . . . 76
7.4.3 Ageing scenarios . . . . . 78
7.4.4 Influence of ageing effects on the ZEUS uranium calorimeter . . . . . 78
7.5 Conclusions . . . . . 80

**8 Water damage effects on the ZEUS calorimeter 83**
8.1 Investigations on the FCAL module 8 . . . . . 83
8.1.1 $^{60}$Co measurements . . . . . 84
8.1.2 The analysis . . . . . 86
8.1.3 Damage scenarios . . . . . 89
8.1.4 Effects of non-uniformity on calibration . . . . . 91
8.2 Investigation on the RCAL module 17 . . . . . 93
8.2.1 $^{60}$Co measurements . . . . . 95
8.2.2 The optical parameters . . . . . 95
8.2.3 Unfolding . . . . . 97
8.2.4 Effects of non-uniformity on calibration . . . . . 97
8.3 Conclusions . . . . . 98

**9 Radiation damage effects in the BPC 101**
9.1 The Beam Pipe Calorimeter . . . . . 102
9.2 The running conditions . . . . . 103
9.3 Investigations of radiation damage . . . . . 105
9.3.1 $^{60}$Co measurements before/after the running period . . . . . 105
9.3.2 Investigations on single scintillators . . . . . 111
9.3.3 Simulation of attenuation curves . . . . . 119
9.4 Effects due to radiation damage . . . . . 120
9.4.1 Reconstruction of the calorimeter response . . . . . 120
9.4.2 Linearity of energy calibration . . . . . 124
9.5 Conclusions . . . . . 126

**10 Conclusions 129**

**A Simulation of light propagation 132**

**B Quality monitoring 147**

# List of Figures


2.1 Schematic overview of HERA and the pre-accelerator complex . . . . . 7
2.2 Feynman diagrams of neutral and charged current deep inelastic scattering . . . 8
2.3 Miscalibration of the hadron energy scale . . . . . 9
2.4 Kinematic region of HERA and other *ep* scattering experiments . . . . . 10

3.1 Cross-section at the ZEUS detector along the beam direction . . . . . 11
3.2 Schematic front view of the the RCAL. . . . . 13
3.3 Accumulated radiation doses at the F/RCAL . . . . . 15

4.1 Sketch of the optical readout of a ZEUS FCAL tower . . . . . 21
4.2 Energy deposition and scintillator response of electromagnatic shower . . . . . 22
4.3 Non-linearity of the energy measurement . . . . . 23
4.4 Structure of scintillator *SCSN-38* and wavelength shifter PMMA . . . . . 24
4.5 Sketch of a scintillator plate and attenuation curve . . . . . 26
4.6 Sketch of a scintillator plate with a Gaussian distributed radiation damage . . . 27
4.7 Attenuation curves of RCAL HAC0 scintillators . . . . . 29
4.8 Light guide with a limited readout shape . . . . . 30
4.9 Attenuation curves of a $PbWO_4$ crystal with a limited readout shape . . . . . 31

5.1 Nuclear level diagram and energy spectra of the $^{60}$Co compound . . . . . 33
5.2 The principle of the $^{60}$Co measurement . . . . . 34
5.3 The $^{60}$Co response of an EMC, HAC1 and HAC2 section . . . . . 35
5.4 Energy deposition of $\gamma$'s into a RCAL HAC0 scintillator . . . . . 36
5.5 Monte Carlo simulation of a $^{60}$Co measurement . . . . . 37
5.6 Monte Carlo simulation of a non-uniform RCAL HAC0 section . . . . . 38
5.7 Sketch of the $^{60}$Co measurement system . . . . . 40
5.8 Comparison of inside/outside signal responses . . . . . 41
5.9 Front view of the source guiding system on a FCAL EMC tower . . . . . 42
5.10 Sketch of the scanning bench . . . . . 44
5.11 Schematic top view on the $^{60}$Co set-up at HMI . . . . . 44
5.12 Energy spectra of different sources . . . . . 45
5.13 Nuclear level diagrams of $^{22}$Na and $^{207}$Bi compounds . . . . . 46

6.1 Sketch of bench measurements on the scintillators . . . . . 49
6.2 Schematic drawing of the set-up used at the DESY testbeam 21 . . . . . 50
6.3 Testbeam profiles of the DESY testbeam 21 . . . . . 51
6.4 $^{60}$Co signal responses of the test calorimeter . . . . . 52
6.5 Wavelength shifter responses of the test calorimeter . . . . . 53
6.6 The optical parameters . . . . . 54

6.7 Test Calorimeter responses from the testbeam . . . . . 56
6.8 Linearity of the energy measurement of the test calorimeter . . . . . 57
6.9 Energy resolution of the test calorimeter . . . . . 58
6.10 Uniformity of light collection of the test calorimeter . . . . . 59
6.11 Left/right ratios of the uniformity scans . . . . . 61
6.12 Correlation between testbeam, $^{60}$Co and scanning bench measurements . . . . . 62

7.1 Front view on the FCAL . . . . . 64
7.2 Comparison of $^{60}$Co signal responses of the FCAL module 11 . . . . . 67
7.3 Distribution of the deviation from reproducibility for the FCAL . . . . . 68
7.4 Right/left ratio for the FCAL towers close to the HERA beams . . . . . 69
7.5 Comparison of $^{60}$Co signal responses of the RCAL module 12 . . . . . 70
7.6 Mean values of the right/left ratio of $^{60}$Co signal responses of the RCAL . . . . 71
7.7 Deviation from reproducibility of $^{60}$Co signal responses of the RCAL . . . . . 71
7.8 Schematic front view of the $^{60}$Co harp scanner . . . . . 72
7.9 Harp scan results for the RCAL module 12, tower 11 . . . . . 73
7.10 $^{60}$Co signal responses of the FCAL module 12, tower 11 . . . . . 74
7.11 Optical parameters of the FCAL module 12, tower 3 . . . . . 75
7.12 Optical parameters of the FCAL module 17 . . . . . 77
7.13 Distribution of the optical parameters of scintillators of the FCAL module 17 . . 79
7.14 EGS4 Monte Carlo simulation of $^{60}$Co scans on a RCAL HAC0 section . . . . . 80

8.1 Ratio of UNO measurements after the accident on the FCAL module 8 . . . . . 84
8.2 Signal responses of the FCAL module 8 . . . . . 85
8.3 The optical parameters of scintillators of the FCAL module 8, tower 21 . . . . . 87
8.4 Transmission as a function of the date of measurement . . . . . 88
8.5 Sketch of the measurement to investigate the influence of water on a WLS . . . 89
8.6 Attenuation curves of the WLS bars . . . . . 90
8.7 Sketch of the measurement to investigate the influence of water on a SCI . . . . 91
8.8 Transmission of water treated scintillators . . . . . 92
8.9 Ratio of response functions of the FCAL module 8, tower 21 . . . . . 92
8.10 Estimate of the water damage on the energy calibration . . . . . 93
8.11 Measurement and simulation of $^{60}$Co signal responses of the RCAL . . . . . 94
8.12 The optical parameters of the RCAL module 17 . . . . . 96
8.13 Ratio of the weight factors of scintillators of the RCAL module 17 . . . . . 98
8.14 Non-linearity of the RCAL module 17 . . . . . 99

9.1 CAD drawing of the BPC . . . . . 101
9.2 Principle structure of the BPC module north without WLS bars . . . . . 102
9.3 Location of TLD's and Si-diodes . . . . . 104
9.4 Dose profile of the BPC north module for the HERA run in 1995 . . . . . 105
9.5 Accumulated Dose profiles of the BPC north module . . . . . 106
9.6 $^{60}$Co scans on the BPC north module before/after the HERA run 1995 . . . . . 107
9.7 $^{60}$Co scans on the BPC north module before/after the HERA run 1997 . . . . . 108
9.8 Measured and simulated $^{60}$Co signal responses of the BPC . . . . . 109
9.9 Ratio of the scintillator responses of the BPC $NXA2$ section . . . . . 110
9.10 Distributions of the ratios of the scintillator responses . . . . . 111
9.11 Change of the scintillator response in percent of all BPC scintillators . . . . . 112

9.12 Methods of measurements on individual scintillator fingers . . . . . 113
9.13 Primary light yield produced by electrons in a damaged scintillator . . . . . 115
9.14 Transmission and radiation induced absorption of a damaged scintillator . . . . 115
9.15 Signal response due to electrons from a $^{106}$Ru scan on a scintillator . . . . . 116
9.16 Schematic overview of the scintillators installed in the BPC module north . . . . 117
9.17 $^{106}$Ru scans on scintillator fingers of the BPC after the HERA run in 1995 . . . 118
9.18 Simulated responses in comparison with single response measurements . . . . . 119
9.19 Comparison of measured attenuation curves with linearly interpolated ones . . . 121
9.20 Radiation dose as a function of the ratio of the scintillator response . . . . . 122
9.21 Simulated attenuation curves from the exclusive $^{60}$Co comparison . . . . . 123
9.22 Radiation dose in the BPC North module after the HERA run 1997 . . . . . 124
9.23 Simulated attenuation curves of scintillators after the HERA run in 1997 . . . . 125
9.24 Reconstructed energy of the BPC from a MC-simulation . . . . . 126
9.25 Non-linearity of the energy measurement in 1995 and 1997 . . . . . 127

A.1 Sketch of an orthogonal light guide . . . . . 132
A.2 The computer code Lightsim . . . . . 135

# List of Tables


2.1 Main parameters of HERA as of the end of the 1997 running period . . . . . 6

4.1 Density and mean refraction index of the basis material (*SCSN-38* and *PMMA*) 23

5.1 Test of the unfolding method . . . . . 39

6.1 Irradiation of the test calorimeter before the testbeam . . . . . 48
6.2 Attenuation curves of the scintillators determined from the scanning bench . . . 49
6.3 The optical parameters of the scintillators . . . . . 55
6.4 Energy resolution of the test calorimeter . . . . . 58
6.5 Attenuation lengths of the scintillators determined from the testbeam . . . . . 60

7.1 Configuration of the measurement systems . . . . . 65
7.2 Attenuation lengths of scintillators of the RCAL module 12, tower 11 . . . . . 74
7.3 Transmission and reduction in percent of the scintillators of FCAL module 17 . 78

8.1 Overview of the measured towers of the FCAL module 8 . . . . . 84
8.2 Overview of the deviation from reproducibility of signal responses . . . . . 86
8.3 Maximum deviation from linearity in percent for all measured EMC/HAC0 sections 94
8.4 Deviation from reproducibility of the signal responses of the RCAL . . . . . 95
8.5 Reproducibility between measured and simulated signal responses . . . . . 97

A.1 Database for *SCSN-38* . . . . . 144
A.2 Database for *PMMA* (30 ppm *Y7*) . . . . . 145
A.3 Database for $PbWO_4$ . . . . . 146

B.1 Results of $^{60}$Co outside scanning on the FCAL in 1994 to 1996 . . . . . 147
B.2 Results of $^{60}$Co outside scanning on the FCAL in 1994 to 1996 . . . . . 148
B.3 Results of $^{60}$Co outside scanning on the RCAL in 1991 to 1998 . . . . . 149
B.4 Results of $^{60}$Co outside scanning on the FCAL module 12 in 1991 and 1998 . . . 150
B.5 Results of $^{60}$Co inside scanning on the FCAL module 17 in 1990 and 1999 . . . . 151

# Chapter 1

# Introduction

The ZEUS experiment is based on a multipurpose detector for the measurement of particle collisions at the world's first $ep$ collider HERA, taking data since June 1992. The primary goals of the ZEUS experiment are

- the investigation of the structure of the proton,
- the development of the field theory of the quarks and leptons including the strong interaction (the quantenchromodynamics) and the electroweak physics, and
- the investigation of the physics beyond the standard model.

The ZEUS detector consists of complex particle detection instruments determining the kinematics of $ep$ scattering within a large kinematic region. The main challenges of the ZEUS detector are to measure precisely the energy and the angle of the leptons (in particular $e^-/e^+$) and the particle jets resulting from charged and neutral particles. Hence the ZEUS detector is based on a high resolution calorimeter. It consists of alternating layers of depleted uranium and plastic scintillator tiles, read out by wavelength shifting light guides and photomultpliers. The accuracy and correctness of the physic results depend on the correct measurement of the energy. The understanding of the response function, and in particular the energy calibration and linearity are of fundamental importance which is demonstrated by the following examples:

- In some kinematic regions a 1% error in the energy results in a 5% error on the extracted proton structure function,
- A non-linearity of high energies appears in the physic results like new contact and interactions, respectively.

Mechanical changes, ageing, humidity and the radiation damage effects of the optical components degrade a calorimeter. Therefore the quality and radiation stability of the ZEUS calorimeter are of vital importance, particulary in view of the data taking period of more than fifteen years. Several calibration systems and methods are applied to ZEUS:

- Electronics calibration,
- light injection using a laser system,
- radioactivity from the uranium absorber plates,
- particle of known energy (kinematic peak events) and

- moveable point-like $^{60}$Co sources.

This thesis describes theoretical and experimental aspects of calorimetry in the field of calibration, uniformity and radiation resistance of plastic scintillators and wavelength shifters. Moreover several methods and techniques for investigating the reliability of the optical components were developed and applied to the ZEUS Calorimeter.
Chapter 2 gives a short description of the motivation of the lepton proton collider HERA. Several essential aspects of the analysis required from the world's first *ep* collider will be discussed. An overview of the ZEUS detector and the running conditions is given in Chapter 3.
Reactions which occur due to the passage of radiation through matter together with the irradiation effects produced by these processes on optical materials such as polymeres are discussed in Chapter 4. A description of light propagation through optical materials has been developed which allows to transfer the knowledge of irradiation effects on small polymere and scintillating samples up to realistic dimensions of rectilinear parallelpipeds. It allows to numerically simulate the light propagation through the latter depending on a non-uniform or uniform radiation damage. This numerical simulation has been incorporated into EGS4 Monte Carlo simulation programs. Thus it allows to simulate the effects of radiation damage in a calorimeter.
Chapter 5 presents online and offline monitoring tools which have been used to investigate the integrity of the optical components of the ZEUS calorimeter and certain components using moving radioactive sources, a UV-light system and thermoluminescence dosimetry (TLD). Scans along the surface of certain calorimeter sections using a $\gamma$ ray source ($^{60}$Co) compose the main off-line monitor system used at ZEUS. Moreover an algorithm is presented which allows the unfolding of $^{60}$Co data to determine the individual scintillator response of the calorimeter section.
Chapter 6 describes testbeam measurements at DESY in connection with $^{60}$Co scans which have been performed using an irradiated ZEUS test calorimeter to investigate both the influence of irradiation of the optical components on the calorimeter and the detection capabilities of the $^{60}$Co monitor system. Investigations on single scintillators of the test calorimeter before and after irradiation using electrons of a $^{90}$Sr source verify the radiation damage. The test calorimeter had been installed into the DESY testbeam for two weeks in June 1998. It was exposed to 1 to 6 GeV electrons in order to study various calibration effects.
During the operating time of HERA the ZEUS Calorimeter sections close to the HERA beams are most exposed to radiation. Within the preceding years $^{60}$Co measurements have been taken in the maintenance period 1996, 1997 and 1998 on these sections in order to control the quality of the optical components with respect to possible variations of the longitudinal uniformity and the light attenuation of the scintillators. However, the evidence of a change of the attenuation of the scintillators due to ageing led to a series of measurements at other locations of the calorimeter in 1998 and 1999. These investigations are summarized in Chapter 7.
Two water damages of a certain cooling system influenced some optical components of the ZEUS calorimeter. Chapter 8 describes $^{60}$Co scans performed with the aim to study the influence of the water damage on the longitudinal uniformity of the calorimeter. Strong recovery effects of the optical components were observed. The measured non-uniformities are used to estimate the influence of water damage on the energy measurement of electrons.
During the winter shutdown in 1994/1995 a small tungsten/scintillator sampling calorimeter was installed in the rear direction of the ZEUS Detector at a short distance from the HERA beams. The accumulated measured dose of the so-called Beam Pipe Calorimeter (BPC) during the 1995 HERA run influenced some of its scintillators which has been determined from the $^{60}$Co monitor system. Therefore the scintillators of the BPC were exchanged after the

1995 HERA run. The monitoring procedures were repeated in 1996 and an exchange of the damaged scintillator sections became necessary again. Since 1997, the accumulated dose significantly dropped and no further replacement of scintillators was to be done. Final Chapter 9 describes the radiation monitoring and the irradiation effects on the calibration of the BPC for the running periods in 1995 and 1997.

# Chapter 2

# HERA

## 2.1 Historical review

In 1911, one of the most important steps in understanding the structure of matter was done by H. Geiger and E. Marsden. They performed an experiment based on the scattering of $\alpha$-particles off a thin gold-foil. The essential result of the experiment concluded first by E. Rutherford, was that the mass of an atom is concentrated in a nucleus much smaller than the atom itself [RU11]. Within the following years several successful experiments have been performed in order to investigate the structure of matter and its interactions based on the same principle: Namely the scattering of a pointlike particle off a target. The development of particle accelerators allowed to reach higher energies than the ones achievable by radioactive processes. Increasing particle energies resulted in more information about the matter and denoted the raid into even smaller spatial dimensions.
Today it is known that electrons are pointlike particles without an inner structure up to $\leq 10^{-18}$ m. Consequently the electrons are particulary well suited to investigate the structure of the nucleus [DR98]. Experiments which scatter electrons with a known momentum and energy off a target are performed to measure physical quantities of interactions. One of them is the cross-section, which characterizes the reaction between the scattering partners. Electron proton scattering experiments resulted in corrections for the formula which describes the measured cross sections. The Rutherford formula describing the scattering of spinless particles was first modified in the 1950s by the Mott correction which took into account the electron spin $\frac{1}{2}$ [PO96]. Several years later the Rosenbluth calculation of the elastic electron proton scattering included the proton spin of $\frac{1}{2}$ and its electromagnetic formfactors. This signified an extended structure of the proton. In the following years rising electron and proton energies led to deep inelastic $ep$ scattering. The Structure Function of the proton resulting from these investigations varies with the momentum transfer between the electron and the proton and depends on the fraction of the proton momentum which takes part in the interaction. The so-called scale invariance or scaling implicates a scattering from point-like charged centers. The parton model of Feynman in the 1960s explained this results assuming the deep inelastic $ep$ scattering as a reaction between electrons and point-like constituents of the proton, the so-called partons. In the late 1960s the partons were identified by Bjorken and Paschos to be the spin $\frac{1}{2}$ quarks. The strong interaction of the quarks by the medium of gluons is described by a comprehensive field theory called Quantum Chromodynamics (QCD) and constitutes in conjunction with the electroweak theory the Standard Model of elementary particle physics [QU98]. HERA follows a long tradition of $ep$ scattering experiments and provides a unique opportunity to investigate the structure of the

proton in a completely new kinematical region [AB98].

## 2.2 The electron-proton collider

The **H**adron **E**lektron **R**ing **A**nlage **HERA** was constructed from 1984 to 1991 at DESY (Deutsches Elektronen Synchrotron) in Hamburg. It is the first lepton proton collider consisting of two storage rings of 6.3 km circumference about 20 m underground. HERA accelerates electrons[1] to 32 GeV and protons to 920 GeV and provides head-on collisions at two interaction points with a centre of mass of about 300 GeV, where two experiments, **H1** and **ZEUS**, are located. These experiments probe the proton substructure of the proton to distances down to a dimension of $10^{-18}$ m. Two additional fixed target experiments have been realized at

| parameter | achieved value in 1997 |
|---|---|
| $E_p$ (GeV) | 820 |
| $E_e$ (GeV) | 27.5 |
| $I_p$ (mA) | 100 |
| $I_e$ (mA) | 40 |
| number of bunches | 189 |
| bunch crossing time (ns) | 96 |
| instantaneous luminosity ($cm^{-2}s^{-1}$) | $1.4 \cdot 10^{31}$ |

Table 2.1: *Main parameters of HERA as of the end of the 1997 running period.*

HERA. **HERMES**, operating since 1995, is performed to investigate the spin structure of the nuclei [HE93]. The experiment investigates the scattering of longitudinally polarized electrons on polarized gas targets. Therefore the natural transverse polarization of the electron beam is rotated before and behind the HERMES experiment by spin rotators. **HERA-B**, which is still under installation, is constructed to study the $CP$ violation in the $B^0\bar{B}^0$ system using a wire target in the proton halo for the production of $B$-mesons [HB94].

The acceleration of the lepton and proton beams is done within several steps using the infrastructure of 7 DESY colliders. The proton acceleration starts with $H^-$-atoms in a 50 MeV linear accelerator (LINAC). Stripping the electrons off the hydrogen, the protons are injected into the storage ring DESY III. 11 proton bunches spaced by 96 ns are accelerated to 7 GeV. The proton bunches are transferred to PETRA (Positron-Elektron-Tandem-Ring-Anlage), where 70 bunches are accumulated and accelerated to 40 GeV before they are injected into HERA. The acceleration of the electrons begins in a 540 MeV LINAC which fills the positron intensity accumulator (PIA), from which the electrons are transferred to DESY II and accelerated to 7 GeV. The bunches are injected in PETRA and accelerated to an energy of 14 GeV. The bunch spacing is 96 ns similar to the protons. The electrons are injected into HERA with a nominal bunch rate of 210. The proton magnets are superconducting components which are supplied by a complex cooling system using liquid Helium at a temperature of 4 to 5 K and a pressure of 4000 hPa. The electron machine of HERA was first commissioned in 1989, the proton ring

[1] Positrons are referred to as electrons unless otherwise stated.

Figure 2.1: *Schematic overview of HERA and the pre-accelerator complex.*

using superconducting magnets and accelerators was first operated in 1991. The first electron proton collisions were achieved in June 1991.

## 2.3 Physics at HERA

One of the primary goals of the HERA program is the investigation of strong and electroweak interactions. A more detailed overview of physics at HERA can be found in [SK98].
The scattering of high energetic electrons on a proton results in an inelastic reaction. If the proton desintegrates a large number of particles forms a hadronical final state. This process is called deep-inelastic-scattering (DIS). The deep inelastic scattering is based on two fundamental classes of events:

$$e^{\pm} + P \to e^{\pm} X \quad \text{and} \quad e^{\pm} + P \to \nu^{(-)} X.$$

$X$ is the hadronic final state. The 4-momenta of the incoming and scattered lepton are given by: $k = (E_e, \mathbf{p_e})$, $k' = (E'_e, \mathbf{p'_e})$. The momenta of the proton and the virtual boson[2] are given by $p = (E_p, \mathbf{p_p})$ and $q = (E_{\gamma^*}, \mathbf{q})$.
In case of a neutral current (NC) DIS, the charge of the lepton is conserved and the intermediate vector boson is neutral. In case of charged current (CC) DIS the lepton converts to a neutrino via the exchange of a charged vector boson. The kinematics of $ep$ scattering can be described by the following quantities:

$$s = (p_p + p_e)^2 \simeq 4E_p \cdot E_e, \tag{2.1}$$
$$q^2 = (p_e - p_{e'})^2 = -Q^2, \tag{2.2}$$
$$W^2 = (q + p_p)^2, \tag{2.3}$$

[2]Its small momentum transfer.

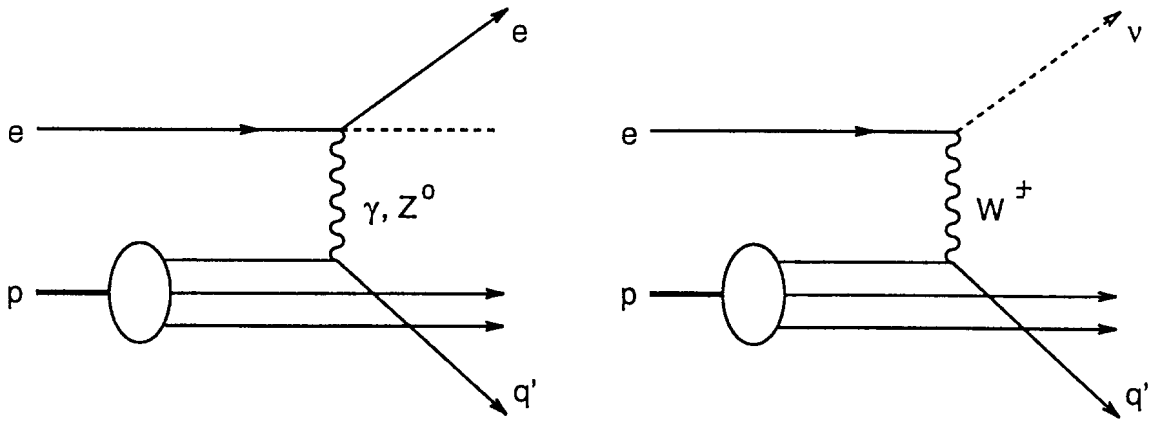


Figure 2.2: *Feynman diagrams of neutral (left) and charged current (right) deep inelastic scattering.*

where s is the square of the centre of mass energy, $Q^2$ is the negative square of momentum transfer $q$ which specifies the virtuality of the exchanged boson, and $W^2$ is the square of the total mass of the hadronic final state. A description by the following kinematic is equivalent to:

$$x = \frac{Q^2}{2pq}, \tag{2.4}$$

$$y = \frac{pq}{sk}, \tag{2.5}$$

$$\nu = \frac{pq}{m_p}, \tag{2.6}$$

where $\nu$ refers to the energy of the exchanged boson in the proton rest frame. Assuming the parton model the Bjorken scaling variable $x$ can be interpreted as the fraction of the proton momentum carried by the struck quark. $y$ is then the fractional energy transfer from the lepton to the proton. The relativistic invariant quantities $s$, $x$, $y$ and $Q^2$ are connected to the following relation:

$$Q^2 \simeq s \cdot x \cdot y. \tag{2.7}$$

The kinematic variables $Q^2$, $x$ and $y$ have to be determined by measurable quantities of the experiment which consist of a measurement of the scattered electron energy $E_{e'}$ and the scattering angle $\theta_e$ or the hadronic final state or a combination of both. The methods are used with respect to the investigated kinematic region. However, the condition is the determination of the energy and the position of the reaction products. This requires a high resolution calorimeter. One of the most important physics approach of HERA is the measurement of the proton structure function. Generally the cross section of DIS can be described by:

$$\frac{d^2\sigma(e^{\mp},p)}{dx\,dQ^2} = \frac{4\pi\alpha P^2(Q^2)}{x}\Big[y^2 x F_1(x,Q^2) + (1-y)F_2(x,Q^2) \pm (y - \frac{y^2}{2})xF_3(x,Q^2).\Big]. \tag{2.8}$$

$F_{1,2,3}(x,Q^2)$ are the Structure Functions of the proton. The propagator $P(Q^2)$ depends on the kind of intermediated boson. The Structure Function allows to determine the distribution of the momentum of the constituents of the proton due to the experiment.

The parton model contains the Callan-Cross-Relation:

$$2xF_1(x) = F_2(x), \qquad (2.9)$$

which shows a dependency on the Structure Function from $x$. The emission of a gluon from the struck quark produces a dependence of the Structure Function from $Q^2$ which yields a violation of scaling; the QCD predicts a varying Structure Function. HERA extends the kinematic region towards very low values in the Bjorken scaling $x$ and allows a detailed test of QCD. Indeed the determination of the cross section is very sensitive with respect to the calibration of the calorimeter. A shift in the absolute energy scale of $1-2\,\%$ at $y \simeq 0.1$ and $x < 0.5$ results a systematic change in the cross section in the order of $10\,\%$ [HE87]. Similar results for effects of a uniform miscalibration of the ZEUS calorimeter were found in [WOE91]. Figure 2.3 displays the ratio of the cross sections of charged current (CC) DIS with ($\sigma_{out}$) and without ($\sigma_{in}$) measurements errors induced by miscalibration of the energy scale for the ZEUS calorimeter. One clearly notices that the energy scale constant has to be $\leq 1\%$. Otherwise substructure or propagator effects might falsely be inferrred. Figure 2.4 displays the kinematic region of HERA and other $ep$ scattering experiments.

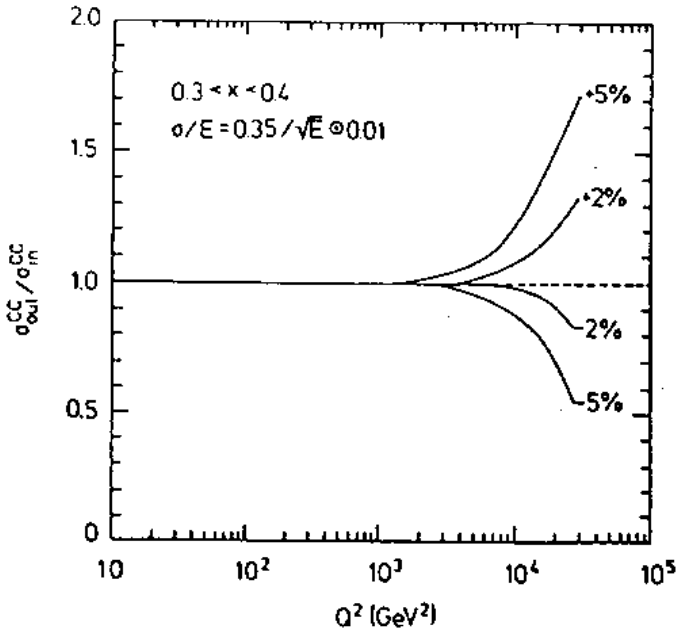


Figure 2.3: *The changes in $\sigma_{out}/\sigma_{in}$ due to miscalibration of the hadron energy scale for $0.3 < x < 0.4$ [ZE85].*

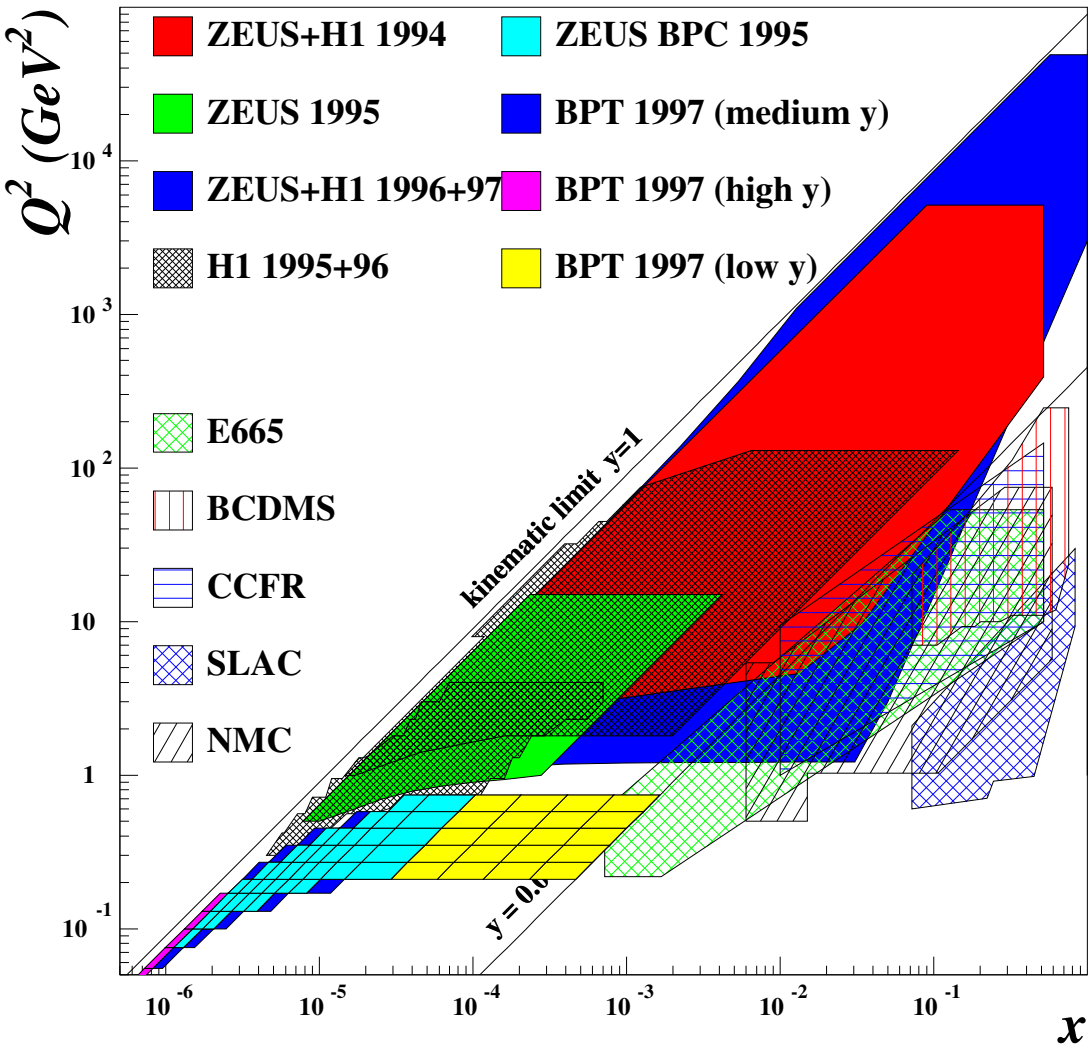


Figure 2.4: *Kinematic region of HERA and other ep scattering experiments.*

# Chapter 3

# The ZEUS detector

## 3.1 Overview

The ZEUS experiment is a multipurpose detector for the measurement of particle collisions at HERA [BR97]. The construction of the experiment has been finalized in autumn 1991. It is a complex instrument to determine the kinematic variables $x$, $y$ and $Q^2$ of $ep$ scattering in a large kinematic region. It is taking data since June 1992. Since then several modifications have been made and new components have been added.
The ZEUS detector is based on typical principles of particle detection. A tracking detector surrounds the interaction point of charged particles. Tracks are bent by a magnetic field and allow to determine the momentum and charge of particles. A calorimeter absorbs particles and measures their total energy deposition.
The ZEUS experiment requires a precise energy measurement with a calibration accuracy at the level of 1% [ZE91]. Therefore a high quality and stability of the components is of vital importance particulary if one considers the data taking time of more than 15 years.

Figure 3.1: *Cross-section at the ZEUS detector along the beam direction.*

Figure 3.1 shows a schematic view of the ZEUS detector. The proton direction is defined as the forward direction, the electron direction is defined as the rear direction. A system of cylindrical tracking devices measures charged particles and tracks. It consists of the vertex detector (**VXD**), the forward, central and rear tracking detectors (**FTD**, **CTD** and **RTD**), and the transition radiation detector (**TRD**). The tracking devices are within a superconducting solenoid (**coil**) which forces charged particles on spiral tracks due to a magnetic field of 1.43 T. A compensator reduces the overall influence of the magnetic field on the HERA beams. A cooling system supplies the magnetic components with liquid helium at a temperature of 4.5 K and a pressure of 1000 hPa. The helium is taken from the on-site cooling system of HERA. The high resolution, uranium scintillator calorimeter (**CAL**) surrounds the tracking devices and is divided into the forward (**FCAL**), the barrel (**BCAL**) and the rear calorimeter (**RCAL**). It has a total weight of 700 tons. It will be described more detailed in section 3.2. All mentioned components are enclosed by the iron yoke with a mass of 2000 t which serves for mechanical support and returns the magnetic field of the main coil. Particles which are not absorbed in the calorimeter deposit the remaining energy in the backing calorimeter (**BAC**). It consists of aluminium proportional chambers and copper coils with an inner magnetic field of 1.6 T. The chambers are filled with Ar-$CO_2$ as detection material. Rear and barrel muon detectors (**RMUON, BMUON**) are situated outside of the yoke and consist of limited streamer tubes. They measure the position direction of muons with a position resolution of 1 mm. A system of magnetized iron toroids and streamer tubes (**Fmuon-Toroids**) detect the muons in proton direction. The **Vetowall** allows the detection of particles produced by the proton beams from proton rest gas interactions upstream of the ZEUS detector.
Several modifications and new components have been realized since 1992. In 1994 a small rear track detector (**SRTD**) was installed. It covers the inner ring of the RCAL towers. Silicon diodes situated inside the calorimeter at a depth of 4 and 7 radiation lengths which serves the electron proton separation (**HES**). They were fully equipped in 1994 for the RCAL and in 1998 for the FCAL. A Forward Neutron Calorimeter (**FNC**), which is a lead scintillator sampling calorimeter has been installed in the HERA tunnel 105.6 m from the central ZEUS detector in the proton beam direction. It allows to measure the energy and scattering angle of neutrons produced in charge exchange of $ep$ collisions. A beam pipe calorimeter (**BPC**) was installed in the rear direction at a small distance with respect to the HERA beams in 1993, the first version was based on a tungsten silicon diode sampling calorimeter. In the maintenance period 1994/1995 it has been exchanged by a scintillator sampling calorimeter. The BPC allows to measure the electron energies at small angles. In 1998 the forward plug detector (**FPC**) was installed in the forward proton direction at a short distance with respect to the HERA beams. The FPC consists of a tungsten-scintillator calorimeter read out by thin wavelength shifter fibers.

## 3.2 Calorimetry at ZEUS

The high resolution calorimeter is a sampling calorimeter consisting of alternating layers of depleted uranium and plastic scintillators. It provides linear and equal response for electrons (e) and hadrons (h, like protons or pions) up to the highest energies. The principles and the functionality is described more detailed in Chapter 4.2. Further information can be found in [HO93]. The ZEUS calorimeter consists of the following three components:

- The forward calorimeter (**FCAL**), which is installed in the proton direction,

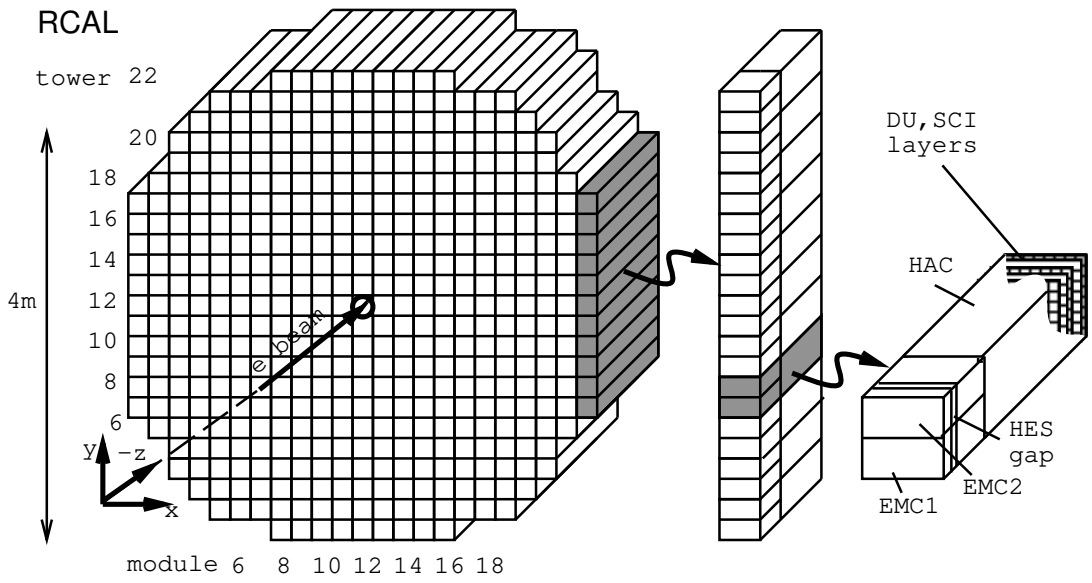


Figure 3.2: *Schematic front view from the interaction point of the RCAL.*

- the barrel calorimeter (**BCAL**), which surrounds cylindrically the tracking devices
- and the rear calorimeter (**RCAL**), which is installed in electron direction.

The calorimeter covers 99.8 % of the full solid angle, i.e. a polar angle $\theta$ from 2.6 ° to 176.1 °. The centre of mass of $ep$ scattering moves in proton direction, therefore the construction of the calorimeter is asymetrical. For a normal incidence, the depth of the CAL is 7 interaction lengths in the FCAL, 5 in the BCAL and 4 in the RCAL. The interaction point of the HERA beams is the origin of the ZEUS coordinate system, the horizontal $x$ axis points into the centre of the HERA storage ring, the $y$ axis points upward and the positive $z$ axis points into the proton direction[1]. The calorimeter has a modular structure consisting of 80 modules. The FCAL and the RCAL consist of 24 modules, respectively. They are separated into a left and a right half and are able to be retracted sideways. The F/RCAL modules are transversally subdivided in towers with a cross-sectional area of $20 \times 20\,\mathrm{cm}^2$. The towers are held together by a steel construction, the so-called C-arm. Stainless steel straps connecting an aluminium front plate to the back HERA beams compress the F/RCAL modules. 32 identical modules surround as barrel calorimeter the tracking devices which vary in width from 24 cm at the front to 43 cm at the outer radius. The transversally subdivision of the BCAL into towers is similar to F/RCAL[2]. The CAL modules are subdivided longitudinally into electromagnetic sections (EMC) and one hadronic section in case of the RCAL (HAC) or two hadronic sections (HAC1, HAC2) of nearly the same length in case of the FCAL. To improve the position resolution the electromagnatic sections are additionally segmented. Usually the FCAL tower has 4 EMC sections, the RCAL tower has 2 EMC sections according to a cross-sectional area of $5 \times 20\,\mathrm{cm}^2$ and $10 \times 20\,\mathrm{cm}^2$, respectively. The towers in the top and bottom of F/RCAL are covered by the barrel calorimeter and not reachable for electromagnetic particles. For those HAC0 sections no additional segmentation is needed. Silicon diodes (HES) are placed into two gaps in case of the FCAL, and one gap in case of the RCAL. The HES detectors are installed in the EMC sections

[1] In the following the algebraic sign of the axis will no further be denoted.

[2] The barrel calorimeter is not part of investigations of this thesis and will not further be described in the following.

at the depth of 3 and 7 radiation lengths.
The sections of the CAL with a total number of 5917 consist of alternating layers of absorber material and scintillator material configured in a sandwich construction. The absorber material is depleted uranium (DU), which offers beside an high density of $\approx 19\,\mathrm{g/cm^2}$ a small constant radioactive signal (uranium noise = UNO). Each uranium layer with a thickness of 3.3 mm is wrapped into a thin steel (0.4 mm for HAC sections). Plastic scintillator plates (*SCSN-38*) with a thickness of 2.6 mm are used as an active material. Each calorimeter section is read out by two photomultipliers connected with the right and left[3] wavelength shifter (*Y7*) using (*Philips XP 1911* for the EMC and *Hamamatsu R-580* for the HAC sections. This segmentation results in a total of 6526 photomultipliers for the electromagnetic sections and 5308 for the hadronic sections for all of the calorimeter sections. The UNO signal is used for a precise calibration of the photomultipliers and allows an accuracy of energy measurements within 1%. The nominal energy resolution of the calorimeter is presented under testbeam conditions [KL88]:

- $\sigma(\mathrm{E})/\mathrm{E} = 18\,\%/\sqrt{E} \oplus 1\,\%$, for electrons,
- $\sigma(\mathrm{E})/\mathrm{E} = 35\,\%/\sqrt{E} \oplus 2\,\%$ for hadrons.

(E in GeV, $\oplus$ means the quadrature sum.) The calorimeter energy response has been calibrated with an accuracy of about 2% [ZE91].

## 3.3 Running conditions

An important condition for calorimetry at ZEUS is the radiation resistance and stability of the optical components, i.e. the scintillators, wavelength shifters, light guides and photomultiplier tubes. Experiences from other experiments have shown that most of the radiation background occurs during the injection or the development of the beams. For this reason the FCAL/RCAL halves are opened during the injection and ramping periods with a distance of 40 cm. Also the synchrotron radiation[4] emitted by the electron beam and traversing the magnets close to the interaction point could play a decisive role with respect to the components closest to the HERA beams. Monitoring the accumulated radiation doses at ZEUS and controlling the optical components using passive and active devices is therefore of vital importance. Several monitoring principles have been used in order to investigate the integrity of the optical components and the photomultipliers of the ZEUS calorimeter [SC93]:

- UNO[5] calibration using the radioactivity of the uranium plates,
- calibration of the electronics using defined LED pulses on the photomultipliers,
- laser calibration to test for amplification and linearity,
- TLD crystals based on a Lithium-7 isotope fluoride ($LiF_2$) are used on the surface of F/RCAL towers close to the HERA beams,
- scans along the surface of F/RCAL towers close to the HERA beams using a $\gamma$ ray source ($^{60}$Co) during the maintenance period ($^{60}$Co monitor).

[3] Right and left side is defined with the respective view in direction of the interaction point.
[4] The upgrade of the HERA luminosity will considerably increase the synchrotron radiation [SU98a].
[5] **U**ranium **NO**ise.

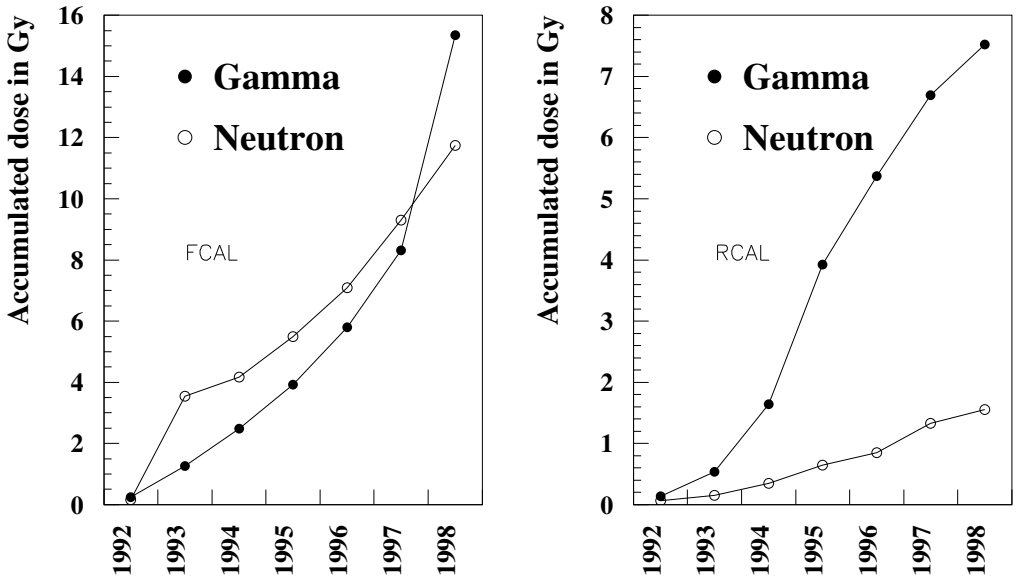


Figure 3.3: *Accumulated radiation doses at the CAL sections closest to the HERA beams due to neutrons and $\gamma$ radiation as a function of the running periods from 1992 to 1998 of the FCAL (left) and the RCAL (right).*

Figure 3.3 displays the accumulated $\gamma$ doses and neutron doses of the FCAL (left diagram) and the RCAL (right diagram) within the operating time from 1992 to 1998 using TLD crystals [PR99]. One has to take into account that the neutron dose measurement is restricted to thermal neutrons. The strong increase with regard to the $\gamma$ dose in the FCAL is correlated with the installation of the FPC and the required change of the beampipe (see section 3.1). Several components of the ZEUS detector remain close to the HERA beams (i.e. tracking devices, FPC, BPC). Radiation damage and other degrading effects have been observed in some calorimeter components[6] of ZEUS by the monitoring tools described above particulary by the $^{60}$Co monitoring system. These investigations will be described in detail in this thesis (see Chapter 7, 8 and 9).

[6] No radiation damage effects have been observed at the ZEUS uranium calorimeter.

# Chapter 4

# Theoretical aspects

The following chapter briefly describes the theory of particle reactions which occur when radiation passes through matter, particularly electromagnetic and hadronic processes. The principles of calorimetry are discussed, especially detection materials based on polystyrene (PS) and polymethylmethacrylate (PMMA) used at ZEUS. The characteristics of these materials with respect to irradiation will be briefly summarized.
A description of light propagation throughout optical materials has been developed which allows to transfer the knowledge of irradiation effects on small polymere samples to realistic dimensions of rectilinear parallelpipeds and scintillator plates. It allows to simulate numerically the light propagation for scintillator plates for both non-uniform or uniform radiation damage. This numerical simulation has been incorporated into EGS4 Monte Carlo simulation programs thus allowing to simulate the effects of radiation damage in a calorimeter.

## 4.1 Passage of radiation through matter

Particle reactions which occur when radiation penetrates matter are the basis of particle detection devices. The interactions depend on the type of radiation, its energy and the penetrated material. A calorimeter absorbs an incident particle completely and transforms a part of its energy into a measurable signal. The penetrated detection material can suffer radiation damage which affects a change of the detection characteristics. Therefore the knowledge of the particle reactions and effects produced by these processes on the material is of fundamental importance. The passage of particles through matter with kinetic energies from several keV upwards is mainly characterized by the following procedures [LE97]:

- Nuclear reactions,
- elastic/inelastic scattering from nuclei,
- Inelastic collisions with the atomic electrons of the material,
- emission of Cherenkov radiation and
- Bremsstrahlung.

Particle reactions resulting from the radiation passage through matter significantly depend on the type of radiation. In case of neutrons the principle means of interaction is through the strong force with nuclei. Because of the short range of this force these elastic/inelastic reactions

with nuclei are much rarer than the Coulomb interactions of charged particles in matter. The main energy loss of heavy charged particles in matter (i.e. particles heavier than an electron) occurs in inelastic collisions with the atoms causing an ionisation or excitation of the latter. The energy transferred in each collision is a small fraction of the total kinetic energy of the particles. The energy deposition $dE/dx$ can be described by the Bethe-Bloch formula [PE82]:

$$-\frac{dE}{dx} = 2\pi N_a r_e^2 m_e \rho \frac{Z \cdot z_c}{A \cdot \beta^2} \cdot \left( ln(\frac{2m_e\gamma^2 v^2 W_{max}}{I^2}) - 2\beta^2 \right), \tag{4.1}$$

where $r_e$ is the classical electron radius and $m_e$ the electron mass. $N_a$ is the Avogadro number, $I$ the mean excitation potential, $Z$ the atomic number, $A$ the atomic weight and $\rho$ the density of the absorbing material. The charge of the incident particle is given by $z_c \cdot e$, its velocity is $v$ with $\beta = v/c$ and $\gamma = 1/\sqrt{1-\beta^2}$, where $c$ is the speed of light. $W_{max}$ is the maximum energy transfer in a single collision. In practice, a density correction and an atomic shell correction has to be added to this formula. During its passage through matter charged particles can also produce Cherenkov radiation, which arises when the velocity $v$ of the particle is larger than the speed of light in the same medium.
The energy loss of electrons and positrons is similar to heavy charged particles, but besides the collisional energy loss an additional effect is observed; it is the electromagnetic radiation due to the electron scattering in the electric field of the nucleus (Bremsstrahlung). For kinetic energies of a few MeV or less the energy loss is dominated by ionisation. As the energy is increased up to a critical energy $E_c$, the energy loss due to Bremsstrahlung $(dE/dx)_{rad}$ is comparable to ionisation loss $(dE/dx)_{coll}$. Above this energy Bremsstrahlung dominates the energy loss of the electron in matter completely. The total energy loss of electrons and positrons is the result of radiation loss and collision loss:

$$\left(\frac{dE}{dx}\right)_{tot} = \left(\frac{dE}{dx}\right)_{rad} + \left(\frac{dE}{dx}\right)_{coll}. \tag{4.2}$$

$(dE/dx)_{coll}$ can be calculated by a modified Bethe-Bloch formula. For relativistic energies ($E > 1\,\mathrm{GeV}$) the energy loss due to Bremsstrahlung yields:

$$\left(\frac{dE}{dx}\right)_{rad} \simeq \frac{E}{X_0}, \tag{4.3}$$

where $E$ is the kinetic energy of the electron and $X_0$ the radiation length of the material which is approximately given by $X_0[\mathrm{g/cm^2}] \approx 180 \cdot \frac{A}{Z^2}$.
The interaction of photons in matter, especially of $\gamma$- or X-rays, is different from that of charged particles:

- Photoelectric effect: The absorption of a photon by an atomic electron with the emission of the latter. The photon energy $E_\gamma$ must have at least the binding energy of the electron.
- Compton scattering: The scattering of a photon on a free electron. The scattered photon transfers a fraction of its energy to the electron in form of a kinetic energy. In case of Thomson or Rayleigh scattering the photon scatters on the electrons of an atom as a whole which remains intact and emits the transferred energy due to $\gamma$-quants.
- Pair production: The transformation of a photon into an electron-positron pair under presence of a third partner, usually an atom. The photon energy $E_\gamma$ has to be bigger than 2 times of the energy at rest of the electron (1.022 MeV).

The attenuation of a photon beam intensity $I_\gamma$ during the passage through matter depends exponentially on the penetration depth $z$ into the absorber:

$$I_\gamma(z) = I_{\gamma 0} \cdot exp(-\mu z). \tag{4.4}$$

$I_{\gamma 0}$ is the incident beam intensity, the absorption coefficient $\mu$ characterizes the magnitude of the absorption of the material. At kinetic energies of a few keV or less the beam intensity loss in matter is dominated by the photoelectric effect. As the photon beam energy is increased Compton scattering dominates the interactions. At higher photon energies pair production dominates the energy loss in matter completely. The characteristics of photon interaction in matter is specified by the absorbing material, especially by its absorption coefficient $\mu$.

### 4.1.1 Electromagnetic and hadronic showers

During the passage in matter electrons and positrons of high energies ($E > E_c$) mainly produce Bremsstrahlung which initiates pair production, if their energy is bigger than 1.022 Mev. The combined effect of Bremsstrahlung emission by electrons and positrons and pair production by high energy photons forms a cascade of photons, electrons and positrons. This **electromagnetic** shower continues until the energy of the particles drops below the critical energy $E_c$. Then collisional energy loss dominates the interactions and no further electron-positron pairs are produced. Thus the propagation of the shower is halted [LO90]. The propagation of an electromagnetic shower converting Bremsstrahlung into pair produced electrons/positrons and vice versa doubles the particle number $N$ and bisects their average energy $E$ after each radiation lengths $X_0$. The maximum number $N_{max}$ of particles produced in the shower can be estimated as:

$$N_{max} \approx \frac{E_0}{E_c}, \tag{4.5}$$

where $E_0$ is the primary energy of the incident particle. The critical energy $E_c$ decreases with increasing atomic number of the absorbing material. Therefore heavy materials such as lead or tungsten are preferred absorbing materials inside calorimeters. Monte Carlo simulations and experimental data show, that the longitudinal profile of the average deposited energy of an electromagnetic shower can be approximated by [GI89]:

$$F(E, X) = \frac{b^{a+1} X^a e^{-bX}}{\Gamma(a+1)}, \tag{4.6}$$

The parameters $a$ and $b$ depend on the energy computed by the critical energy $E_c$. The depth of maximum energy deposition of the shower is given by $X_{max} = (a-1)/b = \ln(E/E_c + C_i)$, where the constant $C_i = e, \gamma$ denotes for electron or photon induced cascades.
A **hadronic shower** in matter is initiated by interactions between incident hadronic particle and nuclei of the absorbing material. Similar to an electromagnetic shower, but accompanied by a large variety of different interactions, a cascade of shower particles is produced. The hadronic shower propagation is dominated by inelastic scattering from nuclei with possible subsequent ejections of atomic particles. The nuclei are left in an excited state which later may decay by $\gamma$- or other forms of emission as vaporization, nucleus fission and neutral pions. These particles and also the decay of $\pi^0$ into two $\gamma$-quants produce electromagnetic sub showers. The longitudinal development of a hadronic shower can be described by the absorption length $\lambda_{int}$ [WOE91]:

$$\lambda_{int} \propto 35 \cdot \frac{A^{\frac{1}{3}}}{\rho} cm \ . \tag{4.7}$$

The energy deposition of a pure hadronic shower depends strongly on the energy of the incident hadrons. A fraction of its energy is deposited due to ionisation. The rest is lost by nuclear interactions and production of neutrinos. The consideration of the absorption length encountered by shower products allows to simulate hadronic cascades [CA98], [IG97].

### 4.1.2 Calorimetry

**Principles of calorimetry:** A calorimeter based on scintillating materials is one of the prime devices for energy measurements in high energy physics. One important condition for a correct energy measurement is the complete energy absorption of incident particles within the calorimeter and a partial transformation of the energy into fluorescense light. The light is transformed into measurable electrical pulses by photo detectors. Several possibilities exist to configure a calorimeter. A homogeneous calorimeter consists of one uniform material which is used for both energy dissipation and measurement (e.g. lead glas calorimeter). A sampling calorimeter is based on alternating layers of passive absorbing material and active detector material. For the absorption of particles mostly a material is used with high density $\rho$ and atomic number $Z$ such as lead, tungsten or iron. Plastic scintillators, liquid argon or silicon diodes as active materials offer possibilities for detection.
**Requirements for calorimetry:** Independently from any particular configuration a calorimeter has to fulfill the following characteristics. It should be sensitive to both charged and neutral particles. The calorimeter has to absorb the total energy of the incident particles. The penetration depth $d_c$ of an incident particle into the absorbing material is proportional to the logarithm of the primary energy $E$. If the measurement uncertainties are dominated only by statistical processes depending on the number of incident particles $N$, the energy resolution $\sigma/E$ decreases with increasing energy $E$ like $\propto 1/\sqrt{E}$ [FU93]. In sampling calorimeters a significant fraction of energy remains in the absorbing material due to the production of fragments of nuclei and does not contribute an amount to the measurable signal. At the same incident energy the ratio of the measurable energies of electromagnetic to hadronic showers, the so-called sampling fraction is larger than unity $e/h > 1$.
**The solution for the ZEUS calorimeter:** In order to reduce the differences from the energy measurement of electromagnetic and hadronic showers, the energy of the latter which remains in the absorber material has to be compensated. For this purpose the ZEUS calorimeter is using depleted uranium (DU) as an absorbing material of a thickness of 3.3 mm (equivalent to the radiation length $X_0$) along with plastic scintillators as active material of 2.6 mm (equivalent to $0.006 \cdot X_0$) per plate. A hadronic shower traversing the DU plates produces fast neutrons whose kinetic energies are proportional to the energy loss due to nuclear reactions of the shower. These neutrons lose most of their energy by scattering elastically off the free protons of the scintillator and hardly due to any scattering off the heavy uranium nuclei. The deposited energy of the neutrons compensates the energy loss of the hadronic shower and achieves a sampling fraction of $e/h \approx 1$ [BR86].

## 4.2 Principle of the ZEUS calorimeter

The ZEUS calorimeter is a sampling calorimeter consisting of depleted uranium plates for absorbing and of plastic scintillator plates (*SCSN-38*) as active material. The detection principle of the ZEUS calorimeter is shown in Figure 4.1. Incident high energy leptons, photons or hadrons produce within the absorber plates electromagnetic and hadronic showers. Secondary particles excite the scintillators due to ionisation processes with a decay time which is within the bunch rate of HERA (96 ns). The excited scintillator molecules decay under emission of ultraviolet light (UV) into the initial state. Absorption and reemission by two fluorescent dyes convert the light from UV into blue light of larger wavelength which traverses the scintillator. A fraction of it reaches the open ends by total inner reflection and enters into the respective wavelength shifter. The wavelength shifter converts the light from blue to green light. This light traverses under attenuation along the wavelength shifter from the active area, which covers the section of the calorimeter, to the passive area, which is wrapped by a black so-called tedlar foil [HO93]. Finally, the light reaches the photomultiplier, where it is transformed into an electrical signal. The observed light output $Q(x)$ of a calorimeter should be independent from the position of light production and its path to the photomultiplier. Therefore both the scintillators and the wavelength shifters are homogenized using special reflectors. The scintillator plates are wrapped with tyvek paper, which guarantees a high reflection coefficient. Additionally the paper is patternd in order to achieve the uniformity of the transverse light output. For the same reason the wavelength shifters are covered by backreflector papers. Moreover an aluminium reflector at the end of the wavelength shifter opposite to the photomultiplier decreases the light loss.

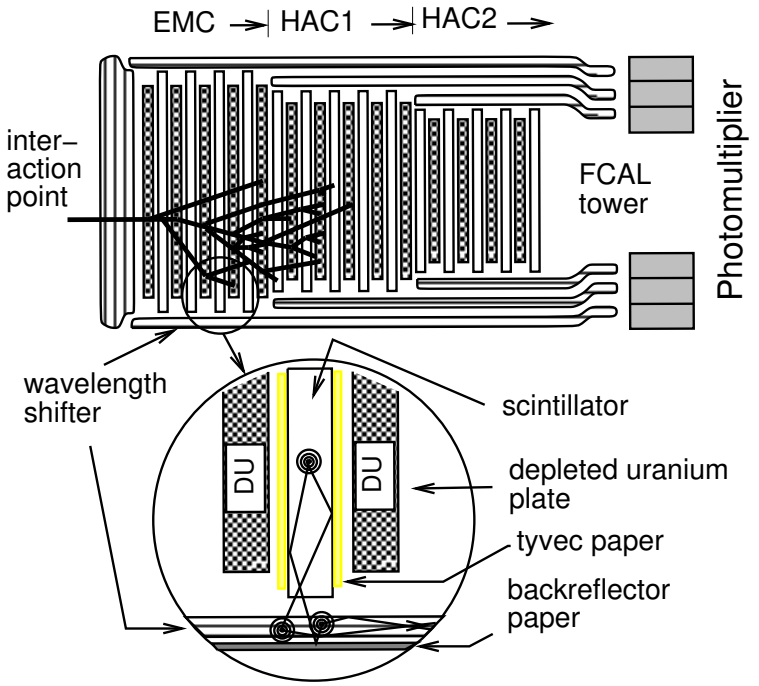


Figure 4.1: *Sketch of the optical readout of a ZEUS FCAL tower.*

Assuming a uniform response function of the calorimeter an incident electron with the energy $E$ produces the total average response $E_m$. This response depends on the energy deposition $F(E,X)$ of the electron-induced cascade (see formula 4.6) and the light output $Q(X)$ of the calorimeter:

$$E_m = E \cdot \frac{\int_o^L F(E,X) \cdot Q(X) dX}{(\int_o^L F(E,X) dX) \cdot (\int_o^L Q(X) dX)/L}. \tag{4.8}$$

The total average response $E_m$ is calculated in terms of the average energy per unit length $F(E,X)$ deposited at the position $X$ in units of radiation length $X_0$, which is in case of the ZEUS EMC section $X_0 = 0.74\,\mathrm{cm}$ with $X = x/X_0$. $L$ is the length of the calorimeter in units of the radiation length $X_0$. The energy deposition depends on two parameters $a$ and $b$

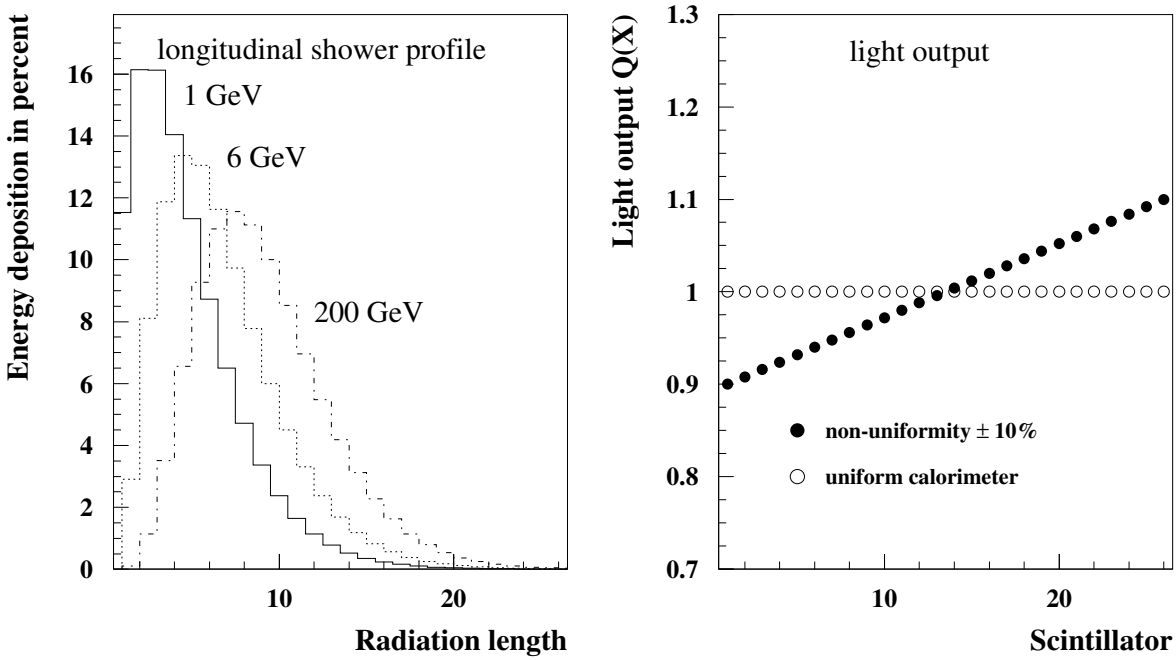


Figure 4.2: *Energy deposition (left) and scintillator response of a FCAL EMC section (right).*

which are computed for the ZEUS EMC section from the critical energy $E_c = 10.6MeV$. For many purposes (as uranium or lead) it is sufficient to take $b(E) \approx 0.5$. The longitudinal light output $Q(X)$ of the calorimeter should be uniform and independent from the position of light production. The summation over all $n$ scintillators yields:

$$E_m = E \cdot \frac{\sum_n F(E, X_n) \cdot Q_n}{(\sum_n F(E, X_n)) \cdot (\sum_n Q_n)/n}, \tag{4.9}$$

The energy deposition for incident electrons with energies of 1 GeV up to 200 GeV has been calculated using equation 4.9 for the FCAL EMC section. The results are presented in the left diagram of Figure 4.2. The right diagram of Figure 4.2 displays the light output of a uniform section in comparison to one with a non-uniformity of $\pm 10\%$. The measured energy $E_m$ versus the impact energy $E$ of the latter is shown in the left diagram of Figure 4.3. The deviation from linearity of the energy measurement in such a case is presented in the right diagram.

## 4.3 The optical components of the ZEUS calorimeter

The scintillator of the ZEUS Calorimeter is *SCSN-38* (manufacturer is KURARAY Co., Ltd., Tokyo, Japan) based on polystyrene (PS, structure is shown in diagram 4.4). Those polystyrene materials scintillate already without additional dyes. *SCSN-38* is using two dyes, the first, Butyl-PBD, shifts UV-light of the scintillating polystyrene matrix (about 300 nm) into wavelengths of about 360 nm. The concentration of the fluor in the scintillator is about 1 %. The emission spectrum of Butyl-PBD is within the absorption spectrum of the second dye, BDB which amounts in the scintillator with 0.02 %. BDB emits blue light (about 430 nm) with an attenuation length of 70 cm. The wavelength shifter material is based on polymetylmethacrylate (PMMA, structure is shown in diagram 4.4). The wavelength shifter (same manufacturer as mentioned above) of the ZEUS Calorimeter is doped with fluorescent dye of 30 ppm and

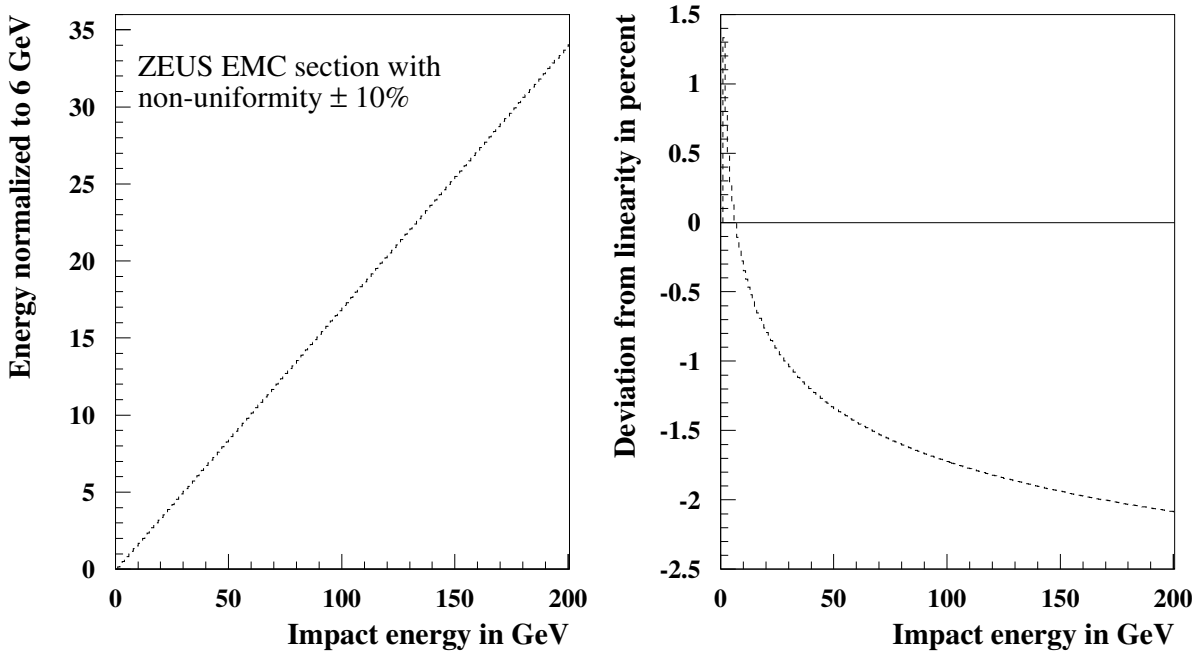


Figure 4.3: *Measured energy versus impact energy (left) and deviation from linearity (right) for a FCAL EMC section assuming a longitudinal non-uniformity of* $\pm 10\%$.

45 ppm of Y7. The absorption and emission spectra of the wavelength shifter matches well with those of the scintillator and the spectral sensivity of the photomultipliers.

| Material | density $\rho$ | refraction index $n$ |
|---|---|---|
| SCSN-38 | 1,06 g/cm$^3$ | 1,6 |
| PMMA | 1,19 g/cm$^3$ | 1,5 |

Table 4.1: *Density and mean refraction index of the basis material polystyrene (SCSN-38) and polymethacrylat (PMMA) used in the ZEUS calorimeter for scintillators and wavelength shifters.*

**Radiation and polymere materials** Radiation from a few eV upwards ionizes polymere materials. In case of the scintillators the ionisation results into the production of fluorescense light. Beside ionisation, it can also cause variation of the polymere structure changing the optical characteristics of the irradiated material. In case of the scintillators, wavelength shifters or light guides two macroscopic effects of radiation damaged material are observed [WU95].
A reduction of the primary light yield and a change in the transmission of the light inside the polymere. These effects result from microscopic processes of irradiation based on reactions between ions, radicals and the polymeres: Ions produced by the radiation recombine by the Coulomb interaction and produce molecules in an excited state leaving radicals in the material. The radicals form additional absorption centers, absorbing fluorescense light. The number of radicals as well as the number of destroyed dyes are proportional to the radiation dose. The dependence on the radiation dose rate is a more complex process [BU93]. Presence and diffusion of oxygen is of significant importance in this case. On the one hand oxygen ties the radicals,

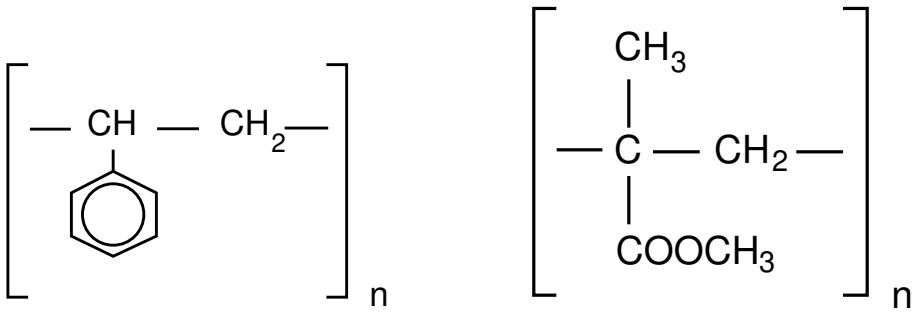


(a) *Structure of polystyrene.*

(b) *Structure of polymethylmethacrylate.*

Figure 4.4: *Structure of scintillator SCSN-38 and wavelength shifter PMMA.*

on the other hand the number of radicals is increased due to transfer reactions. Diffusion of oxygen is influenced by its concentration, temperature and the geometry of the material. In case of higher dose rates the influence of oxygen on the chemical reactions is decreased due to the long diffusion time of oxygen from the outside atmosphere inside the irradiated material. The following processes occur [BU97]:

$$\text{Inition of radicals:} \quad \mathrm{R} \xrightarrow{\gamma} \mathrm{R}\cdot \tag{4.10}$$

$$\text{Propagation of radicals:} \quad \mathrm{R}\cdot \xrightarrow{\mathrm{O_2}} \mathrm{RO_2}\cdot \tag{4.11}$$

$$\mathrm{RO_2}\cdot \xrightarrow{\mathrm{RH}} \mathrm{RO_2H} + \mathrm{R}\cdot \tag{4.12}$$

$$\text{Bifurcation:} \quad \mathrm{RO_2H} \longrightarrow \mathrm{RO}\cdot + \cdot\mathrm{OH} \tag{4.13}$$

$$\mathrm{RO}\cdot \xrightarrow{\mathrm{RH}} \mathrm{ROH} + \mathrm{R}\cdot \tag{4.14}$$

$$\cdot\mathrm{OH} \xrightarrow{\mathrm{RH}} \mathrm{H_2O} + \mathrm{R}\cdot \tag{4.15}$$

$$\text{Decay or networking:} \quad \mathrm{RO_2H},\ \mathrm{RO_2}\cdot,\ \mathrm{R}\cdot \xrightarrow{\mathrm{RH}} \text{further processes.} \tag{4.16}$$

$$\text{Termination reactions:} \quad 2\ \mathrm{RO_2}\cdot \longrightarrow \mathrm{RO_2R} + \mathrm{O_2}. \tag{4.17}$$

These reactions induce chemical variations of the dyes depending on the external conditions like atmosphere and temperature. The consequences are a wavelength dependent reduction of both the primary light yield and a change of its transmission. The change of transmission is wavelength dependent. A destruction of the fluor causes an increase of the transmission. In case of irradiated scintillator material based on *SCSN-38* this effect is seen for wavelengths between 350 – 410 nm. Simultaneously the formation of new absorption centers is possible with a reduction of the transmission (in case of *SCSN-38* from 410 nm upwards). Generally the transmission of the wavelength dependent fluorescense light $I_0(\lambda)$ produced at a distance $x$ can be described by:

$$I(\lambda, x) = I_0(\lambda) \cdot T(\lambda, x), \tag{4.18}$$

$$T(\lambda, x) = e^{-\mu(\lambda)\cdot x}. \tag{4.19}$$

$I(\lambda, x)$ is the measured wavelength dependent intensity at the end of the light guide after a propagation of a distance $x$ from the formation of the light to the open end. The transmission $T(\lambda, x)$ describes the attenuation of the light in the polymere material, whereas $\mu(\lambda)$ is the

wavelength dependent absorption coefficient of the polymere material. The formula is similar to the attenuation of light during the passage through matter described in section 4.4. Radiation damage causes a position dependent change of the primary light yield $I_0(\lambda) \rightarrow I_0(\lambda, x)$ and a position as well as time dependent change of attenuation $\mu(\lambda) \rightarrow \mu(\lambda) + \Delta\mu(\lambda, x, t)$. The absorption coefficient of an irradiated polymere is time dependent with respect to the influence of oxygen. It could be described by a time dependent initial damage and a time independent permanent damage. The following investigations only refer to permanent radiation damage effects of optical components. Any time dependence will be neglected. Radiation damage due to a uniform irradiation with a radiation dose $D$ causes a change of the absorption coefficient and transmission described by:

$$\mu_D(\lambda, D, t) = \mu(\lambda) + \Delta\mu(\lambda), \tag{4.20}$$

$$\Delta\mu(\lambda) = b(\lambda) \cdot D, \tag{4.21}$$

$$T(\lambda, x) = e^{-(\mu(\lambda)+b(\lambda)\cdot D)\cdot x}. \tag{4.22}$$

$b(\lambda)$ is the permanent damage per radiation dose in units of $\mathrm{Gy}^{-1}\cdot\mathrm{cm}^{-1}$. Table A.1 and A.2 of the appendix A present the permanent damage in case of *SCSN-38* and *PMMA*. Within a dose range of 0 – 10 kGy the decrease of the primary light yield $I_0(\lambda)$ of *SCSN-38* and *PMMA* can be described by [DA96]:

$$I(\lambda) = I_0(\lambda) \cdot (1 - c_i \cdot D), \tag{4.23}$$

$$c_i = \begin{cases} (9 \pm 1) \cdot 10^{-6}\mathrm{Gy}^{-1} & : \ \textit{SCSN-38}, \\ (3 \pm 1) \cdot 10^{-6}\mathrm{Gy}^{-1} & : \ \textit{PMMA}. \end{cases}$$

$c_i$ is the respective correlation between the reduction of light yield and radiation dose. In case of 1, 5 and 10 kGy irradiated *SCSN-38*, the intensity of the fluorescence light is expected to decrease by 1%, 4% and 9%. The initial damage recovers completely a few days after irradiation. In case of 1, 5 and 10 kGy irradiated *PMMA*, the intensity of the fluorescence light is expected to decrease by 0.3%, 1.5% and 3%. A 1 kGy irradiation of *PMMA* produces an initial damage which is comparable to a permanent damage in the order of a 6 kGy irradiation [WI98] recovering slowly over a period of several months.

## 4.4 Calculation of light propagation

In the following an algorithm is presented which describes the light propagation through optical materials and light guides, respectively. It transfers the knowledge of irradiation effects on small scintillating samples up to realistic dimensions of rectilinear parallelpipeds and scintillator plates. It allows to simulate numerically the light propagation in light guides for both non-uniform or uniform radiation damage. The algorithm calculates the intensity of the emitted light output as a function of the location of the light production according to the attenuation curve. It integrates over the wavelength of the fluorescense spectrum and all effective emitting angles. The algorithm is based on a numerical calculation of light propagation through orthogonal plates of homogeneous scintillators, wavelength shifters and light guides [DA96]. The algorithm allows the calculation of all possible light propagations of a pointlike excited light source parallel to the optical axis of a light guide added to a total intensity at the open end. Light reflection effects at all sides of the light guide are included.

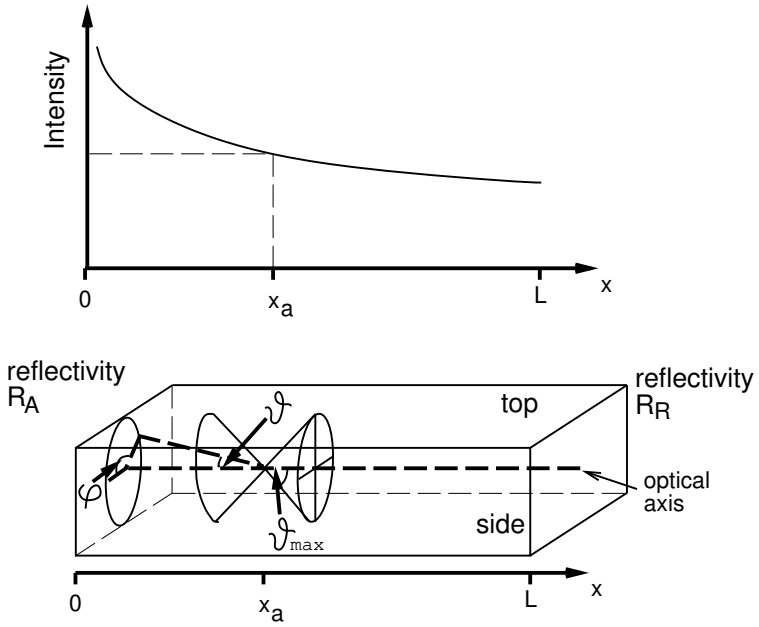


Figure 4.5: *Sketch of a light guide (bottom) and the light intensity measured at the open end as a function of the position of light production (top). Only light which is emitted within two light cones restricted by the angle of total inner reflection will leave the light guide at its end.*

The modification of the algorithm incorporates a non-uniform radiation damage of the light guide into the calculation: A Gaussian distributed radiation damage can be placed at variable positions parallel to the optical axis of the light guide. The calculation program needs a data set including the material dependent absorption coefficients, fluorescense intensities and the parameters describing the radiation dependencies of absorption and primary light yield. For the materials *SCSN-38*, *PMMA* and $PbWO_4$ the data sets are available (see appendix A). The algorithm is translated into a computer application based on the programming language[1] C; a detailed description of the algorithm as well as the the computer code can be found in the appendix A.

**Light yield in case of non-uniform radiation damage:** A radiation damage in a polymere material causes a destruction of fluorescent dyes and a formation of additional absorption centers. The consequence is a reduction of light yield and a wavelength dependent change of the transmission (see 4.23 and 4.22) as a function of the position. If one neglects radiation dose rate effects, the damage is assumed to be proportional to the radiation dose. The ansatz of the light propagation through a non-uniform damaged light guide comes from the radiation dose $D(x, y, z)$ which depends in case of inhomogenous damage on the position $x$, $y$ and $z$.

[1] C is very useable programming language compatible to different operating systems [BU88].

For a specific example, which is relevant for the damage which occurred in the beam pipe calorimeter (see Chapter 9) $D(x,y,z) \approx D(x)$ is assumed to be Gaussian distributed in the longitudinal direction along the optical axis, whereas it is assumed to be uniform over the width and the depth of the light guide. In the case of the beam pipe calorimeter a non-uniform radiation damage of a scintillator plate due to incident high energy particles could be described in good approximation by a Gaussian function with a maximum radiation dose $D_0$ at the position $x_D$ and width $R_D$:

$$D(x) = D_0 \cdot e^{-\frac{1}{2}\frac{(x-x_D)^2}{R_D{}^2}}. \qquad (4.24)$$

The intensity of the fluorescense light $I(\lambda, x)$ produced at a certain position $x$ within the light guide decreases by the radiation damage similar to equation 4.23:

$$I(\lambda, x) = I_0(\lambda, x) \cdot (1 - c_i \cdot D(x)), \qquad (4.25)$$

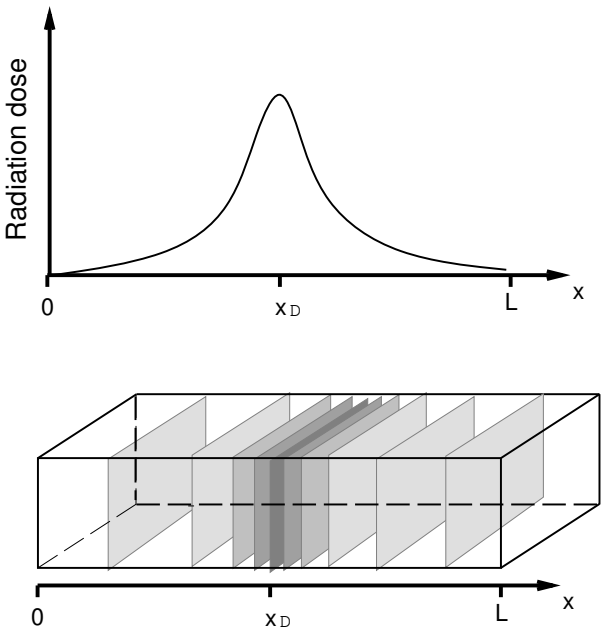


Figure 4.6: *Sketch of a orthogonal plate (bottom) with a Gaussian distributed radiation damage and radiation dose profile in the longitudinal direction (top).*

The fluorescense light will be emitted isotropically over the whole solid angle. Only the light which is emitted within two light cones will leave the light guide at its end contributing an measurable intensity. The maximum opening angle of the light cones is determined by the refraction index $n$ according to the angle of total inner reflection of the material with $\vartheta_{max} = \mathrm{asin}(1/n)$ [BE73]. Light propagating outside these cones remains in the light guide and gets lost at the cover or opposite sides due to reflection losses. Figure 4.5 illustrates the light propagation through a light guide under a polar angle $\vartheta$ and an azimuth angle $\phi$ relative to the optical axis. The light guide is irradiated non-uniformly with a Gaussian distributed dose profile illustrated in Figure 4.6. The light of the wavelength $\lambda$ which propagates within the light cone directly to the open end and transmits through the light guide immediately contributes to the measurable signal the intensity

$$I_{d0}(\lambda, x, \varphi, \vartheta) d\lambda d\Omega = I(\lambda, x) \cdot R_{side}^{N_{side}(x,\varphi,\vartheta)} \cdot R_{top}^{N_{top}(x,\varphi,\vartheta)} \cdot T_A(\vartheta) \cdot T_{dir}(\lambda, x, \vartheta) d\lambda d\Omega, \qquad (4.26)$$

$$T_{dir}(\lambda, x, \vartheta) = e^{-\frac{\mu(\lambda)\cdot x}{\cos\vartheta}} \cdot e^{-\frac{b(\lambda)}{\cos\vartheta}\int_0^x D(x')dx'}. \qquad (4.27)$$

$I(\lambda, x) d\lambda d\Omega$ denotes the intensity of the fluorescense light produced at the location $x$ emitted in the solid angle $d\Omega$ and the wavelength interval $(\lambda, \lambda + d\lambda)$. The transmission $T_{dir}(\lambda, x, \vartheta)$ characterizes the light attenuation during the propagation along the pathlength $x/cos(\vartheta)$ to the open end. The computation of $T_{dir}$ according to equation 4.27 takes into account the non-uniform radiation damage $D(x)$ of the light guide[2]. The reflection losses on side and top surfaces of the light guide are computed by the material dependent factors $R_{side}$ and $R_{top}$. The number of reflections $N_{side}(x, \varphi, \vartheta)$ and $N_{top}(x, \varphi, \vartheta)$ can be calculated by a simple geometrical ansatz (see appendix A). The transmission $T_A(\vartheta)$ determines the part of light transmitted out

[2] In the special case $D(x)$ =const. and $\vartheta = 0^0$ equation 4.27 agrees with equation 4.22.

of the end of the light guide depending on the relative refraction index $n$ and the angle $\vartheta$ with respect to the surface normal. Assuming unpolarized light $T_A(\vartheta)$ is given by the Fresnel formula (see appendix A). The part $R_A(\vartheta) = 1 - T_A(\vartheta)$ of light which is reflected at the open end of the light guide propagates to the opposite side. There it is partially reflected with $R_R(\vartheta)$ and propagates back to the open end, where again a part $T_A(\theta)$ of the light is emitted. The reflected light propagates through the whole light guide again and will undergo single or multiple reflections until the light transmits through the open end. The infinite summation of all intensities of light $\sum_{i=0}^{\infty} I_{di}(\lambda, x, \varphi, \vartheta)$ is a geometrical series and converges to a finite value. The light beam within the second light cone propagates first to the opposite side. A part $R_R(\theta)$ is reflected there and propagates back to the open end of the light guide. The whole pathlength of the light propagation is $(2L - x)/cos\theta$. The first order of intensity $I_{i0}(x, \lambda, \varphi, \vartheta)$ of this light measured at the open end yields:

$$\begin{aligned} I_{i0}(x,\lambda,\varphi,\vartheta) &= I(\lambda)\cdot T_{dir}(\lambda, L, \vartheta)\cdot T_{ind}(\lambda, L-x, \vartheta) \\ &\quad \cdot R_{side}^{N_{side}(2L-x,\varphi,\vartheta)}\cdot R_{top}^{N_{top}(2L-x,\varphi,\vartheta)}\cdot R_R(\vartheta)\cdot T_A(\vartheta), \qquad (4.28) \\ T_{ind}(\lambda, L-x, \vartheta) &= e^{-\frac{\mu(\lambda)\cdot(L-x)}{\cos\vartheta}}\cdot e^{-\frac{b(\lambda)}{\cos\vartheta}\int_x^L D(x')dx'}. \qquad (4.29) \end{aligned}$$

$T_{ind}(\lambda, L-x, \vartheta)$ considers the attenuation of the light during the propagation from the position of light production to the opposite side of the light guide. The infinite summation of all intensities $\sum_{i=0}^{\infty} I_i(\lambda, x, \varphi, \vartheta)$ converges to a finite value, too. Two opposite lightbeams with same angles $\varphi$ and $\vartheta$ can be added to $I_{total}$ assuming an isotropic emission of fluorescense light:

$$I_{total}(\lambda,x,\varphi,\vartheta) = \frac{I(\lambda,x)\cdot T_A(\vartheta)\cdot(I_{direct}(\lambda,x,\varphi,\vartheta)+I_{indirect}(\lambda,x,\varphi,\vartheta))}{1-T_{dir}(\lambda,2L,\vartheta)\cdot R_{side}^{N_{side}(2L,\varphi,\vartheta)}\cdot R_{top}^{N_{top}(2L,\varphi,\vartheta)}\cdot R_A(\vartheta)\cdot R_R(\vartheta)}, \qquad (4.30)$$

with:

$$\begin{aligned} I_{direct}(x,\lambda,\varphi,\vartheta) &= T_{dir}(\lambda,x,\vartheta)\cdot R_{side}^{N_{side}(x,\varphi,\vartheta)}\cdot R_{top}^{N_{top}(x,\varphi,\vartheta)}, \\ I_{indirect}(x,\lambda,\varphi,\vartheta) &= R_R(\vartheta)\cdot T_{ind}(\lambda,L-x,\vartheta)\cdot T_{dir}(\lambda,L,\vartheta)\cdot R_{side}^{N_{side}(2L-x,\varphi,\vartheta)}\cdot R_{top}^{N_{top}(2L-x,\varphi,\vartheta)}. \end{aligned}$$

The integration of equation 4.30 over all possible solid angles and wavelengths of the emission spectrum of the light guide $[\lambda_a, \lambda_e]$ allows to calculate the measurable intensity $I_{meas}$ of the light leaving the light guide at the open end.

$$I_{meas} = \int_{\lambda_a}^{\lambda_e} d\lambda \int_0^{\vartheta_{max}} d\vartheta\ \sin\vartheta \int_0^{2\pi} d\varphi\ I_{total}(\lambda, x, \varphi, \vartheta). \qquad (4.31)$$

The integral 4.31 is transformed into a numerical summation which is incorporated into a computer code in order to simulate the light propagation throughout variable orthogonal materials. Operating as well as comments of input parameters of the source code lightsim will be described in detail in the appendix A. The calculation for a light guide with a certain geometry and a possible non-uniform radiation damage is based on a material specific database including the wavelength $\lambda$, the absorption coefficient $\mu(\lambda)$, and the fluorescense intensity $I(\lambda)$. The parameters $b(\lambda)$ and $c_i$ which describe the influence of the radiation dose on additional absorption centers and the reduction of the primary light yield are also included. The database is derivated from investigations on irradiated scintillator and wavelength shifter materials which are presented in tables. Special detector properties are considered (e.g. different photomultiplier

tubes, filter systems) within the databases[3]. The calculation of light propagation considers the individual geometries, refraction index and fluorescense emission (due to wavelength dependent emission and absorption spectrum). The reflection coefficients consider the surface characteristics as insufficient polish, etc.. The numerical calculation has been applied to different optical components used at ZEUS. The comparison between measured attenuation curves of individual scintillators and the calculated ones show an impressing agreement (see Chapter 9.3.3). An indirect test of the numerical calculation is performed using the calculated attenuation curves presented in Figure 4.7 within a Monte Carlo simulation. The aim is to simulate the ZEUS calorimeter response of a RCAL HAC0 section during a specific measurement procedure (see Chapter 7.4.4). The simulation reproduces the results of the actual measurements very precisely.

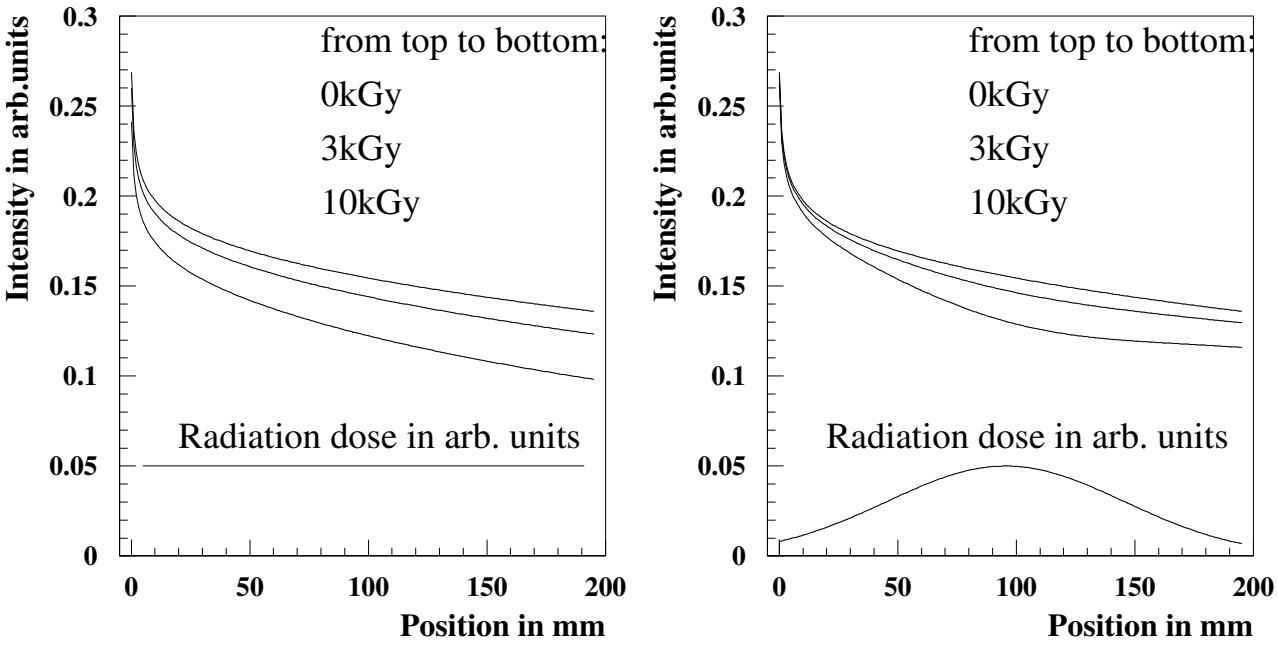


Figure 4.7: *Light yield of RCAL HAC0 scintillators in case of uniform (left) and non-uniform irradiation of 3 and 10 kGy in comparison to a reference scintillator. The longitudinal radiation dose profile is presented on the bottom.*

**Light yield in case of a circular readout shape:** The calculation of the light intensity described above assumes that the open end of the light guide is equivalent to the total readout face. Accordingly the intensity calculated by lightsim results from the light emitted out of the open end. An application which depends on a readout smaller than the total surface reduces the measurable intensity (i.e. a photomultiplier on the surface of the open end with a smaller size). It is interesting to know the intensity measured at the open end of such an application as a function of the longitudinal, vertical and horizontal position of the light production. The exact calculation would require the complete knowledge of all light tracks including the reflections on the surfaces of the light guide. A good approximation is the following simple ansatz consisting of a circular readout shape which is easily implemented into the calculation described above. Figure 4.8 demonstrates a possible application: A homogenous lead tungstate crystal ($PbWO_4$)

[3]The database used in the following for *SCSN-38* is based on the principle configuration of the ZEUS uranium calorimeter readout.

calorimeter[4] based on a orthogonal light guide of $23.8 \times 23.8 \times 200\,\mathrm{mm}^3$ is read out by a circular photomultiplier tube with a diameter of 16 mm centered at one open end covering only about 35% of the total surface. Only fluorescense light propagating directly to the readout face contributes a measurable signal.

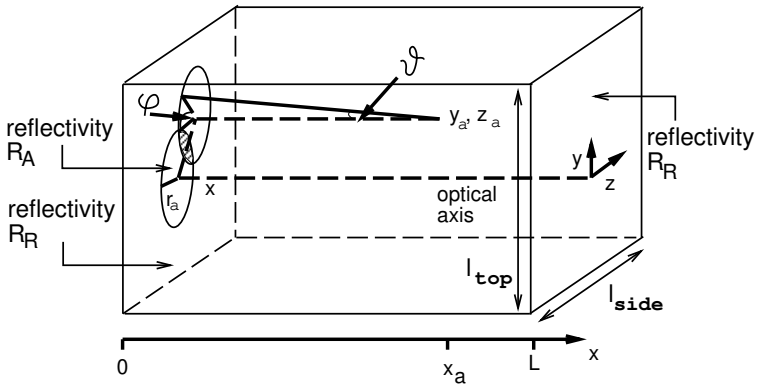


Figure 4.8: *The diagram shows an orthogonal light guide which will be excited parallel to the optical axis. The readout is limited to a small circular window.*

The rest of the light which is reflected or does not hit the readout face directly will be single or multiple reflected during the propagation to the readout until it hits the readout face and is emitted. The probability to hit the readout face depends on the position and the angle of the light emission; an exact calculation is difficult and needs a precise tracing of the light paths. The simplifying ansatz assumes a constant probability $W_A$ for the light to hit the readout face after single or multiple reflections given by the ratio of the readout face with the radius $r_a$ and the total surface $l_{side} \times l_{top}$ of the open end:

$$W_A = \frac{\pi \cdot r_a^2}{l_{side} \cdot l_{top}}. \tag{4.32}$$

The calculation of intensities is separated into the two cases. $j = 0$ denotes the most probably case in which the light will be single or multiple reflected during its propagation to the readout. The transmission of light at the open end is then given by $T'_A = T_A(\vartheta) \cdot W_A$. Accordingly the intensity $I_{total}(\lambda, x, \varphi, \vartheta, T'_A)$ is calculated by the algorithm 4.30. $j = 1$ denotes the second case in which the light propagates directly to the readout face. Then the part $T_A(\vartheta)$ of this light will transmit through the light guide immediately. In that case the part $I_{d0}(\lambda, x, \varphi, \vartheta, T'_A)$ of the total intensity has to be substituted by the part $I_{d0}(\lambda, x, \varphi, \vartheta, T_A)$:

$$\begin{aligned} I_{total}(T_A, T'_A) &= I_{total}(T'_A) - I_{d0}(T'_A) \cdot \delta_j + I_{d0}(T_A) \cdot \delta_j. \\ \delta_j &= \begin{cases} 0 & : \text{ single or multiple reflections,} \\ 1 & : \text{ light traverses directly to the readout.} \end{cases} \end{aligned} \tag{4.33}$$

The dependencies of $\lambda, x, \varphi, \vartheta$ are not noted explicitly. The two cases can be distinguished by the following geometrical calculation: The position of light production is defined at the position $y_a$ and $z_a$ relative to the optical axis with a distance $x_a$ from the open end of the light guide (see Figure 4.8). Then the hit position $r_{hit}$ yields to:

$$r_{hit} = \sqrt{(y_a + x_a \cdot tan\theta \cdot sin\phi)^2 + (z_a + x_a \cdot tan\theta \cdot cos\phi)^2}. \tag{4.34}$$

Case $j = 1$ applies if the hit position is smaller or equal to the radius of the readout face with $r_{hit} \leq r_a$.

Figure 4.9 displays the simulated light yield measured at the open end (corresponding to $x = 0\,\mathrm{mm}$) of a $PbWO_4$ crystal described above as a function of the $x$, $y_a$ and $z_a = 0\,\mathrm{mm}$ position. One clearly notices the strong $y_a$ dependence of the light yield close to the open end, whereas it is almost uniform in case of an unlimited readout shape.

[4] A small beam pipe calorimeter developed to replace the present wolfram/scintillator sampling calorimeter BPC [GE98].

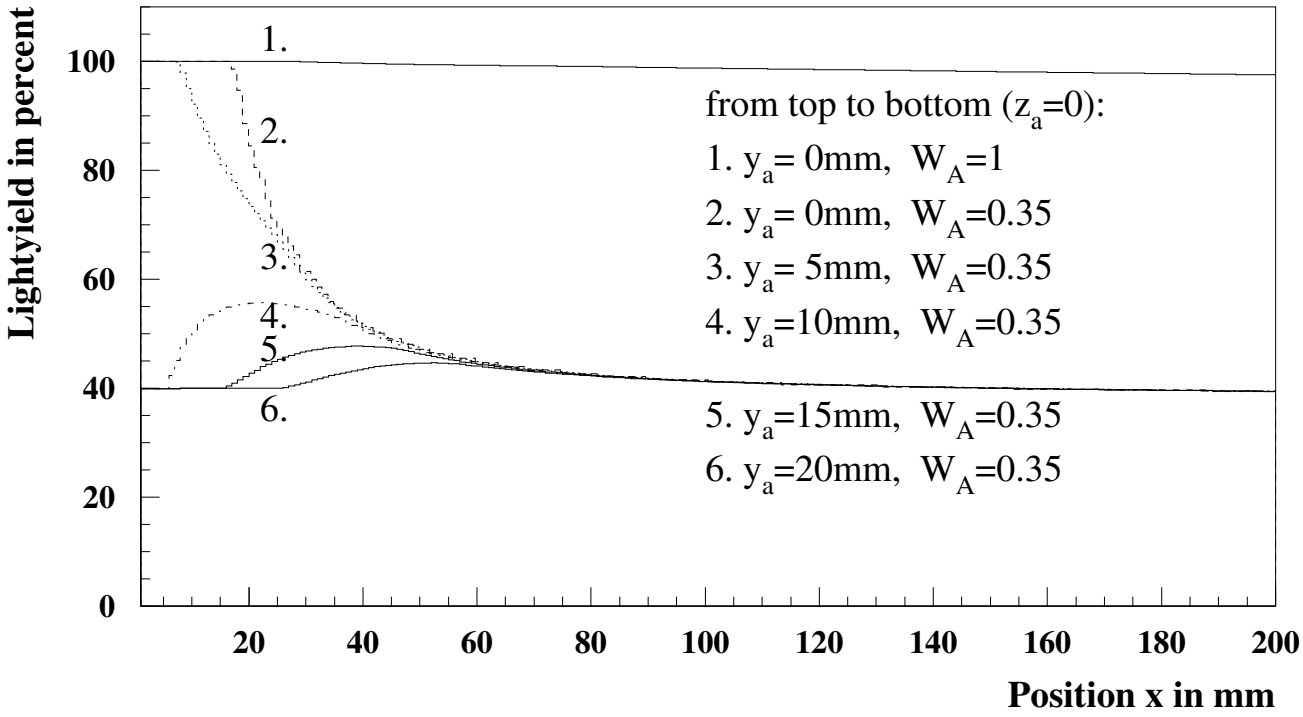


Figure 4.9: *Light yield of a $PbWO_4$ crystal using a limited readout shape as a function of the position x, $y_a$ and $z_a$ of light production. The 1.curve displays the case of an unlimited readout shape over the whole open end.*

## 4.5 Simulation of electromagnetic showers

The simulation of particle detection and energy measurement of a calorimeter using absorbing and detection material depends on two features: The knowledge of the energy deposition of incident particles and the signal processing, i.e. the light production and propagation in the optical components. The calculation of light propagation in polymere materials is described above. The development of electromagnetic showers are described in section 4.1.1. However, the equations 4.5 and 4.6 only give a rough qualitative picture of the shower. A Monte Carlo simulation program is required to make a precise calculation of the average energy deposition of electromagnetic showers. The electron gamma simulation program package EGS4 is an application based on Monte Carlo algorithims for simulating electromagnetic processes in arbitrary geometries [NE85]. It was originally developed at **SLAC**[5] for high energy physics applications and has been extended to applications for lower particle energies. EGS4 simulates the transport of two different types of particles, electrons/positrons and photons in any element, compound or mixture. By including data preparation packages it allows the creation of material data in the required energy interval for photons and electrons/positrons. In addition to the required information about the initial particles the simulation needs further information generated by subroutines which interface with the EGS4 code. The first subroutine defines the geometry of the simulated region. The other determines when to discard a shower particle. Both subroutines have to be generated with respect to the individual device and can be used to extract detailed information about the simulation, i.e. n-tuples or histograms for further

[5]Stanford Linear Accelerator Center.

analyses. More information can be found in [FR99], [NE96], [SU98]. The knowledge of both energy deposition of incident particles and light propagation of the optical components allows to determine the calorimeter response.

# Chapter 5

# Experimental aspects

The ZEUS calorimeter provides precise energy measurements[1] in order to determine the kinematics of $ep$ scattering over a large kinematic region. Several monitor systems have been developed to control the quality and stability of the optical components. The following chapter describes the applications and experimental requirements which are used for investigations of the optical properties on several ZEUS calorimeter components described in this thesis. A flexible and portable $^{60}$Co monitor system has been developed for these investigations. It allows the determination of the optical properties, especially of the scintillators and wavelength shifters. An algorithm is presented which performs the unfolding of the $^{60}$Co data to determine the response of each single scintillator within a calorimeter section. A special scanning bench is presented for the investigation of individual light guides and scintillating materials using different excitation sources. The dosimetry used in this thesis is based on two different methods. It allows to measure the radiation doses with an accuracy of about 10%.

## 5.1 The $^{60}$Co monitor system

One of the primary goals of the $^{60}$Co monitor system is to observe the quality and the status of the Forward and Rear Calorimeter of the ZEUS Calorimeter. Reference measure-

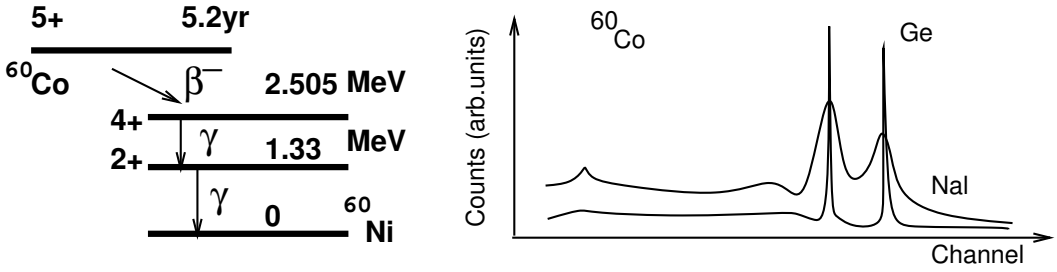


Figure 5.1: *Nuclear level diagram of the $^{60}$Co compound (left) and a sketch of spectra from a $^{60}$Co source (right) measured with a NaI detector (top curve) and a germanium detector [LE97].*

ments were made for all 48 modules of the FCAL/RCAL before the installation at ZEUS in 1990/1991 [KR92]. Since then during each maintenance period $^{60}$Co measurements have been taken on the Forward and/or Rear Calorimeter towers close to the HERA beams. The measurements also are used for quality control and calibration of the BPC [BO98c], FNC [BH97]

[1] See Chapter 3.

and FPC [BO99c]. Several other components are using the $^{60}$Co monitor system occasionally[2]. The $^{60}$Co monitor system allows to monitor a calorimeter section with regard to

- mechanical damage or shifted wavelength shifter and scintillator tiles,
- ageing or radiation damage of the wavelength shifter and scintillator resulting in changes of the absolute light output and attenuation length,
- calibration of the energy response.

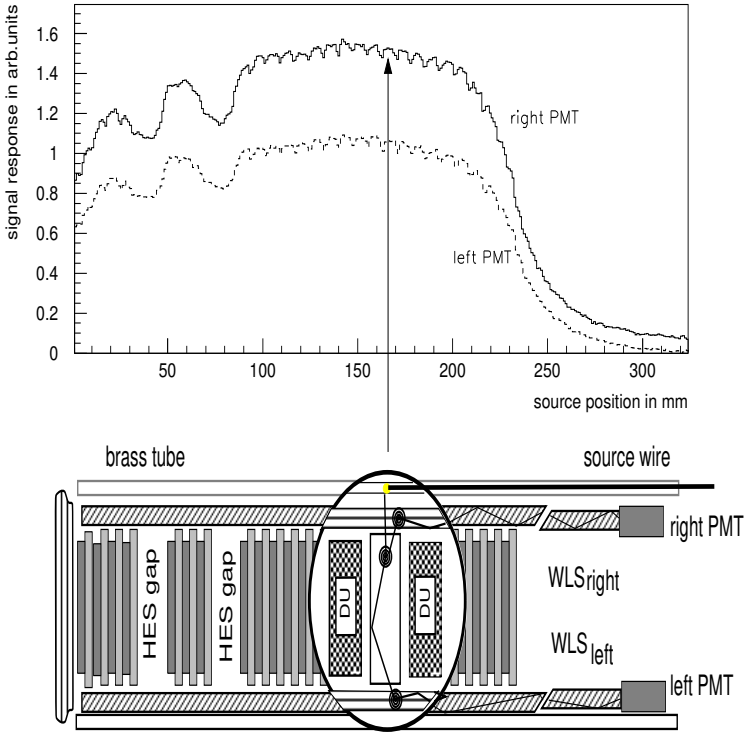


Figure 5.2: *Top view on a FCAL EMC section scanned by a $^{60}$Co source (bottom) and signal response as a function of the source position (top).*

The $^{60}$Co monitor system uses a small $^{60}$Co compound (see Figure 5.1) with an activity of about 2 mCi for local excitation of a calorimeter section. The principle of the measurement is the movement of the $^{60}$Co source (emitting $\gamma$ rays[3] of 1.17 MeV and 1.33 MeV) parallel to the wavelength shifter of the calorimeter section. The source is encapsulated in front of a special wire which is guided inside a brass tube (see Figure 5.2). The $\gamma$ rays emitted by the $^{60}$Co source cause a local energy deposition at the edges of the scintillators. The result is a signal response of the calorimeter section which depends on the $^{60}$Co source position. This signal delivers information about the longitudinal structure and uniformity of the calorimeter section. Figure 5.2 displays the principle of $^{60}$Co measurement on an EMC section of the FCAL. Each maximum in the signal response corresponds to one scintillator, i.e. the first maximum on the left of the signal response results from the scintillator closest to the interaction point. The big minima after the 3. and 7. scintillator correspond to the HES gaps. A possible change of the structure of the measured section can be detected by the comparison of two normalized signal responses which were taken at two different times. The quality of the scintillator tiles and the wavelength shifters (WLS), can be studied by comparing signals from photomultipliers on opposite sides of the calorimeter section.

### 5.1.1 The $^{60}$Co signal response

A $^{60}$Co scan measured at a certain time $t$ on a certain section delivers the signal response depending on the source position $z$. Let $I_{jk}(z,t)$ be the signal response from the photomultiplier

[2] I.e. Presampler [HO97].

[3] The $\beta^-$ rays remain in the source wire tube.

of the tower side $k$ when the source is moved on the tower side $j$. The indices $j$ and $k$ denote the **L**eft or **R**ight side with view in direction of the interaction point. Then the signal response consists of three components: The light $Co_{jk}(z,t)$ produced by the $^{60}$Co source located at the position $z$, the uranium noise $U_k(t)$ and the Cherenkov light $\check{C}_j(z,t)$ in the wavelength shifter due to *Compton* electrons (see Figure 5.3). The Cherenkov light is generated only on the side where the source is situated. It is about 5% of the signal $Co_{jj}$ [SC95].

$$\begin{aligned} I_{jk}(z,t) &= Co_{jk}(z,t) + U_k(t) + \check{C}_j(x,t)\cdot\delta_{jk}, \\ \delta_{jk} &= \begin{cases} 0 & : \text{, if} \quad j \neq k, \\ 1 & : \text{, if} \quad j = k. \end{cases} \end{aligned} \tag{5.1}$$

In the following the time and position dependence of the signal response will not be specially denoted. The normalization of the signal response is done by:

$$\hat{I}_{jk} = \frac{I_{jk}-U_k}{U_k} = \frac{Co_{jk}}{U_k}\cdot\left(1+\frac{\check{C}_j\cdot\delta_{jk}}{Co_{jk}}\right) \approx \frac{Co_{jk}}{U_k}. \tag{5.2}$$

The $^{60}$Co monitor system is suited for calibration: A relative calibration using the $^{60}$Co signal response is used for the BPC (see Chapter 9). An absolute calibration assumes an unchanged measurement performance and the well known activity of the $^{60}$Co source. These conditions are fulfilled with the $^{60}$Co measurements on the FPC, which is scanned and calibrated on a regular monthly basis [BO99c]. For the ZEUS calorimeter the $^{60}$Co/UNO ratio is also suitable for absolute calibration.

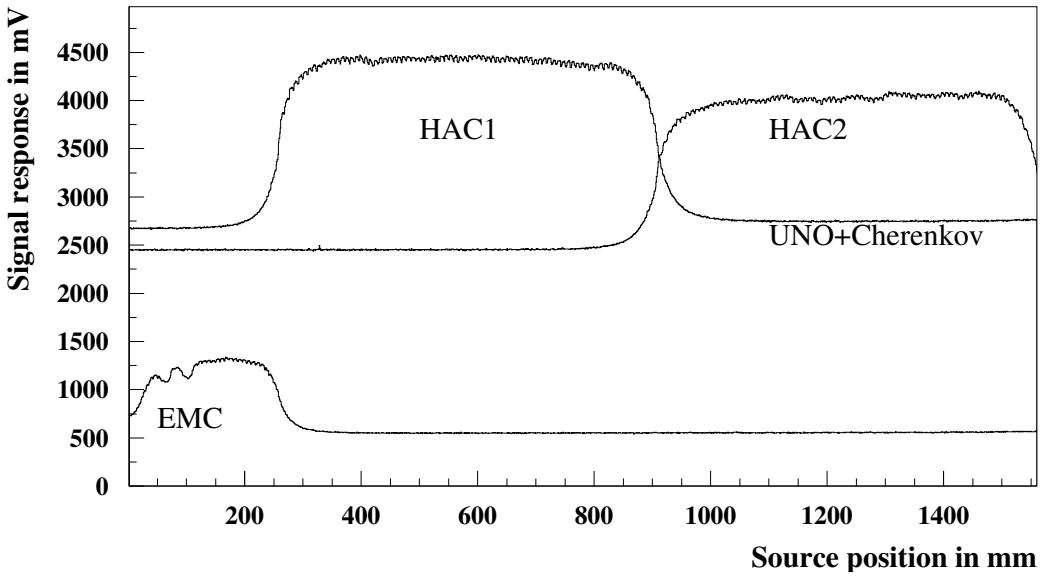


Figure 5.3: *The $^{60}$Co response of an EMC, HAC1 and HAC2 section. The $^{60}$Co source is on the same side as the photomultipliers. According to the smaller size the light output of the EMC scintillators is smaller than the one of the HAC scintillators.*

### 5.1.2 The optical parameters

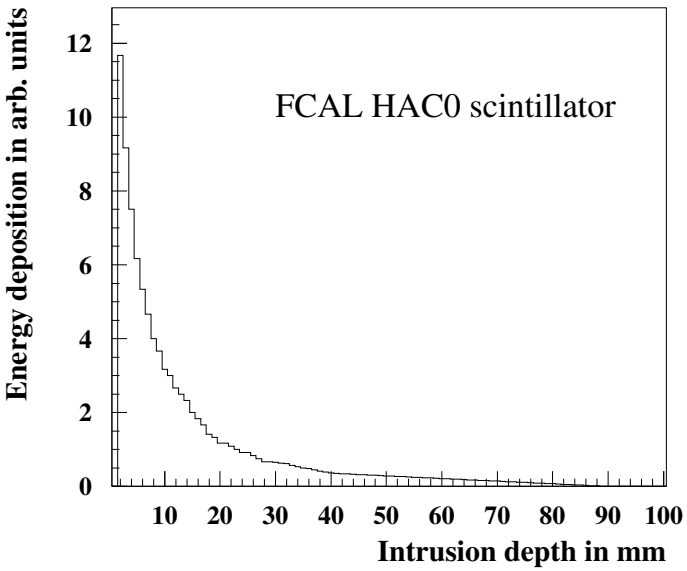


Figure 5.4: *Energy deposition of $\gamma$'s of the $^{60}$Co source as a function of the intrusion depth d into a HAC0 scintillator.*

Figure 5.4 shows a MC simulation of the energy deposition of $\gamma$'s of the $^{60}$Co source into a RCAL HAC0 scintillator as a function of the intrusion depth $d$ [KR92]. Most of the light induced by the cobalt source comes from the edge of the scintillator tile which is closest to the source. This means that light exciting the wavelength shifter which is on the same side of the section as the source comes directly from the edge of the scintillator whereas light in the wavelength shifter on the opposite side has to traverse the entire length of the scintillator tile. The comparison of the signals from both tower sides can be used to compute the effective attenuation length of the scintillator tile and to describe the optical components by a simple optical model: One $^{60}$Co run on a ZEUS calorimeter section delivers 4 signal responses. Let $\hat{I}_{jk}$ be the normalized response from the photomultiplier of the tower side $k$ (**L**eft or **R**ight) and the tower side $j$ where the source is moved (**L**eft or **R**ight). Let $S_j$ be the light yield emitted on the side $j$ by the scintillator when the source is on the same side, then $S_j \cdot T$ denotes the part of light traversing the scintillator and emitted on the opposite side. The transmission $T$ describes the attenuation of fluorescense light passing the scintillator tile. If $W_j$ denotes the response of the wavelength shifter (excluding Cherenkov light effects), then 4 signals $\hat{I}_{jk}$ can be written as[4]:

$$\hat{I}_{LL} = S_L \cdot W_L, \tag{5.3}$$
$$\hat{I}_{LR} = S_L \cdot W_R \cdot T_{LR}, \tag{5.4}$$
$$\hat{I}_{RR} = S_R \cdot W_R, \tag{5.5}$$
$$\hat{I}_{RL} = S_R \cdot W_L \cdot T_{RL}. \tag{5.6}$$

$T_{LR}$ is the transmission of light from left to the right of a scintillator tile, $T_{RL}$ the transmission with the opposite direction. Usually one assumes that $T_{LR} = T_{RL}$. It is therefore possible to compute the transmission and the ratio of the side depending light yield emission of each scintillator, and the ratio of the wavelength shifter responses. The following formulae present

[4]The contribution of Cherenkov light will be neglected in the following discussion.

the calculable parameters and their nominal values (based on reference data):

$$\frac{S_L}{S_R} = \sqrt{\frac{\hat{I}_{LL} \cdot \hat{I}_{LR}}{\hat{I}_{RR} \cdot \hat{I}_{RL}}} \approx 1. \tag{5.7}$$

$$\frac{W_L}{W_R} = \sqrt{\frac{\hat{I}_{LL} \cdot \hat{I}_{RL}}{\hat{I}_{RR} \cdot \hat{I}_{LR}}} \approx 1. \tag{5.8}$$

$$T = \sqrt{T_{LR} \cdot T_{RL}} = \sqrt{\frac{\hat{I}_{LR} \cdot \hat{I}_{RL}}{\hat{I}_{LL} \cdot \hat{I}_{RR}}} \approx 0.67. \tag{5.9}$$

### 5.1.3 Model of unfolding

Generally the $^{60}$Co signal response is the weighted sum of the response of all scintillators of the source scanned section. In case of the FCAL/RCAL EMC sections the part of response which comes from the scintillator directly in front of the source is less than 30% of the total signal, the two adjacent scintillators contribute about 10% to the total signal. In order to determine the amount of a single scintillator response the total signal response has to be unfolded. Several unfolding methods have been developed and applied at ZEUS [AN91], [DA91]. The following unfolding procedure is based on a simple ansatz applicable to different calorimeter geometries. The unfolding procedure uses the EGS4 simulations of different $^{60}$Co measurements [NE96], i.e. $^{60}$Co scans on the RCAL HAC0 section (see Figure 5.5) and on the BPC. The method depends on the iterative comparison of a measured $^{60}$Co signal response with a simulated one in order to determine the weight factors $g_i$ for each scintillator. The comparison of two unfolded $^{60}$Co signal responses measured at different times allows to determine the possible relative variation of each scintillator in between this time. The simulation calculates the single responses $f_i(z)$

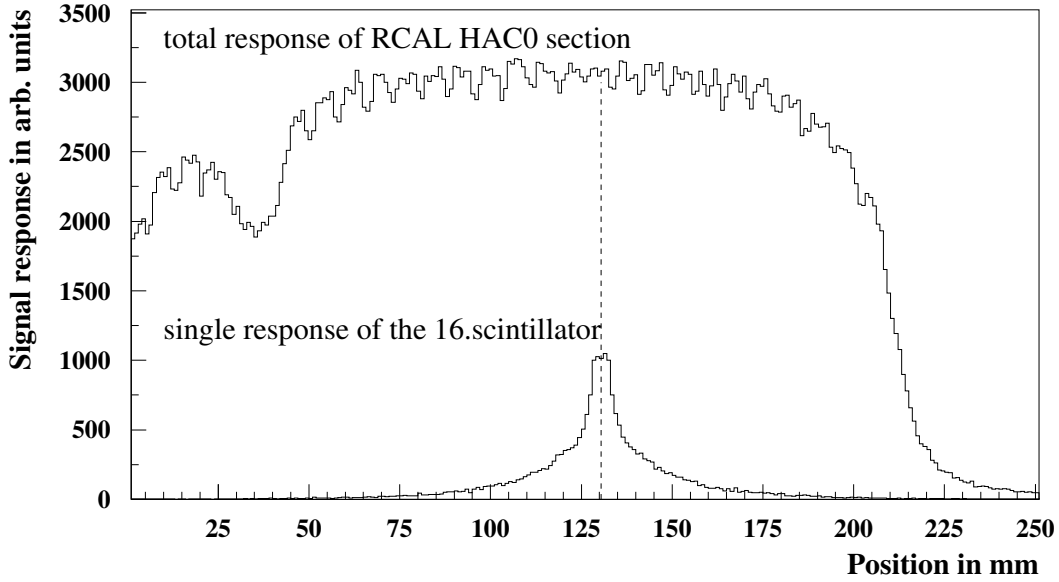


Figure 5.5: *Monte Carlo simulation of a $^{60}$Co measurement on a RCAL HAC0 section.*

of all scintillators ($i = 1, 2, ..., N$) of a section as a function of the source position $z$. It takes into account the individual geometries, materials and set-up characteristics of the real section

including the measurement performance. The total $^{60}$Co signal response $I_{mc}$ results from the sum of all simulated single scintillator responses of the section.

$$I_{mc} = \sum_{i=1}^{N} f_i(x) \cdot g_i. \tag{5.10}$$

The individual response $I^{i.SCI}$ of a particular scintillator $i$ can be approximately obtained by integrating the response of the $^{60}$Co scan around the maximum in the signal response, i.e. from the $i$th minimum to the next $(i+1)$ around the maximum of the $i$th scintillator. This procedure has to be performed for both the real $^{60}$Co signal response as well as for the total simulated one.

$$I^{i.SCI}_{real} = \sum_{i.min}^{(i+1).min} I_{real}, \qquad I^{i.SCI}_{mc} = \sum_{i.min}^{(i+1).min} I_{mc}, \tag{5.11}$$

thus the integrated response $I^{i.SCI}$ is an approximation for the light output of the $i$th scintillator

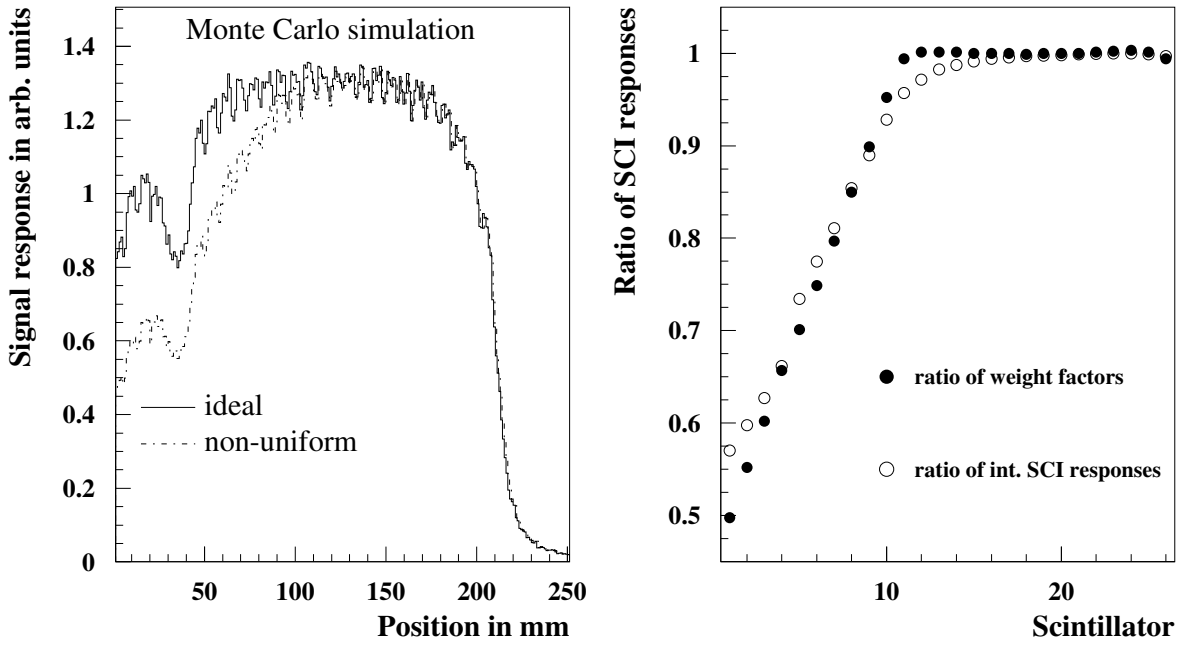


Figure 5.6: *The left diagram shows the MC signal responses of an ideal calorimeter section (solid line) in comparison with a non-uniform one (dashed line). The ratio of the weight factors (filled circles) of the scintillators from the unfolding and the simple ratio of the integrated scintillator responses (circles) are shown in the right diagram.*

response. Each total $^{60}$Co signal response provides $N$ values depending on the number of $N$ scintillators. The ratio $R^{i.SCI} = I^{i.SCI}_{mc} / I^{i.SCI}_{real}$ of the integrated scintillator responses are expected to be equal. A deviation of the ratio $R^{i.SCI}$ from unity requires a change of the weight factor $g_i \rightarrow g_i \cdot 1/R^{i.SCI}$. An iterative comparison between the measured and simulated signal responses is performed fitting the weight factors of the simulated single responses until the ratio $R^{i.SCI}$ converges to unity for all scintillators. After several iterations the simulated response converges with the measured one at the level of 1% and the procedure will be interrupted. In order to determine a possible relative variation of scintillator responses of two $^{60}$Co signal

responses measured at two different times, the whole unfolding procedure is repeated for the second $^{60}$Co measurement resulting in $N$ weight factors $g_i'$. The ratio of the weight factors $G_i = g_i'/g_i$ of two $^{60}$Co signal responses compensates possible systematical uncertainties between the measured and the simulated curves. $G_i$ is expected to be unity provided that no radiation damage or any other change degraded the scintillator performance in time.

A test of the unfolding algorithm is performed based on two well known weighted signal

| **test of the unfolding method** | | | | | | |
|---|---|---|---|---|---|---|
| scintillator number i | weight factor (ideal) $g_i$ | weight factor (non-uniform) $h_i$ | result of unfolding $G_i = g_i'$ | relative error $\frac{\lvert h_i - g_i' \rvert}{h_i}$ | result of simple ratio $R^{i.SCI}$ | relative error $\frac{\lvert h_i - R_i \rvert}{h_i}$ |
| 1 | 1 | 0.5 | 0.498 | 0.4% | 0.570 | 14.0% |
| 2 | 1 | 0.55 | 0.552 | 0.4% | 0.598 | 8.7% |
| 3 | 1 | 0.6 | 0.602 | 0.3% | 0.627 | 4.5% |
| 4 | 1 | 0.65 | 0.657 | 1.1% | 0.662 | 1.8% |
| 5 | 1 | 0.7 | 0.701 | 0.1% | 0.735 | 5.0% |
| 6 | 1 | 0.75 | 0.749 | 0.1% | 0.775 | 3.3% |
| 7 | 1 | 0.8 | 0.797 | 0.4% | 0.811 | 1.4% |
| 8 | 1 | 0.85 | 0.85 | 0 % | 0.854 | 0.5% |
| 9 | 1 | 0.9 | 0.899 | 0.1% | 0.890 | 1.1% |
| 10 | 1 | 0.95 | 0.952 | 0.2% | 0.928 | 2.3% |
| 11 | 1 | 1 | 0.994 | 0.6% | 0.957 | 4.3% |
| 26 | 1 | 1 | 0.994 | 0.6% | 0.997 | 0.6% |

Table 5.1: *Test of the unfolding method: The input parameters $h_i$ (column 3) of a non-uniform RCAL HAC0 section are compared with the calculated weight factors $g_i'$ (column 4) from the unfolding and the simple ratio of the integrated scintillator responses $R^{i.SCI}$ (column 6).*

responses. The first signal response $I_{ideal}$ is the EGS4 simulation of a $^{60}$Co scan on an ideal RCAL HAC0 section using unity weight factors $g_i = 1$ for all scintillators $i = 1, 2, ..., 26$. The second signal response $I_{inhom}$ is the simulated $^{60}$Co signal response of the same section using varying weight factors $h_i$ for the scintillators corresponding to a non-uniform radiation damage. Accordingly the weight factors of the scintillators closest to the interaction point are the ones which are most strongly degraded. The left diagram of Figure 5.6 displays both simulated signal responses. The right diagram in this Figure presents the ratio of the weight factors $G_i = g_i'/g_i = g_i'$ of the unfolding of the two $^{60}$Co signal responses (filled circles) in comparison to the simple ratio $R^{i.SCI} = I^{i.SCI}_{inhom}/I^{i.SCI}_{ideal}$ of the integrated scintillator response (circles). Table 5.1 describes the input and output parameters of the unfolding and the simple ratio. The relative error between the weight factors $h_i$ of the non-uniform section and the ones $g_i'$ calculated by the unfolding procedure is usually less than 1%. Whereas the simple ratio is a rough estimation of the weight factors of the scintillators with a maximum error of approximately 14%.

### 5.1.4 The $^{60}$Co measurement system

The $^{60}$Co measurement system has been described elsewhere several years ago [BE92a]. The principle is still unchanged, but several new components have been developed. In the following the components will be shortly described. More details can be found in [NE96], [BO96]. The

measurement system is a *Linux* PC based system[5]. The measurement system uses the software package driver communicating with a motor controller and an ADC-card. The ADC-card (*PCL-812PG* of *Spectra*) is a 16 channel enhanced multi-function card for the measurement of voltages in a range of $\pm 10\,\mathrm{V}$ with a resolution of 12 bit, thus one ADC channel is about 5 mV. The motor controller runs two stepping motors on the ground-plate. The ground-plate performs both the selection of the device based on a rotating dial and the movement of the source wire using polyurethane rollers. A shaft encoder mounted coaxially with one of the readout rollers measures the amount of the wire which has been rolled off. The reference position of the wire is determined by light switches. The motor controller is based on commercial components of *ISEL* and a special electronic card. An important feature of this card is a *HCTL*-2016 chip decoding the signals of the shaft encoder. The light switches are also read out by the electronic card of the motor controller. The setting of the high voltage for the photomultiplier tubes can be performed by *CAMAC* HV cards via a *GPIB*-bus under control of the PC system. Therefore an additional software package exists called *HV* [HE98]. The measurement system executes the data acquisition which moves the source for one step, stops it and measures directly the currents $i = dQ/dt$ of the photomulitpliers by a multiplexer circuit[6] of the ADC-card (stop and go) with a sufficient repetition rate[7].

The $^{60}$Co source is guided in brass tubes with an inner diameter of 2.1 mm which are located

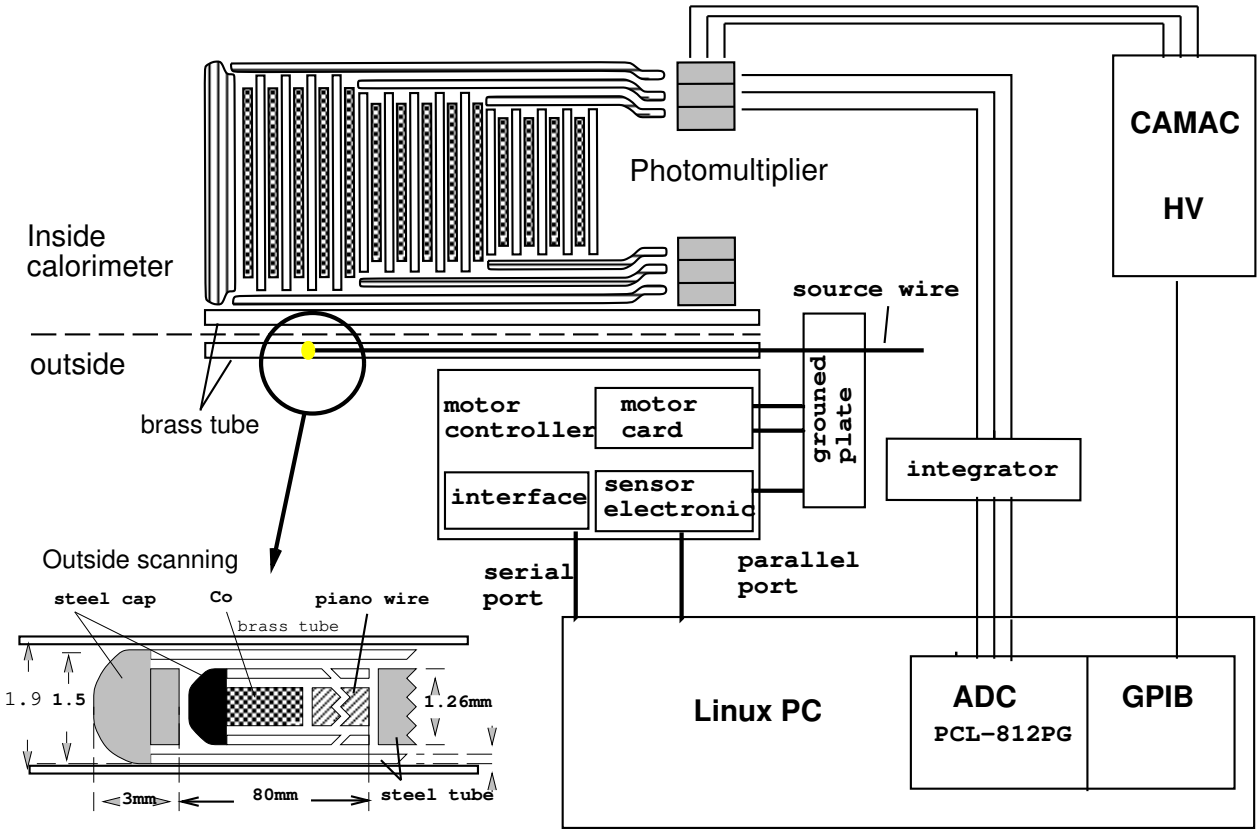


Figure 5.7: *Sketch of the $^{60}$Co measurement system. The source wire configuration of the outside scanner is shown on the left.*

[5] *Linux* is a derivative of *Unix* for **p**ersonal **c**omputers [SC94].

[6] The currents of the photomultipliers are measured serially [RO83].

[7] Normally a repetition rate of 3500 is used. Alternatively an integrator can be used integrating the currents over a time of 24 ms.

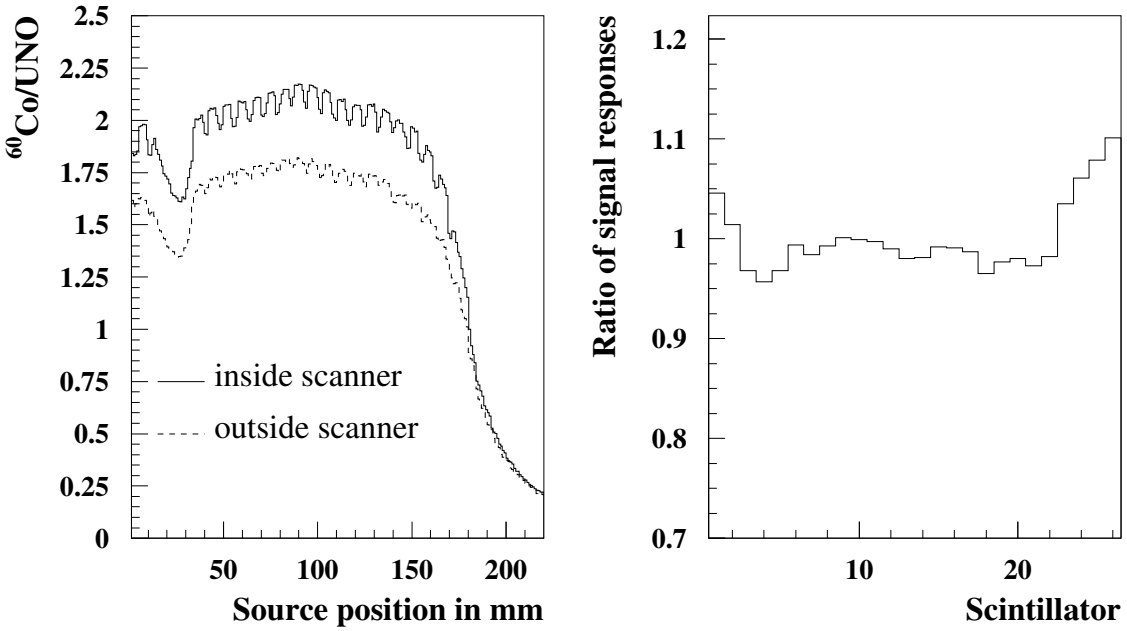


Figure 5.8: *Comparison of two signal responses with respect to inside/outside scanning of the EMC3 section of the FCAL module 17, tower 8 (left). The $^{60}$Co scans begin after the 5th scintillator. The ratio of mean of these signal responses (right) is averaged over 8 mm (similar to the radiation length). The HES gap region is extracted and the beginning of the function is extrapolated. The ratio demonstrates the different pulse heights of inside/outside scanning.*

inside or outside the ZEUS uranium calorimeter. The two methods are called inside and outside scanner. Figure 5.7 displays the measurement system using the outside scanner. In 1990 an OS-9/VME based system was used (see Chapter 7.1) rather than the present PC-system[8]. The **outside scanner** was mainly applied to the ZEUS calorimeter until 1996. For outside scans the source wire is guided through a brass tube system (so-called wing) which is specially installed outside the calorimeter. Additionally the source wire is double encapsulated into steel tubes with an outer size of 1.6 mm. Otherwise the possibility of a misplacement of the wing and accordingly the source itself exists, which influences the solid angle between the $^{60}$Co source and the excited section. The **inside scanner** uses guiding tubes which are mounted inside the calorimeter modules. The main difference between the outside and the inside scanner is the location of the $^{60}$Co source with respect to the scintillators of the calorimeter section. In case of the FCAL scans the difference between the methods depends on the distance between source and scintillators (see Figure 5.9) resulting in more flat signal response from outside scans in comparison with inside scans. Figure 5.8 shows two EMC signal responses from 1990 with respect to inside/outside scans of the FCAL module 17, from which only reference data for both $^{60}$Co inside and outside scans exists (left diagram). The ratio demonstrates the different pulse heights of inside/outside scans (right diagram). In case of the RCAL outside/inside scans the differences of the scanning methods should be much bigger, because during RCAL inside scans the source is guided between the EMC1/2 sections whereas the outside scanner guides the source in the middle of the section. The consequence is both different pulse heights depending on the scanning method and possible additional variations in the longitudinal structure. For the inside scanner a new source wire (activity 74 MBq/2 mCi) was developed and delivered in

[8]The reproducibility of $^{60}$Co measurements due to OS/9- and PC-measurements is well established [BO96].

1996 in order to use the fixed installed brass tubes inside the ZEUS calorimeter and to measure calorimeter sections which are not accessible from outside. The risk to loose the source in the calorimeter was reduced by two preventive measures. The new source with a size of 1.1 mm has a 8 m long steel tube which is more than the largest path length of the source in the calorimeter. Secondly steel tubes with an inner size of 1.4 mm which are closed at one end were pushed into the brass tubes. A specially developed adapter system guides the inside source wire from the ground-plate into the steel tube. In case of an accident it would be possible to remove the steel tube with the source wire outside the fixed installed brass tubes.
A so-called $^{60}$Co run commences when the operator selects a specific tube to be scanned. The host instructs the motor controller to select the correct tube and to drive the source into the tube. When the encoder indicates that the source is no longer moving the data taking is beginning by pulling the source wire out of the tube.

**Estimate of errors**

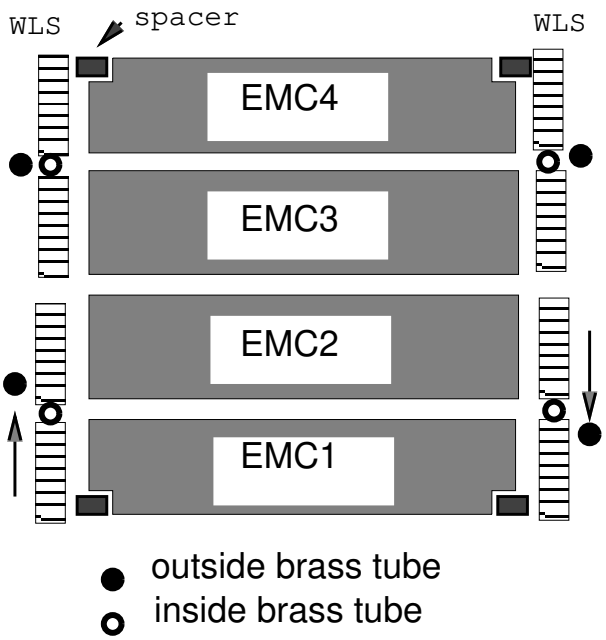


Figure 5.9: *Front view of the source guiding system on a FCAL EMC tower. The outside scanner is misplaced here on both tower sides with respect to the EMC1 and 2 section.*

One essential goal of the $^{60}$Co analysis is the comparison of the signal responses. Therefore it is important to know the error $\Delta F_{exp}$ with respect to the reproducibility of signal responses which can be written as a sum of three terms:

$$\Delta F^2_{exp} = \Delta F^2_{pos} + \Delta F^2_{stat} + \Delta F^2_z. \quad (5.12)$$

The error $\Delta F_{pos}$ is produced due to a misplacement of the guiding tube which may occur due to a wrong installation of the $^{60}$Co set-up of the outside scanner. A change of the solid angle between the $^{60}$Co source and the excited section influences significantly the signal response and makes it useless to compare signal responses measured at different times. $\Delta F_{stat}$ denotes the statistical error with respect to the data acquisition, while $\Delta F_z$ denotes the error of the measurement of longitudinal source position $z$. Due to the high repetition rate and the integration of the currents over 24 ms the statistical error is much less than the longitudinal source position error measured by the encoder electronics.
The reproducibility of measurements using the outside scanner is well established through the quality control of the FCAL/RCAL towers near to the HERA beams, which is done every maintenance period (see Chapter 7). The ratios of two signal responses of the same section measured at different times were found to be constant at the 1 – 2% level. The reproducibility of inside scans is much better, because the error $\Delta F_{pos}$ disappears almost completely.
The influence of the vertical location of the $^{60}$Co source on the error $\Delta F_{pos}$ will be deduced for the optical parameters in the following. Generally the calculation of the optical parameters requires 4 signal responses resulting from two $^{60}$Co scans on both tower sides of the investigated section. This procedures had been used with respect to the reference measurements in 1990/1991 on all single-standing FCAL/RCAL modules before the installation into

the calorimeter. Figure 5.9 shows possible locations of the source on the FCAL EMC sections using the outside scanner. In the ideal case the source is guided exactly between two EMC sections (i.e. the FCAL EMC3 and EMC4 sections) without exciting one section more than the other. In case of an ideal calorimeter section the right and left signal responses of both $^{60}$Co scans yield to $I_{RR} = I_{LL}$ and $I_{RL} = I_{LR} = T \cdot I_{RR} = T \cdot I_{LL}$. The first index denotes the tower side where the source is located (right or left), whereas the second index denotes the right or left photomultiplier. Given the assumption of an ideal scintillator the ratio of the right/left signal response of one $^{60}$Co scan is equal to the transmission $T$. Then the ratio of the wavelength shifters $W_L/W_R$ and the ratio of the scintillator responses $S_L/S_R$ are unity. A vertical misplacement of the guiding tube shifts the source on one EMC section exciting the scintillators more than those of the adjacent section. Let the misplacement of the source be as shown in Figure 5.9, then the signal responses of the EMC1 section yield $I_{RR} = f_R \cdot I_{LL}$ and $I_{RL} = f_L \cdot I_{LR}$ with $f_R > 1$ and $f_L > 1$. The error factors $f_R$ and $f_L$ describe the effects on the signal responses due to the misplacements. The calculation of the optical parameters of an ideal section yields:

$$T' = \sqrt{\frac{I_{LR}^2 \cdot f_R}{I_{LL}^2 \cdot f_L}} = \sqrt{\frac{I_{RL}^2 \cdot f_L}{I_{RR}^2 \cdot f_R}} = \frac{I_{LR}}{I_{LL}} \cdot \sqrt{\frac{f_R}{f_L}}, \tag{5.13}$$

$$\frac{S_L{}'}{S_R} = \sqrt{\frac{I_{LL} \cdot I_{LR}}{I_{RR} \cdot I_{RL} \cdot f_R \cdot f_L}} = 1 \cdot \sqrt{\frac{1}{f_R \cdot f_L}}, \tag{5.14}$$

$$\frac{W_L{}'}{W_R} = \sqrt{\frac{I_{LL} \cdot I_{RL} \cdot f_R}{I_{RR} \cdot I_{LR} \cdot f_L}} = 1 \cdot \sqrt{\frac{f_L}{f_R}}. \tag{5.15}$$

The error $\Delta F_{pos}$ on the optical parameters decreases or increases according to the misplacements of the $^{60}$Co source. Small misplacements of the source with $f_R \approx f_L$ lead to effects on the ratio of the scintillator responses, whereas the effects on the transmission and on the ratio of wavelength shifter responses can be neglected.

## 5.2 Investigations on individual samples

The $^{60}$Co monitor system allows to get information about the status of an implemented calorimeter. Moreover, other methods are available and used in this thesis to investigate individual optical samples, especially single scintillators and wavelength shifters.

### 5.2.1 Scanning bench

A scanning bench exists for the purpose of investigating light guides with different geometries (see Figure 5.10). It allows a position dependent excitation of the samples using UV-light and $\gamma$'s or $\beta$'s of radioactive sources. The bench has a length of about 120 cm and a width of 60 cm where the samples are placed. Three independent moving axis allow movements in all three dimensions carrying either the sample or the excitation source. The reproducibility of the positioning of the axis is $(0.5 \pm 0.02)$ mm (see Chapter 9.3.2). The measurement system is based on a *Linux* PC-386/40 with a mathematical coprocessor using a special developed data taking system WLS [ME96]. This software communicates with the commercial motor controller of *ISEL* which steers the stepping motors of the axis. The readout of the sample is taken by a 12-Bit ADC (SPECTRA) similar to the one used for the $^{60}$Co monitor system. The data

taking, including performance information as well as gain factors and channel mapping, is done in a defined table format and stored in ASCII-code. A command interpreter allows flexible configurations taking into account the individual measurement performance (i.e. geometry).

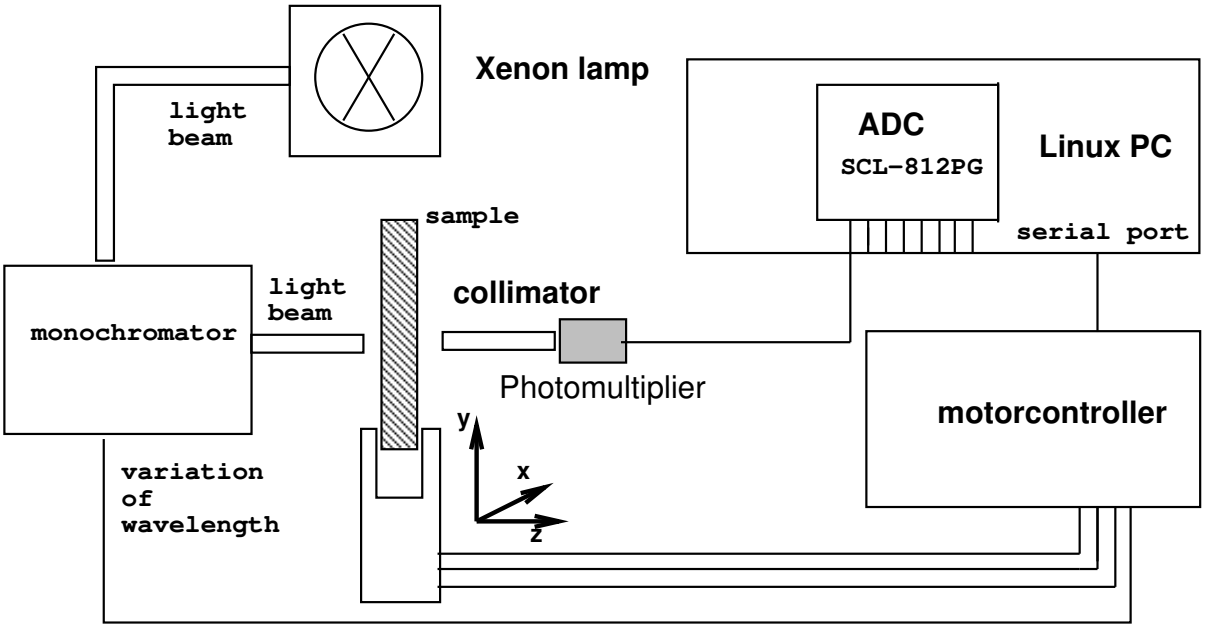


Figure 5.10: *Sketch of the scanning bench using the UV-light set-up.*

### 5.2.2 Excitation sources

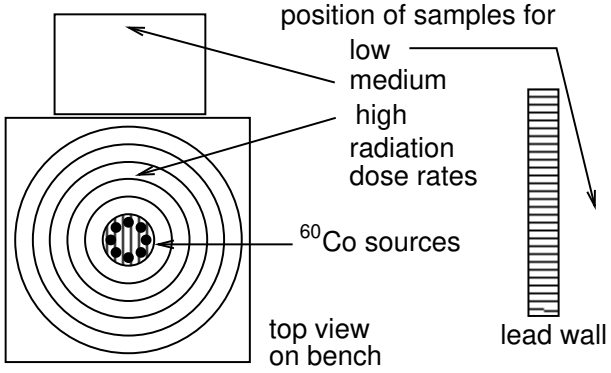


Figure 5.11: *Schematic top view on the $^{60}Co$ set-up at HMI.*

In order to excite different samples of light guides in connection with the scanning bench a UV-light source and radioactive sources are used. A Xenon high pressure lamp (type HAMAMATSU L 2175) produces light which is guided by flexible quartz fibers (manufacturer is SCHOTT GLASWERKE) to the surface of the investigated sample. A monochromator between light source and sample allows wavelength dependent investigations. The main advantages of using UV-light consists of possible wavelength dependent investigations, the large intensity of the source and that the measurement performance is easy to handle. The excitation of polymere samples due to radioactive sources responds to similar processes during their operating time in particle experiments. Two sources are applied in the following. A $^{106}$Ru source with an activity of $\approx 30\,\mu$Ci emits $\gamma$'s and $\beta$'s and a $^{90}$Sr source with an activity of about 2 mCi which emits nearly exclusively $\beta$'s. Figure 5.12 shows the electron energies of both radioactive sources in comparison with the ones of a $^{22}$Na and $^{207}$Bi source. The energy measurement has been taken by a lithium doped silicon detector. The energy spectrum of converting electrons of the $^{207}$Bi source is particularly suitable for calibration (see Figure 5.13 and [MA91]). The energies of electrons from the $^{90}$Sr source are up to 2 MeV, a small rate of electrons are emitted

from the $^{106}$Ru source with higher energies. The dose rate of these sources including the $^{60}$Co source of the monitor system are in the order of mGy per hour or less and not sufficient to irradiate polymere samples. Therefore the irradiation of samples in the order of several kGy has been performed at the Hahn-Meitner-Institut (HMI). There a $^{60}$Co source exists consisting of 8 cylindrical bars which are placed in the circle of a certain bench. The radiation dose rate varies as a function of the distance from the source between few Gy/h up to several kGy/h [JA98].

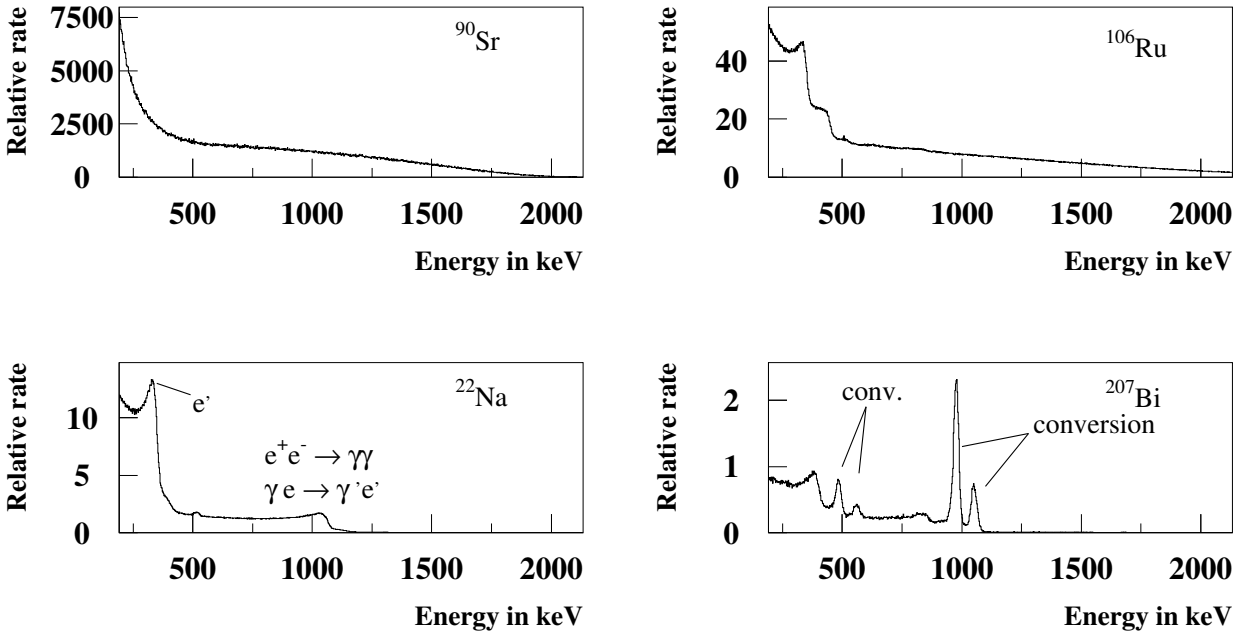


Figure 5.12: *Energy spectra of different sources measured by a lithium endowed silicon detector. From left to right it is shown on the top diagrams the energy spectra of $^{90}$Sr and $^{106}$Ru, on the bottom diagrams the energy spectra of $^{22}$Na and $^{207}$Bi. The well known Compton electrons of $^{22}$Na and conversion peaks of electrons in the energy spectrum of $^{207}$Bi are used for calibration.*

## 5.3 Dosimetry

Radiation monitoring is of vital interest for particle experiments, especially for the ZEUS experiment where a radiation background occurs from Gy up to kGy close to the HERA beams. Therefore the running conditions of ZEUS are monthly controlled (see Chapter 3.3). Several methods exist. The dose measurements presented in this thesis are the following:

- **Thermoluminescense dosimetry**: It depends on a special crystal (Harshaw TLD-700). This type of TLD crystal is based on a Lithium-7 isotope fluoride ($LiF_2$) which allows to measure accumulated doses of up to 3 kGy. The calibration of the crystals is performed using a $^{137}$Cs source and analyzed using an automated apparatus by measuring the glow curve of exposed TLD crystal [PR99]. The accuracy of the measured dose has been estimated to be approximately 10%. The acccuracy significantly decreases if the range of applicability of 3 kGy is exceeded.

- **Alanin dosimetry**: A special developed polymere material in form of a 4.8 mm thick cabel is available (manufacturer KABELMETALL HANNOVER) consisting of 33% of ethylene

propylene rubber and 67% of DL-$\alpha$-Alanin. Irradiation of the material produces stable radicals. The radical density of the irradiated material is correlated with the radiation dose. The number of radicals can be determined by the measured electron-spin-resonance (ESR) [BO97] which allows the determination of the radiation dose with an accuracy of approximately $\pm 100$ Gy.

Thermoluminescense dosimetry is used for radiation dose measurements for the ZEUS calorimeter towers close to the HERA beams and the beam pipe calorimeter. The radiation dose of samples irradiated at HMI have been determined by alanin dosimetry.

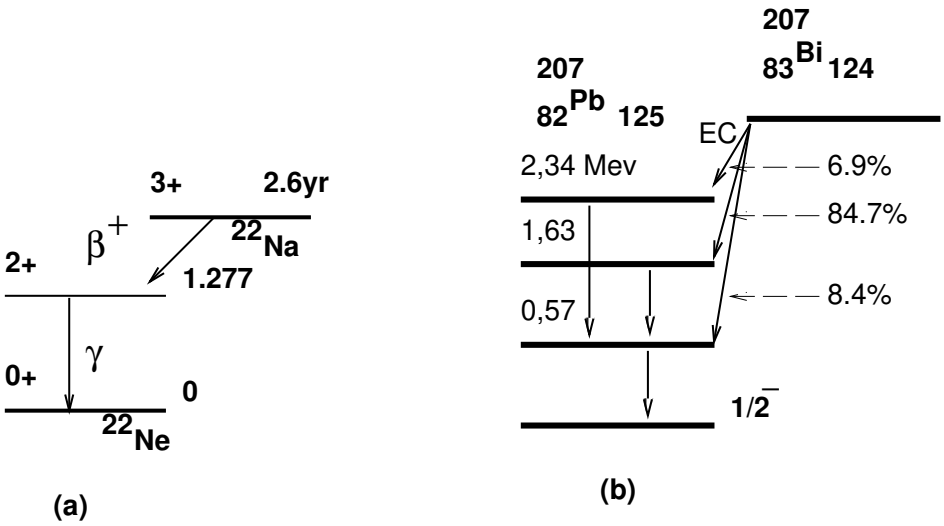


Figure 5.13: *Nuclear level diagrams of the $^{22}Na$ (a) and $^{207}Bi$ compounds (b) used for calibration.*

# Chapter 6

# Testbeam measurements and $^{60}$Co scans

In case of a sampling calorimeter based on scintillators and wavelength shifters irradiation causes a variation of the optical properties resulting in possible non-uniformities and non-linearities of the calorimeter. In order to investigate the influence of irradiation on calorimetry testbeam measurements have been performed at DESY using an irradiated ZEUS test calorimeter. $^{60}$Co monitor measurements allow to compute the optical status during the testbeam measurements. Scintillators of two electromagnetic sections have been irradiated at HMI with 5 and 10 kGy, while one wavelength shifter was exposed to a dose of 1 kGy. Another two EMC sections served as reference sections. Individual investigations of single scintillators before and after irradiation using electrons of a $^{90}$Sr source indicate the variation due to radiation damage. The test calorimeter was installed into the DESY testbeam for two weeks in June 1998. The device was tested with respect to effects on linearity and uniformity with 1 to 6 GeV electrons[1]. The correlation between testbeam, $^{60}$Co measurements and the individual investigations is presented.

## 6.1 Description of the test calorimeter

The test calorimeter is a lead/scintillator sampling calorimeter [BO93]. The configuration of the test calorimeter with respect to geometry and optical components such as scintillators, wavelength shifters and photomultipliers is similar to a FCAL EMC tower. It consists of the longitudinal direction of one electromagnatic (EMC) section and two hadronic (HAC) sections. The electromagnetic section is subdivided vertically into 4 EMC sections. The optical components including the scintillators, wavelength shifters and photomultipliers are equivalent to those in a FCAL EMC tower. The absorber material of the test calorimeter is lead (alloy PbSb6 with 6% Antimon) instead of uranium. The thickness of the lead plates is 6 mm. The scintillator and wavelength shifter material are spare parts of the ZEUS detector. Each EMC sections contains 21 scintillators. The HAC1 section has 63 scintillators (there is no HAC2 section except for the wavelength shifters). Two wavelength shifters on each side read out the section guiding the light to the photomultipliers. The installation of two irradiated sections required a completely new production of EMC scintillators, because no sufficient quantity of scintillators was on stock at DESY. The scintillators of the EMC1 and the EMC2 sections (corresponding

[1] The measurement scheme is similar to investigations of [BE87].

to 42 scintillators) have been cut from existing $1 \times 1\,m^2$ plates, tailored to $19.1 \times 5\,cm^2$, polished at the edges and wrapped into tyvek-paper[2]. The pattern of the wrapping is similar to the one used at the ZEUS calorimeter. In June 1998 the finished EMC1 and the EMC2 scintillators were irradiated uniformly by a $^{60}$Co source at the Hahn-Meitner-Institut (HMI) in Berlin with nominal radiation doses of 5 kGy and 10 kGy. Additionally the right wavelength shifter of the EMC1 section was uniformly irradiated with a nominal radiation dose of 1 kGy. The radiation dose of these samples have been determined by alanin dosimetry (see Chapter 5.3).

- Plastic scintillators such as *SCSN-38* ($d$ = 2.6 mm) are based on a polysterene matrix. One day after irradiation the initial damage of the scintillators will recover in air reaching the permanent damage (see Chapter 4.3).

- The wavelength shifter *Y7* ($d$ = 2.0 mm) is based on a *PMMA* matrix. The recovery effects will take several months. The initial damage[3] will significantly influence the optical properties within this time.

Scanning bench measurements on individual scintillators have been taken before and after the irradiation. These measurements based on a similar readout as the one of the test calorimeter using electrons of a $^{90}$Sr source allow to determine the attenuation curves of the scintilllators in order to investigate the effects due to the radiation damage. Table 6.1 presents the overview of the optical status of the test calorimeter during the testbeam.

| **status of optical components during testbeam** | | | | |
|---|---|---|---|---|
| section | EMC1 | EMC2 | EMC3 | EMC4 |
| radiation dose of SCI | $\approx$ 5 kGy | $\approx$ 10 kGy | 0 kGy | 0 kGy |
| radiation dose of WLS | right side $\approx$ 1 kGy | 0 kGy | 0 kGy | 0 kGy |

Table 6.1: *Irradiation of the optical components before installation into the test calorimeter.*

Figure 6.1 displays the attenuation of two scintillators before and after irradiation of nominal 5 and 10 kGy. The curves are normalized at $x = 0$ to unity. The attenuation curve of the scintillator can be described by the following simple ansatz:

$$\bar{I}(x) = \bar{I}_0 \cdot e^{-\bar{\mu} \cdot x} + \bar{I}_0 \cdot R \cdot e^{-(2L-x)\cdot\bar{\mu}}. \tag{6.1}$$

$\bar{\mu}$ is the effective absorption coefficient of *SCSN-38*. The effective fluorescense light is denominated with $\bar{I}_0$. A reflection term is given at the end using the reflection coefficient $R$ = 0.2 [WI98]. $L$ denotes the length of the scintillator of 191 mm. The attenuation curve measurements allow to determine the effective attenuation $\lambda_{att} = \bar{\mu}^{-1}$. The attenuation curves in absolute units are fitted with formula 6.1 within the region of 60 to 110 mm. The results are described in table 6.2 based on the investigations of 10 scintillators. One has to notice the big variances of the mean attenuation which results from differences of the scintillators with respect to geometry, wrapping, polishing, etc.

[2] The scintillators of the EMC1 and the EMC4 section have a recess at each side for a spacer.

[3] A 1 kGy irradiation of *PMMA* produces an initial damage which is comparable to a permanent damage in the order of a 6 kGy irradiation [WI98].

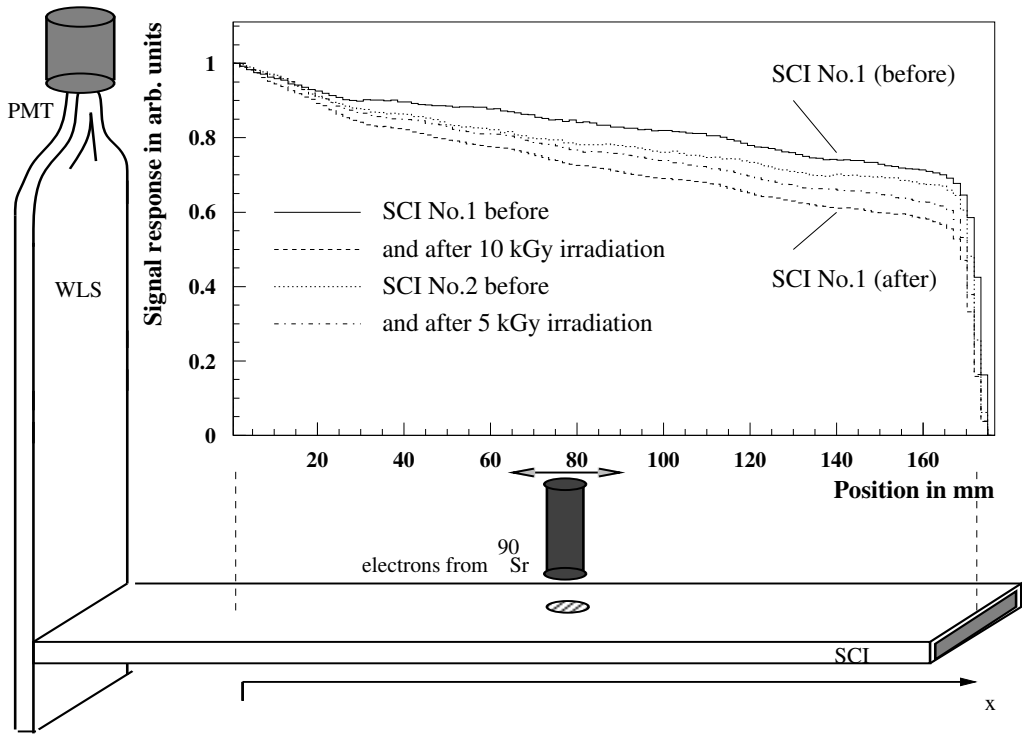


Figure 6.1: *Sketch of the bench measurements on the scintillators using electrons of a $^{90}Sr$ source and attenuation curves of the FCAL EMC scintillators before and after irradiation.*

| attenuation in mm from bench scans | | | | |
|---|---|---|---|---|
| type | EMC1 | EMC2 | EMC3/2 | EMC4/1 |
| dose | 5 kGy | 10 kGy | 0 kGy | 0 kGy |
| $\lambda_{att}$ | $487 \pm 36$ | $404 \pm 73$ | $690 \pm 108$ | $694 \pm 35$ |

Table 6.2: *Attenuation length of the SCSN-38 scintillators of the reference sections and the EMC1/2 sections before and after irradiation.*

## 6.2 The testbeam set-up and beam generation

The test calorimeter has been installed into the DESY testbeam 21 for two weeks in June 1998 and exposed to electrons of 1 to 6 GeV. Two independent readout systems based on *Linux*-PC's have been set up parallel; one for the $^{60}$Co monitor system (described in Chapter 5.1.4) and another one for the testbeam measurement. The data acquisition system of the latter is using fast CAMAC ADC cards (several nanoseconds processing time) read out via a *GPIB*-Bus. The software package CAM based on the HV setting program of [HE98] was specially developed [HE99]. The measurement system guarantees the signal processing of each readout channel simultaneously and the succeeding storage of the measurements on event-by-event basis in ASCII data files. The testbeam 21 uses the DESY II electron synchrotron halo which generates Bremsstrahlung photons from a 10 $\mu$m thick carbon target. The photons leave the vacuum chamber through a 0.5 mm thick Alumminium foil and pass the DESY III vacuum chamber via two 0.5 mm Aluminium foil windows in the same horizontal plane as the electron synchrotron. Passing another vacuum chamber through two Kapton foils the photons hit a

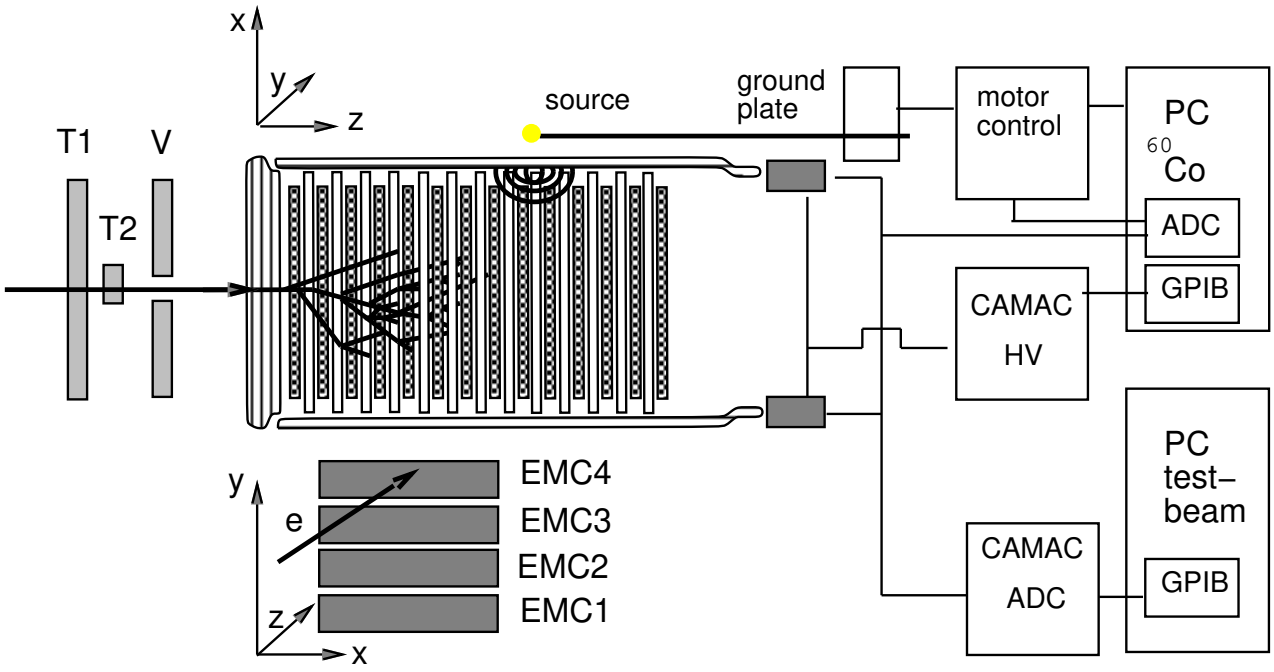


Figure 6.2: *Schematic drawing of the set-up used at the DESY testbeam 21.*

copper conversion target resulting in secondary electrons and positrons of energies up to 7 GeV. A dipole magnet selects the particles as a function of the momentum by variation of the magnet current. The selected electrons pass first through a collimator which is lockable by a beam shutter and then a second one, traverse the trigger set-up and hit finally the test calorimeter. The orthogonal trigger set-up consists of a vertical trigger (T1), a horizontal trigger (T2) with $5 \times 1\,\mathrm{cm}^2$ and a veto counter (V) which is a large area scintillator with $20 \times 30\,\mathrm{cm}^2$ with a hole in its centre of 3 cm diameter. The trigger signals are processed by NIM discriminators [SC86]. The beam trigger enables the readout by the ADC if a coincidence of the triggers T1 and T2 and an anti-coincidence of the vetocounter V is detected. The gate width for the readout is about 100 ns. The test calorimeter is mounted on a three axis moving bench, so that optionally all 4 EMC sections can be moved into the test beam. The testbeam period included the following measurement scheme:

- The beam profile was measured at an electron energy of 3 GeV varying the position of the beam triggers (see Figure 6.3).
- The high voltage (HV) of the photomultiplier was fixed.
- $^{60}$Co measurements have been taken on both tower sides of the EMC section.
- Linearity scans: The beam was positioned in the middle of the sections and 10 k events have been taken per energy which was varied between 1 and 6 GeV in 1 GeV steps.
- Uniformity scans: At an energy of 6 GeV the beam position was horizontally varied at six positions of the sections with 10 k events per position.
- $^{60}$Co measurements have been repeated on the sections.

Pedestal measurements have been taken before each $^{60}$Co scan while the source was in a lead bunker. According pedestals measurements have been taken for the electron measurements using random triggers during the closed beam shutter. Figure 6.2 shows a sketch of the testbeam set-up including the $^{60}$Co monitoring and the fast read out system.

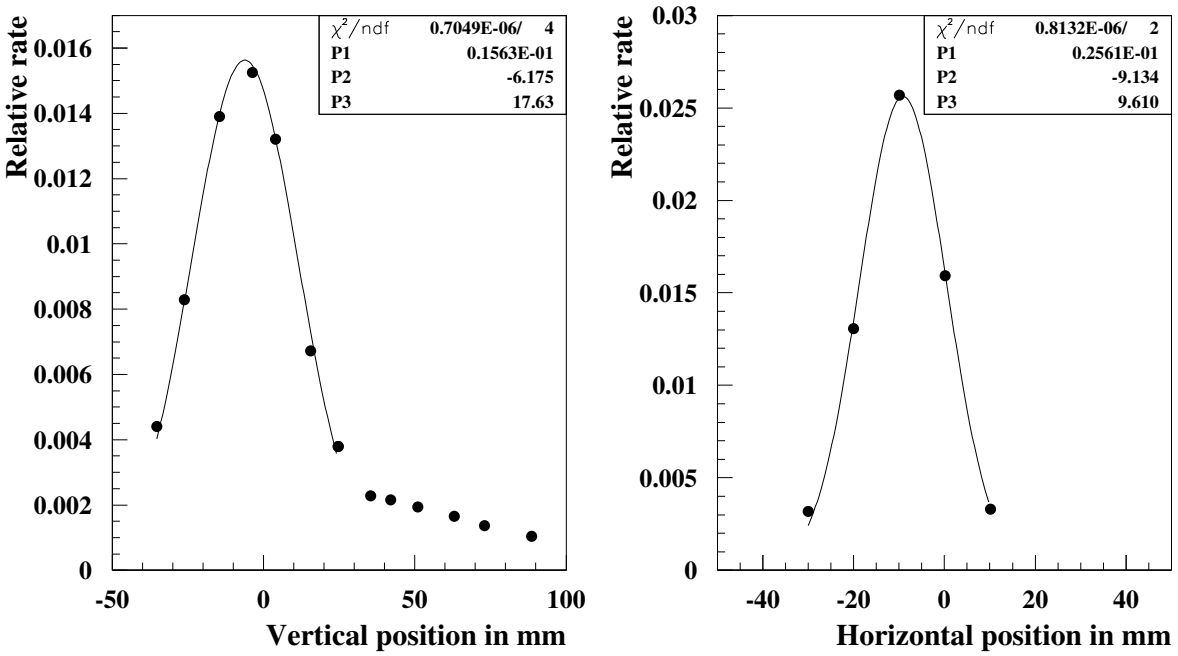


Figure 6.3: *Testbeam profiles of the DESY testbeam 21 at 3 GeV for the vertical (left) and horizontal (right) position.*

## 6.3 Results of $^{60}$Co measurements

$^{60}$Co measurements have been executed alternatively on each EMC sections before and after the electron measurements. The measurement performance of the $^{60}$Co scans corresponds to the inside scans of the ZEUS calorimeter described in Chapter 5.1.4 and 7.1. Brass tubes between the EMC1/2 and EMC3/4 sections on each tower side of the test calorimeter allow to guide the source parallel to the wavelength shifters. The high voltage of the photomultiplier was fixed by the $^{60}$Co monitor system (see 5.1.4). Measurements without the $^{60}$Co source serve to determine the pedestal of the readout system.
The $^{60}$Co measurements are used for calibration of the left and right photomultiplier and deliver information about the longitudinal structure and the optical status of the EMC section. The $^{60}$Co calibration is similar to the calibration procedure practised at the ZEUS calorimeter, where the constant background signal from the radioactive uranium absorber plates (UNO) is used to calibrate a signal $I$ with $\hat{I} = I/UNO$. At the test calorimeter using lead absorber plates no defined background signal exists. Yet for both cases, the $^{60}$Co source at the test calorimeter and the uranium plates of the ZEUS calorimeter, a certain energy is deposited inside the calorimeter section.

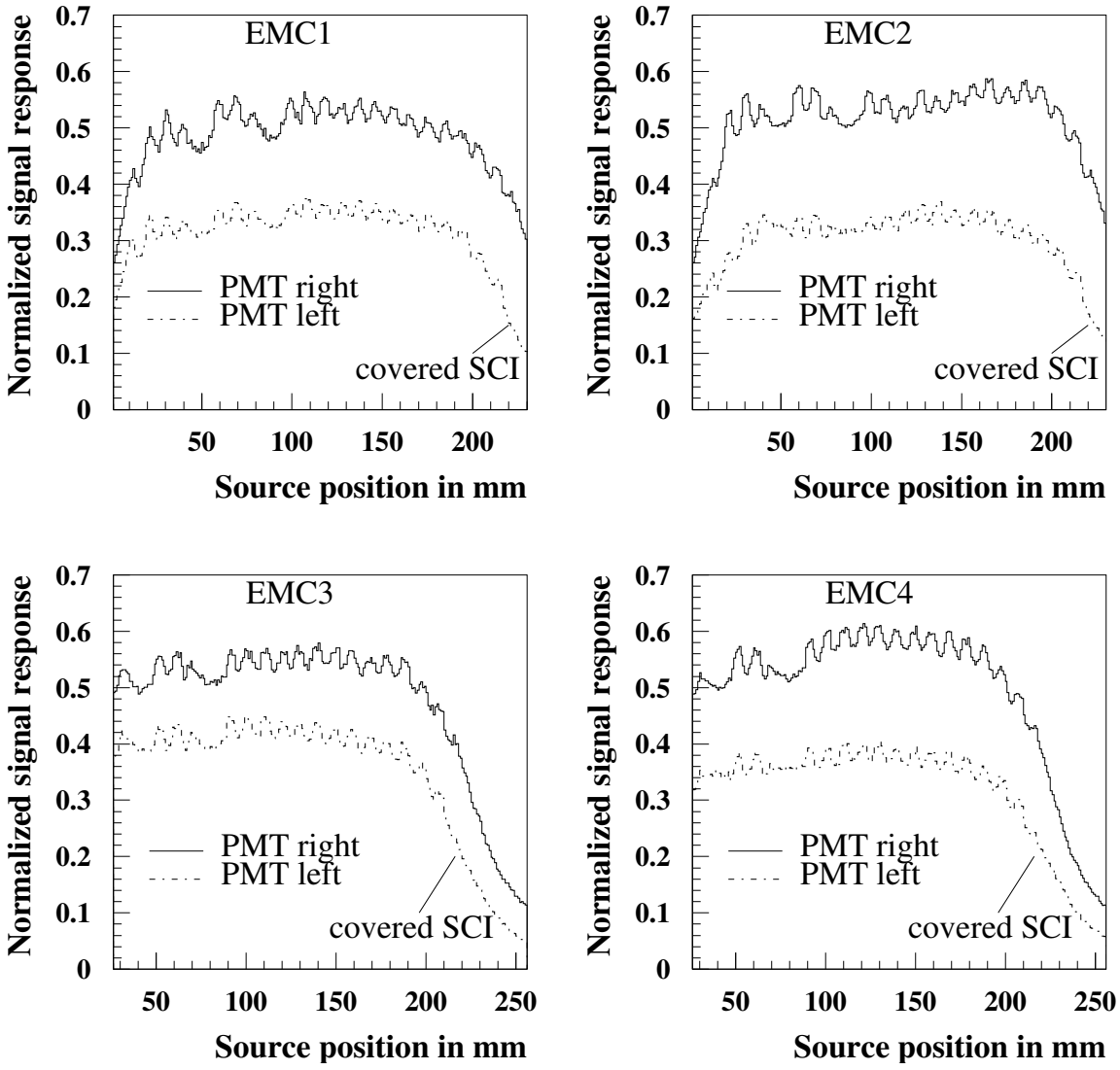


Figure 6.4: $^{60}$*Co signal responses from scans on the right tower side of the test calorimeter. The first maxima in the signal responses correspond to the scintillators closest to the testbeam. One has to notice, that the 21st maximum of the last scintillator in the left signal responses of all EMC sections (≡ left PMT) is almost missing.*

In contrast to the UNO signal which results in a homogeneous excitation of the scintillator, the $^{60}$Co source excites only the edges of the latter. Therefore the integrated sum over the active area of $^{60}$Co signal responses $I_{jj} + I_{kj}$ from two $^{60}$Co scans on both tower sides $j, k$ is used to normalize the photomultiplier signal $I_j$:

$$\hat{I}_j = \frac{I_j}{\int (I_{jj}(z) + I_{kj}(z))dz}. \tag{6.2}$$

This sum includes the energy deposition of the source on each tower side as well as the light loss due to transmission $T < 1$ inside the scintillators of the section. Uniform changes in the optical properties can therefore be recalibrated. The diagrams in Figure 6.4 show the normalized signal responses of the EMC sections. No significant differences are visible in the longitudinal structure between the signal responses of irradiated sections and those of the references. This

result is to be expected with respect to the uniform irradiation of the sections (EMC1 $\approx$ 5 kGy, EMC2 $\approx$ 10 kGy). The first maxima in the signal responses of the EMC1 and 2 sections correspond to the first scintillator closest to the testbeam. In case of the EMC3 and 4 sections this scintillator and the adjacent ones have not been reached by the $^{60}$Co source and therefore were not measured. One has to notice, that the 21st scintillator, which is the last one of the section, is not clearly visible in the left signal response ($\equiv$ left PMT) of all EMC sections. Evidently the scintillator is covered somehow on the left tower side and not completely read out by the wavelength shifter. Figure 6.5 displays the left and right $^{60}$Co signal responses of the

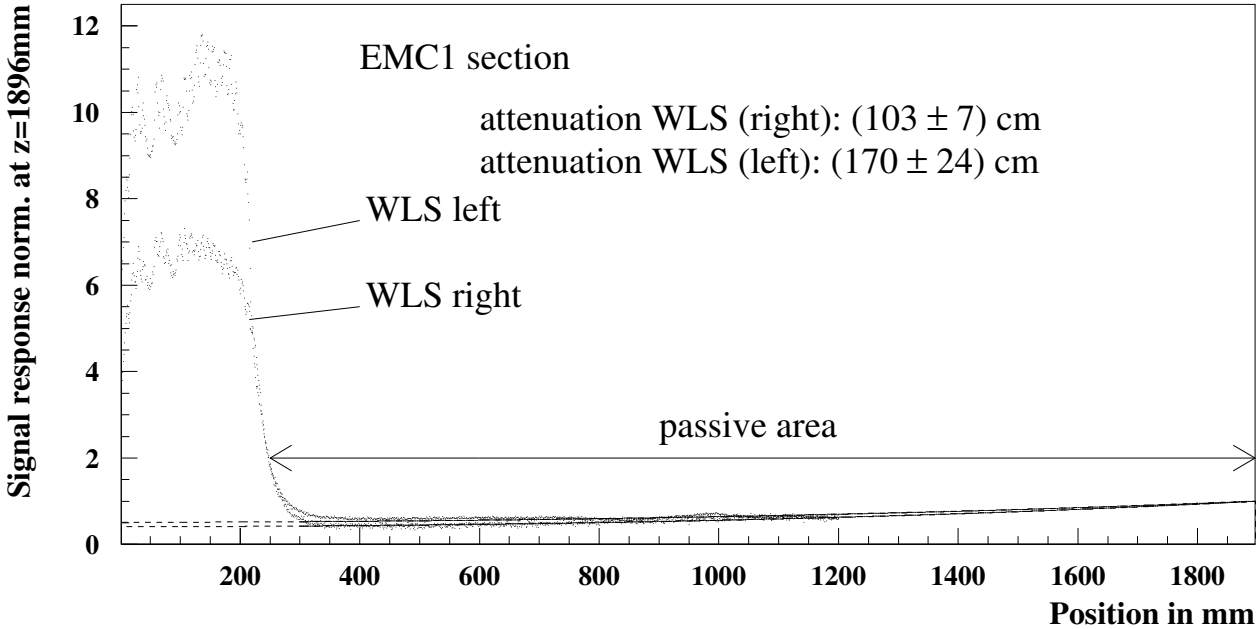


Figure 6.5: *Signal responses from $^{60}$Co scans on the right and left tower side of the EMC1 section including both the active and passive area with the pure wavelength shifter response. The significant reduction of the right signal response results from the 1 kGy irradiation of the wavelength shifter.*

EMC1 section. The signal responses have been normalized using the $^{60}$Co calibration and set to unity at $z$=1896 mm. The source is situated on the same tower side as the photomultiplier producing a small additional signal due to Cherenkov light produced by Compton electrons inside the wavelength shifter. The signal can clearly be seen outside the active area. The slope of the signal results from a significant attenuation $\lambda_o$ of the wavelength shifter. The signal response $W(z)$ of the wavelength shifter depending on the longitudinal source position $z$ can be described assuming the following ansatz:

$$W(z) \;=\; W_o \cdot (e^{-z/\lambda_o} + R \cdot e^{-(2L-z)/\lambda_o}). \tag{6.3}$$

Here is $R$ the reflection coefficient at the end of the wavelength shifter due to the endreflector and $L$ = 1896 mm denotes its length. Formula 6.3 is fitted with the wavelength shifter responses of all EMC sections. In table 6.3 the results of these investigations are presented. The reduction of the signal response due to light loss of the 1 kGy irradiated wavelength shifter is in the order of 50%. The short attenuation length of the 1 kGy irradiated wavelength shifter yields $\approx$ 1000 mm in comparison to the mean attenuation length of $\approx$ 1720 mm of the undamaged ones. Two $^{60}$Co scans on each tower side of an investigated section deliver an ensemble of 4 signal responses which allows to compute the optical parameters.

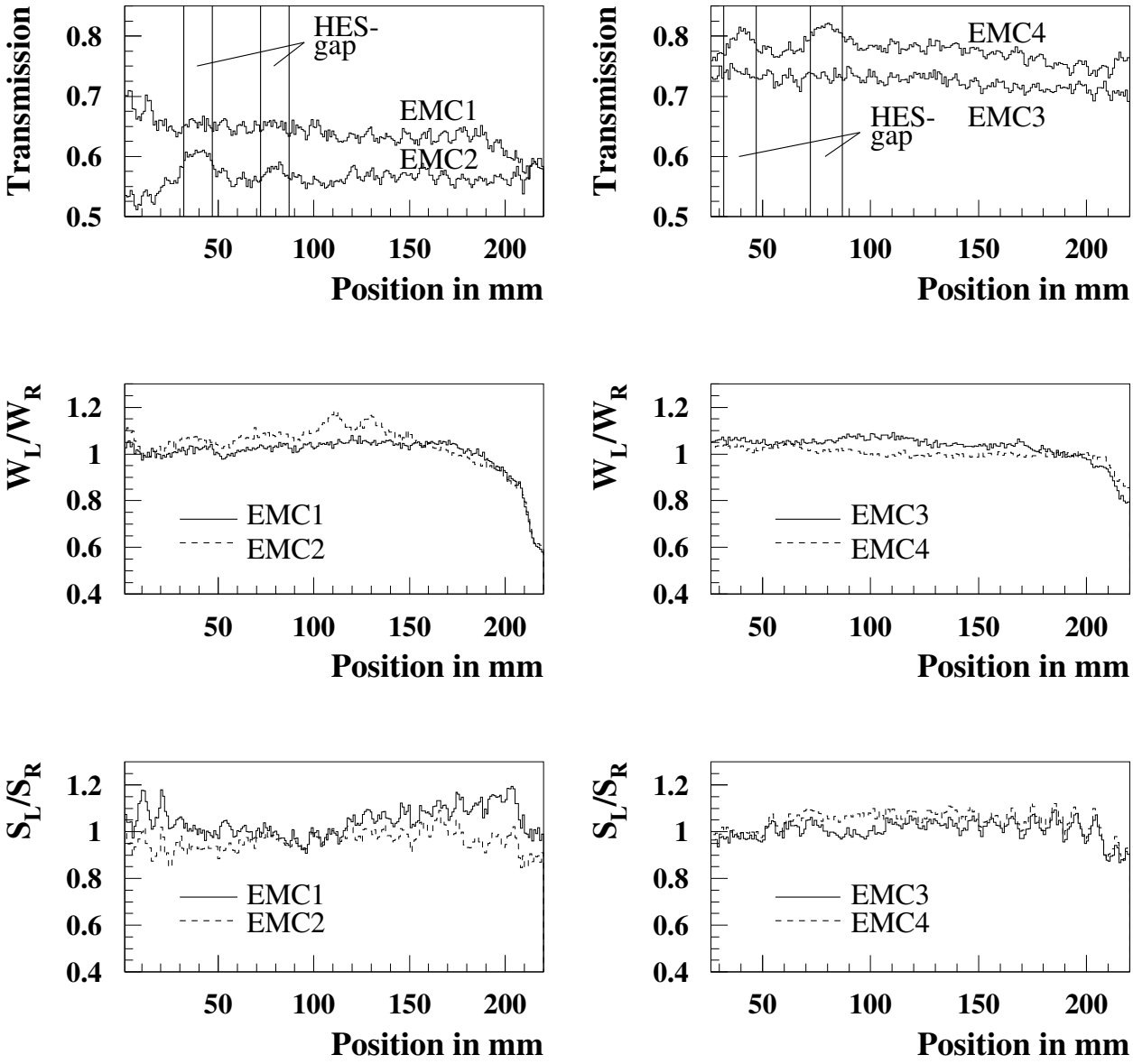


Figure 6.6: *The transmission (top diagrams), the ratio of the wavelength shifter responses (middle diagrams), and the ratio of the scintillator responses (bottom diagrams) of the EMC1/2 (left column) and EMC3/4 sections (right column), cf. text.*

Figure 6.6 presents the optical parameters of the irradiated sections (diagrams on the left) and of the references (diagrams on the right) as a function of the source position. The calculation is based on formulae 5.7. The top diagrams of Figure 6.6 demonstrate the transmission for each section. Unexpectedly the mean transmission of the reference sections differs significantly from each other. The reason is not clearly understood, but geometrical differences between these sections are very probable. Also the absolute values differ from those measured at the ZEUS calorimeter. That does not astonish due to the differences with respect to the absorber materials and the thickness of the plates. A reduction of the transmission is measured for the EMC1 section, a much bigger one is seen for the EMC2 section according to the radiation doses of 5 and 10 kGy. Certain maxima are visible in the transmission around the HES gap region. The

4th and 7th scintillator of each section is unshielded due to the empty HES gap. The $^{60}$Co source in front of the HES-gap excites these scintillators along their whole width which leads to an artificial increase of the transmission at this position. This is clearly visible in form of two additional maxima in the transmission of the EMC2 and EMC4 sections (see top diagrams of Figure 6.6). The ratio of the wavelength shifter responses of the EMC sections are shown in the middle diagrams of Figure 6.6. At first the big influence of the missing 21st scintillator in the left signal responses is obviously indicated by the strong decrease of the ratios of the wavelength shifter responses at a distance of $z \approx 220$ mm. Contrary to the expectation the ratio of the wavelength shifter responses of the EMC1 section shown in the middle left diagram in Figure 6.6 does not differ significantly from the others. But the ratios of the reference sections in the middle right diagram show a more uniform behaviour. Accordingly the ratios of scintillator responses of the irradiated sections (diagram in the bottom left) show larger fluctuations than the ones of the references (diagram in the bottom right). Table 6.3 displays the mean values of the optical parameters for each section including the attenuation lengths of the wavelength shifters. The results of the $^{60}$Co measurements can be summarized as follows:

| **results of $^{60}$Co monitoring** | | | | |
|---|---|---|---|---|
| section | EMC1 | EMC2 | EMC3 | EMC4 |
| transmission | $0.65 \pm 0.02$ | $0.56 \pm 0.02$ | $0.72 \pm 0.01$ | $0.78 \pm 0.02$ |
| $W_R/W_L$ | $1.03 \pm 0.02$ | $1.06 \pm 0.05$ | $1.02 \pm 0.07$ | $1.0 \pm 0.04$ |
| $S_R/S_L$ | $1.04 \pm 0.06$ | $0.97 \pm 0.04$ | $1.00 \pm 0.04$ | $1.04 \pm 0.05$ |
| $\lambda_{WLS(right)}$ | $(103 \pm 7)$cm | $(215 \pm 14)$cm | $(131 \pm 6)$cm | $(198 \pm 19)$cm |
| $\lambda_{WLS(left)}$ | $(170 \pm 24)$cm | $(182 \pm 22)$cm | $(155 \pm 12)$cm | $(152 \pm 14)$cm |

Table 6.3: *Optical parameters of irradiated (EMC1/2) and unirradiated (EMC3/4) sections.*

- A missing scintillator on one tower side should be detected by both the signal response as well as the ratio of the wavelength shifter response. This is confirmed by the experiment.
- The uniform irradiation of the scintillators changes the transmission, no variation is detected with regard to the ratio of the wavelength shifter and scintillator responses (see table 6.3).
- The change of the transmission results from the reduction of the attenuation length of the scintillators (see table 6.2).
- The 1 kGy irradiation of the right wavelength shifter of the EMC1 section leads to a loss of light yield in the order of 50% and to a strong reduction of the attenuation length $\lambda_{WLS}$. Within the range of the experimental errors it does not have a significant influence on the ratio of the wavelength shifter responses.

## 6.4 Linearity tests

An ideal sampling calorimeter requires a linear relation between impact energy of an incident particle and the measured signal. One important assumption is the uniform, position independent signal response of the optical components. In case of irradiation this condition is not guaranteed. A radiation damage of a wavelength shifter causes non-uniformities in the longitudinal response function effecting the linearity of the energy measurement.

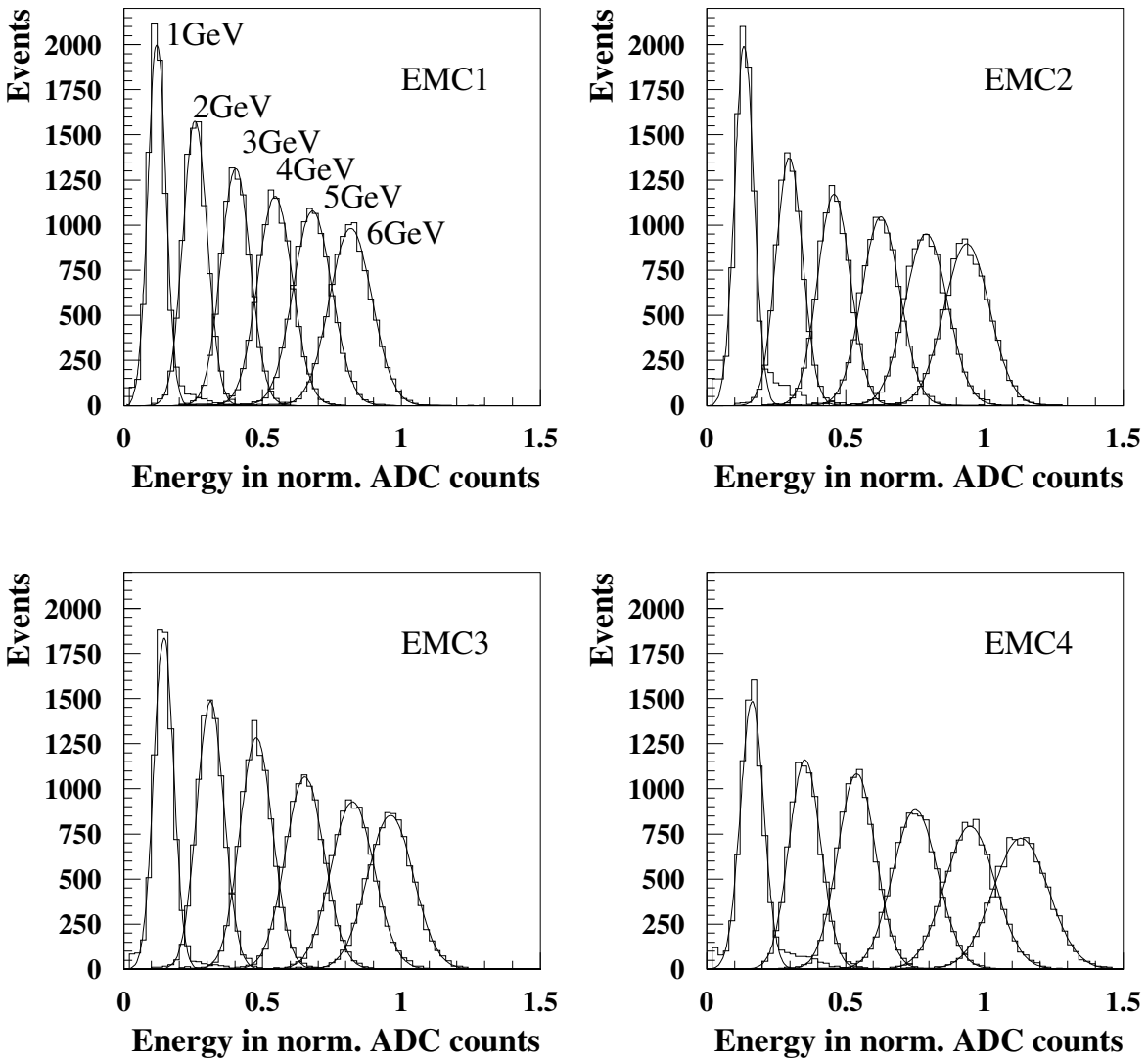


Figure 6.7: *Test Calorimeter response in normalized ADC counts of the EMC sections to 1 – 6 GeV electrons. A pedestal substraction has been performed. The normalization has been made using the $^{60}$Co relative calibration (cf. text).*

The irradiation of scintillators and wavelength shifters reduces the primary light yield. Accordingly the relative contribution of the photo-electron statistics increases. This deteriorates the energy resolution $\sigma$ of the concerned calorimeter. In order to inspect the non-linearities and the energy resolution due to irradiation linearity measurements have been taken on each EMC section of the test calorimeter. The beam was aligned in the middle of the section and the energy was varied between 1 and 6 GeV in 1 GeV steps with 10 k events per energy. The test calorimeter responses of each EMC section are shown in Figure 6.7. The left and right signal responses of each section have been normalized using the $^{60}$Co calibration with formula 6.2. The sum of both measured distributions is fitted by a Gaussian function and the mean measured energy $\hat{E}_M$ for each beam energy $E$ is determined. The left diagram of Figure 6.8 displays the mean measured energies versus the impact energies in GeV for each test calorimeter section.

The deviation of the measured energy from linearity can be obtained with:

$$\delta \;=\; \frac{\hat{E} - \hat{E}_M}{\hat{E}} \cdot 100\,\%. \tag{6.4}$$

$\hat{E}$ denotes the beam energy normalized at $\hat{E}_M(6\,\mathrm{GeV})$. The deviation of the measured energy from linearity of the EMC sections is shown in the right diagram of Figure 6.8. No significant difference is visible between irradiated (EMC1/2) and unirradiated (EMC3/4) sections. According to the UNO normalization used at the ZEUS calorimeter the $^{60}$Co relative calibration renormalizes the calorimeter response and almost compensates the uniform irradiation effects. But nevertheless the maximum deviations are outside of the expected range[4]. At 1 GeV there is a maximum deviation in the order of 14%. The deviation results not only from non-linearities of the EMC section but also from miscalibration of the nominal beam energy as confirmed by the DESY machine group [ME98].

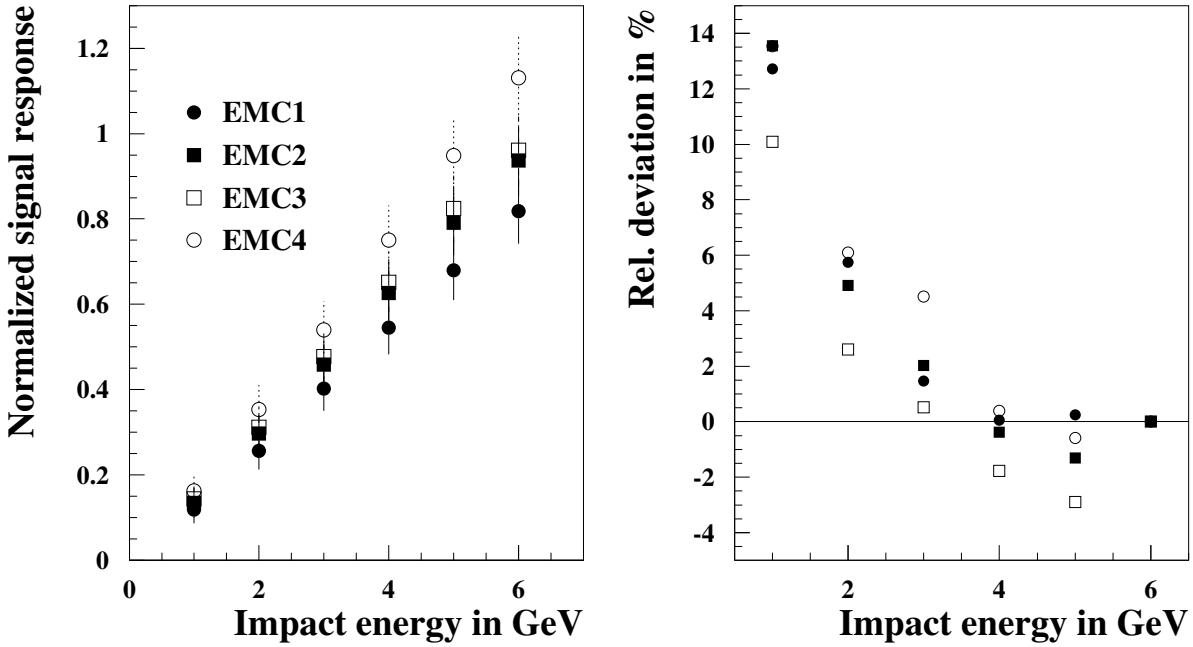


Figure 6.8: *Linearity of the EMC sections (left) and the deviation from linearity in percent (right) for all EMC sections.*

The relative energy resolution can be described by the following ansatz:

$$\frac{\sigma}{\hat{E}} \;=\; \frac{P}{\sqrt{\hat{E}_M}}, \tag{6.5}$$

where $P$ denotes the sampling term. Figure 6.9 presents the results including the fitted curves using formula 6.5. No significant difference can be observed between the EMC2 section and the references, so that the 10 kGy irradiation of the scintillators does not have a significant influence on the energy resolution. In contrast to the influence of the 1 kGy irradiated wavelength shifter of the EMC1 section. In order to simulate the case of two irradiated wavelength shifters on

[4]Theoretically a longitudinal non-uniformity of ±10% of a ZEUS calorimeter EMC section produces a maximum deviation in the order of ±2% within 1–6 GeV (see Chapter 4.2).

each tower side the signal response of the irradiated wavelength shifter of the EMC1 section was taken twice and associated with an additional fictive section (EMC$_{fictive}$). The energy resolution deteriorates dramatically if both wavelength shifters are irradiated. The results of the fits using equation 6.5 are presented in table 6.4. The influence of the irradiated wavelength

| results from linearity scans | | | | | |
|---|---|---|---|---|---|
| section | EMC$_{fictive}$ | EMC1 | EMC2 | EMC3 | EMC4 |
| energy resolution | $29.9\%/\sqrt{E}$ | $23.3\%/\sqrt{E}$ | $22.2\%/\sqrt{E}$ | $21.6\%/\sqrt{E}$ | $22.0\%/\sqrt{E}$ |

Table 6.4: *Relative energy resolution of the lead/scintillator calorimeter measured in the testbeam experiment.*

shifter on the energy resolution of the EMC1 section is clearly visible, especially for the fictive section assuming two 1 kGy irradiated ones. The energy resolution $\sigma$ is the sum in quadrature

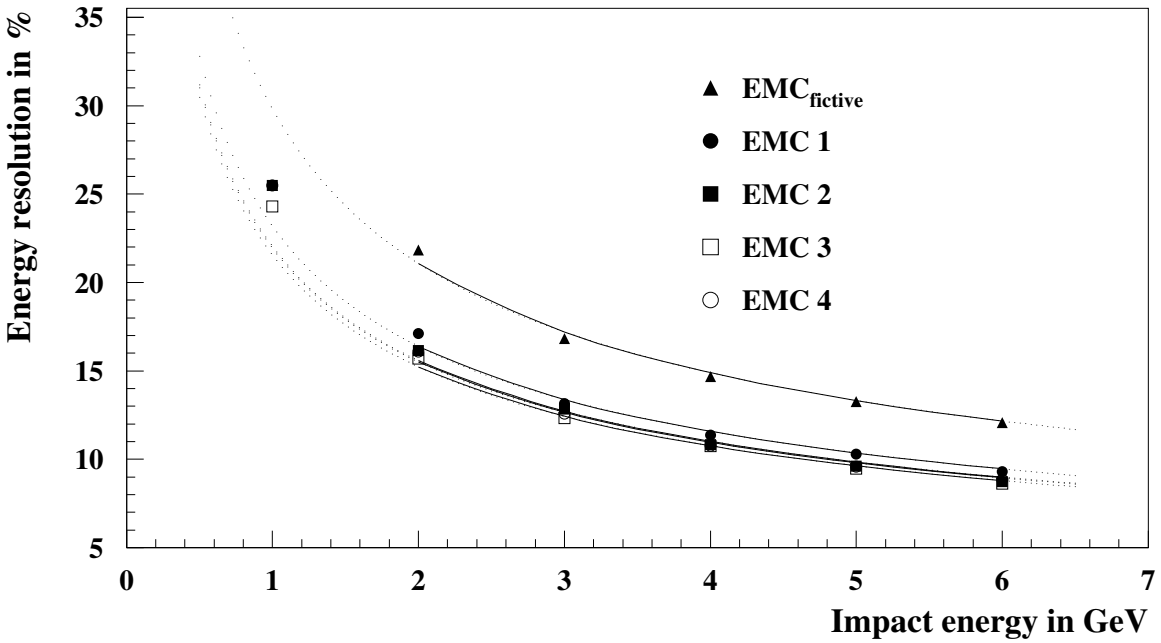


Figure 6.9: *Energy resolution of the EMC sections.*

of the errors $\sigma_p$ due to photons and electrons and other general errors $\sigma_g$. In case of irradiation the number of photo-electrons is decreased by a factor $L_{pm}$ which depends on the radiation dose $D$. The energy resolution of an irradiated calorimeter section $\sigma_D$ as a function of the energy $E$ can be computed with:

$$\sigma_D(E) = \frac{1}{E} \cdot \sqrt{\sigma_g^2 + \sigma_p^2 \cdot (\frac{1}{L_{pm}} - 1)}, \tag{6.6}$$

$$L_{pm}(D) = I_{SCI}(D, \bar{x}_{SCI}) \cdot I_{WLS}(D, \bar{z}_{WLS}). \tag{6.7}$$

$L_{pm}(D)$ is the radiation dose dependent calorimeter response of the section equal to the product of the light yields of the scintillators and the wavelength shifter assuming effective light paths $\bar{x}_{SCI}$ and $\bar{z}_{WLS}$.

**Consequences of 3 kGy irradiation for the ZEUS calorimeter:** The energy resolution for the ZEUS uranium calorimeter in case of a uniform 3 kGy irradiation has been calculated in [DA96]. There it is demonstrated, that the effects in the energy resolution resulting from 3 kGy irradiation should be small and negligible. The variation in the energy resolution of the FCAL EMC sections increases from $18.0\%/\sqrt{E(\mathrm{GeV})}$ to about $18.5\%/\sqrt{E(\mathrm{GeV})}$, in case of the FCAL HAC sections from $35\%/\sqrt{E(\mathrm{GeV})}$ to about $35.1\%/\sqrt{E(\mathrm{GeV})}$. These relative variations correspond roughly to the one of the testbeam measurements with respect to the pure irradiated scintillators of the EMC2 section presented in table 6.4.

## 6.5 Uniformity tests

In order to verify the transverse uniformity of the light collection the electron beam at energies of 6 GeV was aligned at certain positions in the horizontal plane of each EMC section. The horizontal scan was performed on the sections in steps of about 3 cm. The result is displayed in Figure 6.10, where the sum of the right and left photomultiplier signals is plotted versus the impact position of the incident electron beam. The response of the reference sections is seen to be uniform within $\pm 2\%$ in a region of $\pm 60$ mm around the centre of each section, whereas the uniformity of the irradiated sections yields $\pm 1\%$ within the same region. Obviously the reduction of the attenuation length of the scintillators improves the transverse uniformity in the order of 1% which could results from a compensation of a wrong influence of the correction pattern printed on the tyvec-paper to achieve uniformity. Nevertheless a strong enhancement is observed at the edges of the scintillators. This effect can be attributed to an increase of the light yield in the scintillators and to Cherenkov light produced in the wavelength shifter itself. The change of the attenuation length of the scintillators is demonstrated in Figure 6.11.

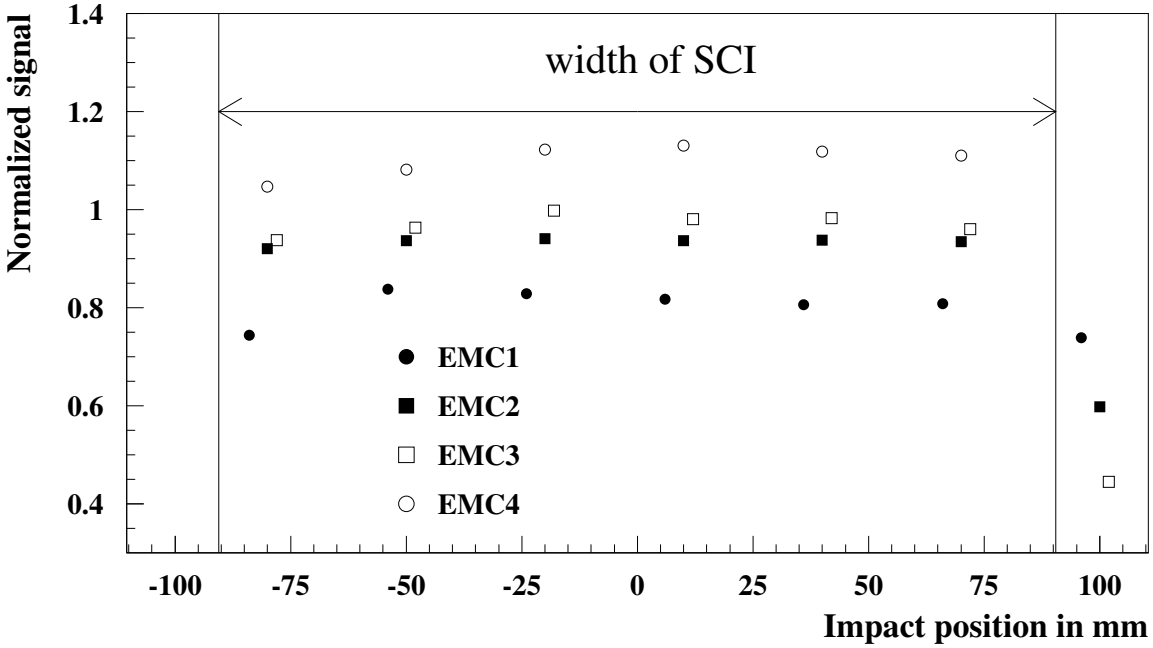


Figure 6.10: *Result of horizontal scans on the EMC sections with 6 GeV electrons. The signal is the sum of both photomultiplier signals normalized by the $^{60}Co$ relative calibration. The centre of the section corresponds with x=0 mm.*

It displays the left/right ratio for the irradiated sections (left diagram) in comparison to the reference sections (right diagram). The left/right ratio of two photomultipliers including light reflection at the opposite end of the photomultiplier as a function of the incident position $x_i$ of the electron beam can be described by:

$$f(x_i, \mu') = \frac{\hat{I}_{left}(x_i)}{\hat{I}_{right}(x_i)} = \frac{\hat{I}_0 \cdot e^{-\mu' \cdot x_i} + \hat{I}_0 \cdot R \cdot e^{-(2L - x_i)\cdot \mu'}}{\hat{I}_0 \cdot e^{-\mu' \cdot (L - x_i)} + \hat{I}_0 \cdot R \cdot e^{-(L + x_i)\cdot \mu'}}. \tag{6.8}$$

The reflection coefficient $R$ at the opposite side is assumed to be 0.2; $\mu'$ is the unknown mean absorption coefficient of the scintillators; $x_i$ is set to zero in the centre of the sections. The function 6.8 is used to describe the left/right ratio within the fiducial area of $x_i = \pm 6\,\mathrm{cm}$. An optimized fit with respect to the measurements determines the attenuation length $\lambda' = 1/\mu'$. The Least Squares Method which is also sometimes referred as chi-squares minimization allows the optimization of the function 6.8: This method states that the optimal values of parameters $a_j$ at $x_i$ measurement points of a function $f(x_i, a_j)$ are those for which the sum

$$S = \sum_{i=1}^{n} \left| \frac{y_i - f(x_i; a_j)}{\sigma_i} \right|^2 \tag{6.9}$$

is a minimum. The values of $a_j$ have to solve the system of equations $\delta S / \delta a_j = 0$. The errors $\sigma_j$ on the parameters $a_j$ are given by the error matrix V

$$(V^{-1})_{ij} = \frac{1}{2} \cdot \frac{\delta^2 S}{\delta a_i \cdot \delta a_j}, \tag{6.10}$$

where the second derivatives are evaluated at the minimum and form the inverse of the error matrix $V$. In case of the left/right ratio the number of unknown parameters is one, namely the absorption coefficient $\mu'$. Therefore the calculation is reduced to the simplest case. The numeric solution for the left/right ratio fitted on the measurements $\pm 70\,\mathrm{mm}$ around the centre of the section yields the functions presented in Figure 6.11. The resulting attenuation lenghts $\lambda' = 1/\mu'$ are presented in table 6.5.

| **attenuation in mm from uniformity scans** | | | | |
|---|---|---|---|---|
| section | EMC1 | EMC2 | EMC3 | EMC4 |
| attenuation | $396 \pm 18$ | $318 \pm 11$ | $599 \pm 46$ | $664 \pm 57$ |

Table 6.5: *Attenuation lengths of scintillators determined from 6 GeV electrons of irradiated (EMC1/2) and unirradiated (EMC3/4) sections of the lead scintillator calorimeter.*

## 6.6 Conclusions

The aim of the testbeam measurements at DESY using an uniformly irradiated test calorimeter was the investigation of the influence of irradiated optical components on calorimetry and its monitoring possibilities. Therefore a lead/scintillator sampling test calorimeter with a configuration similar to the FCAL EMC tower has been constructed consisting of two irradiated EMC sections with 5 and 10 kGy and two reference EMC sections. Additionally the left wavelength

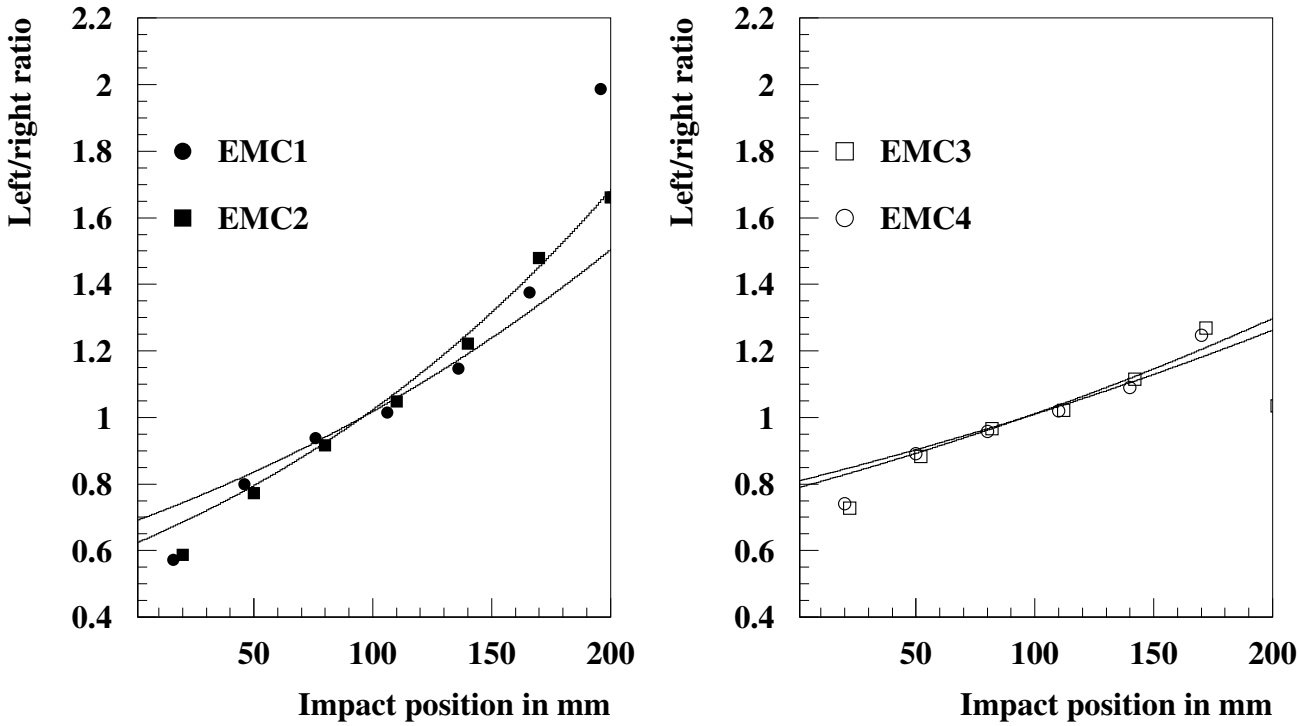


Figure 6.11: *The left/right ratios of uniformity scans for the irradiated sections (left) in comparison to the respective ones of the reference sections (right). The centre of the section corresponds with x=100 mm. The solid lines denotes the functions optimized by the Least Squares Method.*

shifter of the EMC1 section was irradiated with a dose of 1 kGy. Scanning bench measurements on single scintillators of the test calorimeter before and after irradiation using electrons of a $^{90}$Sr source allowed to determine the radiation damage. For a dose of 5 and 10 kGy a reduction of the attenuation lengths of 32% and 45%, respectively was measured. The test calorimeter was installed at the DESY testbeam in June 1998 for two weeks. The EMC sections were tested with respect to effects on linearity with 1 to 6 GeV and transverse uniformity scans with 6 GeV electrons were performed. No significant influence of irradiation is visible on the linearity of the test calorimeter within the used range of electron energies. The irradiation of the scintillators does not have a significant influence on the energy resolution, whereas the irradiated wavelength shifter influences the energy resolution strongly. The transverse uniformity scans allowed to determine the effective attenuation length of the scintillators resulting a reduction of 40% and 50% in case of 5 kGy and 10 kGy. The uniformity of the calorimeter response of the irradiated sections is within $\pm 1\%$ in a region of $\pm 60$ mm around the centre of the scintillators. It is obviously better than the uniformity of the reference sections. $^{60}$Co measurements allowed to compute the optical parameters of the test calorimeter monitoring a reduction of the transmission $T$ of the scintillators in case of 5 kGy of 17% and in case of 10 kGy of 23% with respect to the mean transmission of the reference sections. Figure 6.12 show the correlation between testbeam, $^{60}$Co and $^{90}$Sr measurements. In the left diagram of Figure 6.12 the scintillator attenuation of all EMC sections determined from testbeam measurements is plotted versus the transmission determined from $^{60}$Co measurements. Both, the testbeam as well as $^{60}$Co measurements show a difference between the undamaged EMC3 and EMC4 section. The reason is not understood, but geometrical differences between these sections are possible. In the right

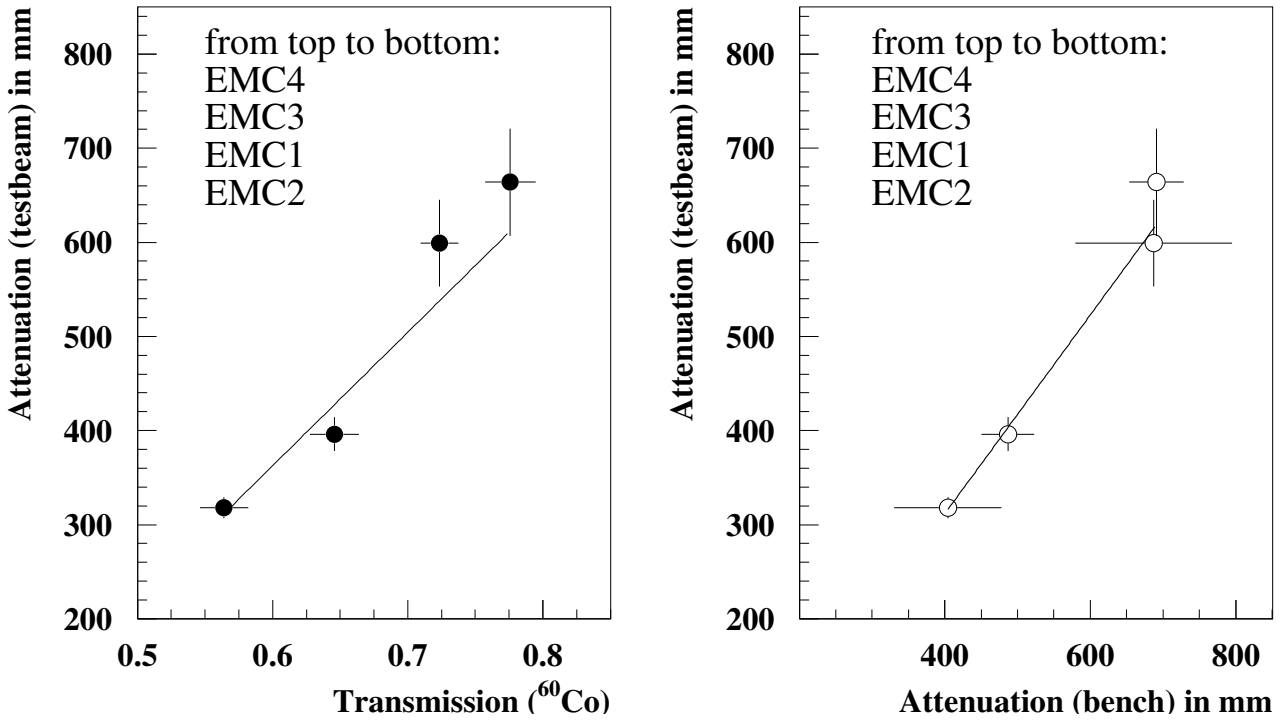


Figure 6.12: *The attenuation lengths of the scintillators of the EMC sections determined from testbeam measurements as a function of the transmission determined by $^{60}$Co monitoring. The right diagram shows the same attenuation lengths plotted versus the attenuation lengths from scanning bench measurements.*

diagram of Figure 6.12 the scintillator attenuation length is plotted versus the attenuation from scanning bench measurements. It demonstrates the good correlation between the attenuation determination of testbeam measurements and the bench investigations of scintillators using electrons of a $^{90}$Sr source. The $^{60}$Co monitor system is well suited to determine the status of the optical components of calorimeters, especially of the ZEUS calorimeter.

# Chapter 7

# Uniformity measurements on the ZEUS calorimeter

The uniformity of the ZEUS calorimeter can be degraded by mechanical changes, ageing, humidity or radiation effects on the optical components. Especially the ZEUS Calorimeter towers close to the HERA beams are expected to be irradiated during the operating time. Almost each maintenance period $^{60}$Co measurements have been taken on these towers controlling the quality with respect to possible variations of the longitudinal uniformity and the transmission of the scintillators since 1992. The following chapter describes $^{60}$Co measurements and the analysis of the FCAL (1996) and the RCAL (1997/1998) in comparison to reference measures (1990/1991). The evidence of a possible change in the transmission of the scintillators due to ageing led to special investigations on the FCAL module 12, which was accessible from both tower sides in the maintenance period 1997/1998. Investigations on the FCAL module 17 took part in 1999, from which reference data from both $^{60}$Co inside and outside scans exists. These measurements confirmed the evidence of ageing effects of the scintillators. The location of measurement as well as the different scanning methods described in this chapter are illustrated for investigations on the FCAL in Figure 7.1.

## 7.1 Measurement performance

In 1990/1991 $^{60}$Co measurements of all 48 FCAL/RCAL modules have been taken before the installation into the calorimeter using the outside scanner. The measurements were based on an OS/9 and VME-bus operating system. The data acquisition was done by 12-bit multiplexer analog to digital converter, which reads out the photomultiplier signals integrated over 24 ms. The scanner consisted of a driver controlled by a microprocessor (Motorola 68HC11), which was moving the source with constant speed while data taking (in the fly). The scanner was mounted on an assembly which rolled along the front plate of a single calorimeter module. Two wings each with four guide tubes 5 cm apart from one another, hung parallel to the wavelength shifters, one on each side of the module. The $^{60}$Co source at one end of the source wire was guided in such a tube between the EMC1/2 and EMC3/4 sections during the FCAL scans and between the EMC1/2 section during the RCAL scans [KR93]. The main advantage of outside scans is the use of a double encapsulated source. Besides, there is no risk of the source getting stuck inside the calorimeter. The mechanical precise of the installation is limited and leads to a worse reproducibility (see Chapter 5.1.4). The present measurement system is a PC based system described in Chapter 5.1.4. It is used for the first time in 1996. The data acquisition is

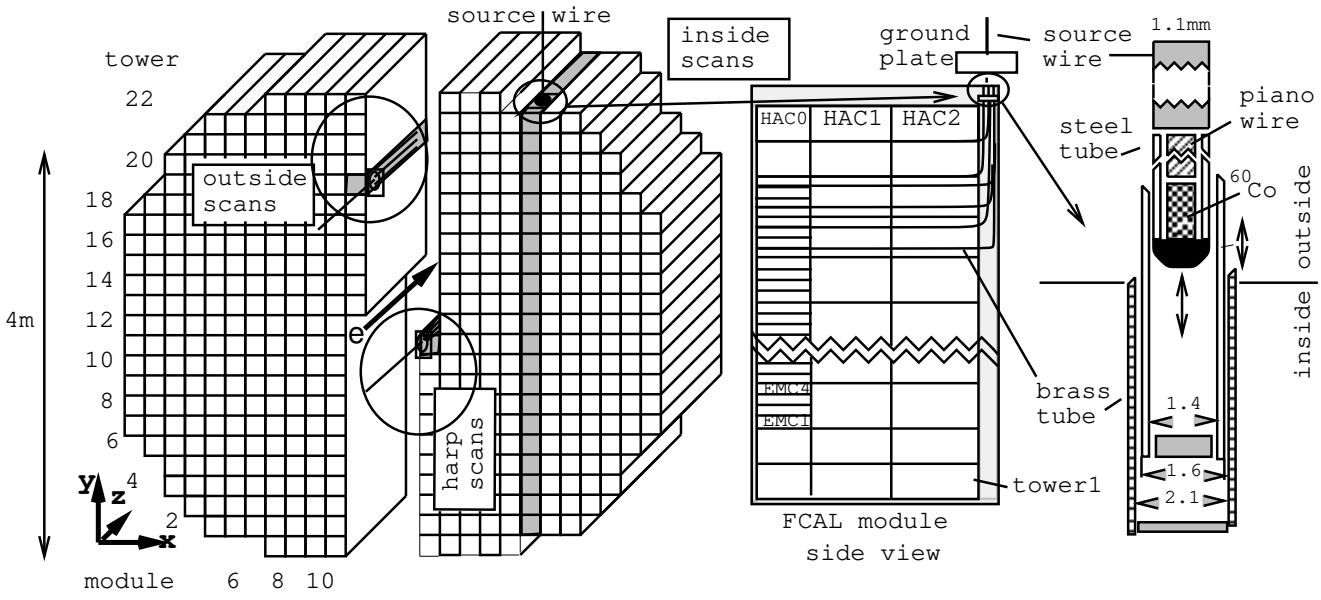


Figure 7.1: *Front view in direction to the vertex point on the Forward Calorimeter (FCAL) in an opened state. The different $^{60}Co$ scanners at their locations (outside, inside, harp scanner) described in this chapter are illustrated.*

done by moving the source for one step, then stopping it and measuring directly the currents of the photomultipliers by an 812-PCL-ADC-card of *SPECTRA* (stop and go). The range of the 812-PCL-ADC-card is about $\pm 10\,V$, thus one ADC channel was about $5\,mV$. The main improvements of the PC-system are efficiency, accuracy of measurement and stability. In order to demonstrate that any observed changes in the $^{60}Co$ measurements are due to changes in the components and not just artefacts of the scanning process or random fluctuations from run to run, it is necessary to test the reproducibility with respect to the different measurement systems. The reproducibility of $^{60}Co$ measurements is demonstrated by $^{60}Co$ inside scans on the test calorimeter[1] using both the OS/9 system and the PC system [BO96]. Repetition scans on the ZEUS calorimeter using the outside scanner demonstrated the reproducibility after the replacement of the whole measurement set-up. The results of these measurements were found to differ below the 1-2% level. Table 7.1 describes the main differences of the OS-9/PC based measurement systems.

During the maintenance period the calorimeter halves are positioned at a distance of at least $70\,cm$ from each other, so that the calorimeter towers close to the HERA beams are accessible from one side. Then $^{60}Co$ measurements are conventionally realized by a similar outside scanning procedure as described above. An aluminium wing containing brass tubes in connection with the ground-plate is mounted on a small steel frame. The assembly is pressed on the side plate of the investigated tower and allows to guide the source wire parallel to the section. Since 1994 the source is guided generally over the middle of the EMC sections of both the RCAL and the FCAL. This change of the measurement procedure was necessary due to the strong influence of misplacements of the source.

[1] See Chapter 6.1.

| measurement system | measurement time per scan | source velocity | number of data per mm | repetition per data |
|---|---|---|---|---|
| OS/9 in the fly | ≈ 7 min. | 4.4 mm/s | ≈ 3 | 1 |
| | | signal integration | distance integration | conversion of ADC |
| | | 24 ms | 0.33 mm | 17 - 11 KHz |
| PC stop and go | ≈ 25 min. | source velocity | number of data per mm | repetition per data |
| | | 1.2 mm/s | ≈ 1 | 3500 |
| | | signal integration | distance integration | conversion of ADC |
| | | - | 0 mm | max. 90KHz |

Table 7.1: *Configuration of the OS/9 and PC system used for ZEUS measurements*

## 7.2 Strategy of analysis

The $^{60}$Co source moving parallel to the wavelength shifters of a calorimeter section causes a local energy deposition at the edge of the scintillators close to the source. The result is a signal response of the $^{60}$Co source depending on the source position. This measures about the longitudinal uniformity of the section and allows to estimate the transmission of the scintillators. The normalization is performed by formula 5.2. An extensive software package exists processing and modulating the $^{60}$Co signal responses with respect to the algorithms which are described in the following. More detailed information can be found in [SC95], [HE95], [BO99d].

### Reproducibility

The comparison between two normalized signal responses which were taken at two different times delivers information about the longitudinal structure and shows possible variations of the measured section. A position dependent reference response $I_a$ should have N components $(a_1, a_2, ..., a_N)$ with $a_i = \mathbf{I_a}(z_a + i \cdot \Delta z_a)$, a second signal response $I_b$ should have the number $M$ of components $(b_1, b_2, ..., b_M)$ with $b_i = \mathbf{I_b}(z_b + i \cdot \Delta z_b)$. The stepsize of the source scan is given by $\Delta z_a$ and $\Delta z_b$. In order to compare these two different $^{60}$Co signal responses one has to adjust them on each other based on the position calibration: The second signal response will be shifted along the position, stretched or compressed and normalized to the same number $N$ of components until it fits optimally with the reference one. The linear correlation $r$ of the signal responses $\mathbf{I_a}$ and $\mathbf{I_b}$ is calculated with [SP85]:

$$r(\mathbf{I_a}, \mathbf{I_b}) = \frac{\sum_{i=1}^{N}[(a_i - \overline{a}) \cdot (b_i - \overline{b})] \cdot \frac{1}{N-1}}{\sqrt{\sum_{i=1}^{N}[a_i - \overline{a}]^2 \cdot \frac{1}{N-1}} \cdot \sqrt{\sum_{i=1}^{N}[b_i - \overline{b}]^2 \cdot \frac{1}{N-1}}}. \quad (7.1)$$

$\overline{a}$ an $\overline{b}$ denote the mean of the signal response. An optimized linear correlation of the signal responses yields a maximum with $\mid r \mid \leq 1$. The comparison is quantified by the deviation from reproducibility $R_d$ calculated at an optimized linear correlation $r$: The deviation from

reproducibility $R_d$ of the signal responses is then defined as [SC95]:

$$R_d = \sqrt{\sum_{i=1}^{N} (\frac{b_i}{\bar{b}} - \frac{a_i}{\bar{a}})^2 \cdot \frac{1}{N-1}} \cdot 100\,\%. \tag{7.2}$$

The deviation from reproducibility referred as chi-squares minimization allows the quantification of the comparison of two signal responses measured at two different times. A variation of the signal response $I_b$ with respect to the reference $I_a$ causes a greater value $R_d$. Theoretically one could assume that the increase of deviation $R_d$ is caused alone by additional non-uniformities of one of the two response functions[2]. The reproducibility of two signal responses depends on the error of the source position, a statistical error with respect to the data acquisition and the error of the measurement of the longitudinal source position (see Chapter 5.1.4). Using the outside scanner the positioning error results mainly from wrong replacement of the guiding tube system with respect to reference measurements. In order to reduce statistical effects, the calculation of the deviation from reproducibility is performed using signal responses which are averaged over steps of 8 mm corresponding to the distance of the scintillators in the ZEUS uranium calorimeter.

### Test of wavelength shifters

Outside scans on one tower side restrict the capabilities of $^{60}$Co analysis, because the calculation of the optical parameters described in Chapter 5.7 is not possible due to the onesided source scan. Nevertheless a test of the wavelength shifter which is on the same side as the source is performed by the ratio of two signal responses measured at two different times $t_o$ and $t$:

$$\frac{\hat{I}_{jj}(t)}{\hat{I}_{jj}(t_0)} = \frac{S_j(t) \cdot W_j(t)}{S_j(t_o) \cdot W_j(t_o)}, \tag{7.3}$$

$$\approx \alpha(t - t_o) \cdot \frac{W_j(t)}{W_j(t_o)}. \tag{7.4}$$

The notation is similar to the formula 5.7. The wavelength shifter is more sensitive to irradiation effects than the scintillators (see Chapter 4.3). At low radiation doses ($D < 1$ kGy) the primary light yield of the *SCSN-38* scintillators does not change. Hence the ratio $S_j(t)/S_j(t_o)$ should depend on the mean life-time $\tau = 5.2$ a of the $^{60}$Co source with $S_j(t)/S_j(t_o) \approx \alpha(t - t_o) = e^{-(t-t_0)/\tau}$. Here it is assumed that the same source was used in both scans at the time $t$ and $t_o$. Any larger variation of the ratio is expected to result directly from a radiation damage of the wavelength shifter.

### Transmission

In a first approximation the right/left ratio of the signal responses of the right and left photomultiplier from one $^{60}$Co scan specifies the transmission of the scintillators of the measured section.

$$\frac{\hat{I}_{jk}(t)}{\hat{I}_{jj}(t)} = \frac{S_j(t) \cdot W_k(t) \cdot T(t)}{S_j(t) \cdot W_j(t)}, \tag{7.5}$$

$$\approx T(t) \quad \text{for } W_k(t) \approx W_j(t). \tag{7.6}$$

[2] That means not necessarily a real physical non-uniformity; a bad reproducibility could also be simulated by several measurement faults.

The assumption is a uniform behaviour of the wavelength shifter responses $W_j(t)$ and $W_k(t)$. Since 1992 outside scans can only be performed onesided on the towers close to the HERA beams[3]. The analysis from onesided $^{60}$Co outside scans is restricted and strongly sensitive to source positioning errors. On the other hand a big data base from outside scans exists which enables an extensive statistic and points out general trends of the properties of the ZEUS calorimeter assisting the predictions of other $^{60}$Co investigations described in this thesis.

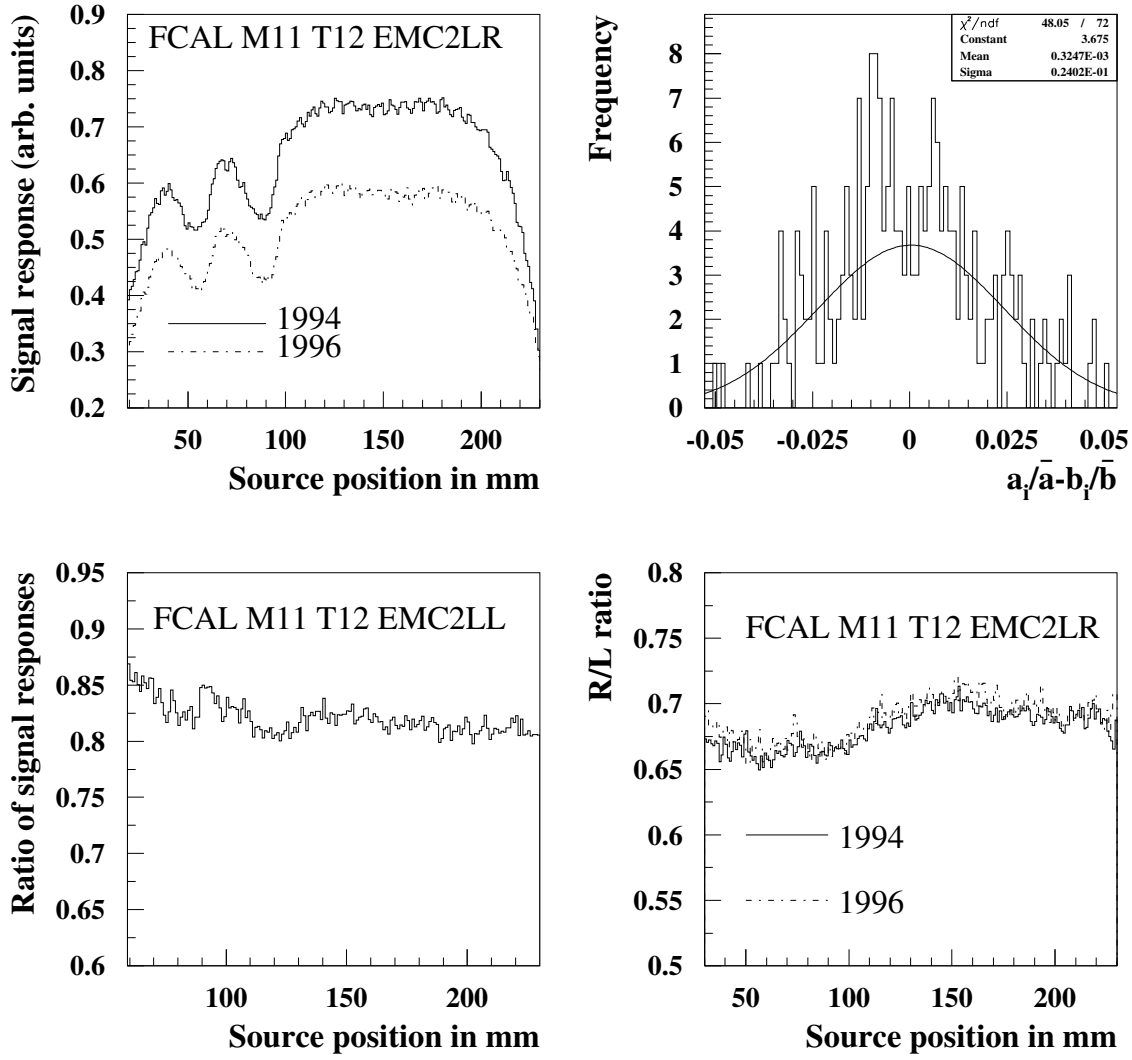


Figure 7.2: *Comparison of $^{60}$Co signal responses of the FCAL module 11, tower 12, EMC2 section (cf. text).*

## 7.3 Investigation on radiation damage effects

The following chapter describes the last results of $^{60}$Co outside scans of the FCAL and the RCAL in comparison with previous measurements. In the first place the analysis concentrates on the reproducibilities of the signal responses and the right/left ratios. It will be demonstrated that no

[3]One exception is the disassembling of the FCAL module 12 in the maintenance period 1997/1998 (see section 7.4.1.)

significant change in the longitudinal structure of the investigated sections is observed according to a good reproducibility of the measurements with respect to the reference data. Nevertheless a small time dependent decrease of the right/left ratio is observed which refers to a change in the transmission of the scintillators. This effect is measured in almost all investigated sections and shows evidence for an ageing effect of the scintillators of the ZEUS calorimeter. Therefore further investigations have been performed in order to verify the presumption described in this chapter.

### 7.3.1 Results of investigations on the FCAL

The main aim of $^{60}$Co outside scans is the comparison of present data with the references. The assumption for a reasonable comparison is a similar measurement performance. In 1990/1991 the outside scans of the FCAL EMC towers were performed by moving the $^{60}$Co source in the middle of EMC1/2 sections and then in the middle of the EMC3/4 sections to economize the scanning procedure. Two EMC sections were excited simultaneously per scan reducing the

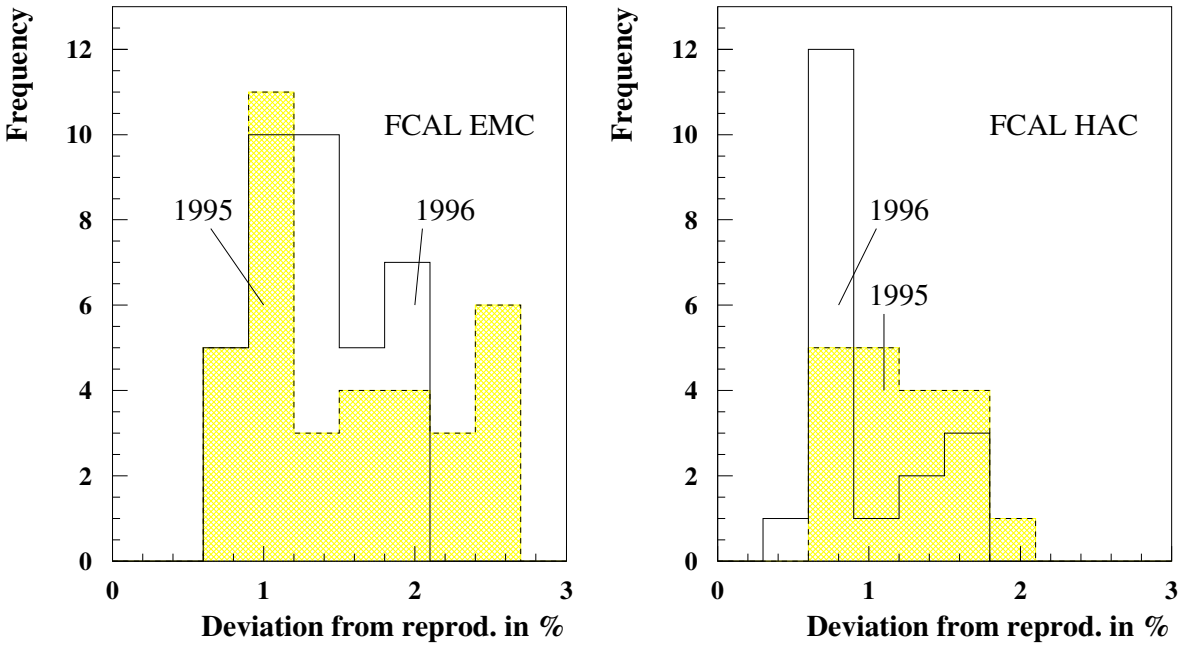


Figure 7.3: *Distribution of the deviation from reproducibility for the FCAL EMC (left) and the HAC (right) signal responses of 1995 and 1996 with respect to 1994. The analysis refers to the sections close to the HERA beams.*

total measurement time for a whole tower. Two scans on each tower side were necessary for a whole FCAL EMC tower. The disadvantage of this scanning procedure is the possibility of positioning errors due to a misplaced guiding tube set-up. Different vertical source positions change the signal response of EMC sections and can be wrongly interpreted as a radiation damage (see section 7.4.1).
In 1994 the guiding tube system for outside scans of the FCAL was changed. Since then the source has been guided in the middle of each EMC section parallel to its wavelength shifter, so

that the signal response is less sensitive to the exact source positioning. The analysis of the last FCAL outside scans described in the following refers to the period from 1994 to 1996. A typical example of the $^{60}$Co analysis of a FCAL section is demonstrated in Figure 7.2. The diagram on the top left shows the right signal responses of the EMC2 section of tower 12, module 11. The source is situated on the left side of the section. The solid and dashed line, respectively refers to the measurements in 1994 and 1996. The deviation from reproducibility is demonstrated in the diagram on the top right as the difference distribution of the normalized signal responses. The deviation from reproducibility is $R_d = 1.37\%$ which is a typical value for FCAL EMC sections. It is mainly caused by statistical errors of the data acquisition, the signal responses show no variation in the longitudinal structure of the section.

The diagram on the bottom left of Figure 7.2 displays the ratio of the left signal responses of this section corresponding to the test of the left wavelength shifter (see formula 7.3). The ratio is unity within $\pm 4\%$ and confirms no significant variation of the wavelength shifter close to the HERA beams. The diagram on the bottom right shows the ratio of the right/left signal responses of the measurements in 1994 (solid line) and 1996 (dashed line). Figure 7.3 displays the frequency of the deviation from reproducibility in 1995 and 1996 for all measured EMC (left) and HAC sections (right) with respect to the reference data of 1994. Figure 7.4 shows the mean of all measured right/left ratios of the FCAL signal responses in 1994, 1995 and 1996. The results for all sections are presented in the tables B.1 and B.2 of the appendix B. All in all the analysis of the FCAL sections measured by the outside scanner shows no evidence for significant variations in the time 1994–1996.

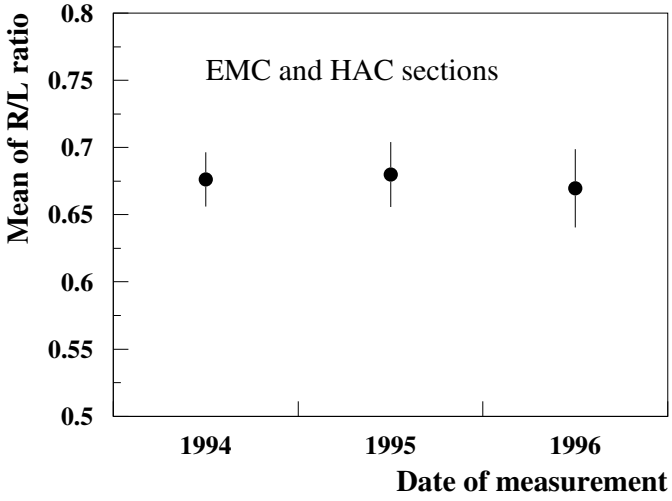


Figure 7.4: *Right/left ratio for the FCAL towers close to the HERA beams in dependence of the date of measurement.*

## 7.3.2 Results of investigations on the RCAL

Reference and also further $^{60}$Co measurements on the RCAL were executed under the same measurement performance. This allows to compare directly the present measurements with the references in 1990/1991. The $^{60}$Co source is guided in the middle of the EMC section. The analysis procedure is similar to the FCAL investigations. The following investigations refer to the tower 12 of module 13, the towers 11 and 13 of module 12 and tower 12 of module 11. A typical example of the 1998 analysis of a RCAL section is shown in Figure 7.5. The diagram on the top left shows the right signal responses of the EMC1 section of tower 11, module 12. The source is positioned on the left side of the section. The solid line and the dashed line, respectively refers to the measurement of 1991 and 1998, respectively. The difference distribution of the normalized signal responses of 1991 and 1998 is shown in the diagram on top right. The deviation from reproducibility yields $R_d = 2.06\%$ which is a typical value for RCAL EMC sections. It shows no variation in the longitudinal structure. The present ratio of the left signal responses of the section which is more or less unity shown on the bottom

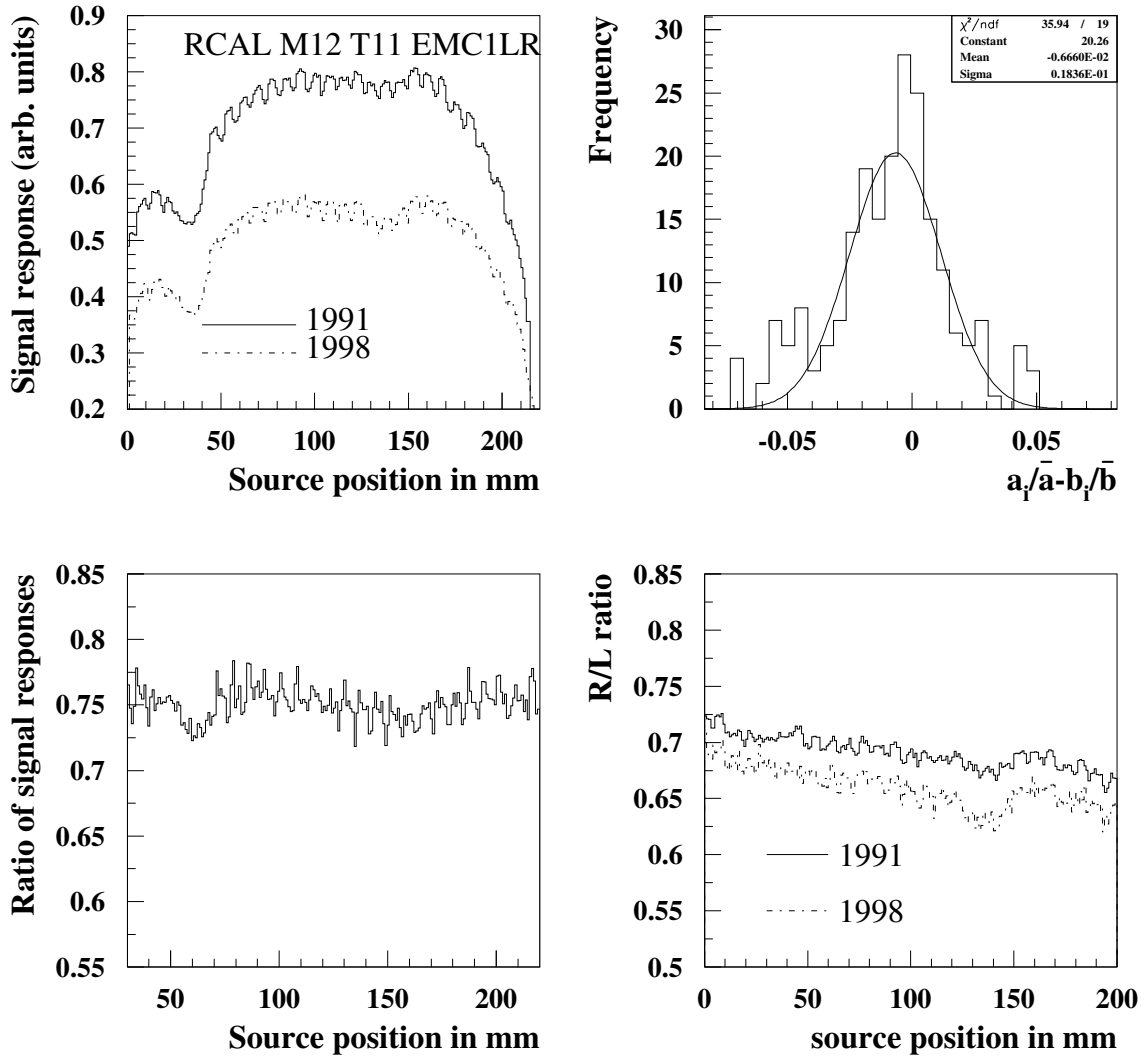


Figure 7.5: *Comparison of $^{60}Co$ signal responses of the RCAL module 12, tower 11, EMC1 section (cf. text).*

left diagram. It confirms the stability of the left wavelength shifter close to the HERA beams. The diagram on bottom right displays the ratio of the right/left signal responses of 1991 and 1998. The small shift of about 5% in 1998 indicates a possible change in the transmission of the scintillators of the section. This effect is also observed in other measured sections of the RCAL within this period. Figure 7.6 presents the mean development of right/left ratios of 8 EMC and 4 HAC sections of the towers closest to the HERA beams. A reduction for the EMC sections within the period 1991-1995 is clearly visible which has been more or less stable since then. Whereas the right/left ratio of the 4 HAC sections shows a very weak decrease with strong reduction in 1998. But this is primary caused by light leakage effects of two HAC sections.

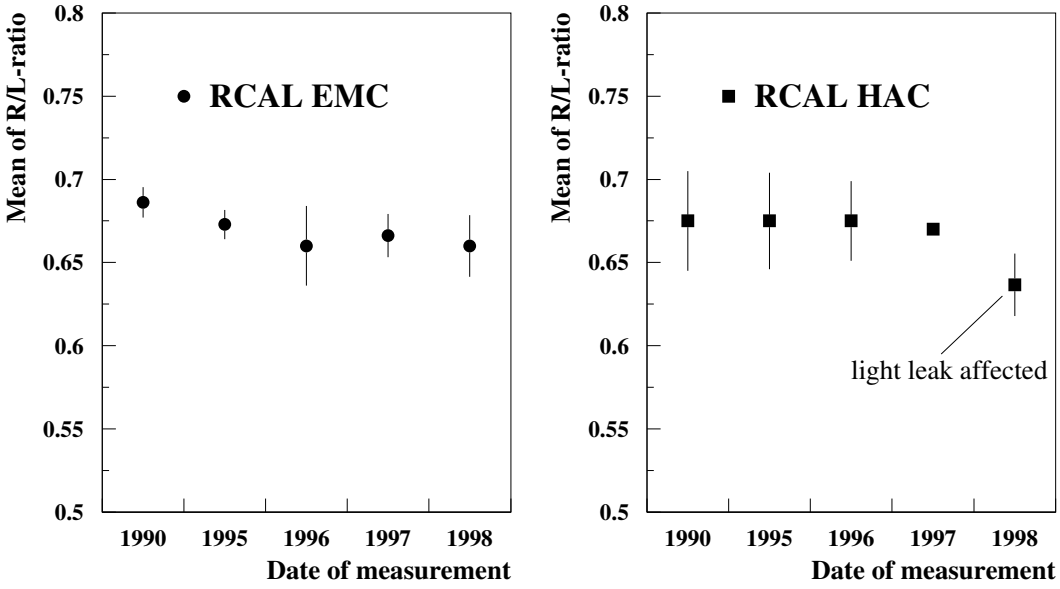


Figure 7.6: *Mean values of the right/left ratio of $^{60}Co$ signal responses of the RCAL of 1991 and 1995, 1996, 1997 and 1998.*

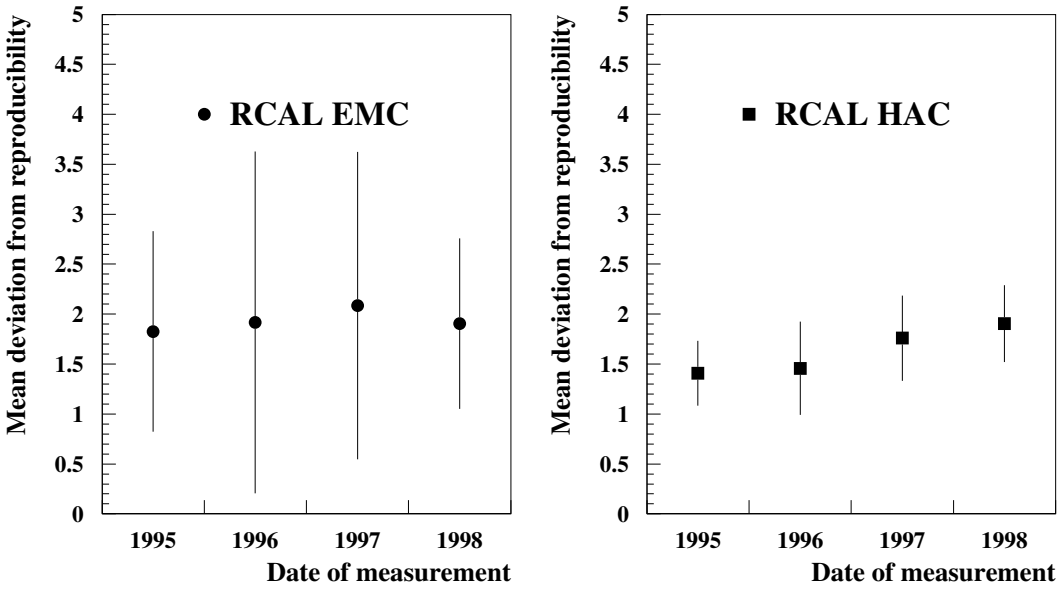


Figure 7.7: *Mean values of the deviation from reproducibility of $^{60}Co$ signal responses of the RCAL of 1995, 1996, 1997 and 1998 with respect to 1991.*

Beside these artificial effects a small decrease of the transmission is indicated by these measurements, whereas the reproducibilities of the signal responses show no significant deviation as displayed by Figure 7.7. The detailed results for each section of the outside scans on the RCAL can be found in the table B.3.

### 7.3.3 Harp scans

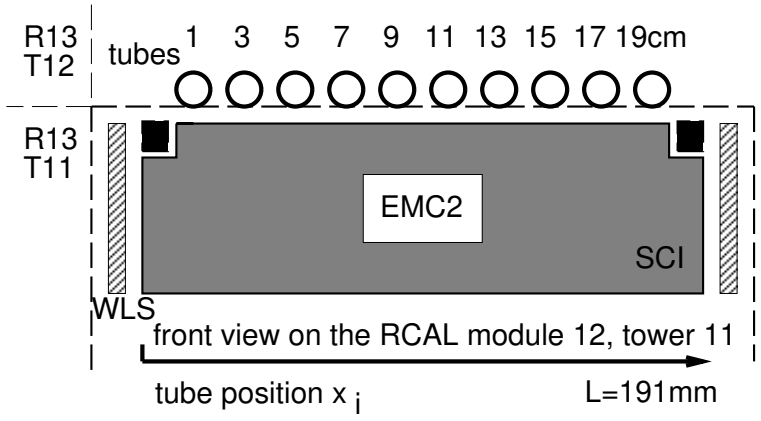


Figure 7.8: *Schematic front view of the $^{60}Co$ harp scanner allowing to excite the upper scintillator edges.*

In order to get more information about the attenuation of the scintillators a special investigation has been performed, the so-called $^{60}$Co harp scans. During the maintenance period an access exists on the top and on the bottom of F/RCAL module 12, tower 11 and tower 13, respectively (see Figure 7.1). $^{60}$Co outside scans can be performed parallel to the $z$-axis of the EMC sections at certain transverse positions $x_i$. The $^{60}$Co source on the top and the bottom of a tower excites the upper and lower edge of the scintillators. This allows to determine the attenuation length of the scintillators using a similar calculation to the one performed in Chapter 6.5. Harp scans were taken on tower 11 of the RCAL in 1992, 1997 and 1998. The $^{60}$Co harp scanner uses a special assembly to guide the $^{60}$Co source. Twenty-one parallel brass tubes are installed in a certain wing, which could be pressed on top of the tower. Each second brass tube is used for scans in order to excite the upper edge of the scintillators of the EMC2 and the HAC section of tower 11. An ensemble of 10 harp scans at 10 different tube positions $x_i$ allow a position $z$ dependent excitation parallel to the wavelength shifters for all scintillators of the measured section (see Figure 7.8). The left/right ratio of the signal responses $I_{left}(x_i, z)$ and $I_{right}(x_i, z)$ can be described by the exponential ansatz 6.8:

$$f(x_i, z, \overline{\lambda}_{sci}) = \frac{I_{left}(x_i, z)}{I_{right}(x_i, z)} = \frac{I_0(x_i, z) \cdot \Omega(x_i, z) \cdot (e^{-\frac{x_i}{\overline{\lambda}_{sci}}} + R \cdot e^{-\frac{(2L - x_i)}{\overline{\lambda}_{sci}}})}{I_0(x_i, z) \cdot \Omega(x_i, z) \cdot (e^{\frac{(L - x_i)}{\overline{\lambda}_{sci}}} + R \cdot e^{-\frac{(L + x_i)}{\overline{\lambda}_{sci}}})}. \qquad (7.7)$$

The primary light yield $I_0(x_i, z)$ as well as the factor $\Omega(x_i, z)$ which describes solid angle effects depending on the source position are eliminated due to the ratio. The reflection coefficient $R$ is assumed to be 0.2 [WI98]; the length of the scintillators is in the case of the FCAL/RCAL EMC section about $L = 191\,\text{mm}$. The effective attenuation $\overline{\lambda}_{sci}$ is the mean attenuation of the scintillators in the section and assumed to be the only free parameter. Figure 7.9 displays the mean left/right ratio $\overline{f}(x_i, \overline{\lambda}_{sci})$ averaged over the longitudinal distance $z$ as a function of the tube position $x_i$ for the $^{60}$Co harp scans on the RCAL module 12, tower 11, EMC2 (top diagram) and HAC section (bottom diagram). The measurements were taken in the years 1992, 1997 and 1998. The function 7.7 can be fitted and optimized to the data using the Least Squares Method similar to formulae 6.9 and 6.10. Table 7.2 presents the results of the harp scans for tower 11. The attenuation lengths show large variances. In case of the EMC section a small reduction is observable with regard to the reference measurement in 1992. How far this effect is due to a real change of the optical properties or just artifacts due to mechanical variations cannot be determined in detail. As a matter of fact several modifications of the calorimeter performance have happened, i.e. a vertical movement of module 12 top and bottom closer to the HERA beams in the maintenance period 1994/1995. Obviously an artificial effect happened with respect to the harp scans of the HAC section. The ratios are almost flat between a distance of 30 and 50 mm. However, in summary it can be said: Both the right/left ratios of outside scans

and the harp scans show a small variation of the transmission of the scintillators[4]. But these scanning procedures suffer measurement uncertainties and allow only a rough determination of the transmission and the light attenuation of the scintillators. Therefore further investigations have been made described in the following.

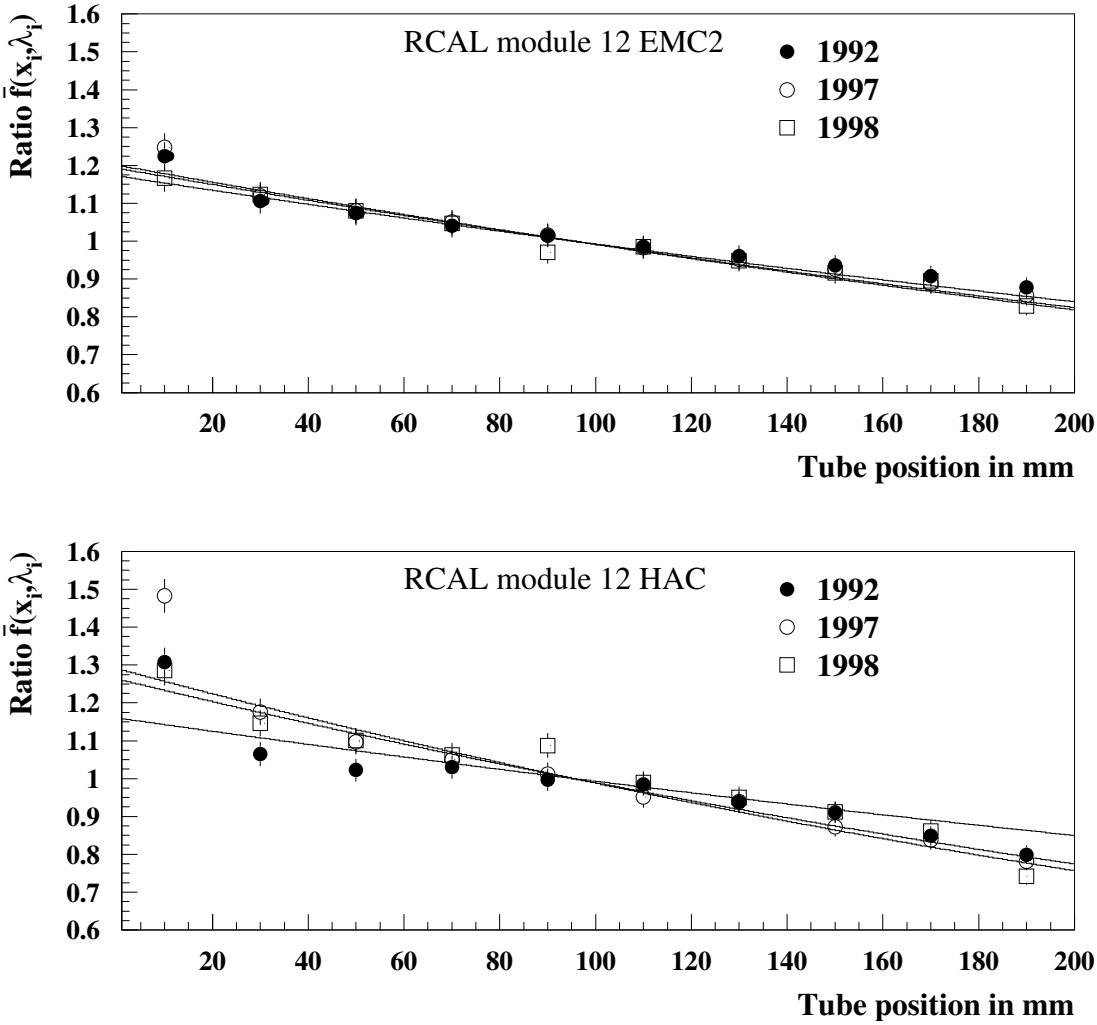


Figure 7.9: *Harp scan results for the RCAL module 12, tower 11, EMC2 (top diagram) and HAC section (bottom diagram) between 1992, 1997 and 1998. The ratio of the averaged signal responses are plotted versus the tube position.*

## 7.4 Investigations on ageing effects

In order to specify the transmission of the scintillators more precisely special investigations have been performed[5]. During the maintenance period 1997/1998 outside scans have been executed on the FCAL module 12 on both tower sides when it was separated from the calorimeter.

[4]Special investigations using the inside scanner on the FCAL module 8 and the RCAL module 17 described in Chapter 8.1.2 confirm these results.

[5]Already in 1997 inside scans on the FCAL module 9 were taken. Processing problems with the reference data led to further investigations on other modules.

| Harp scans on module 12 in 1992/1997/1998 | | | | |
|---|---|---|---|---|
| *tower* | *section* | $\lambda_{1992}$ in mm | $\lambda_{1997}$ in mm | $\lambda_{1998}$ in mm |
| 11 | EMC2 | $869 \pm 102$ | $764 \pm 66$ | $791 \pm 75$ |
| 11 | HAC1 | – | $562 \pm 35$ | $609 \pm 41$ |

Table 7.2: *The mean effective attenuation length $\overline{\lambda}_{sci}$ of EMC/HAC scintillators of the RCAL module 12, tower 11 as a function of the date of measurement.*

In May 1999 inside scans on the FCAL module 17 have been taken. In contrast to previous measurements these measurements were performed under similar conditions as the references allowing an optimal comparison. Both investigations confirm the hypothesis of ageing effects of the scintillators. The resulting effects on the ZEUS calorimeter with respect to energy resolution will be estimated and briefly summarized at the end.

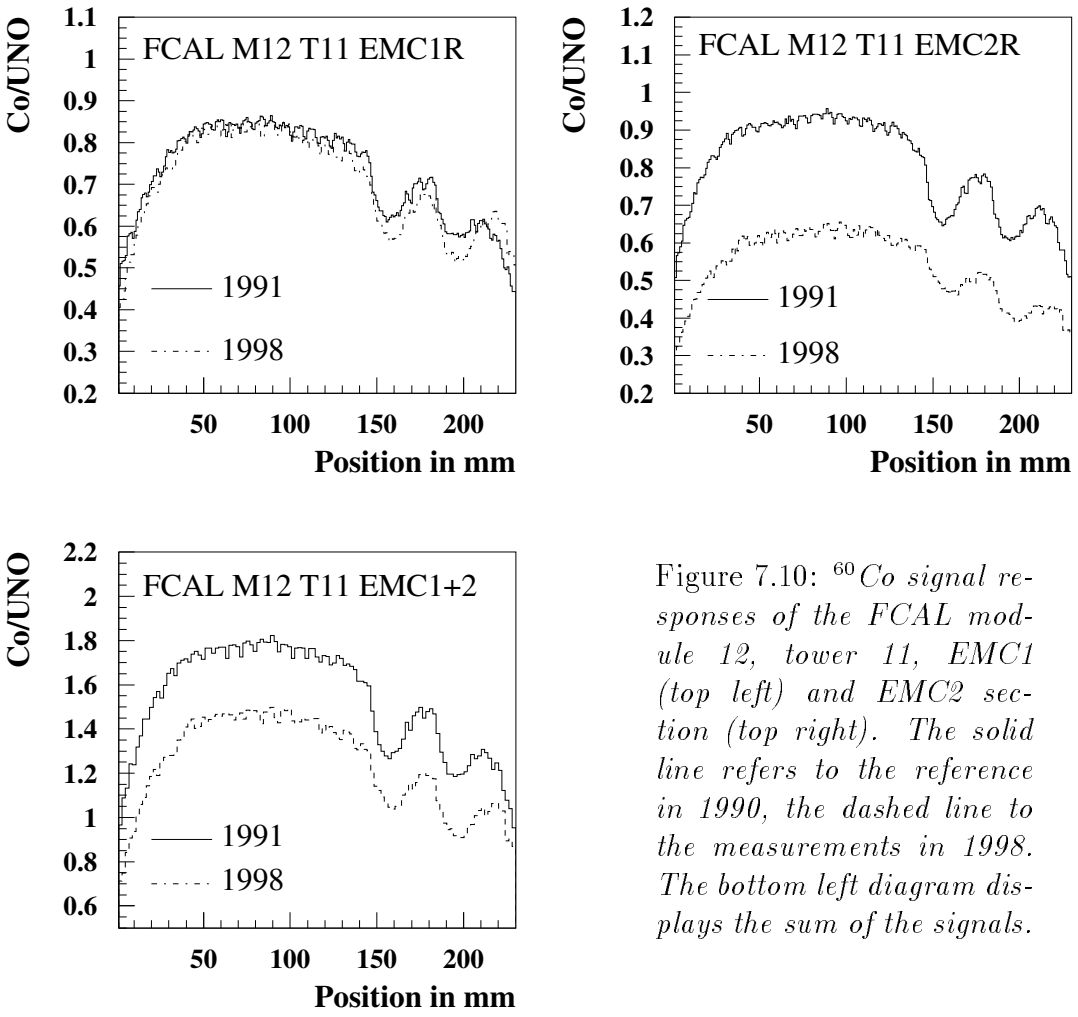


Figure 7.10: *$^{60}$Co signal responses of the FCAL module 12, tower 11, EMC1 (top left) and EMC2 section (top right). The solid line refers to the reference in 1990, the dashed line to the measurements in 1998. The bottom left diagram displays the sum of the signals.*

### 7.4.1 Outside scans on the FCAL module 12 bottom

During the maintenance period in 1997/98 the bottom and top halves of the FCAL module 12 have been temporary removed from the ZEUS detector to allow the installation of the Forward Plug Calorimeter[6] (FPC). Access to both sides of the calorimeter halves was possible at that time. $^{60}$Co outside scans were taken on two EMC towers of the bottom module. Tower 11 which is closest to the HERA beams was chosen to determine a possible radiation damage, and accordingly tower 3, which is the furthermost EMC tower at the bottom of the module. Except

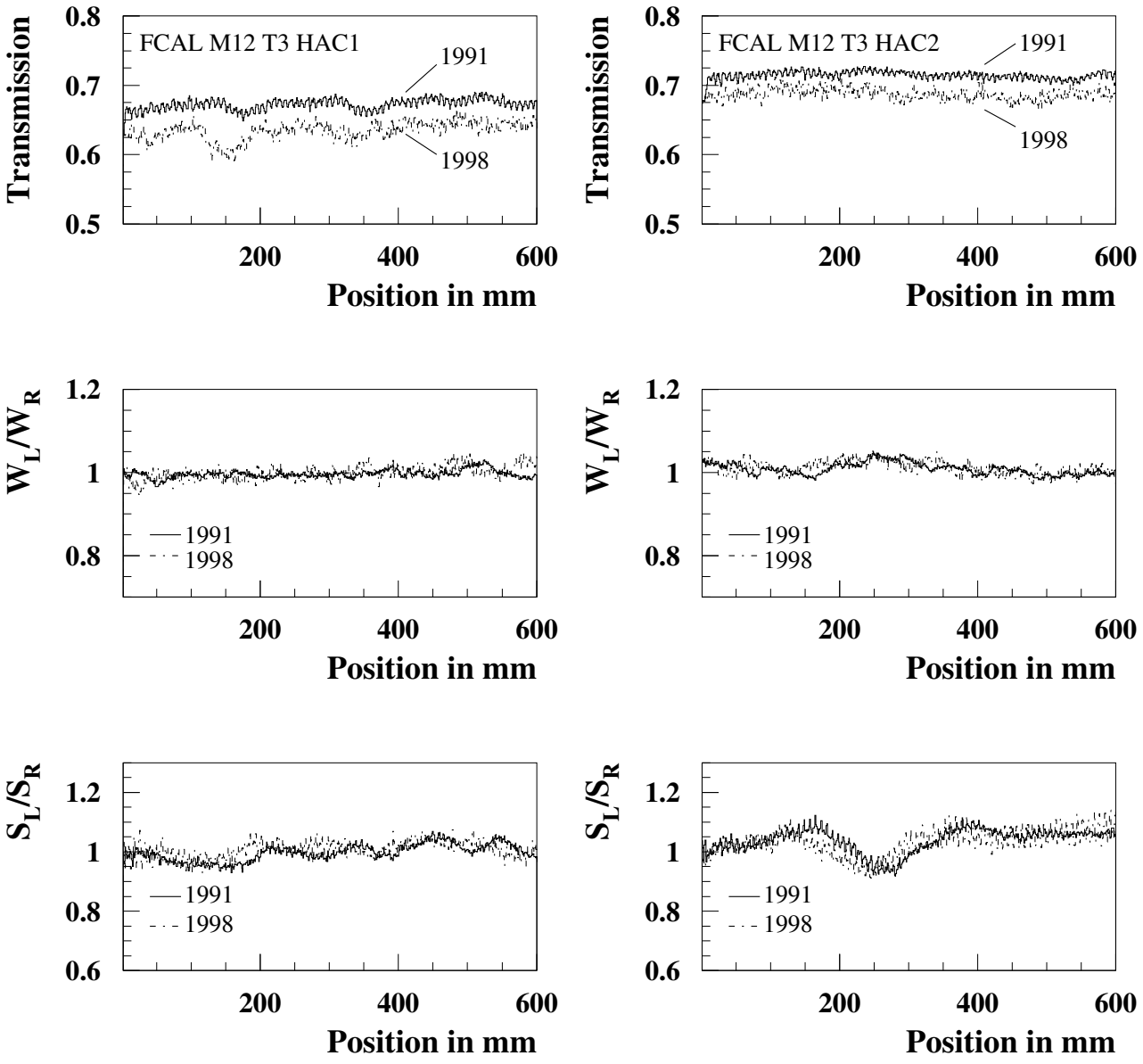


Figure 7.11: *Optical parameters of the FCAL module 12, tower 3, HAC1 section (left column) and HAC2 section (right column) of 1998 with respect to the reference data of 1991.*

for the PC-system the measurement performance[7] was identical to the system used in 1991

[6] See Chapter 3.1.

[7] Based on original tools, i.e. assembly and integrator cards for the data acquisition.

(see section 7.1). Tower 11 was scanned on the right side, tower 3 completely on both sides. In case of tower 3 the reproducibilities of the measurements with respect to the references are determined at the 1–2 % level. No change in the longitudinal structure of the optical components of the EMC and HAC sections of tower 3 is seen, whereas the signal responses of the EMC sections of tower 11 show some variations. The top diagrams of Figure 7.10 presents the signal responses of the EMC1 (left) and EMC2 sections (right) from 1998 (dashed lines) and 1991 (solid lines). The $^{60}$Co scans were executed in the opposite direction, so that the last maximum on the right of the signal responses correspond to the scintillator closest to the interaction point. A change between the present and the reference measurements is visible for both EMC sections. The reason for the change is a positioning error of the source during the measurements in 1998. Obviously the $^{60}$Co source traversed mainly the area of the EMC1 section which results in different heights of the signal responses with respect to the references. The sum of the signal responses $I_{EMC1}(t,z) + I_{EMC2}(t,z)$ is nearly insensitive to misplacements effects and therefore allows a comparison with the sum of the reference responses $I_{EMC1}(t_o,z') + I_{EMC2}(t_o,z')$, demonstrated in the bottom diagram of Figure 7.10. The deviation from reproducibility of the sum of the EMC signals is in the order of 1 to 2 %. Similar results are found for the HAC sections of tower 11. No change of the longitudinal structure nor any radiation damage can be seen. However, a significant change of the transmission[8] is observed for all sections of tower 3. Figure 7.11 presents the optical parameters of the HAC1 and HAC2 section of the FCAL module 12, tower 3. The present transmissions (dashed line in the top diagrams) show a small shift with respect to the references (solid lines). The ratio of wavelength shifter responses (middle column) as well as the ratio of the scintillator responses (bottom diagrams) show a very well agreement with the references. The detailed results can be found in the appendix B, table B.4.

### 7.4.2 Inside scans on the FCAL module 17

In 1990 inside scans were taken only on a few FCAL modules, among others on the FCAL module 17. After mechanical problems with regard to the source wire it was decided to perform further $^{60}$Co measurements only by using the outside scanner. Since 1997 inside scans have been restarted based on a special security system (see Chapter 8). Therefore it was possible to repeat the inside scans on the FCAL module 17 in the maintenance period in 1999. The requirement for such measurements was the minimization of risk of the source getting stuck inside the calorimeter. The solution of this problem is a double encapsulated tube system. Steel tubes were installed in the original brass tubes of the calorimeter which were closed at the end and removable (with a diameter of 1.6 mm). In case of handling problems, it was guaranteed that the simple encapsulated source wire together with the guiding steel tubes were removable (see right diagram in Figure 7.1). Due to the fixed installed source guiding system the positioning errors were almost eliminated. The towers 8, 16, 20, 21, and 22 of the FCAL module 17 were scanned. The results are presented in table B.5 in the appendix B. The reproducibility of the signal responses of the FCAL module 17 are at the level of 1 %, so that no change of the longitudinal structure is indicated.
Also the passive area of the signal responses have been analyzed. Cherenkov light is produced in the wavelength shifter on the tower side where the source is situated, so that it is possible to measure the pure wavelength shifter response. The slope observed outside the active area of the sections is related with the attenuation length of the wavelength shifter (see also Figure 6.5).

[8] The right/left ratios of tower 11 show a similar trend.

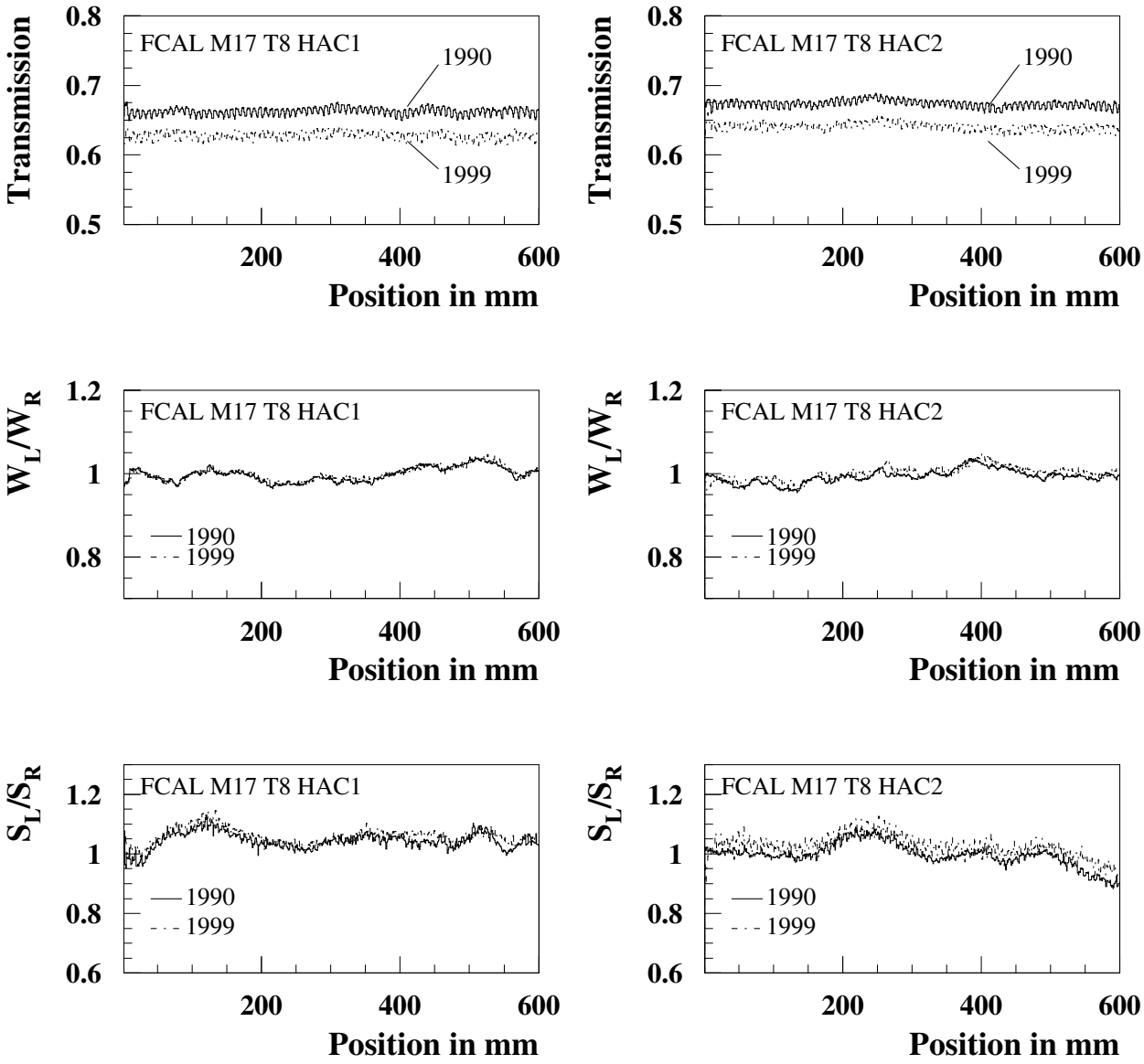


Figure 7.12: *Optical parameters of the FCAL module 17, tower 8, HAC1 (dashed lines in the left column) and HAC2 section (dashed lines in the right column) of 1999 with respect to the reference data of 1990 (solid lines).*

The attenuation lengths determined by this method are within the expected range. Figure 7.12 displays an example of the optical parameters of the HAC sections. The transmissions of both sections of tower 8 (dashed lines in the top diagrams) show a small shift with respect to the references. The ratio of wavelength shifter responses (middle row) as well as the ratio of the scintillator responses show a good agreement with the references. The curves were averaged over 8 mm corresponding to an absorber/scintillator layer in order to calculate the optical parameters for each scintillator. The distribution of the optical parameters of HAC scintillators of 1990 and 1999 are illustrated in Figure 7.13. One clearly notices the systematic shift of the transmission within that period, whereas no significant change is observed with respect to the other parameters. The mean transmissions of the EMC, HAC0 and HAC scintillators are presented in table 7.3 in the appendix B. The results of the inside measurements confirm

definitely a general reduction of the transmission of the ZEUS calorimeter scintillator tiles.

| **results of $^{60}$Co inside scans on the FCAL module 17** | | | |
|---|---|---|---|
| section | EMC | HAC0 | HAC1/2 |
| $T_{1990}$ | $0.698 \pm 0.019$ | $0.669 \pm 0.022$ | $0.671 \pm 0.007$ |
| $T_{1999}$ | $0.663 \pm 0.021$ | $0.646 \pm 0.020$ | $0.640 \pm 0.009$ |
| $\Delta T$ | 5.1% | 3.4% | 4.6% |

Table 7.3: *Mean transmission and reduction in percent of the scintillators of each section between 1990 and 1999.*

### 7.4.3 Ageing scenarios

The reason for the reduction of the attenuation length is not clearly understood. But a radiation damage due the incident high energy particles is improbable [LO97]. The most strongly exposed calorimeter sections closest to the HERA beams suffer a radiation dose in the order of several Gy, whereas 1 kGy is the lower detection limit for the $^{60}$Co monitor system [NE96]. Also the uniform radioactive background due to the uranium plates has only a small radiation dose rate, which is in the order of 1 Gy per year [ZE98]. Pure ageing effects on different scintillators including *SCSN-38* have been studied over a period of four years by [HA91]. It has been found that the attenuation length of *SCSN-38* is fairly stable within this period. The change in the observed light yield was less than 5% over 1000 days. Also certain investigations of very low dose rate effects on *SCSN-38* have been carried out in [DA90]. The scintillators had been irradiated by plates of depleted uranium of the ZEUS calorimeter. The radiation dose was 42 Gy with 1.6 mGy/h over 500 days. The measurements had shown no significant change of the light yield of the scintillators within this time. But a decrease of the attenuation length of several percent was observed reaching a saturation at the end. The damage was stronger than expected from the applied radiation dose, so that other reasons than radiation were probable, e.g. ageing or chemical reactions of oxygen with shorter lived radicals (see chapter 4.3). Similar results were found in a long-term observation of two *SCSN-38* scintillator plates of a length of 590 mm. One of them was embedded by two uranium plates [RO87]. Within the period of seven years exponential reduction of the light attenuation in the order of 10% and 20% was observed for the unirradiated and the DU irradiated one [RO99], respectively. No significant change was observed with regard to the primary light yield. The essential result is the observation of a pure ageing effect in addition to a radiation effect of the same order reducing the light attenuation while no significant change of the light yield is measured. Same effects could have led to ageing effects of the ZEUS calorimeter scintillators.

### 7.4.4 Influence of ageing effects on the ZEUS uranium calorimeter

$^{60}$Co measurements show a change of the transmission of FCAL/RCAL scintillators within the operating time of the ZEUS detector in the order of 3 to 5%. In the following are presented the consequences of this variation with respect to the uniformity of the scintillators and the energy resolution of the ZEUS calorimeter. Although the reason for the reduction of the transmission is not understood, irradiation effects from the HERA beams are most probable. However, it will be demonstrated that studies on irradiation effects can be used to estimate the consequences of ageing effects for the ZEUS calorimeter. The left diagram of Figure 4.7 (see Chapter 4.4) presents the attenuation curves of a uniformly 3 kGy irradiated and a non-irradiated RCAL HAC0 scintillator calculated by the numerical simulation program lightsim. These curves were

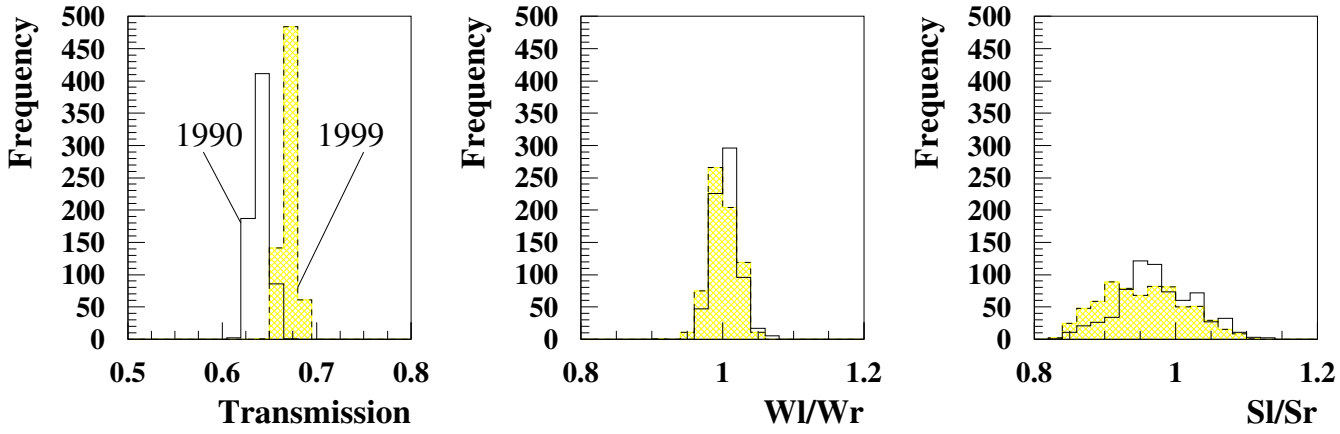


Figure 7.13: *Distribution of the optical parameters of the HAC1 and HAC2 scintillators of the FCAL module 17, tower 8, 13, 16, 21 and 22 between 1999 and 1990.*

incorporated within an EGS4 MC-simulation of a $^{60}$Co scan on a RCAL HAC0 section [BO99a]. The energy deposition of the $\gamma$'s of the $^{60}$Co source inside the scintillator tiles was weighted with the attenuation curves. Figure 7.14 displays the result of this investigation. The top diagrams show the right (dashed line) and the left (solid line) signal response of the $^{60}$Co scan in case of no (left) and 3 kGy irradiation (right). The $^{60}$Co source is assumed to be on the left tower side. The bottom left diagram presents the right/left ratio of these signals which corresponds to the transmission. The transmission yields in case of the reference a value about 0.67, which is an impressing validation of the Monte Carlo including the attenuation curves calculated by the numerical simulation program. The reduction of the transmission due to the 3 kGy irradiation in comparison with the reference is in the order of 6%. Accordingly the reduction of the transmission correlates with a change of attenuation length which is comparable with the one resulting from a uniform 3 kGy irradiation.

**Uniformity:** The effects on the transverse uniformity of the light collection are expected to be small. The uniformity of 5 kGy and 10 kGy irradiated scintillators were determined earlier in Chapter 6.5 within $\pm 1\%$ in a region of $\pm 60$ mm around the center of the scintillator. This is a similar result as the theoretical calculation of [DA96] based on simulated attenuation curves which shows in case of a 3 kGy irradiation a non-uniformity of 1% at the edges of the scintillators. Moreover the testbeam measurements show an improvement of the uniformity of the scintillators of 1% in comparison with the reference ones.

**Energy resolution:** A change of the attenuation length comes along with a reduction of the number of photo-electrons which impairs the energy resolution of the calorimeter $\sigma_D$ (see equation 6.6). The effects on energy resolution were estimated in case of 3 kGy irradiation of the ZEUS calorimeter scintillators and wavelength shifters in [DA96] and will be briefly summarized: Here the number of photo-electrons decreases by a radiation dose dependent factor resulting from both the reduction of the primary light yield and the change of the attenuation length of scintillators and wavelength shifters. The energy resolution has been calculated for the sections of the ZEUS calorimeter in case of 3 kGy irradiation. Indeed the effects in the energy resolution resulting from 3 kGy irradiation are small and negligible. The variation in the electromagnetic energy resolution of FCAL is about $18.4\%/\sqrt{E(\mathrm{GeV})}$ instead of $18.0\%/\sqrt{E(\mathrm{GeV})}$. The change of the hadronic energy resolution is about $35.1\%/\sqrt{E(\mathrm{GeV})}$ instead of $35.0\%/\sqrt{E(\mathrm{GeV})}$. The effects resulting from the reduction of the attenuation length only should be much smaller than

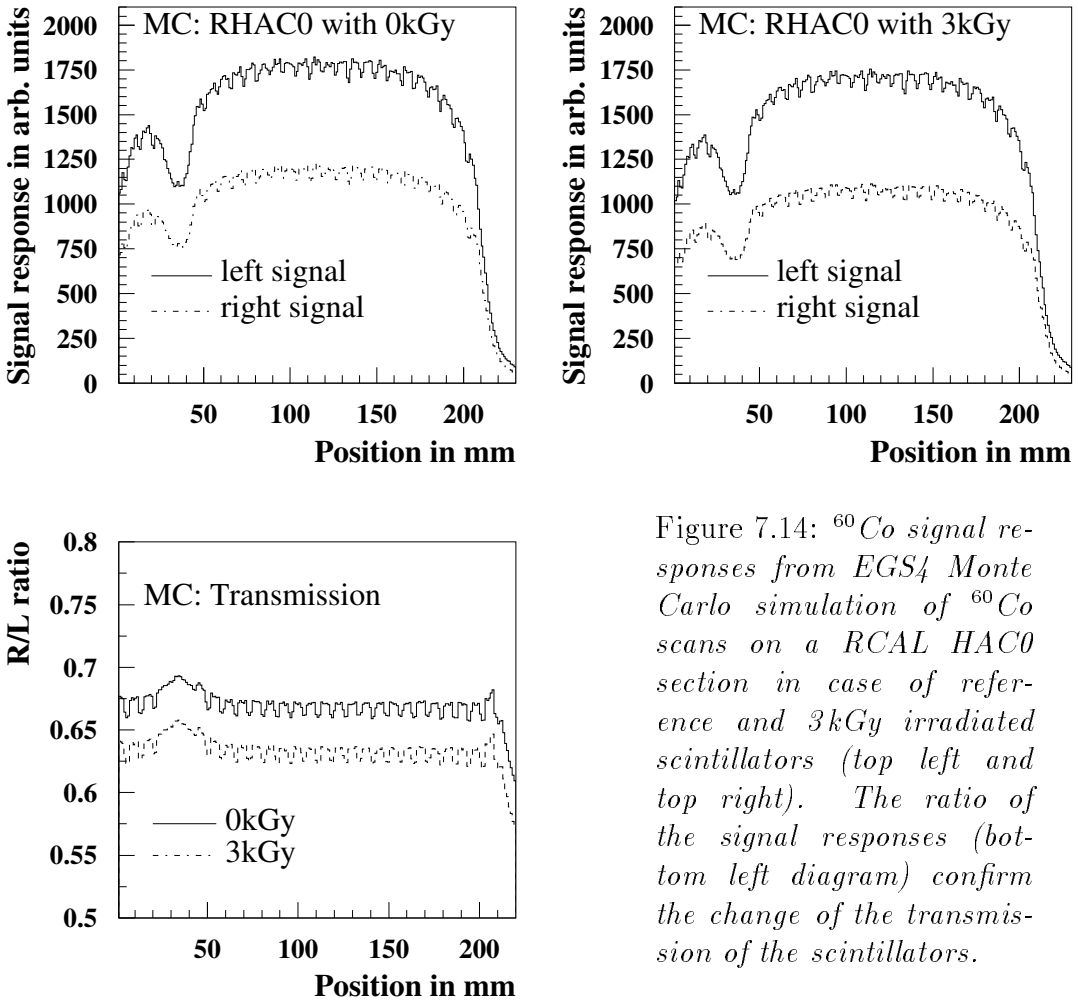


Figure 7.14: *$^{60}$Co signal responses from EGS4 Monte Carlo simulation of $^{60}$Co scans on a RCAL HAC0 section in case of reference and 3kGy irradiated scintillators (top left and top right). The ratio of the signal responses (bottom left diagram) confirm the change of the transmission of the scintillators.*

those presented in table A.3. As a matter of fact the electromagnetic energy resolution of the test calorimeter section using 10 kGy irradiated scintillators does not differ significantly from the ones of the reference sections (see table 6.4).

## 7.5 Conclusions

The uniformity of the calorimeter can be degraded by mechanical changes, ageing and the effects of radiation on the optical properties of the components. Therefore within almost every maintenance period $^{60}$Co measurements have been taken on several FCAL and RCAL sections controlling the quality with respect to possible variations of the longitudinal uniformity and the optical parameters, especially the transmission of the scintillators. The following components have been investigated:

- The FCAL/RCAL towers close to the HERA beams within the period of 1993 to 1998 using the outside scanner . These measurements were complemented by harp scanner measurements on the RCAL module 12, tower 11, in the period from 1992 to 1998.

- The FCAL module 12 during the reinstallation in 1998 using the outside scanner on both tower sides.

- The FCAL module 17 in 1999 using the inside scanner.

The outside scans on one tower side delivers information about the longitudinal structure of the investigated section; the right/left ratio refers to a rough determination of the transmission of the scintillators. The harp scans allow to determine the attenuation length of scintillators of two sections of the RCAL module 12 tower 11. Both methods are sensitive with respect to misplacements of the $^{60}$Co source; whereas the inside scans offer the best reproducibility of the mechanical measurement procedures. They allow to obtain information about both the longitudinal structure and the optical parameters, especially the transmission. The results of these measurements can be summarized as follows: No significant variation is observed in the longitudinal structure of signal responses of the investigated sections, thus no radiation damage of the wavelength shifters or scintillators can be seen. Yet a systematic reduction of the transmission of the scintillators is visible between the present data and the references. The change is in the order of 3 to 5 %. This is comparable with the change of the transmission of 6% of the scintillators resulting from a uniform 3 kGy irradiation. The effects of irradiation on the ZEUS cal have been well studied and can be quoted.
In case of 3 kGy irradiation of both the scintillators and the wavelength shifters the following can be noticed:

- The effects on the transverse uniformity of the light collection of the scintillators are expected to be smaller 1%. Moreover testbeam measurements have been shown an improvement of the transverse uniformity of irradiated scintillators in comparison with references (see Chapter 6.5).

- The electromagnetic energy resolution of the FCAL increases to 18.4% and the hadronic energy resolution increases to 35.1% without considering measurement uncertainties.

These effects are small in comparison to other systematic errors of measurements and overestimate the real effects of the ZEUS calorimeter. Due to smaller changes of the transmission of the scintillators and no evidence for a change of the wavelength shifters the real effects should be much smaller and not significant.

# Chapter 8

# Water damage effects on the ZEUS calorimeter

At the end of the maintenance period in January 1995 a water leak due to an damaged valve of the cooling system of the hadron electron separator (HES) in module 17 caused a small damage to some optical components of RCAL module 17. As a consequence the UNO signal induced by uranium radioactivity in the electromagnetic sections of this calorimeter module decreased by several percent. Moreover a more severe accident happened at the end of the maintenance period in January of 1997, when the cooling water system of the hadron electron separator (HES) broke on the top of FCAL module 8. The water influenced the optical components of the module dramatically. The UNO signal decreased by up to 40% in the electromagnetic sections of this calorimeter module. Within the following 10 months $^{60}$Co inside scans were performed on the FCAL module 8 for 4 times with the aim to study the influence of the water damage on the longitudinal uniformity of the calorimeter response [BO98b]. Strong recovery effects were observed within that time similar to the time dependent effects observed due to the UNO signal on RCAL module 17 within the previous years (see Figure 8.1). At the end to those investigations $^{60}$Co inside scans were performed on the RCAL module 17 in order to compare the water damage effects of both modules. The measured non-uniformities are used to estimate the influence of water damage on the energy calibration of electrons.

## 8.1 Investigations on the FCAL module 8

On January 13, 1997 the water cooling system of the hadron-electron-separator (HES) broke on top of the FCAL module 8 (see Figure 7.1). Several litres of water flowed through the 2nd HES gap of this module. The Uranium noise signal (UNO) of the photomultipliers decreased uniformly by 40% for the EMC and the HAC0 sections with no significant change for one month. On February the 3rd the towers 20, 21 and 22 of the FCAL module 8 were scanned using the $^{60}$Co source. After that a cassette containing water absorbing material was inserted into the 2nd HES gap. During access on March the 4th, the towers 1, 2, 4, 21 and 22 were scanned by $^{60}$Co. The cassette was exchanged again. The old cassette removed 250 ml of water [HE97]. The UNO signal recovered at this time by 10%. In March the 30th the UNO signal recovered further with values 20-25% lower than before the water damage [YO97]. During an access in August the 14th and in the beginning of the maintenance period 1997/1998 in November the 15th, the towers 1, 2, 21 and 22 were scanned again by $^{60}$Co. Figure 8.1 illustrates the UNO reduction and recovery as a function of the time after the accident. Table 8.1 gives an overview

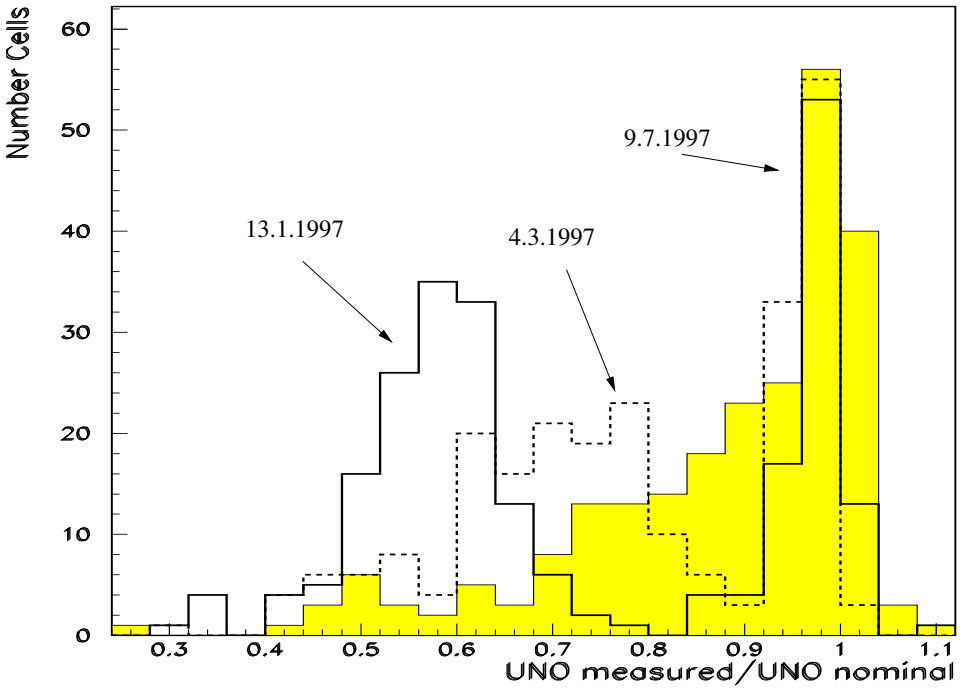


Figure 8.1: *Ratio of $UNO_{measurements}/UNO_{nominal}$ after the accident on the FCAL module 8. One clearly notices the recovery effects as a function of time.*

of the investigations on the FCAL module 8 described in this chapter.

| date | tower 22 | tower 21 | tower 20 | tower 4 | tower 2 | tower 1 |
|---|---|---|---|---|---|---|
| 1990 | $\star$ | $\star$ | $\star$ | $\star$ | $\star$ | $\star$ |
| 3.2.1997 | * | * | * | - | - | - |
| 4.3.1997 | * | * | - | * | * | * |
| 14.8.1997 | * | * | - | - | * | * |
| 4.11.1997 | * | * | - | - | * | * |

Table 8.1: *Overview of the measured towers (*) of the FCAL module 8. The first measurements have been taken due to the outside scanner ($\star$).*

### 8.1.1 $^{60}$Co measurements

$^{60}$Co measurements for the quality control of the ZEUS calorimeter has had several variations and improvements from 1990 until now although no change in the principle of the method has been made (see chapter 7.1). In case of the investigation of the FCAL module 8 one has to notice that the module itself was modified and reinstalled after the $^{60}$Co reference measurements had been taken in 1990, so that no real reference data of the FCAL module 8 for further measurements exists. The principle differences between the reference measurements of the FCAL module 8 in 1990 and the present can be stated as follows:

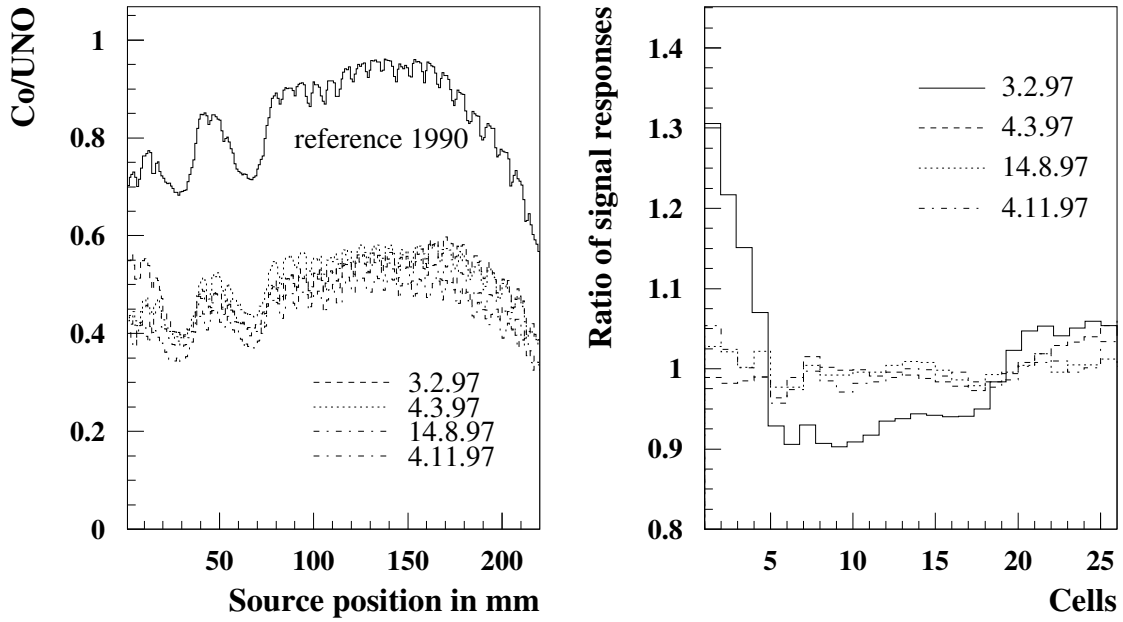


Figure 8.2: *Right signal responses of the FCAL module 8, tower 21, HAC0 sections before and after the accident (left). The source is guided on the right tower side. The ratio of mean of the signal responses after and before the damage averaged over 8 mm is shown on the right. The HES gap regions are here extracted and the beginning of each function is extrapolated.*

- Reference measurements were taken before the minor modification described below.
- In 1990 the outside scanner was used for all FCAL/RCAL modules, while in 1997 inside scans were performed.
- In 1990 an OS-9/VME based system was used instead of a PC-system.

The differences between the measurements of the reference data and the present data due to those differences are expected to be much smaller than the effects caused by the water damage. The large reduction of the UNO signal of the FCAL module 8 after the accident made it necessary to investigate the status of the optical components, which due to the installation of the modules could be done only by the inside scanner. Therefore a special tube set-up was developed to minimize the risk of the source getting stuck in the calorimeter. A much bigger difference between reference and actual data is caused by a certain modification of the C-arm of module 8, to which the ends of the absorber plates are fastened and which houses the electronics and distribution system for HES; the $^{60}$Co brass tubes, light fibre system and the cooling system [?]. The outside scanning reference data had shown that the front plate was somewhat bent (but not the first four towers 23, 22, 21, 20) and most of the wavelength shifters were irregulary shifted. As result of these measurements the module was partially disassembled and repaired. No further $^{60}$Co scans has been taken after this repair in 1990. In 1994 HES skis were installed into the first HES gaps of the EMC and HAC0 sections of the module 8, which cause a lower $^{60}$Co signal response of the scintillator tiles close to this gap [SC95].
The $^{60}$Co scans in 1990 and 1997 were not performed under identical conditions. The comparison of the data delivers the same kind of reproducibility, but there is a systematic difference in the pulse heights which come from different distances between source and scintillator de-

pending on the scanner method (inside/outside, see Figure 5.8). A comparison between the data of inside/outside scans has to take this difference into account. In case of the FCAL module 8 the modifications after the scans in 1990 and the different geometrical conditions may have changed the slope of response functions by a few percent. However, at least for the electromagnetic sections these effects are small compared to those of the water damage.

| tower | time | HAC0RR | HAC0RL | HAC0LR | HAC0LL |
|---|---|---|---|---|---|
| 21 | 3.2.1997 | 6.45 | 7.14 | 9.70 | 3.89 |
| | 4.3.1997 | 2.49 | 6.70 | 6.57 | 3.23 |
| | 14.8.1997 | 1.55 | 3.36 | 2.80 | 3.11 |
| | 4.11.1997 | 2.09 | 4.04 | 2.56 | 3.51 |
| tower | 3.2.1997 | 4.61 | 7.91 | 4.08 | 8.58 |
| 22 | 4.3.1997 | 4.35 | 4.77 | 5.03 | 4.78 |
| | 14.8.1997 | 2.87 | 4.26 | 2.29 | 4.00 |
| | 4.11.1997 | 3.12 | 4.60 | 3.13 | 4.88 |

Table 8.2: *Overview of the deviation from reproducibility of signal responses of tower 21 and 22 of the FCAL module 8 in percent as a function of the date of measurement. I.e. HAC0RL refers to the left photomultiplier response of the HAC0 section while the $^{60}Co$ source is located on the right tower side.*

### 8.1.2 The analysis

After the accident $^{60}$Co measurements were repeated several times on a few calorimeter sections of the FCAL module 8. This allows to see the time development of the signal responses. The measurements give the information of the optical parameters[1], which are independent from previous measurements:

- The transmission $T$ of each scintillator of the measured sections, which should be about 0.67 according to reference measurements,
- the ratio $W_L/W_R$ of the wavelength shifter responses, which should be a value about 1,
- the ratio $S_L/S_R$ of the light yield emission of the two sides of the scintillators, which should be also a value about 1.

The comparison of measured signal responses with the reference data could be described by:

- The ratio of the signal responses which is assumed to be the longitudinal uniformity of the calorimeter response and
- the deviation from reproducibility of the present signal responses from the references.

In the following the results of the measurements will be described. Figure 8.2 displays the signal responses of HAC0 sections of the FCAL module 8, tower 21 before and after the accident.

[1]See Chapter 5.1.2.

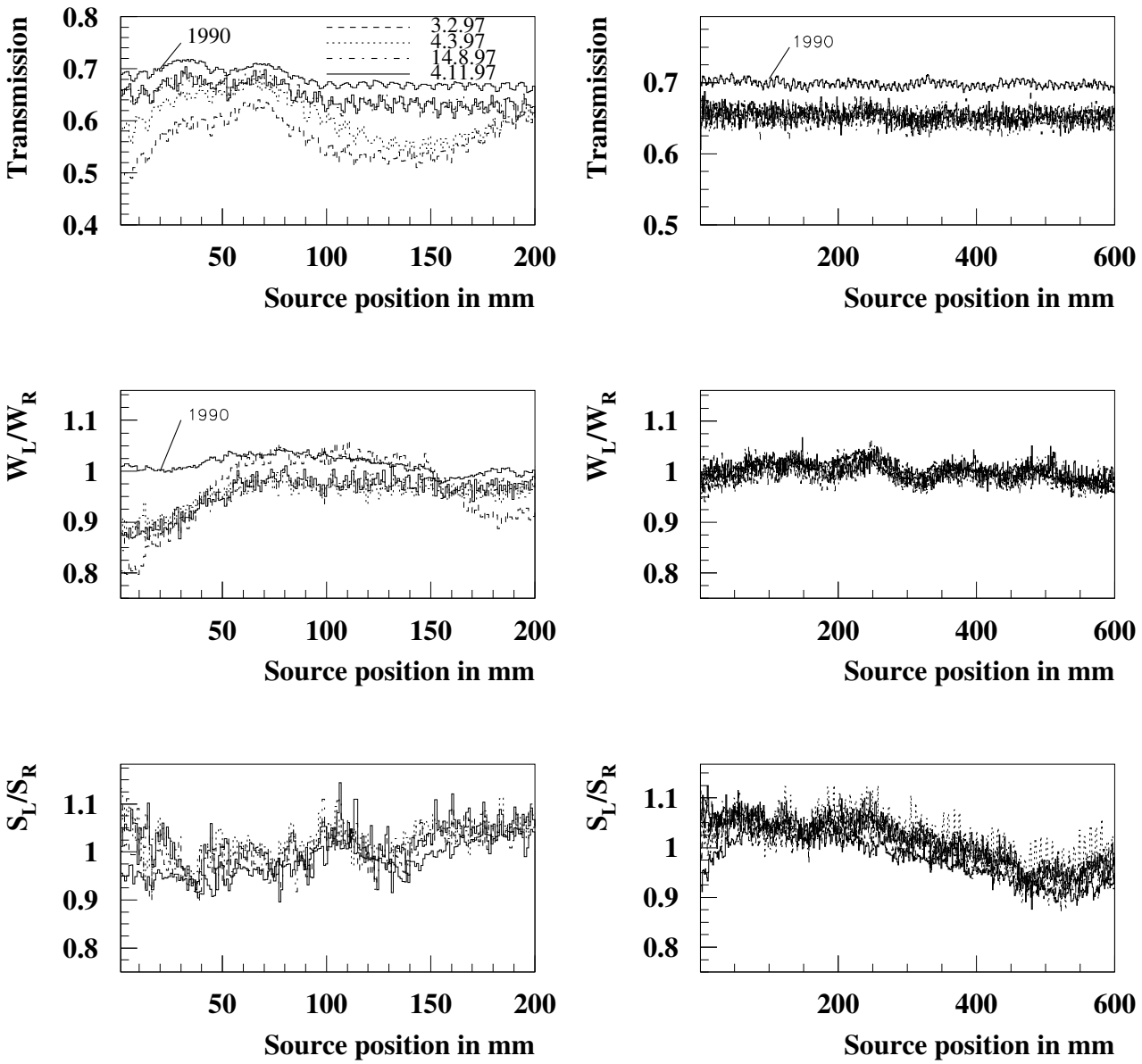


Figure 8.3: *The optical parameters of scintillators of the FCAL module 8, tower 21, HAC0 section (left column) and HAC2 section (right column) before and after the accident.*

One clearly notices the maximal variation immediately after the accident with strong recovery effects in the following time. Table 8.2 gives an overview of the deviations from reproducibility of left and right HAC0 signal responses which verify the recovery effects although the reproducibility fluctuates within the last measurements[2] of about $\pm 0.5\%$.

### The optical parameters

The optical parameters computed from the first inside scans after the accident show significant differences from the references which reduce considerably during the following time. The largest

[2]The reproducibility decreased due to a smaller repetition rate of the data acquisition system of 1500 instead of 3500 used for the last measurements.

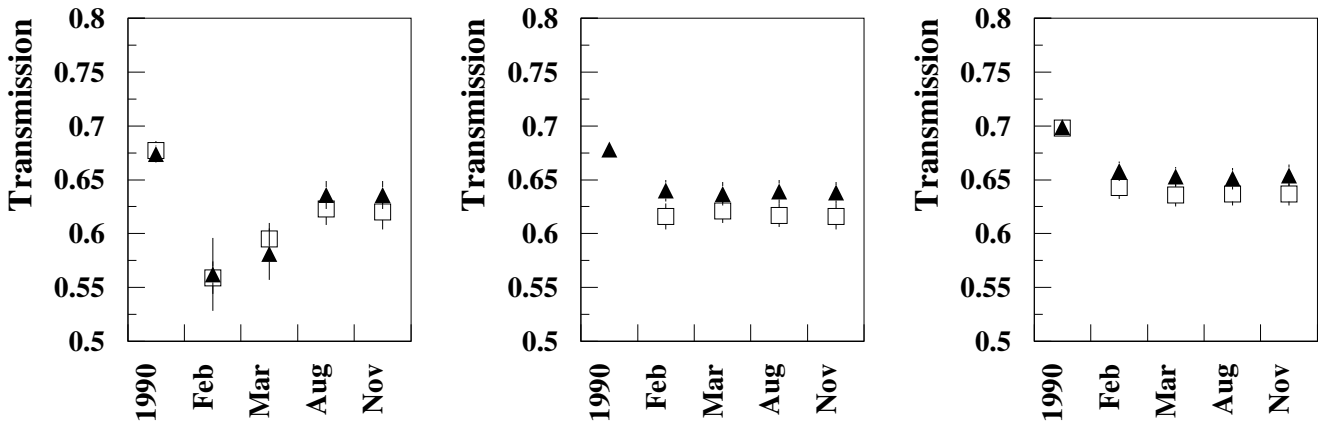


Figure 8.4: *The transmission averaged over the HAC0 (left), the HAC1 (middle) and the HAC2 section (right) of tower 21 (triangle) and tower 22 (square) for successive measurements as a function of the date of measurement.*

difference can be seen in the HAC0 and the EMC sections. Especially the transmission at the first inside measurements is reduced down to 80% of the reference value. The uniformity of the transmission as well as the ratio of the scintillator tile responses $S_L/S_R$ is in a range of $\pm$ 5%. The ratio of the wavelength shifter responses $W_L/W_R$ show variations up to 10%. These results are similar for EMC sections and HAC0 sections. Figure 8.3 shows the optical parameters of the damaged HAC0 section and the undamaged HAC2 section of tower 21.
It can be concluded from these results that both the scintillators and especially the left wavelength shifter became wet. The HAC1 and the HAC2 sections seem to be not affected by the water and show no significant variations, whereas the transmission of their scintillator tiles is different to the expected nominal value. This systematical and constant variation has been observed by these measurements for the first time and led to further investigations (see Chapter 7.4). It is most probably caused by ageing effects of the scintillator tiles[3]. UNO measurements after the accident have shown the recovery of the damaged sections, which could be verified by the $^{60}$Co measurements. Figure 8.4 shows the mean values of the transmission of damaged HAC0 (left diagram) and the undamaged HAC1 (middle diagram) and HAC2 scintillators (right diagram) of tower 22 and tower 21 for successive measurements. The first measurement is the reference of 1990, the following ones after the accident in 1997. The results of these data show clearly the recovery effects in the HAC0 section for the transmission.

### Uniformity of wavelength shifter

Additional longitudinal non-uniformities are demonstrated by a slope in ratio of two signal response functions measured at two different times. Figure 8.2 shows some typical plots of these ratios. They are similar for EMC and HAC0 sections. For these sections the ratio of signal responses show $\pm$10% non-uniformities with respect to the first measurements after the accident. One clearly notices the sharp rise at the beginning of the ratio. This is affected in addition to a possible non-uniform damage by the comparison between outside and inside scanning data (see Figure 5.8). Similar to the time dependence of the optical parameters, the non-uniformity of the signal responses of the EMC/HAC0 sections decreased successively after

[3]Inside scans on the FCAL module 17 confirm this result.

the accident. The ratio of the signal responses indicates non-uniformities decreasing down ± 5%. The HAC1 and HAC2 sections of the FCAL module 8 did not seem to be affected.

### 8.1.3 Damage scenarios

The water which flowed down the HES gaps of the FCAL module 8, caused a change in the properties of the optical components. Figure 4.1 illustrates the calorimeter structure including the optical components. Possible reasons for a change of the signal response might be the scintillator tiles and wavelength shifters [KL97]:

- A change in the light yield caused indirectly by wet tyvek-paper or optical contact between wavelength shifters and scintillator tiles due to the water. Light loss might be the consequence.
- A reduction of the attenuation length caused by dust on the optical components or on the front side between the optical components. Also wet tyvek paper on the scintillators/backreflector paper on the wavelength shifters reduce the effective attenuation length of the optical components.

Concerning the influence of water in contact with the wavelength shifter and the scintillator tile, two independent test measurements were done.

**Wavelength shifter set-up:** A FCAL EMC wavelength shifter was installed horizontally. The active area is UV-illuminated by a scintillator tile which was longitudinally moved by a stepping motor to several positions. The signal response of the water influenced wavelength shifter was compared with the undamaged one. The $z$ position dependent signal response $W(z)$

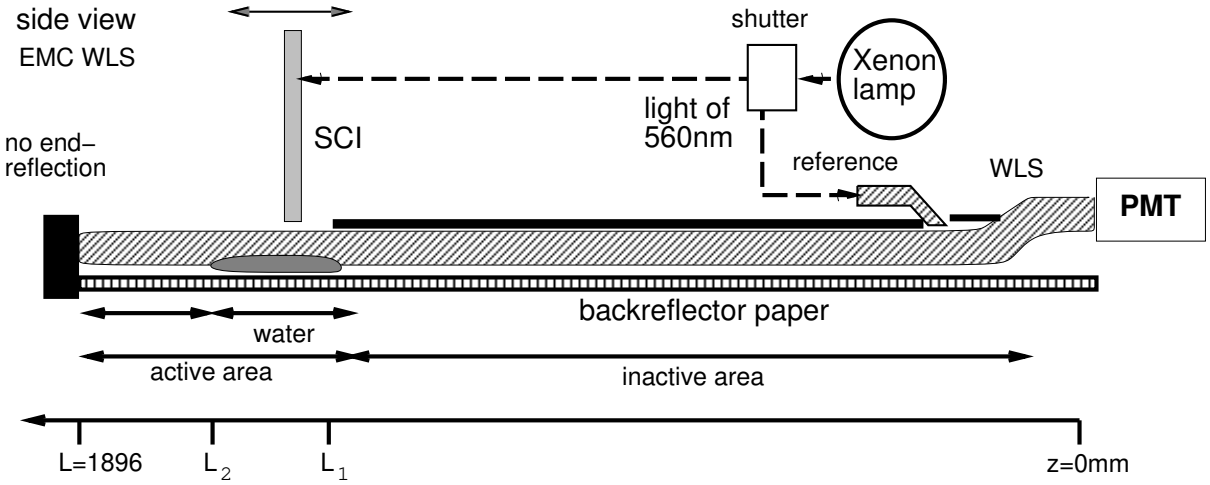


Figure 8.5: *Sketch of the measurement set-up in order to investigate the influence of water on a wavelength shifter.*

of the wavelength shifter with the length $L = 1896\,\mathrm{mm}$ can be described based on an effective attenuation length $\overline{\lambda}_{WLS}$ and assuming a reflection coeffecient $R$ at the end of the wavelength shifter (see formula 6.3). The signal response should be almost independent of $z$ as it is normally guaranteed due to an attenuation length of $\lambda_o > 130\,\mathrm{cm}$ and the usage of a special backreflector paper, which compensates the position depending signal to be uniform. The wavelength shifter

set-up has at its end black paper instead of the aluminium end-reflector, so that the reflection coefficient is reduced to $R \approx 0$. The first measurement is done without a water damage. Before further measurements could be done a certain area between the wavelength shifter and the backreflector paper is wetted by 0.5 ml of distillated water, which covers the active area in the range of $L_1 < z < L_2$ (see Figure 8.5). The signal responses before and after the water damage

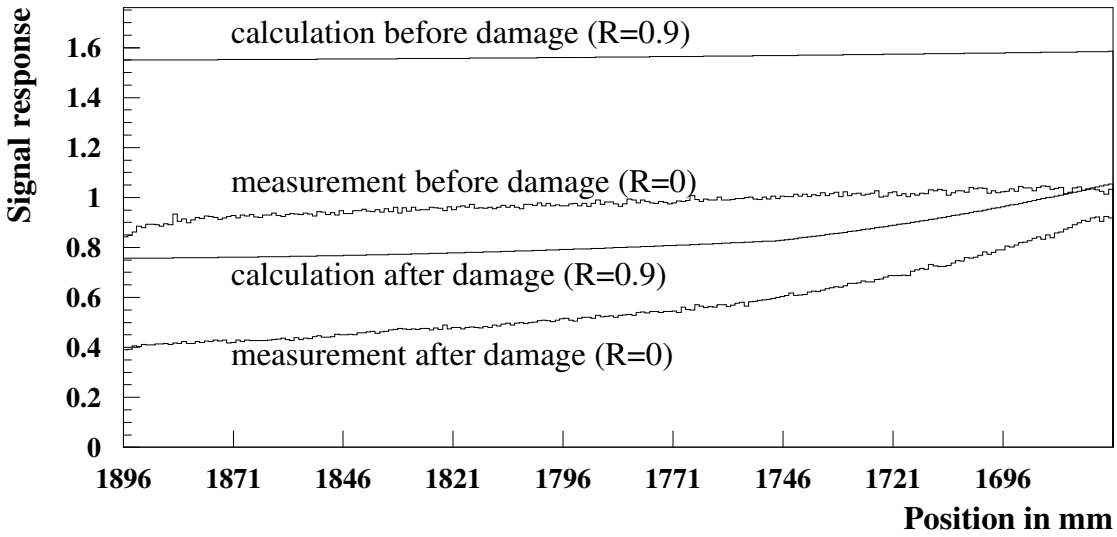


Figure 8.6: *Test experiments to simulate the water damage at wavelength shifters: The attenuation curves of the WLS bars were measured before and after the damage. The reflection at the end of the WLS (position $z = 1896$) was suppressed (reflection coefficient $R \approx 0$).*

are displayed in Figure 8.6. The signal responses of the wavelength shifter are readout on the right side of the diagram corresponding to $z = 0$. In a first approximation the damage between back reflector and wavelength shifter can be described dividing the longitudinal area of the wavelength shifter into three parts with constant effective attenuation lengths. The detailed calculation can be found in [HE98]. This rough assumption allows to fit the signal response of the water damaged wavelength shifter resulting the attenuation lengths $\lambda_0 = 1330\,\text{mm}$ for the inactive undamaged area $0 < z < L_1$; $\lambda_1 = 180\,\text{mm}$ for the second part $L_1 < z < L_2$ which is the wet region; and $\lambda = 380\,\text{mm}$ for the third part $L_2 < z < L$ without visible humidity. The results of the calculation assuming a reflection coefficient of $R = 0.9$ are also presented in Figure 8.6. Then the ratio of the integrated signal responses for the damaged and undamaged wavelength shifter yields $\int W_{damage} dz / \int W_{reference} dz = 0.54$, which agrees with the first UNO measurements after the accident.
The essential result is that the attenuation length decreases dramatically not only in the wet region but also in the region where no water is visible.

**Test calorimeter set-up:**

The $^{60}$Co measurements on a test calorimeter[4] demonstrate the influence of water on the transmission of the scintillators. Two scintillators are installed into the middle of an empty HAC2 section of the test calorimeter together with lead plates of thickness of 5 cm (see Figure 8.7). One of the scintillators is systematically treated by water, while the second one is not touched directly. After each processing the transmission of both scintillators was measured using $^{60}$Co scans on each tower side. The first step is the reinstallation of the scintillators in order to determine the reproducibility which is at the 4% level. The second step is to put 0.5 ml of water on the surface of the scintillator. The third step is uniform water damage of the scintillator. An additional water damage between wavelength shifter and scintillator is induced in the fourth step. The fifth measurement is a repetition $^{60}$Co scan after one day. Figure 8.8 shows the influence of the water on the transmission. Obviously the reference scintillator was affected after one day, probably due to the humidity in the section.

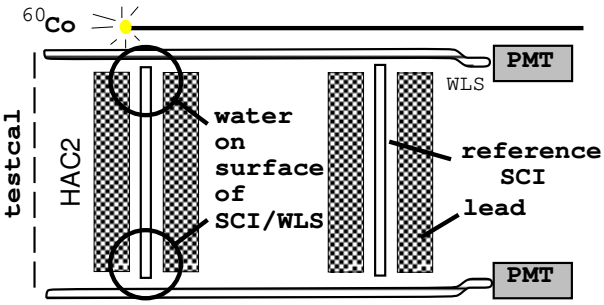


Figure 8.7: *Sketch of the measurement set-up in order to investigate the influence of water on a scintillator tile.*

The results of test measurements can be summarized as follows:

- the water damage is not only in the wet scintillator tiles but also in those ones which were never in direct contact with water,
- the strong decrease of the UNO signal of the FCAL module 8 measured just after the accident is probably mainly resulting from the reduction of the effective attenuation length of the wet wavelength shifters.

### 8.1.4 Effects of non-uniformity on calibration

In order to calibrate the towers of the ZEUS Calorimeter the ratio particle energy/UNO has been measured in a CERN[5] test experiment [ZE91]. Hence only one has to set the high voltage of the photomultipliers in such a way that the UNO signal has a specified value. After the accident the energy calibration was done in the same way. However, due to the non-uniformity of the water damaged EMC/HAC0 sections this procedure would yield an incorrect energy (see chapter 4.2). In the following ansatz the error of electron energy measurements will be estimated from the source scans performed at the EMC and HAC0 sections. The calculation were performed under the following assumptions:

- During the reference scan in 1990 the response of the sections was uniform at least in good approximation, i.e. the ratio $Q(i) =$ light yield/absorbed energy was constant for all scintillator tiles (i=1,2,...,26). The following calculation takes into account the non-uniformity along the $z$ direction induced by the water damages. Approximately it can be determined from the ratio $Q_{jk}(z)$ of the 4 response functions $I_{jk}(z)$ which one obtains from the two source scans on the left and right tower side after and before the accident.

[4]It is a lead/scintillator sampling calorimeter with a similar configuration as a FCAL EMC tower (see chapter 6.1).

[5]European Laboratory for Particle Physics at Geneva, Suisse.

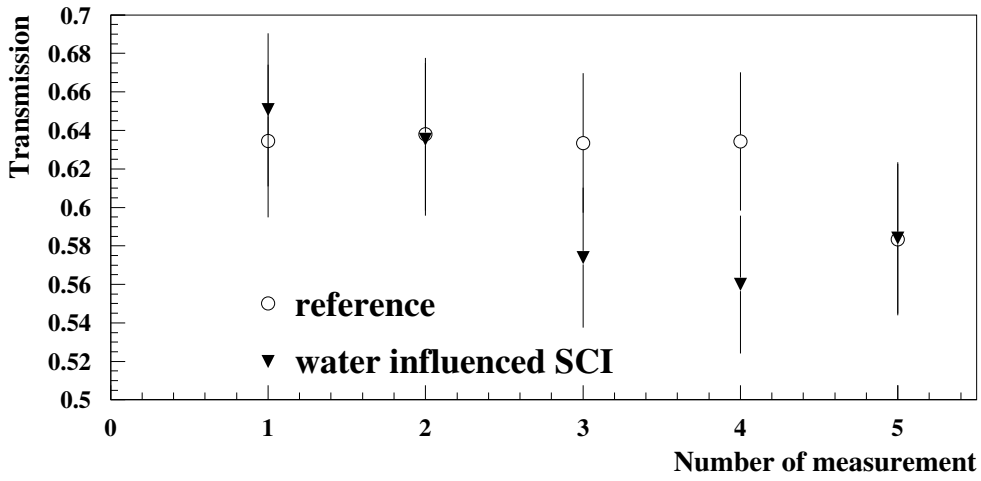


Figure 8.8: *Transmission of a water treated (triangle) and a reference scintillator (circle). One clearly notices the change of scintillator transmission after different types of water treatment. The reference scintillator which was not directly damaged shows an influence after one day corresponding to measurement No.5.*

- The $^{60}$Co method delivers only the information of the edges of the scintillator tiles whereas the longitudinal electromagnetic shower profile is calculated assuming an incident electron in the middle of the calorimeter. In order to minimize the influence of edges the calorimeter response as a function of the energy $E$ is taken as the mean value $\bar{E}_m(E)$ of the 4 calorimeter responses $E_{jk}(E)$ determined from the two $^{60}$Co scans and from the following calculation.

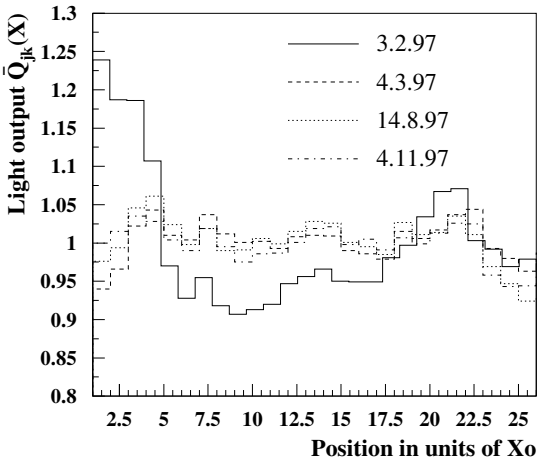


Figure 8.9: *Ratio of the normalized response functions of tower 21, HAC0 section after/before the damage including the correction of the different pulse heights from inside/outside scans.*

The average deposited energy profile for an electromagnetic shower can be approximated with formula 4.6. The total calorimeter response $E_m$ has to be calculated in terms of the average energy per unit length $F(E,X)$ deposited at the position $X$ in units of the radiation length $X_0 = 0.74\,\mathrm{cm}$ with $X = z/X_0$. The observed light output $Q(X)$ of a section should be unity if there is no variation between two signal responses measured at two different times. The ratio of the $^{60}$Co signals $Q_{jk}(X)$ in units of $X_0$ is assumed to be equal to the light output $Q(X)$. The indices $j,k$ denote the source scan position and the readout position (left or right). Taking into account the differences between inside/outside measurements (see section 8.1.1) the 4 ratios of signals are corrected to the ratio of outside/inside scanning responses. Averaged over 8 mm it yields the light output $\bar{Q}_{jk}(i)$ for the $i$th scintillator. The right light output in units of radiation length of the HAC0 section of tower 21 as a function of the time is shown in Figure 8.9. The source was guided on the right

tower side. One has to notice the influence of humidity on the scintillators close to the HES gap between February and March 1997. The measured energy $\bar{E}_m$ of an electron-induced cascade in a certain section with the length $L$ in units of $X_o$ can be computed similar to equation 4.8 and 4.9. It is the mean value of the 4 calorimeter responses $E_{jk}(E)$ determined from the two $^{60}$Co scans. The summarization over all 26 scintillators yields:

$$\bar{E}_m(E) = \frac{\sum_{j,k} E_{jk}(E)}{4} = \frac{1}{4}\sum_{j,k} E \cdot \frac{\sum_{i=1}^{26} F(E,X_i)\cdot \bar{Q}_{jk}(i)}{(\sum_{i=1}^{26} F(E,X_i))\cdot(\sum_{i=1}^{26} \bar{Q}_{jk}(i)/26)}. \qquad (8.1)$$

The calculation has been done for electron energies of of 1 to 200 GeV using the light output $\bar{Q}_{jk}$ of the measured EMC and HAC0 sections of the FCAL module 8. The left diagram of Figure 8.10 displays the effect on the energy linearity of the HAC0 section of tower 21 in the period of January to November. The relative error in percent counts here from approximately $\pm 3\%$ in February down to approximately 1% since August. The behaviour of the other measured EMC/HAC0 sections of module 8 is similar; the relative error for them yields at last about $\pm 3\%$. Table 8.3 gives an overview of the maximal deviation from linearity for the EMC and HAC0 sections.

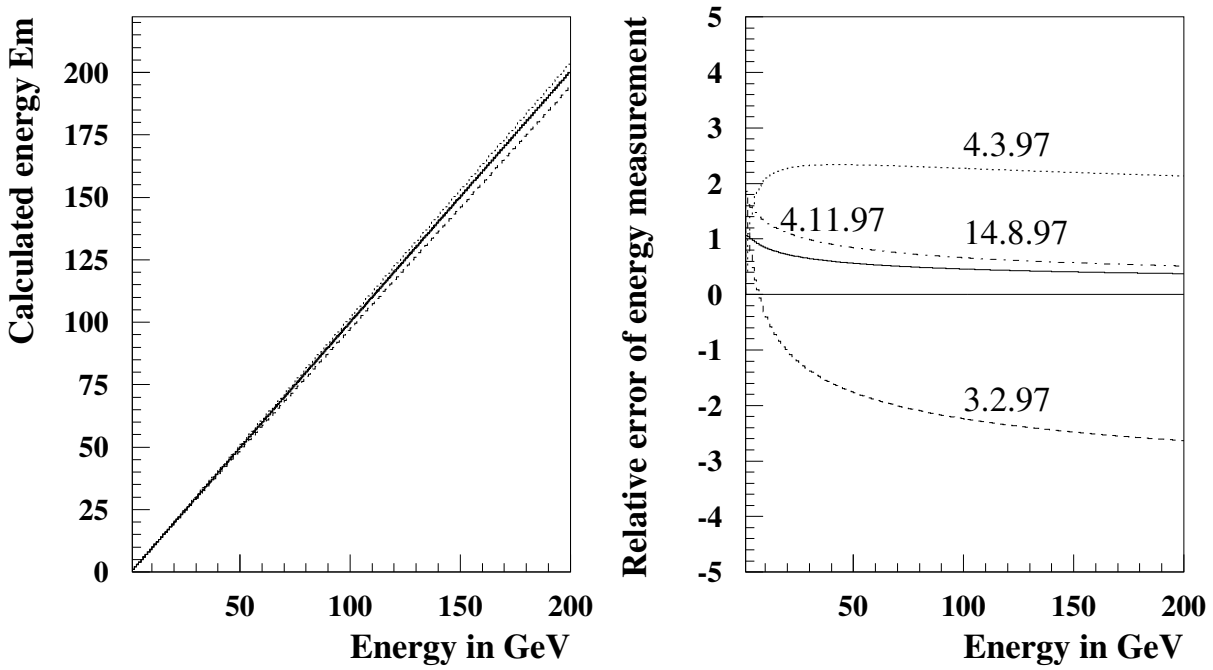


Figure 8.10: *Estimate of the water damage on the energy calibration of tower 21 (FCAL module 8). The calculation of energy measurement (left) and the energy deviation from the true energy (right) is plotted as a function of electron energy.*

## 8.2 Investigation on the RCAL module 17

Already in 1995 a cooling water accident happened to the ZEUS calorimeter similar to the one happened to the FCAL module 8 in 1997. Due to a leak valve of the HES water cooling system several litres of water flowed from the top of the RCAL module 17 into a gap, where the $^{60}$Co fan-out[6] is located. The uranium noise signal (UNO) of the photomultipliers decreased for

[6]Special adapter system in order to connect the $^{60}$Co brass tubes with the ground-plate.

| max. relative error of energy measurement in % | | | | | | | | | | | | |
|---|---|---|---|---|---|---|---|---|---|---|---|---|
| tower | T22 | T21 | T20 | | | | T4 | | | | T2 | T1 |
| section | H0 | H0 | E1 | E2 | E3 | E4 | E1 | E2 | E3 | E4 | H0 | H0 |
| 3.2.1997 | 5.8 | 2.6 | 7.0 | 3.6 | 8.0 | 13.9 | - | - | - | - | - | - |
| 4.3.1997 | 5.4 | 2.3 | - | - | - | - | 4.4 | 9.8 | 1.9 | 4.9 | 4.8 | 2.3 |
| 14.8.1997 | 3.4 | 1.6 | - | - | - | - | - | - | - | - | 2.0 | 3.1 |
| 4.11.1997 | 4.6 | 1.1 | - | - | - | - | - | - | - | - | 2.9 | 4.1 |

Table 8.3: *Overview of the maximum deviation from linearity in percent for all measured EMC and HAC0 sections of the FCAL module 8.*

several EMC and HAC0 sections down to minimal 60% [KO95]. As well seen later with respect to the accident of the FCAL module 8, the HAC sections did not seem to be affected. The UNO signal of the affected sections recovered slowly in the following time. A vital discussion began about the possibilities of $^{60}$Co inside scanning. But for the time being no measurements had been performed. In 1997 inside scans were made possible due to a new security concept which allowed to perform intensive investigations of the FCAL module 8 in that year. Finally also inside scans on the RCAL module 17 were performed in order to compare the water damage effects, especially the non-uniformities of both water influenced modules. An unfolding method is used for the worst damaged EMC section calculating the relative change of weight factors of the scintillators due to the water damage.

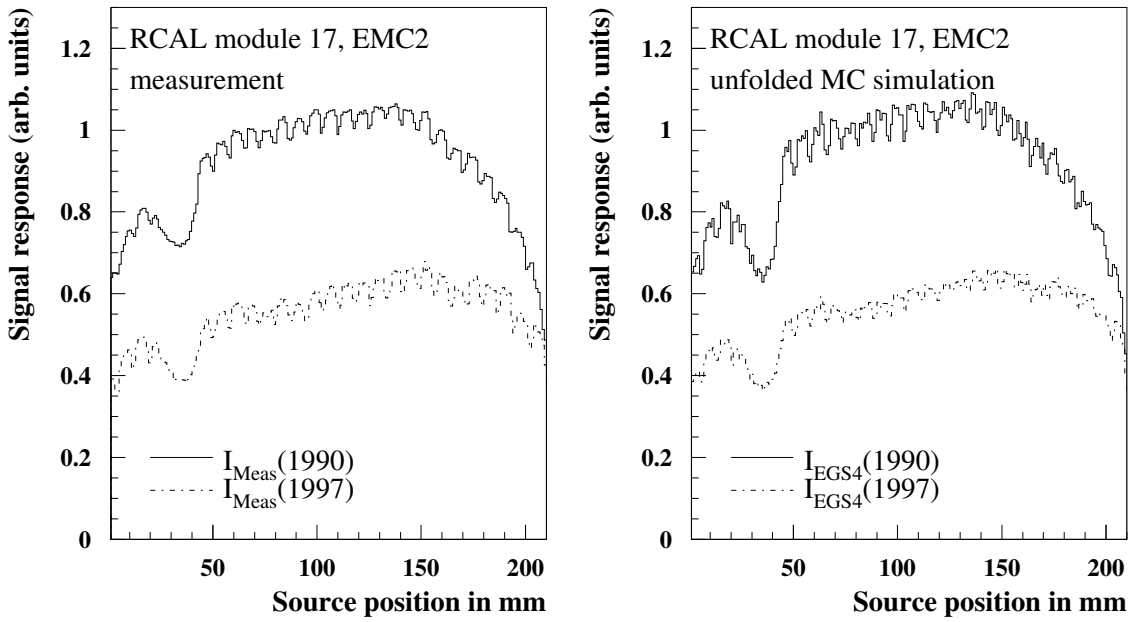


Figure 8.11: *Measured signal responses (left) and simulated ones (right) of the EMC2 section of RCAL module 17, tower 17. The $^{60}$Co scan was performed on the left tower side.*

### 8.2.1 $^{60}$Co measurements

In November the 6th in 1995 $^{60}$Co inside scans were performed on the towers 16 and 17 of the RCAL module 17 corresponding to 4 EMC and 2 HAC sections. As described in section 8.1.1 the present measurement performance differs in some features from the reference ones in 1990. Mainly the difference with respect to outside/inside scanning produces artificial variations in the signal responses. In 1990 the RCAL outside scans were performed moving the source parallel to the wavelength shifter in the middle of the EMC section, whereas the inside scanner guides the source between both EMC sections. $^{60}$Co signal response depends significantly on the solid angle of the excitation which is directly correlated with the respective scanner method. However, this effect should be uniform and refers to all scintillators of an investigated RCAL section[7]. Except of one single case the comparison of the $^{60}$Co signal responses with the references show reproducibilities with no signifcant or only very small deviations[8]. The deviation from reproducibility is presented for each measured section in table 8.4. The EMC2 section of tower 17 shows a maximal deviation of $R_d = 7.67\%$.

| tower | time | EMC1RR | EMC1LL | EMC2RR | EMC2LL | HACRR | HACLL |
|---|---|---|---|---|---|---|---|
| 16 | 6.11. | 2.89 | 3.80 | 1.89 | 3.36 | 1.52 | 1.76 |
| 17 | 6.11. | – | – | 2.53 | 7.67 | 2.29 | 2.92 |

Table 8.4: *Overview of the deviation from reproducibility of the signal responses of the EMC and HAC sections of the RCAL, tower 16 and 17, in comparison to the references.*

### 8.2.2 The optical parameters

Except for the EMC2 section of tower 17, the optical parameters of the investigated sections are more or less similar to those of undamaged RCAL and FCAL sections. The uniformity of these parameters is within the $\pm 4\%$ level. The transmission of scintillators is reduced in the order of 5% in all measured sections, also in those ones, which did not show any variation in the UNO signal after the water damage accident. This underlines the possibility of ageing effects of the scintillator tiles. An additional reduction of the transmission is not clearly visible. Probably a similar recovery process happened on the RCAL module 17 after the accident as well as on the FCAL module 8 during 1997. Figure 8.12 presents the optical parameters of the EMC2 (left column) and the HAC section (right column) of tower 17. A big non-uniformity up to $\pm 10\%$ is visible with respect to the ratio of the wavelength shifter responses of the EMC2 section (middle left diagram of Figure 8.12). This case indicates clearly a change in the wavelength shifter response. Further investigations were performed on this section and will be briefly summarized below:

[7] The signal response of the EMC section is more sensitive to the scanner method than the one of the HAC section.

[8] In the meantime inside scans on the modules 13 and 14 of the RCAL have been performed resulting similar reproducibilities.

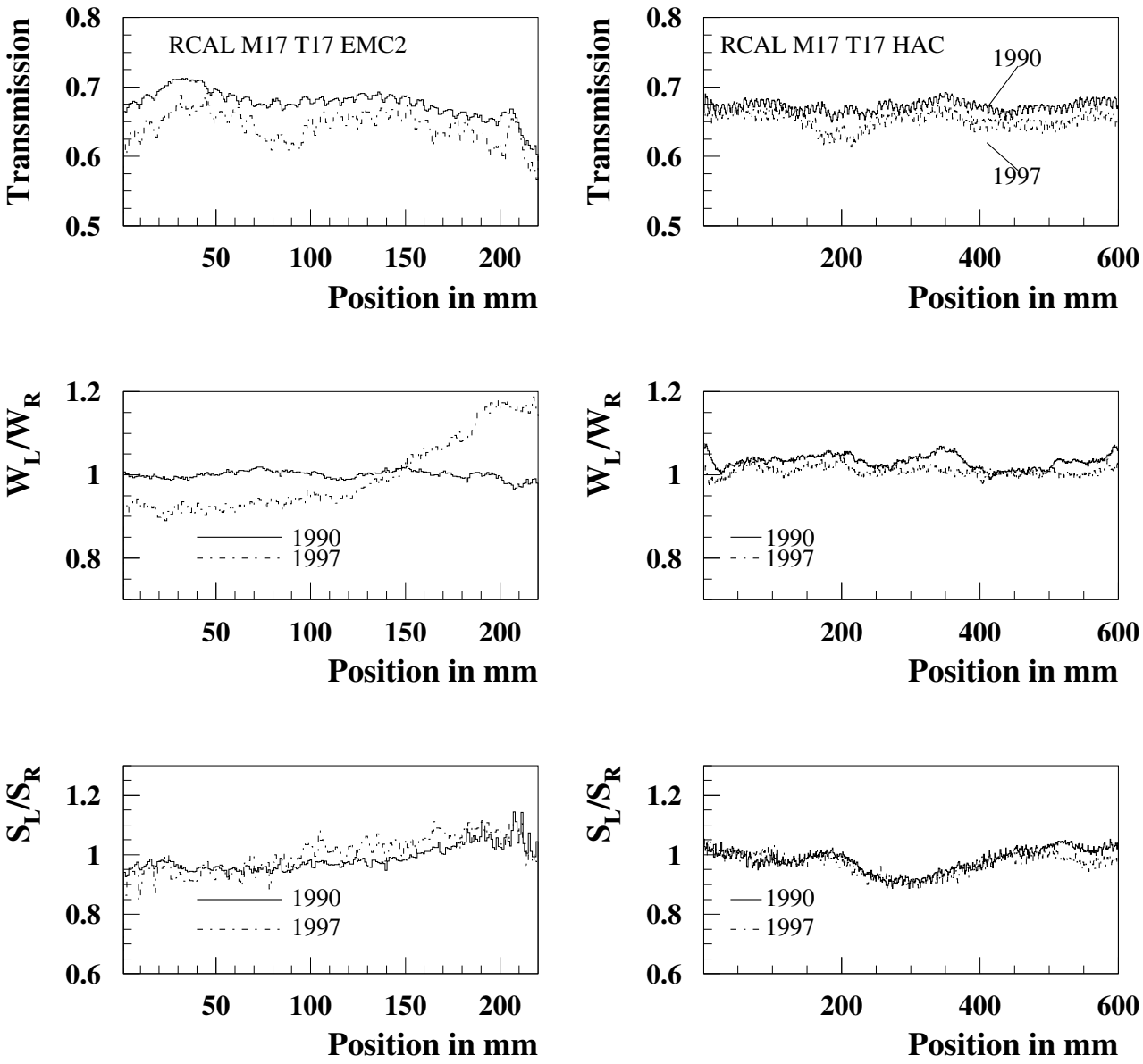


Figure 8.12: *The optical parameters of the RCAL module 17, tower 17, EMC2 section (left column) and HAC section (right column) before and after the accident. A big non-uniformity up to* $\pm 10\%$ *is visible with respect to the ratio of the wavelength shifter responses of the EMC2 section in the middle left diagram.*

### 8.2.3 Unfolding

In order to estimate the water damage effects on the the longitudinal light output, an unfolding method is applied on the worst damaged signal responses, namely those ones of the EMC2 section of tower 17. The method is described in detail in chapter 5.1.3. Based on an EGS4 Monte Carlo, it allows to unfold a signal response to determine the weight factor of each scintillator. The ratio of the weight factors of 1997 and 1990 yield the relative variation of the scintillators. The left diagram in Figure 8.11 displays the signal responses EMC2 section

| signal response | $I_{Meas}(1997)$ | $I_{EGS4}(1990)$ |
|---|---|---|
| $I_{Meas}(1990)$ | 7.89 % | 1.98 % |
| $I_{EGS4}(1997)$ | 1.10 % | 7.67 % |

Table 8.5: *Overview of the deviation from reproducibility between measured and MC simulated signal responses of EMC2 section, RCAL 17, tower 17.*

before (solid line) and after the water damage (dashed line) of the left photomultiplier. The right diagram of Figure 8.11 shows the EGS4 simulated ones. Table 8.5 displays the deviation from reproducibilities between the measured and simulated signal responses of the section. The unfolding method is able to reproduce the measured signal responses at the 1–2% level which is an impressing validation for the unfolding method. The essential result of the unfolding method is the ratio of the weight factors of the scintillators for the right and left wavelength shifter before and after the water damage. No variation is represented by unity, any change is seen in a deviation of the relative weight factors from unity. In Figure 8.13 the relative weight factors of the scintillators for the left and right wavelength shifter of the EMC2 section, tower 17 are presented. One clearly notices the significant reduction for scintillator responses of the left wavelength shifter at the beginning of the section (filled circles) and the strong increase for the scintillator numbers $n > 16$, whereas the scintillator responses for the right wavelength shifter are uniform within $\pm 5\%$. The differences between inside and outside scans are corrected. This result corresponds with the ratio of the wavelength shifter responses of this section (see the middle left diagram in Figure 8.12). Accordingly the change refers most probably to a water damage of the left wavelength shifter.

### 8.2.4 Effects of non-uniformity on calibration

The non-uniformity of the EMC2 section of the RCAL module 17, tower 17, yields an error of the energy measurement which is estimated by the same calculation as described in section 8.1.4. The assumption is that the observed light output $Q(X)$ of scintillators for the left and right wavelength shifter is almost similar to the relative weight factors calculated by the unfolding method. The measured energy of an electromagnetic shower can be approximated as the product of the energy profile times the light output of the calorimeter section[9]. The left diagram in Figure 8.14 displays the calculated energy versus the impact energy in a range of 1 to 200 GeV electrons. The deviation from linearity is shown in the right diagram. The effect is in the order of 3%.

[9] The correction of different pulse heights due to the differences of inside and outside scans is included.

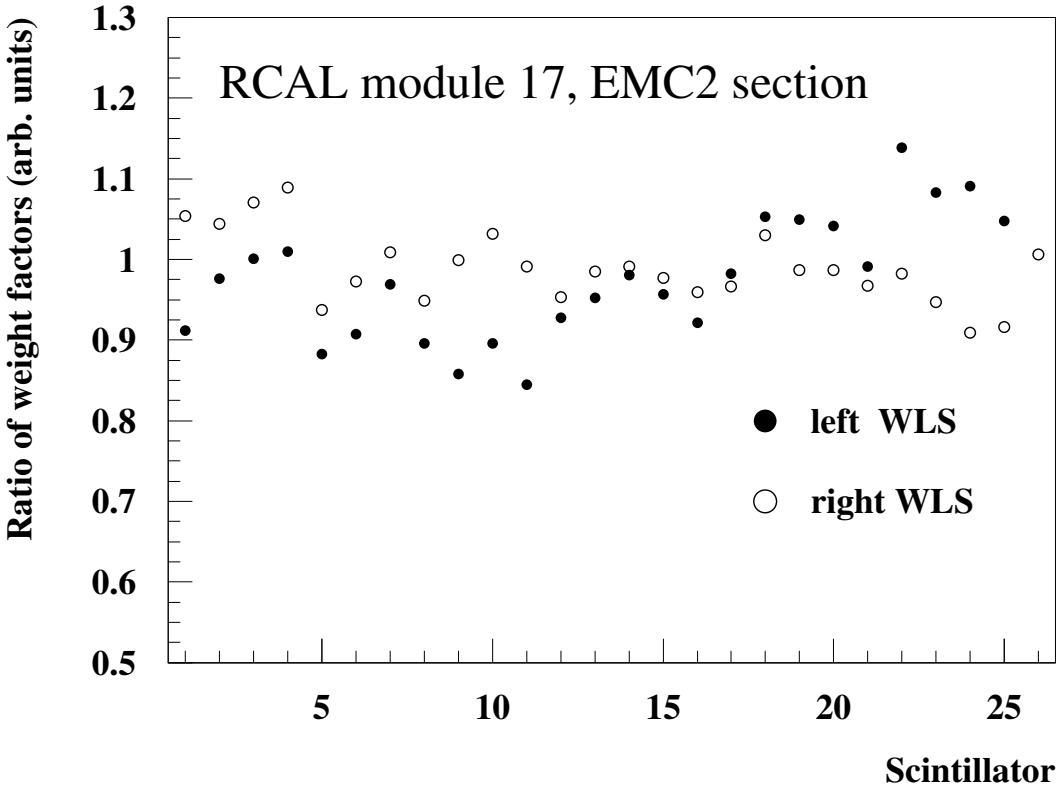


Figure 8.13: *Ratio of the Weight factors of the scintillators of the RCAL module 17, EMC2 section for the right and left wavelength shifter.*

## 8.3 Conclusions

The investigations described in this chapter will be briefly summarized: Two similar water damage accidents happened on the ZEUS calorimeter resulting in small effects on the calibration in the energy range of 1 – 200 GeV:

**FCAL module 8:** The accident in the HES water cooling system at the end of the maintenance period in January 1997 damaged mainly the electromagnetic sections. One consequence was the reduction of the UNO signal in the electromagnetic sections of this calorimeter module decreased by up to 40%. Within the following 10 months 4 $^{60}$Co measurements were performed with the aim to study the influence of the water damage on the optical components and on the longitudinal uniformity of the calorimeter response. A qualitative understanding of the water damage with respect to the wavelength shifters and the scintillator tiles was performed via two test calorimeter set-ups. $^{60}$Co inside scans and UNO measurements of the FCAL module 8 showed the following:

- No influence of the water damage on the hadronic sections could be detected.
- The electromagnatic sections show a significant reduction of the transmission of the scintillators immediately after the accident.

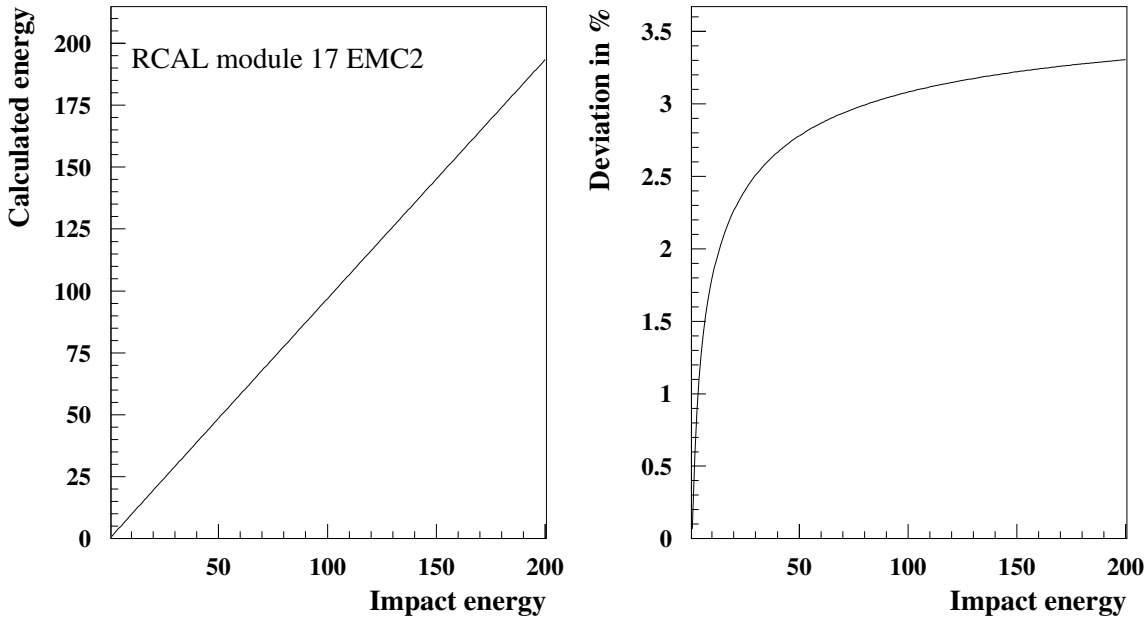


Figure 8.14: *Linearity (left) and deviation from linearity (right) of the RCAL module 17, EMC2 section.*

- Yet the uniformity of the transmission as well as the ratio of scintillator responses is still in a range of ± 5%, the non-uniformities of the wavelength shifters are in a range of ±10%.
- A strong recovery effect of the optical parameters is observed in the following time with approximately nominal values since August in 1997.
- The effect on energy calibration with assumptions could be calculated and was found to be ±3% in case of tower 21 after the accident and decreased to be less than 1% since August 1997. Similar results can be obtained for the other measured EMC/HAC0 sections of module 8, the relative error for them yields at last about 3%.

**RCAL module 17:** The accident in the HES water cooling system at the end of the maintenance period in January 1995 induced the electromagnetic sections. The UNO signal in the electromagnetic sections of this module decreased by up to 40%. In November 1997 $^{60}$Co inside scans were performed on the towers 16 and 17 of the RCAL module 17 with the aim to compare the effects with those occurred in the FCAL module 8. The results showed that:

- There is no influence of the water damage on the hadronic sections.
- A certain influence of the water can only be verified for the EMC2 section of tower 17. The left wavelength shifter shows a non-uniformity of ±10%.
- The effect on energy calibration for this section could be calculated using the unfolding method. In November 1997 it was found to be of 3%.

# Chapter 9

# Radiation damage effects in the BPC

The ZEUS Beam Pipe Calorimeter (BPC) consists of two small tungsten/scintillator sampling calorimeters, which have been installed in the winter shutdown 1994/1995 in the rear direction of the ZEUS detector [BR97]. They are located right and left in the z position at a distance of approximately 4 cm from the HERA beams. Figure 9.1 shows a sketch of the configuration of the BPC at the HERA beampipe. The accumulated dose of the BPC during the 1995 HERA run was about 12 kGy. This radiation dose influenced the scintillators of the BPC. The degradation of some of the BPC scintillators due to radiation damage has been determined from different monitor systems, especially from $^{60}$Co scans. Therefore all scintillators of the BPC after the 1995 HERA run were replaced [BO98c]. The monitoring procedures were repeated in 1996 and an exchange of the damaged scintillator sections were done again. Since 1997 the accumulated dose significantly dropped and no further replacement of scintillators was necessary [BO99b]. The following chapter describes the radiation monitoring and the effects of the accumulated dose on the optical properties of the scintillator inside the BPC with respect to the running periods 1995 and 1997.

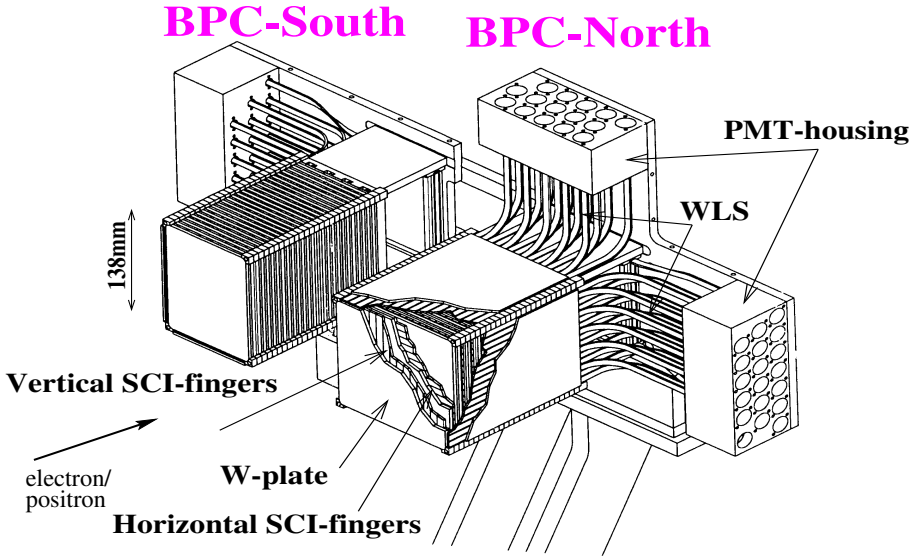


Figure 9.1: *CAD drawing of the BPC.*

## 9.1 The Beam Pipe Calorimeter

In 1994/1995 the ZEUS Beam Pipe Calorimeter[1] (BPC) has been installed as the extension of the ZEUS detector in the rear direction in order to measure the angle of the scattered electrons in neutral current events in the region of $Q^2 < 1.5\,\mathrm{GeV}^2$ and very low $x_{Bj}$. The BPC allows the investigation of

- the structure of the proton structure function $F_2(x_{Bj}, Q^2)$ [SU98],
- the structure of the photon [KC99] and
- the diffraction [MO98]

at low $Q^2$ and very low $x$ with an high accuracy in a kinematic region which had not been accessible at HERA before (see Chapter 2.3).
The BPC consists of two electromagnetic sampling calorimeter modules (BPC north and BPC south) located on each side of the HERA beams along the x-axis at a distance of approximately $z = -2937\,\mathrm{mm}$ from the ZEUS interaction point. The modules are centered in the plane of the HERA collider ($y = 0$).

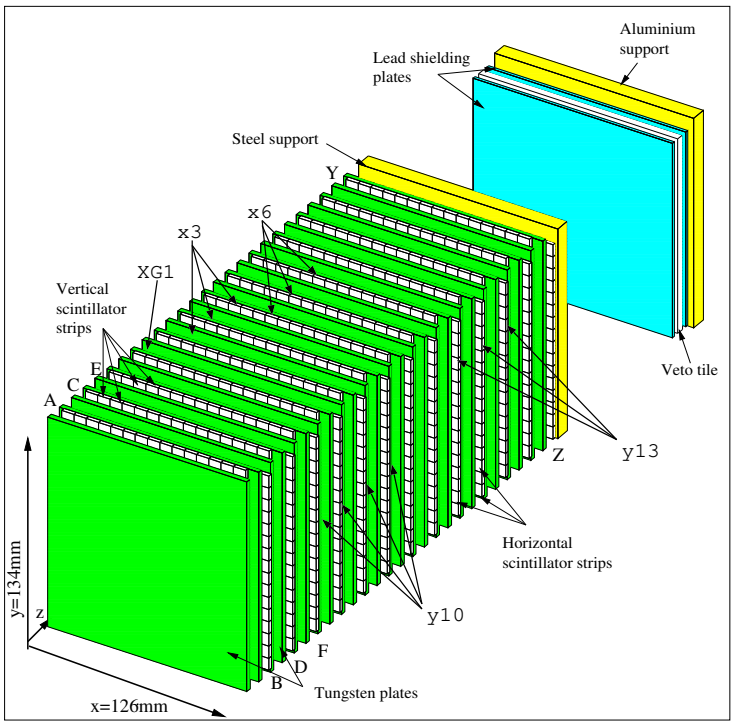


Figure 9.2: *Principle structure of the BPC module north without WLS bars.*

A schematic view on the BPC module north is shown in Figure 9.2. Each module consists parallel to the HERA beams of 26 alternating layers of 8 mm wide and 2.6 mm thick scintillator fingers (*SCSN-38*) and tungsten absorption plates (3.5 mm deep and a radiation length of 3.87 mm). The orientation of the scintillators alternates from the vertical direction (so-called x-fingers) to the horizontal direction (so-called y-fingers), from layer to layer; 13 alternating scintillator layers compose a section. Accordingly 26 layers exist for each BPC module labeled from $A$ corresponding to the first layer to $Z$ corresponding to the last one. In case of BPC north the y-fingers have a length of 126 mm, the x-fingers have a length of 134 mm; 16 y-fingers and 15 x-fingers compose a horizontally and vertically oriented scintillator layer. The geometrical structure of BPC south is similar, but only 11 x-fingers compose a vertically oriented scintillator layer, the length of the y-fingers is 88 mm. The vertically oriented scintillator sections providing the $x$ position measurement are labeled $NX1$ to $NX15$ for BPC north ($SX1$ to $SX15$ for BPC south) counting from the HERA beams. The horizontally oriented scintillator sections providing the $y$ position measurement are labeled $NY1$ to $NY16$ for BPC north ($SY1$ to $SY16$ for BPC south) counting from the bottom. The layer number of the scintillators is included

[1] Already in 1994 a tungsten calorimeter based on a silicon readout was used at ZEUS at this position [LO96], [RU95].

into the notation, accordingly the BPC north x-finger of the first section and seventh layer is labeled with $NXG1$. A set of tungsten plates and scintillator layers corresponds to 0.91 radiation lengths. The scintillators are polished, wrapped into a a 27.5 $\mu$m thick aluminium foil and aluminized at the end which is not read out to provide an efficient end reflector. The open end of the scintillators are read out by 7 mm wide and 2 mm thick wavelength shifters based on the same material used in the ZEUS calorimeter (*PMMA* dotted with *Y7*). Except for the usage of only one wavelength shifter per section the readout scheme is similar to the one of the ZEUS calorimeter (see Chapter 4.2). The x-fingers are read out from the top (bottom) face of the BPC. The y-fingers are read out from the opposite side of the HERA beams. The light is guided to a new type of photomultiplier tubes (*Hamamatsu Photonics R5600U-03*) with a diameter of 12 mm. A pulse light calibration system allows to monitor each photomultiplier. But no constant scintillator signal exists for the BPC like the one at the ZEUS calorimeter from the uranium noise (UNO). Therefore the usage of the $^{60}$Co monitor system is of vital importance with regard to relative calibration and quality monitoring.
The measured accumulated dose of the BPC during the 1995 HERA run was approximately 12 kGy. That radiation dose influenced the optical components of the BPC. The degradation of some of the BPC scintillators due to radiation damage has been determined from different monitor systems. The monitoring procedures were repeated in the following years determining a reduced irradiation from one running period to the next. Still in 1996 the damaged scintillators were exchanged. Since 1997 the accumulated dose dropped by a factor of five. Since then no further replacement of scintillators was necessary.

## 9.2 The running conditions

Contrary to the main calorimeter which is retracted by 40 cm from the HERA beams during injection and ramping periods the BPC is exposed to additional irradiation of the HERA beams like synchrotron radiation (see Chapter 3.3). Therefore monitoring of the accumulated radiation dose using passive and active radiation devices is of vital importance of the BPC. Since 1995 several online and offline monitoring tools have been used to investigate the integrity of the optical components of the BPC:

- Silicon diodes are used for online radiation detection,
- TLD crystals used on the surface of the BPC during the running period are based on a Lithium-7 isotope fluoride ($LiF_2$),
- scans are executed along the surface of the complete BPC modules using the $^{60}$Co monitor system,
- investigations of individual scintillator fingers are performed using electrons from radioactive sources and UV-light and
- calibration using scattered electrons from HERA (kinematic peak events).

The accumulated dose has been measured since the installation of the BPC on a regular monthly basis. Figure 9.3 shows a front view of both BPC modules as seen from the interaction point. Groves with a cross section of $1.5 \times 1.5\,\mathrm{mm}^2$ were machined on two sides of the first and the last tungsten plates as shown in Figure 9.3. Prior to the assembly of the BPC modules brass tubes with a diameter of 1.5 mm were glued inside these groves. Their respective ends are accessible

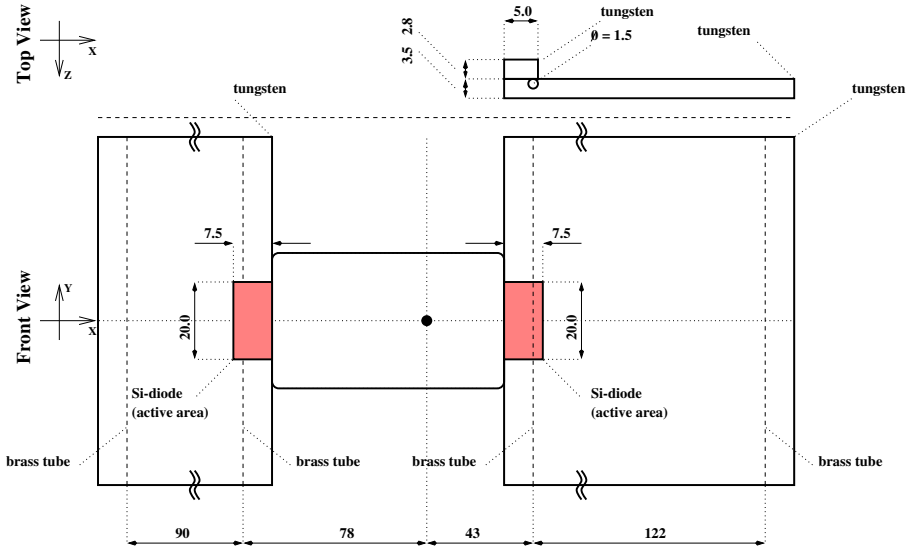


Figure 9.3: *Top view and front view of both BPC modules showing the location of the brass tubes (TLD's) and the Si-diodes.*

outside the BPC modules. The tubes are filled with TLD crystals (Harshaw TLD-700) and exchanged monthly. After the first months of data taking in 1995, a very high accumulated dose was measured in the front inner brass tube of the BPC north module. Figure 9.4 shows the accumulated dose as a function of the central position of each TLD crystal within the front inner brass tube. The alignment accuracy of the TLD crystals was estimated to be approximately 2 mm. Over the whole data taking period, a characteristic dose profile was measured. It shows a clear peak in the horizontal plane of the HERA beams which falls off towards larger distances. Within the period of one month it has been measured that the accumulated dose across the front face of the BPC north module shows approximately an exponential fall-off. In case of the running period 1995 as well as 1996 the measured peak values reached the linear response of the TLD's. The accumulated dose in the BPC north module drops down significantly for larger distances away from the HERA beams. It shows as well a significant difference between the front and the back plane of the BPC north module, which indicates that a particle flux leading to such a high dose has to be in direction of the positron beam. The measured dose in the BPC south module amounts to approximately 50 Gy or less per running period which is lower by a factor 40 compared to the monthly dose measured in the BPC north module.
The instantaneous radiation dose of the BPC has been monitored by the leakage current of a Si-diode. This allowed to determine the origin of the measured accumulated dose as a function of the HERA operation (injection, luminosity run, dumping). Two silicon diodes enclosed inside a light-tight cover were installed in front of both BPC modules [SU98], [FR99]. The accumulated dose during injection as well as during the luminosity operation have been found to be negligible. The measured current of the silicon diodes was clearly correlated with several dumping schemes of the running period 1995 and 1996 [BO98a]. It can be concluded that a significant fraction of the accumulated dose in 1995 and 1996 is due to the dump of positrons and accidental beam losses in particular during machine studies. Since 1997 no further strong incidences have been observed anymore (see Figure 9.5), the measured dose decreased to less than 0.5 kGy per month.

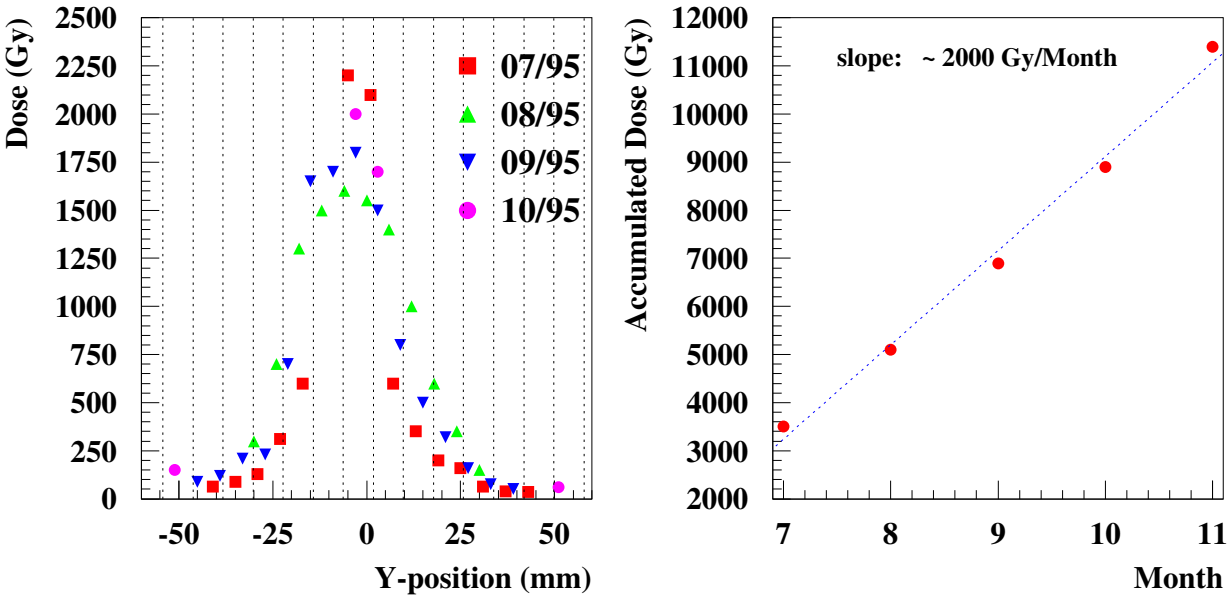


Figure 9.4: *Dose profile accumulated per month in the front inner tube of the BPC north module for the HERA run in 1995.*

## 9.3 Investigations of radiation damage

The high accumulated doses on the BPC north after the running period 1995 measured by the TLD's required further investigations on the BPC. Several monitoring tools have been used to inspect the integrity of the optical components of the BPC using moving radioactive sources and an UV-light system:

- Scans along the surface of the complete BPC module north using the $^{60}$Co monitor system and
- investigations of individual scintillator fingers using electrons and UV-light.

These investigations will be briefly summarized below:

### 9.3.1 $^{60}$Co measurements before/after the running period

Prior to the installation of the BPC, both BPC modules were scanned using the $^{60}$Co monitor system. The scanner was mounted on an assembly which was pressed on the front plate of the BPC. The point-like $^{60}$Co source was moved in $z$ direction on the opposite side of the wavelength shifter bars along the BPC within a brass tube. The outside scanning principle is similar to the procedure shown in Figure 5.2. The resulting $^{60}$Co signal response depends on the $^{60}$Co source position which provides information about the longitudinal response of the BPC section. Each maximum of the signal response is associated to a particular scintillator finger of the measured section. A possible variation of the longitudinal response due to radiation damage can be obtained by comparing the responses of the BPC before and after the HERA run.

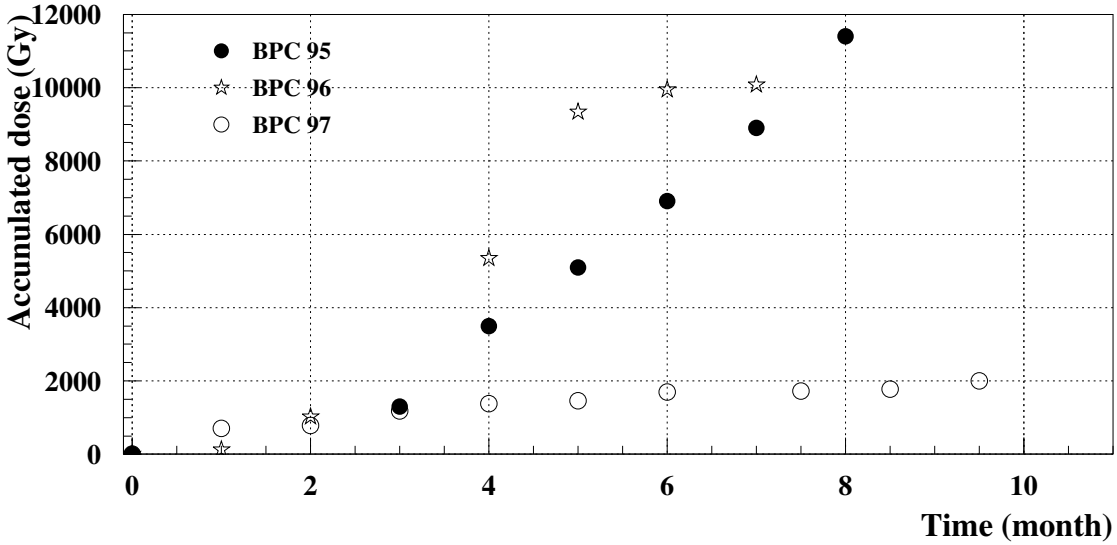


Figure 9.5: *Dose profile accumulated per month in the front inner tube of the BPC north module for the HERA run in 1995, 1996 and 1997.*

### Relative calibration of BPC

Since 1995 $^{60}$Co scans have been performed on each BPC section before the running period. This allows to determine assembly faults and is used for relative calibration. Therefore, the response for each readout channel has been integrated and used to adjust the HV of the photomultipliers using the gain measurements of the BPC photomultipliers. This allowed a first relative calibration at the level of approximately $\pm 7\%$.

### Comparison of $^{60}$Co signal responses

After each running period between 1995 and 1998 the BPC module north has been disassembled and $^{60}$Co scans have been repeated to evaluate the effect of radiation damages on the optical components of this module. The total accumulated dose during the HERA runs measured in the front inner brass tube of the BPC north module amounted to about 12 kGy in 1995, 10 kGy in 1996 and 2 kGy in 1997 (see Figure 9.5). The consequences of radiation damage in the BPC north module were determined using $^{60}$Co scans. For 1995 as well as for 1996, radiation damage was clearly identified which showed a position dependence as expected from the dose profile measurements. The scintillators which are closest to the beams or in the plane of the beams are expected to be most damaged. The comparison procedure is described below in detail, some exemplary results will be presented before: Figure 9.6 shows results of four $^{60}$Co scans of the $NX1$ and $NX5$ sections as well as the $NY9$ and the $NY13$ sections after the running period in 1995 (dashed line) in comparison to the reference $^{60}$Co measurements (solid line). One clearly notices the significant loss of light yield in the individual scintillator fingers towards the front of the BPC for the sections $NX1$ and $NY9$ in contrast to the sections $NX5$ with small variations and $NY13$, where no change is detected. Variations are almost no longer visible for the sections $NX7$ and $NY12$. Therefore it was decided to disassemble the BPC north module after the HERA run in 1995 and to investigate the response of individual scintillator fingers. The scintillator fingers were completely replaced. Also in 1996 irradiation effects on the BPC module north were detected by the $^{60}$Co monitor. The irradiation was smaller than

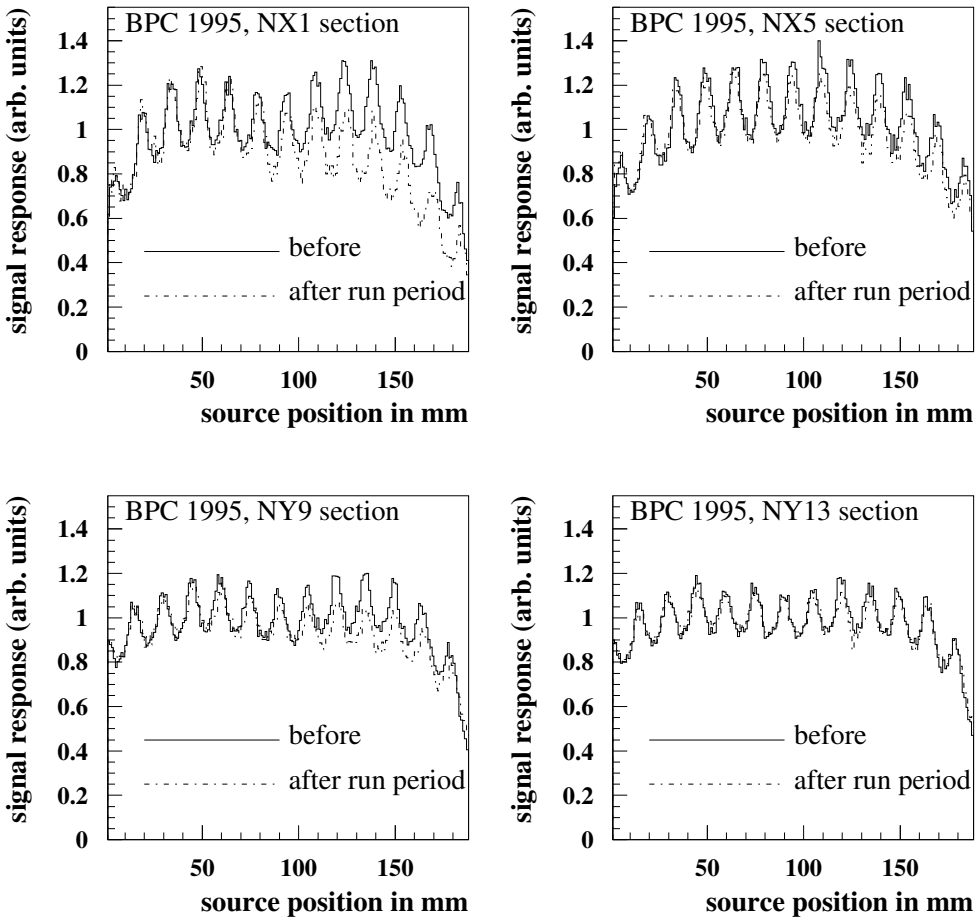


Figure 9.6: $^{60}$Co *scan of BPC north module before (solid line) and after (dashed line) the HERA run in 1995. The distance is measured with respect to the last scintillator finger ($z = 0$). The maxima on the right correspond to the scintillator closer to the interaction point. The last scintillator finger of the horizontal layers (bottom diagrams) were not completely reachable by the $^{60}$Co source, therefore the area of these signal responses is shorter.*

in 1995, but of the same order. No further stock existed for an exchange of scintillator fingers. Therefore the damaged BPC scintillators were exchanged for those undamaged ones of the running period 1995. The decision whether a scintillator finger is damaged or not was based on the $^{60}$Co comparison (described below). Since 1997 no significant irradiation has been detected by the $^{60}$Co monitor system (see Figure 9.7) anymore. In 1998 the BPC module south[2] was $^{60}$Co scanned for the second time. Corresponding to TLD measurements on this module no significant change of the signal responses has been measured.

In order to quantify the radiation damage one is interested in the decrease of light yield of individual scintillators measured in a $^{60}$Co scan. Two methods were applied to evaluate the ratio $Q_{ij}(^{60}\mathrm{Co})$ of the $i$th scintillator responses after/before the running period based on the $^{60}$Co scan on the $j$th section. Both methods will be described in the following to determine this quantity. The comparison of $^{60}$Co signal responses of the BPC follows the principles of the $^{60}$Co analysis described in Chapter 5.1: A $^{60}$Co signal response is the sum of the scintillator responses of the section. The individual response of a particular scintillator finger has been obtained by

[2]This module is less important due to a small event rate during the HERA runs.

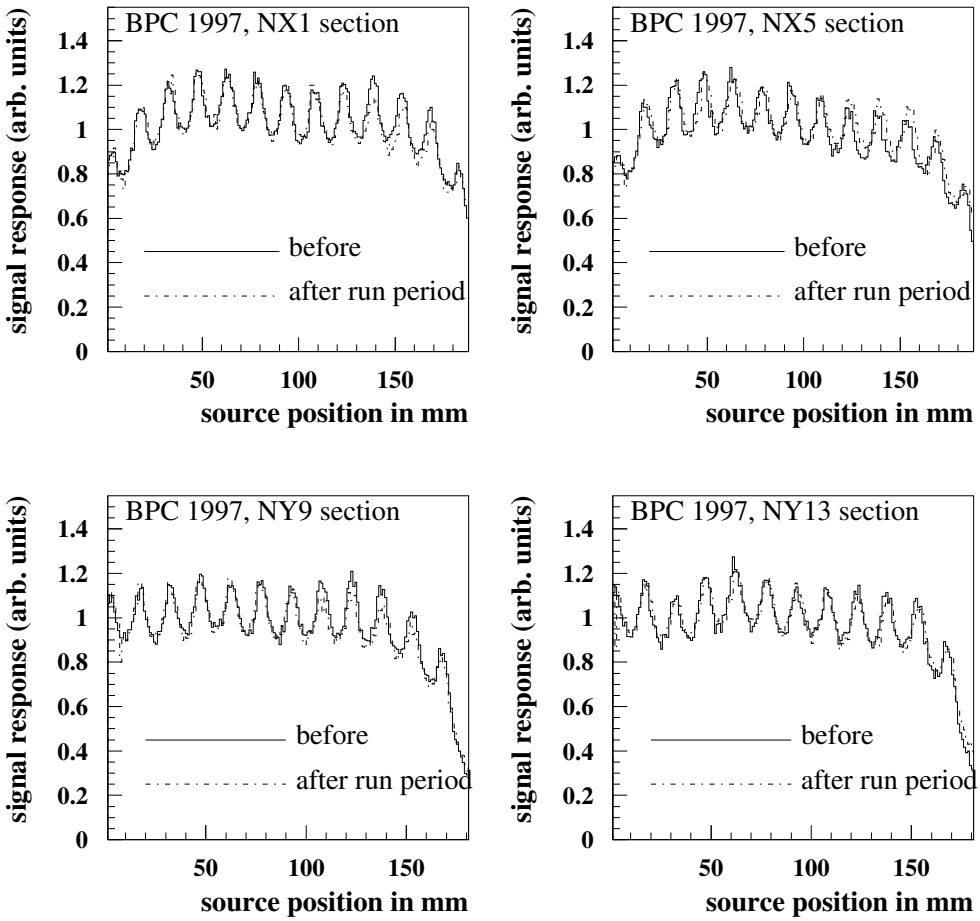


Figure 9.7: $^{60}$Co *scan of BPC north module before (solid line) and after (dashed line) the HERA run in 1997. No significant variation of the longitudinal structure of the sections is visible.*

integrating the $^{60}$Co signal response around the maximum in the signal response, i.e. from one minimum to the next around the maximum in the signal response. The obtained response is an approximation for the true scintillator response. A $^{60}$Co signal response provides 13 values, each associated to one particular scintillator. The mean response of the four furthermost scintillators with respect to the HERA beams of this signal response are used for normalization. This is justified, because no significant irradiation is expected for these scintillator fingers. The comparison between two normalized $^{60}$Co signal responses is to adjust them on each other based on the position calibration. The ratio of scintillator responses determined from two $^{60}$Co scans of the same section is expected to be unity providing that no radiation damage degraded the scintillator performance. This kind of comparison is based on the assumption that the integrated $^{60}$Co signal response around the respective maximum is equivalent to the response of a particular scintillator. In fact the $^{60}$Co signal response is the weighted sum of the response of all scintillators. In case of a BPC section the part of response which comes from the scintillator directly in front of the source is about 50% of the total signal, the adjacent scintillators contribute less than 14% [BO99b]. In order to get the amount of a single scintillator response the total $^{60}$Co signal response has to be unfolded. An unfolding procedure using the signal sharing obtained from the EGS4 Monte Carlo will be described briefly in the following. More details can be found in Chapter 5.1.3. The method depends on an iterative comparison

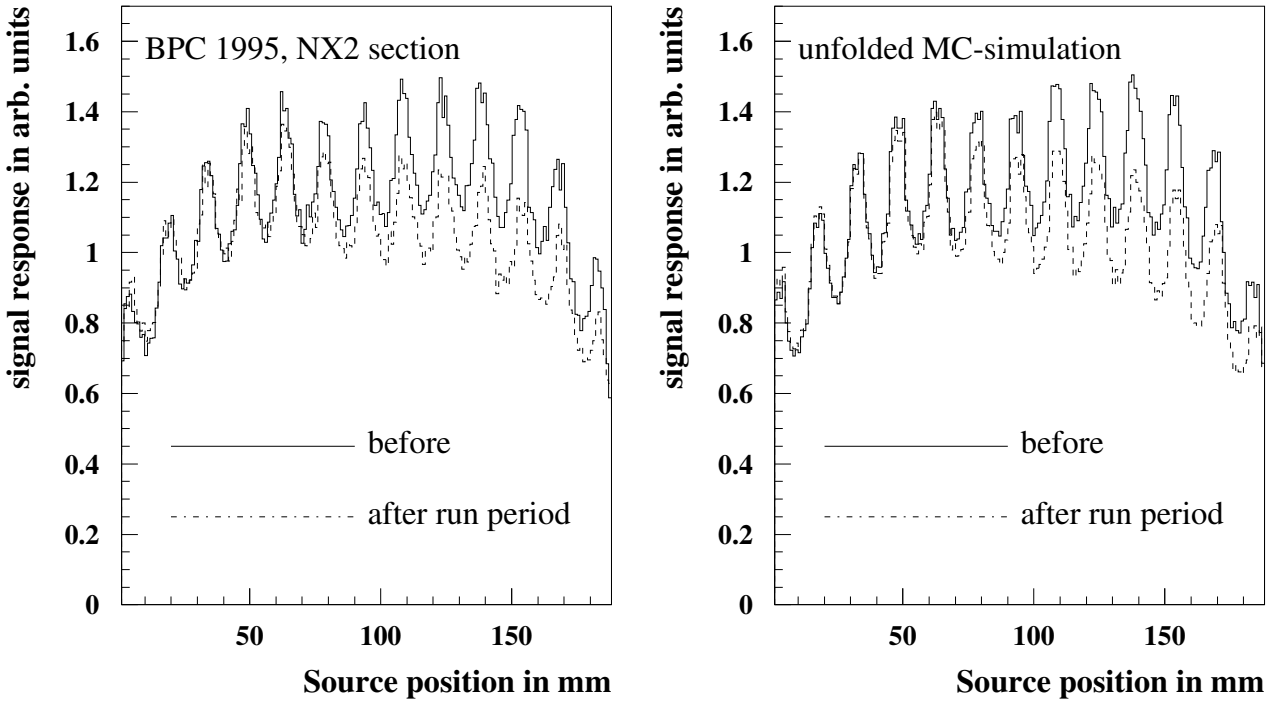


Figure 9.8: $^{60}$*Co signal responses of BPC north module before (solid line) and after (dashed line) the HERA run in 1995 (left diagram). The results of the* EGS4 *simulated signal responses after unfolding are shown in the right diagram. The mean of the four integrated scintillator responses furthermost from the interaction point is used for normalization.*

of a measured $^{60}$Co signal response with a simulated one in order to determine the weight factors $g_i$ for each scintillator. The simulated $^{60}$Co signal response is composed of the 13 single scintillator responses. Accordingly an unfolded $^{60}$Co signal response provides 13 weight factors of scintillators of a section. The comparison of two unfolded $^{60}$Co signal responses measured at different times allows to determine a possible relative variation of each scintillator. This comparison is expected to be more precise than the simple ansatz based on the ratio of the integrated scintillator responses. A test of the unfolding method is performed similar to the one described in Chapter 5.1.3 based on two well known weighted signal responses of the BPC from an EGS4 Monte Carlo. The relative error of the weight factors calculated by the unfolding procedure is usually less than 2%. Figure 9.8 presents two $^{60}$Co signal responses of the BPC module north of the second vertical section $NX2$ before and after the running period 1995 (left diagram) and the simulated responses after the unfolding (right diagram). Both the ratio of the integrated scintillator responses and the ratio of the weight factors of this section are shown in Figure 9.9. Values bigger than unity result from fluctuations due to the normalization using the mean of the integrated scintillator responses of the 10th to 13th scintillator. It is obvious that the ratio of the weight factors shows a more distinctive variation than the simple ratio of integrated scintillator response values with a maximum deviation from unity of about 20%. The $^{60}$Co signal responses of the BPC with regard to the running period from 1995 to 1997 were analyzed by the procedure described above. The diagrams in the left column of Figure 9.10 display the distribution of the ratio of integrated scintillator response values for the x-fingers (top) and y-fingers (bottom) of the BPC module north after the running period

1995; the diagrams in the right column show the ratio of the weight factors for these scintillator fingers. The ratios are distributed around unity denoting no variation for most of the scintillator fingers. The Gaussian curves with a standard deviation of $\approx 0.03$ resulting from fits on the distributions for values larger than 0.95 are included. Second distributions with a maximum at $\sigma \approx 0.93$ are clearly visible overlapping the Gaussian distributions. This difference from pure Gaussian distributions considers the variation of several scintillator fingers of the BPC within the running period 1995. In case of the most damaged scintillator ($NXA1$) the ratio of integrated scintillator responses $Q_{A1}(^{60}\mathrm{Co})$ yields a deviation from unity of about 30% and 40%, respectively. Indeed processing problems during the second $^{60}$Co scan on the $NX1$ section increased the statistical error of the signal response for the vertical scintillator *NXA1*, therefore the change of this scintillator response is overestimated. Figure 9.11 shows graphically (grey scale) the percent deviation of the integrated scintillator responses (left column) for the x-fingers (top) and y-fingers (bottom) of the BPC module north at the end of the running period 1995. The diagrams in the right column present the percent deviation of the ratio of the weight factors for the x-fingers and y-fingers. The results are corresponding to the non-uniform radiation dose profile[3] measured by the TLD's.

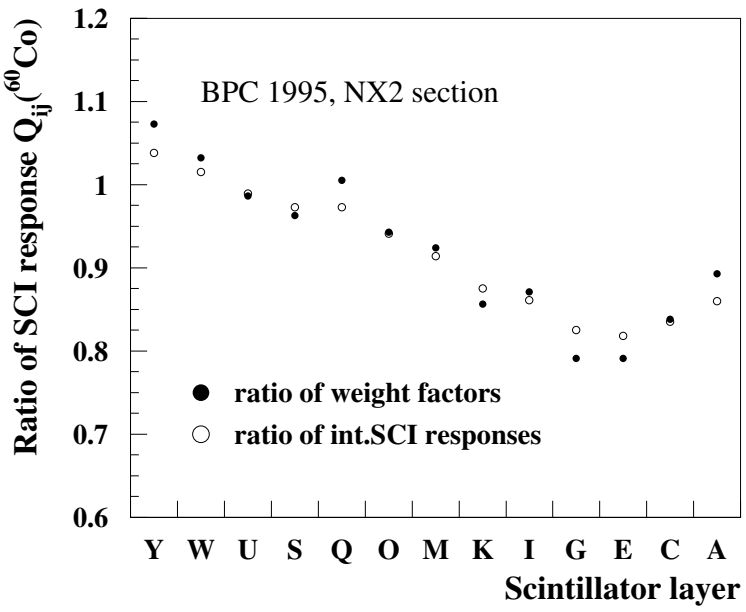


Figure 9.9: *The ratio of the integrated scintillator response values (blank circles) and the ratio of the weight factors of the scintillators (filled circles) of the $^{60}$Co signal responses is presented for each scintillator. The scintillator $NXA2$ of the section is closest to the interaction point.*

The ratio of the weight factors deliver a more distinct radiation distribution (also demonstrated in Figure 9.9) corresponding with a bigger percent deviation as calculated by the simple ratio of the individual integrated scintillator responses. The $^{60}$Co measurements have shown that 1995 several scintillator fingers were radiation damaged. It was therefore decided to rebuild the BPC module north after the 1995 HERA run and to exchange all scintillators. The monitoring procedures were repeated in 1996 and a smaller radiation dose was measured. A second exchange of the irradiated scintillators was performed. The ratio of the integrated scintillator responses was quoted to indicate the radiation damage and to decide whether a scintillator is damaged or not. A lower threshold for undamaged scintillators was set with $Q_{jk}(^{60}\mathrm{Co}) > 0.95$ corresponding to the FWHM of the Gaussian distributed ratios. Since 1997 the monitored radiation doses decreased by a factor 10. As it is demonstrated in section 9.4 this order of radiation damage effects on calibration and uniformity of the BPC can be neglected. Therefore no further new exchange of the scintillators of the BPC module north has been performed

[3]Dose profile measurements in 1996 using a $GS-218$ sample of $100 \times 100\,\mathrm{mm}^2$ in front of the BPC north module confirm these results [NE97].

since then. The $^{60}$Co analysis has well established, that the radiation damage in 1995 and 1996 was found to be increasing in direction of the positron beam from the first active layers towards approximately the maximum of energy deposition and then strongly decreasing.

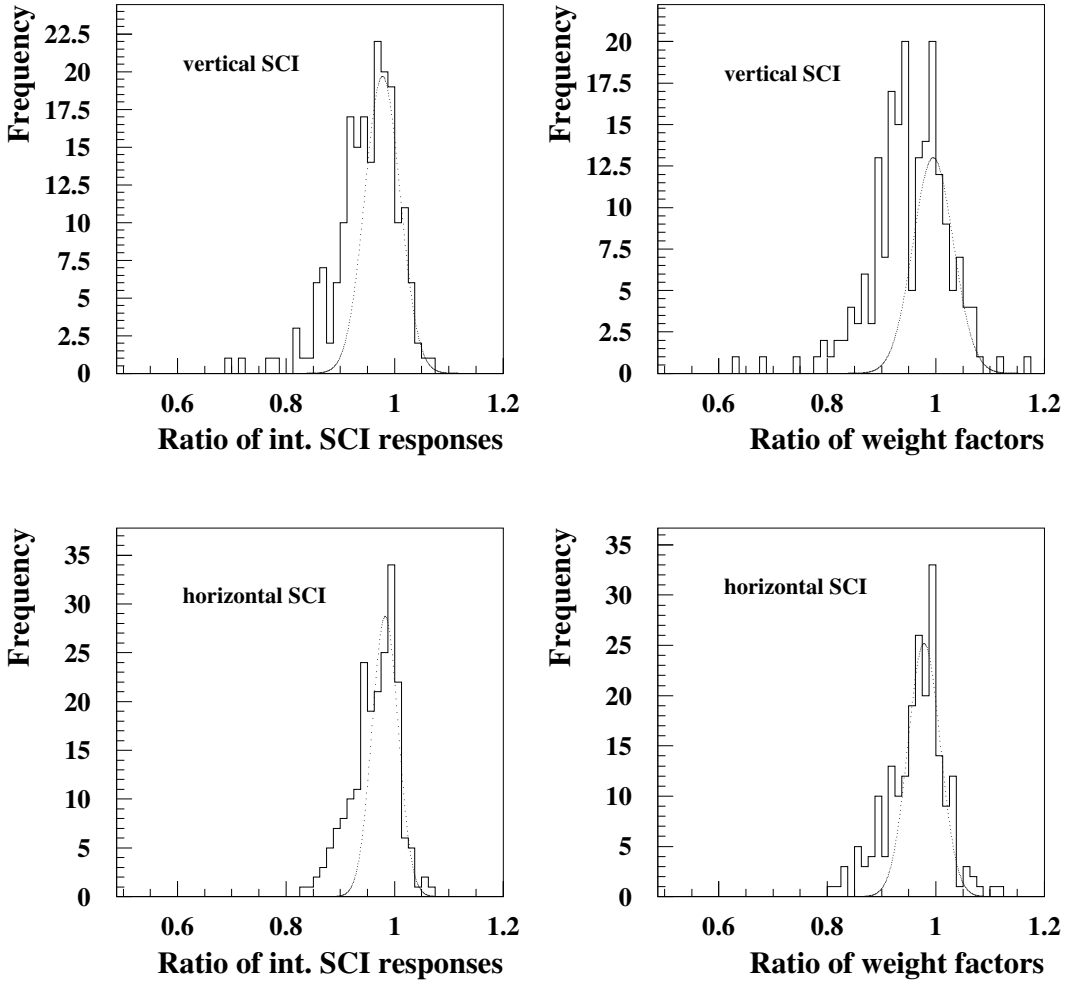


Figure 9.10: *Distributions of the ratios of the integrated scintillator responses (left diagrams) and of the weight factors (right diagrams) of all individual x-fingers (top) and y-fingers (bottom) in the BPC north module after the running period in 1995. Both the ratio of the integrated scintillator responses as well as the ratio of the weight factors should be unity, a deviation to smaller values is the evidence of a radiation damage or any other change of the scintillator responses.*

### 9.3.2 Investigations on single scintillators

Radiation damage in scintillator materials causes mainly two effects: The formation of new absorption centres results in an decrease of the attenuation length, while the destruction of fluor molecules results in a reduction of the primary light yield. Both effects were studied separately in order to determine the radiation dose. Single response measurements using a $^{106}$Ru source will show an overlapp of both effects. Due to the disassembling of the BPC in 1995 and 1996 it was possible to investigate systematically individual scintillators. The

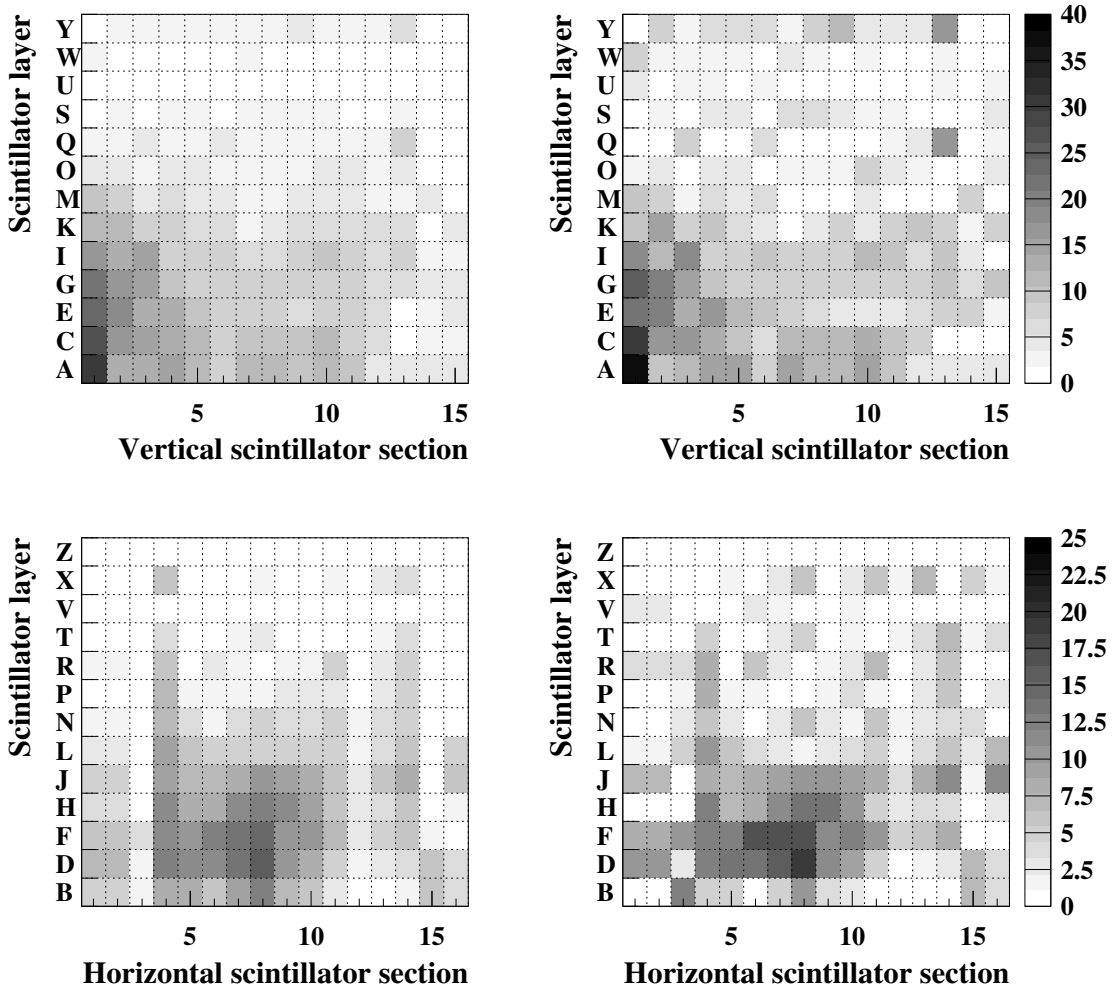


Figure 9.11: *Change of the scintillator response in percent of all individual x-fingers (top) and y-fingers (bottom) in the BPC north module after the run period 1995. The diagrams on the left present the ratio of the integrated scintillator responses. The right diagrams present the ratio of the weight factors resulting from the unfolding method.*

investigations have been performed using a scanning bench with different excitation forms (see Chapter 5.2.1). The following both investigations refer to a vertical scintillator of the 7th layer of the first vertical section, namely $NXG1$, which was one of the most irradiated ones of the BPC in the running period 1995.

### Reduction of primary light yield

In order to quantify the primary light yield emission of a scintillator finger, independent from other effects (e.g. the attenuation of scintillator light), one excites the surface of the scintillator finger which is directly readout by a wavelength shifter (*Y7*) guiding the light to a photomultiplier (*Hamamatsu Photonics R5600U-03*). A sketch of the measurement is shown in Figure 9.12 (c). Such a measurement has been performed using a $^{90}$Sr source on scintillator fingers of the BPC north after the running period 1995. Figure 9.13 shows the measured light yield as a function of the longitudinal source position $s$ of the scintillator $NXG1$. A significant reduction of the primary light yield in the middle of the scintillator finger has been observed.

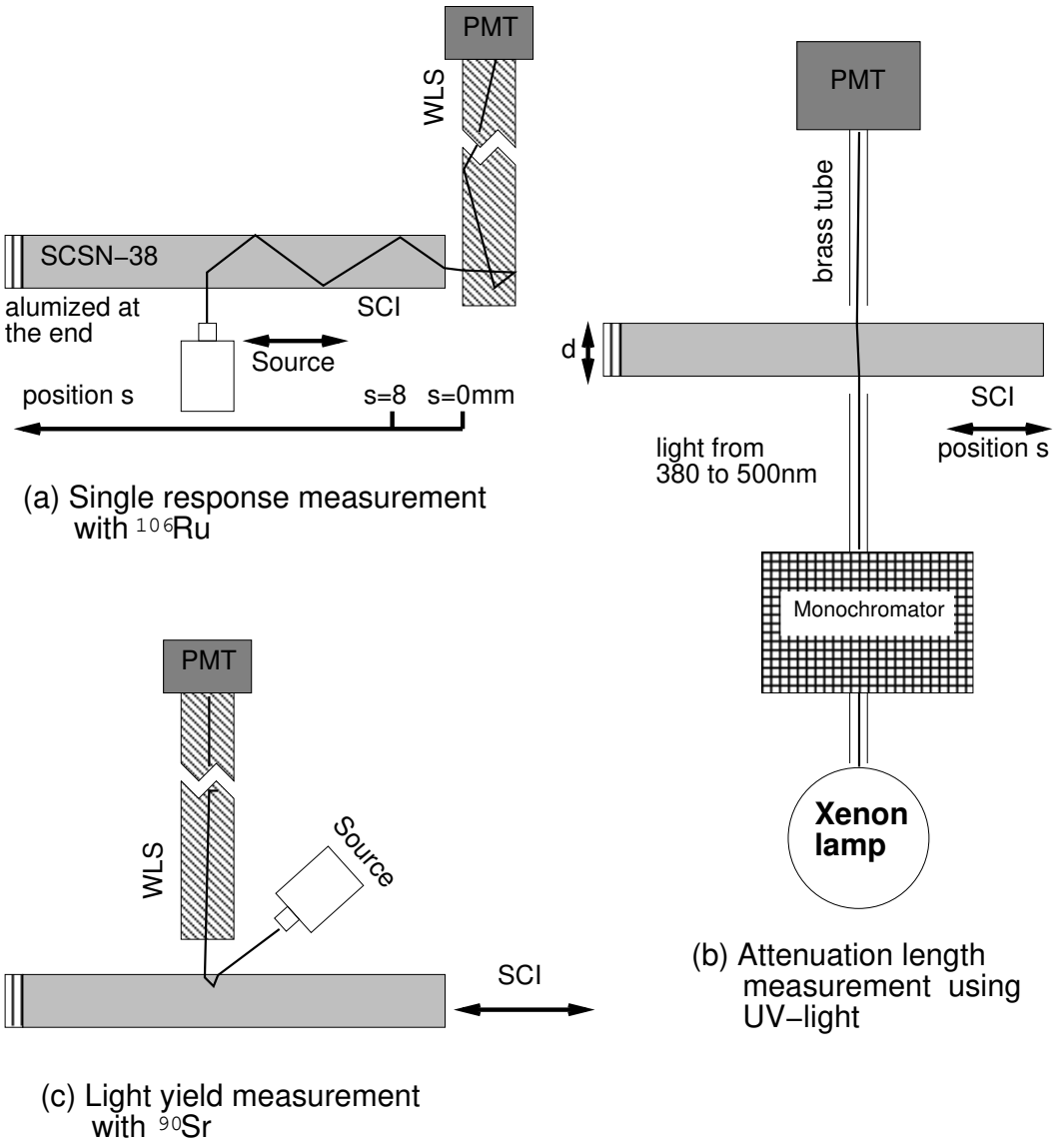


Figure 9.12: *Methods of measurements on individual scintillator fingers using the scanning bench with different excitation forms.*

This demonstrates the expected non-uniform structure of the radiation damage. The light yield distribution as shown in Figure 9.13 allows to estimate the dose distribution for this scintillator. The assumption is made that both scintillator finger ends have not been damaged. Introducing a position dependent radiation damage, the effective light yield follows the formulae 4.23 and 4.24:

$$\bar{I}(s) = \bar{I}_0(s) \cdot (1 - c \cdot D_{G1}(s)), \tag{9.1}$$

$$D_{G1}(s) = D_{G1} \cdot exp(-(s - s_o)^2/(2 \cdot \sigma_{G1}^2)). \tag{9.2}$$

The indices $G1$ denote the layer and the section of the scintillator, $c$ denotes the correlation between the radiation dose $D_{G1}(s)$ and the reduction of the primary light yield with $c = (9 \pm 1) \cdot 10^{-6} Gy^{-1}$ [DA96]. $D_{G1}(s)$ accounts for the Gaussian distributed radiation dose in s direction with a maximum $D_{G1}$, whereas it is assumed to be uniform over the width of 8 mm and the depth of 2.6 mm of the scintillator. This approach allows only a rough estimate of the

maximum radiation dose since the determination of the damage constant $c$ has been carried out with UV-light[4] instead of using electrons from a $^{90}$Sr source. From the light yield distribution in Figure 9.13 and the above two equations, the maximum radiation dose $D_{G1}$ has been estimated to be approximately 7 kGy.

### Absorption length measurements with UV-light

A wavelength dependent light transmission measurement as a function of the longitudinal scintillator position $s$ allows to determine the absorption coefficient $\Delta\mu(\lambda, s)$ of the scintillators. Figure 9.12 (b) illustrates the principle idea of the measurement. UV-light of a certain wavelength $\lambda$ passes vertically through the scintillator and produces a signal response $I(\lambda, s)$ of the photomultiplier (*Philips XP 2262B*), which is sensitive to UV-light. The measurement is repeated firstly without the scintillator finger to obtain a reference signal $I_o(\lambda, s)$, and secondly without UV-light to measure the pedestal $I_p(\lambda, s)$. This procedure is performed in steps of 0.5 mm along a scintillator finger. The wavelength $\lambda$ was varied in 5 nm steps in the range of 390 nm up to 490 nm. Figure 9.14 shows the result of the measurement of the scintillator finger $XG1$ after the running period 1995. The transmission $T(\lambda, s)$ is computed as follows:

$$T(\lambda, s) = \frac{I(\lambda, s) - I_p(\lambda, s)}{I_o(\lambda) - I_p(\lambda, s)} = T_o(\lambda, s) \cdot e^{-\Delta\mu(\lambda, s)\cdot d}, \tag{9.3}$$

$$\Delta\mu(\lambda, s) = \frac{1}{d} \cdot (ln(T_o(\lambda, s)) - ln(T(\lambda, s))), \tag{9.4}$$

where $\Delta\mu = {\lambda_{sci}}^{-1}$ is the radiation induced absorption coefficient, $d = 2.6$ mm the width of the scintillator finger and $T_o(\lambda)$ the transmission in the undamaged region. $\Delta\mu$ is negative at $\lambda < 410$ nm, accordingly the transmission increases at these wavelengths. This indicates that a part of the second dye BDB in *SCSN-38* was destroyed during irradiation. The maximum absorbed dose $D_{G1}$ at the position $s_o$ can calculated using the results given in [DA96]:

$$\Delta\mu(\lambda = 430nm, s_o) = b \cdot D_{G1} = 0.033cm^{-1}, \tag{9.5}$$

where $b = (2.0 \pm 0.2) \cdot 10^{-6} cm^{-1} \cdot Gy^{-1}$ [BI90]. $D_{G1}(s)$ accounts for the Gaussian distributed radiation dose. This procedure[5] yields a maximum dose of $D_{G1} \approx 16$ kGy.
Both calculations described above depend significantly on right assumptions for the radiation dose parameters $c$, $b(\lambda)$ and $\Delta\mu(\lambda, y_o)$. However, the calculation from the reduction of the primary light yield will possibly underestimate the radiation damage.

### Attenuation curve measurements

In order to examine the longitudinal signal response of a scintillator finger, a $^{106}$Ru source was moved parallel along a scintillator finger while the light yield was measured in the same configuration as in the BPC. Diagram (a) in Figure 9.12 demonstrates the principle of the measurement. The collimated electron beam causes a local energy deposition inside the investigated scintillator whereby a primary light yield is produced as a function of the beam position. The longitudinal scan over the scintillator allows to measure the attenuation curve of the latter. In order to calibrate both the beam position and the stepsize of the longitudinal scan

[4] The intrusion depth of UV-light into the scintillator material is smaller than the one of keV electrons. Therefore the damage constant $c$ will possibly underestimate the irradiation.

[5] The disadvantage of the calculation is that $\Delta\mu(\lambda, y_o)$ is rather small at $\lambda = 430$ nm.

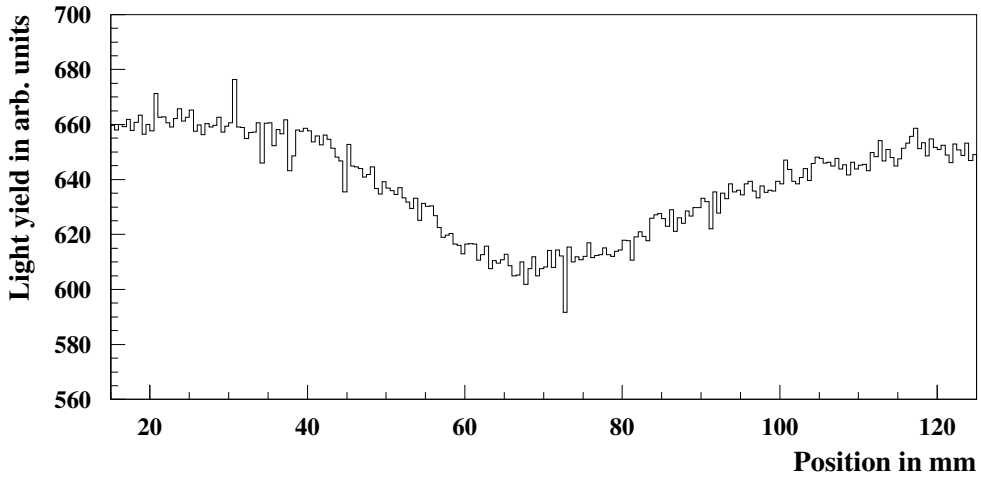


Figure 9.13: *The primary light yield produced by electrons in a damaged scintillator (NXG1) of the BPC north module as a function of the $^{90}Sr$ source position (corresponding to the y direction).*

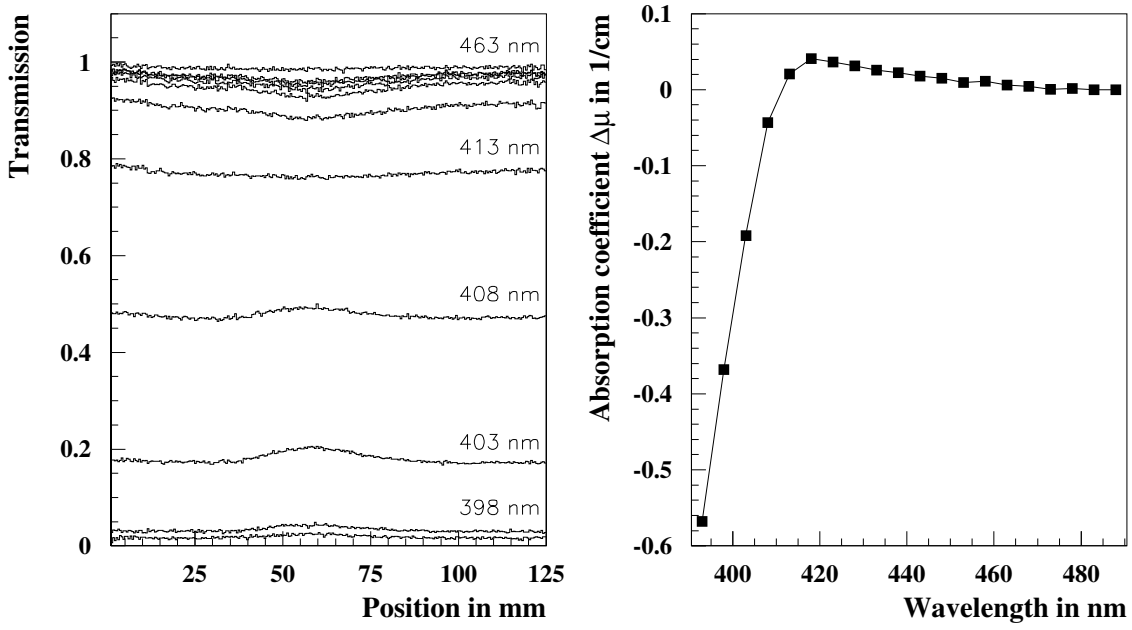


Figure 9.14: *Transmission (left) and radiation induced absorption coefficient $\Delta\mu$ (right) of a damaged scintillator (NXG1) as a function of the wavelength of the UV-light and the scintillator position.*

a calibration measurement is performed on a reference scintillator. Two thin steel sticks with a width of 2 mm are pasted on the surface of a reference scintillator. This leads to two minima in the longitudinal signal response due to electron absorption of the sticks. The knowledge of the distance between the sticks allows to calculate the beam position and the stepsize of the electron scan (see the left diagram in Figure 9.15). The stepsize was to be $0.5 \pm 0.02$ mm. The derivative of the attenuation curve at the end of the scintillator displays the electron beam profile of the source which was found to have a standard deviation of 3 mm (see the right diagram in Figure 9.15). The attenuation curve measurements have been taken on several x-fingers and y-fingers of the BPC module north after the running period 1995 and 1996. Figure 9.16 displays an overview of the scintillators (grey pads) of the BPC which were measured by $^{106}$Ru source scans after the running period 1995.

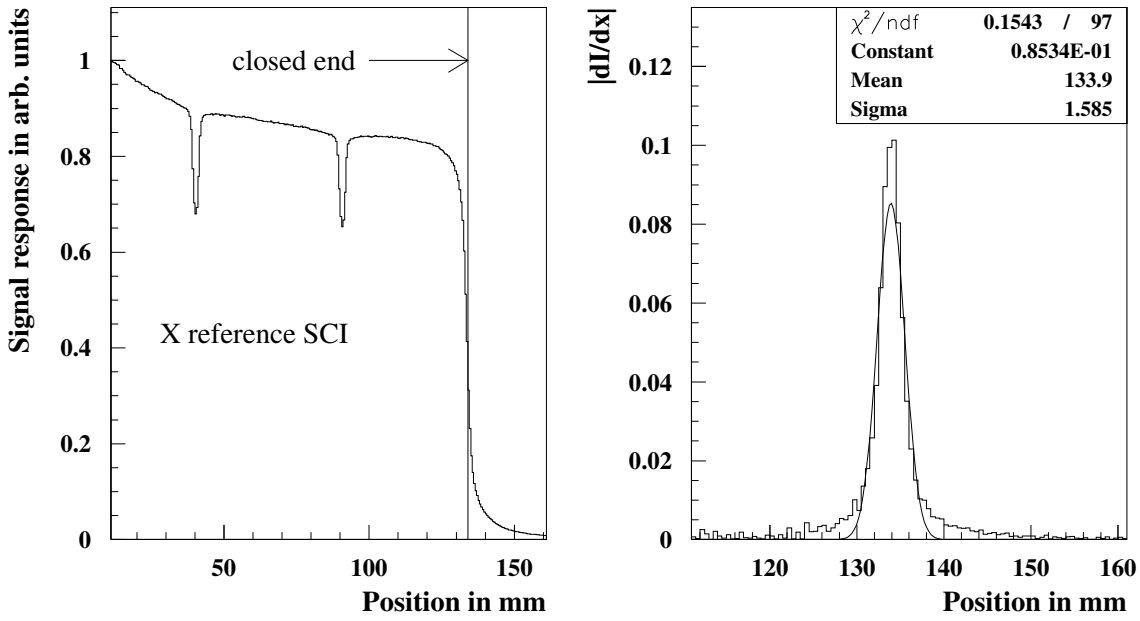


Figure 9.15: *Signal response due to electrons from a $^{106}$Ru scan on a reference scintillator (left). Two thin absorber sticks pasted in a certain distance on the surface of the scintillator allow a position calibration. The electron beam profile is presented by the derivative of the signal response at edge of the scintillator (right diagram).*

No absolute calibration of the $^{106}$Ru signal responses was performed. Therefore the attenuation curves of the scintillators have been normalized by a certain procedure using the $^{60}$Co comparison which will be briefly described below:
Let $I'_{ij}(s)$ be the measured signal response of the scintillator of the layer $i = A, B, ..., Z$ and of the section $j = 1, 2, ..., 16$. It is measured in arbitrary units. $s$ is the longitudinal position ($s = x$ for y-fingers and $s = y$ for x-fingers) and begins at the position $s \approx 8$ mm. The normalized attenuation curve has to agree with the results of the $^{60}$Co measurements. During a $^{60}$Co scan the $^{60}$Co source excites primary the edges of the scintillators[6]. Accordingly the main part of the signal response results from the light yield $I'_{ij}(\bar{s}_{edge})$ produced at the edge $\bar{s}_{edge}$ of the scintillator[7] closest to the $^{60}$Co source. Let $\hat{I}_{ref(j)}(s)$ be the mean signal of the rearmost four

[6] See also Chapter 5.1.2.

[7] In case of the x-fingers and y-fingers the mean incident position $\bar{s}_{edge}$ corresponds with the vertical and horizontal position at a distance of $\bar{y}_{edge} \approx 122$ mm and $\bar{x}_{edge} \approx 114$ mm.

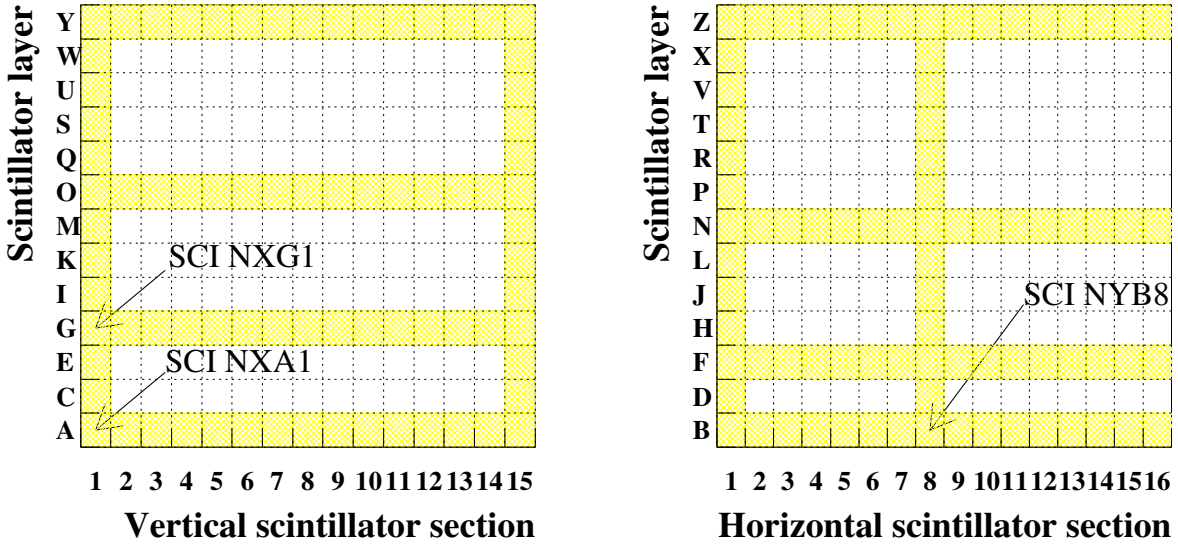


Figure 9.16: *Schematic overview of the vertical (left) and horizontal scintillators (right) installed in the BPC module north. The grey pads indicates the scintillator fingers which have been examined by electrons of a $^{106}Ru$ source after the running period 1995. The scintillator fingers $NXA1$ and $NYB8$ are closest to the HERA beams.*

scintillators[8] from the HERA beams of the same section, which is normalized to unity at the open end:

$$\hat{I}_{ref,j}(s) = \frac{I'_{ref,j}(s)}{I'_{ref,j}(s = 8\,\mathrm{mm})}. \tag{9.6}$$

Then the ratio of the normalized attenuation curves at the edges of the scintillator $i$ and the reference ones has to be equivalent to the result from the $^{60}$Co comparison. This yields the normalization:

$$\hat{I}_{ij}(\bar{s}_{edge}) \;=\; \hat{I}_{ref,j}(\bar{s}_{edge}) \cdot Q_{ij}(^{60}\mathrm{Co}). \tag{9.7}$$

$Q_{ij}(^{60}\mathrm{Co})$ denotes the ratio of the $i$th scintillator response of the $j$th section measured after and before the running period (see Figure 9.9). Based on the applied method it is either the ratio of the integrated scintillator responses or the ratio of the weight factors. Figure 9.17 presents the results of $^{106}$Ru scans on scintillators of the 1st to 10th scintillator layer of the BPC module north after the running period 1995. In the top diagrams the attenuation curves of the vertical scintillators (left) from the 1st and 5th section (right) are shown. In the bottom diagrams of Figure 9.17 the attenuation curves of the horizontal scintillators (left) from the 4th and 8th section (right) are shown. The 1st section of x-fingers and the 8th section of y-fingers are closest to the HERA beams. Horizontal arrows indicate the location of the fiducial volume of the BPC module north. The amount of radiation damage increases towards the beam pipe edge of the BPC and the central position of the BPC associated with a characteristic loss of light yield. Therefore the radiation dose is concentrated in the middle of the x-fingers and at the edges of the y-fingers. The scintillator response due to the $^{60}$Co excitation of the radiation

[8] Whose mean signal is also used to normalize the $^{60}$Co signal responses.

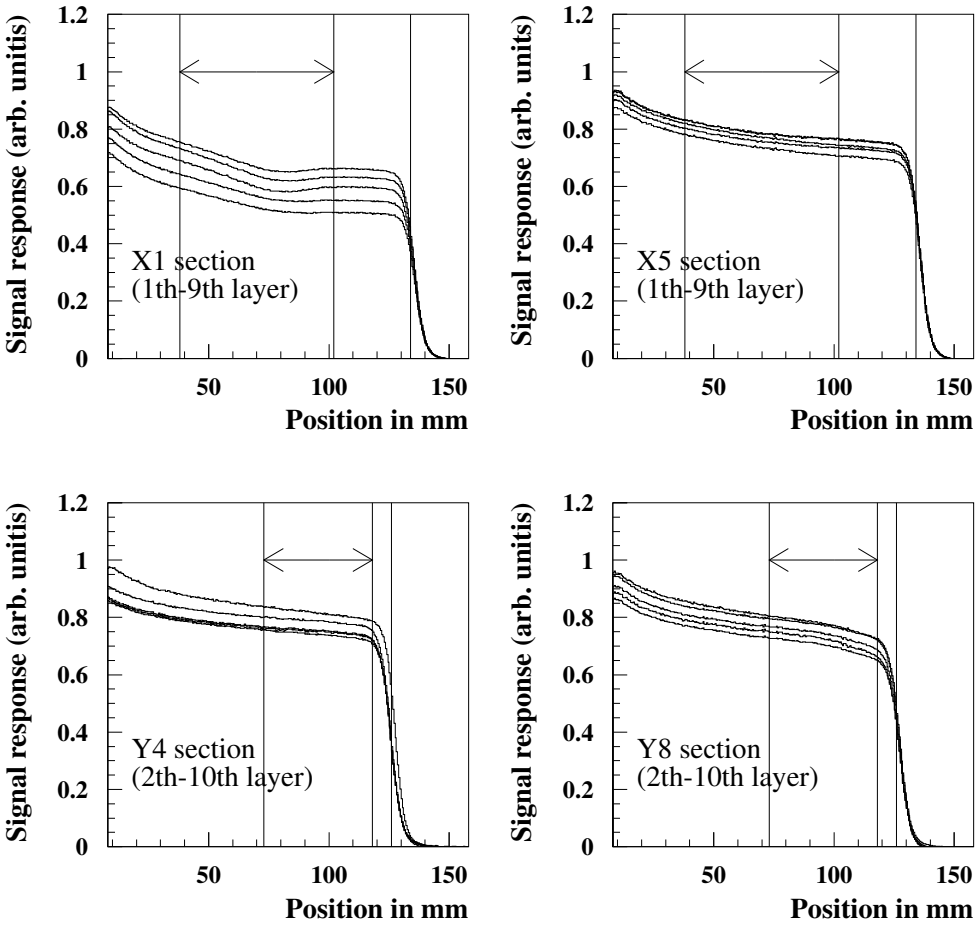


Figure 9.17: *Scans of individual vertical (top) and horizontal (bottom) scintillator fingers of the BPC module north with electrons ($^{106}Ru$) after the HERA run in 1995. The arrows indicate the fiducial volume of the BPC.*

damaged edge of a y-finger is degraded by both a reduction of the primary light yield and a change in the transmission of the scintillator. Therefore the ratio and the relative weight factor of a particular y-finger (with $i = B, D, ...Z$ and $j = 1, 2, ..., 16$)) is proportional to:

$$Q_{ij}(^{60}\mathrm{Co}) \propto (1 - c \cdot D_{ij}(s)) \cdot e^{-b \int_0^{\bar{L}} D_{ij}(s) ds}. \tag{9.8}$$

In case of x-fingers (with $i = A, C, ...Y$ and $j = 1, 2, ..., 15$) whose edges are more or less undamaged hence equation 9.8 reduces to:

$$Q_{ij}(^{60}\mathrm{Co}) \propto e^{-b \int_0^{\bar{L}} D_{ij}(s) ds}. \tag{9.9}$$

$D_{ij}(s)$ is assumed to be Gaussian distributed in the longitudinal direction of the scintillators along the mean path length $\bar{L}$, whereas it is assumed to be uniform over their width of 8 mm and their depth of 2.6 mm.
Light, produced at the edges of the scintillators traverses in case of a Gaussian distributed radiation dose with a standard deviation of 21 mm and a maximum of 1 kGy an integrated radiation dose of 52 kGy·mm and 31 kGy·mm during the passage from one end of the scintillator

to the other. This leads to a ratio of scintillator responses $Q_{ij}(^{60}\mathrm{Co}) \approx 0.97$ which is is still within the Gaussian distributed ratios of undamaged scintillator responses as demonstrated in Figure 9.10. Accordingly the radiation dose of about 1 kGy is the lower detection threshold of the $^{60}$Co monitor system for the BPC. It was found that the loss of light yield increases from the 1st active layers towards approximately the shower maximum and then quickly decreases to the case of a reference sample (see Figure 9.9). This underlines that the radiation damage has to be associated with high energetic positrons, which have been found to be most likely resulting from the dump and accidental losses of positrons within HERA. This behavior follows the expectations from the dose profile measurements and $^{60}$Co measurements.

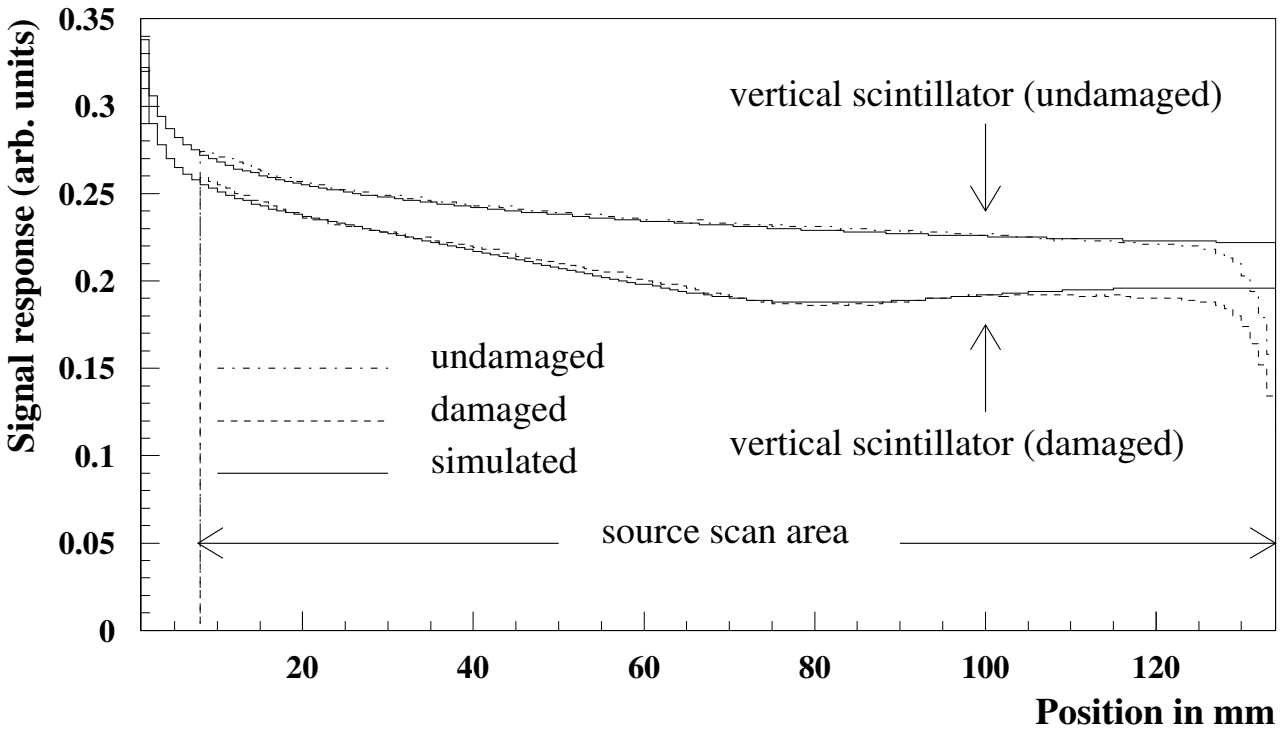


Figure 9.18: *Simulated responses in comparison with single response measurements using electrons of a $^{106}$Ru source of a damaged (NXG1) and undamaged x-finger. The strong decrease of the measured curves at a distance of 130 mm results from the spread of the electron beam.*

### 9.3.3 Simulation of attenuation curves

To understand a strongly localized, non-uniform damage within a scintillator finger a detailed wavelength dependent quantitative understanding is demanded: The loss of light yield or the change in the attenuation coefficient alone does not allow to describe the observed light yield behaviour. It is the effect of both, which have to be taken into account to provide a proper description. A numeric simulation has been developed using this ansatz which allows to compute the attenuation curves of scintillator plates with a radiation damage (see Chapter 4.4). Let $D_{ij}(s)$ the radiation dose which depends on the longitudinal direction on the position $s$. The numerical simulation Lightsim considers the light propagation through the scintillator fingers and integrates over the wavelength and fluorescense spectrum and all effective angles. It takes into account the non-uniform dose profile $D_{ij}(s)$, determined from $^{106}$Ru measurements, the

reduction of primary light yield $I(\lambda, s)$ as a function of dose, and the change of the absorption coefficient $\mu(\lambda, s)$ due to the formation of absorption centres/destruction of dyes. Light reflection effects at all sides of the sample are included. Figure 9.18 shows the comparison of simulated scintillator responses and single response measurements using electrons of a $^{106}$Ru source of a damaged and an undamaged x-finger. These measurements refer to the scintillator $XG1$ and a reference of the BPC module north after the running period 1995. The simulated attenuation curves agree very well with the single response measurements. The optimal fit between measurement and simulation of the attenuation curve of the scintillator finger $XG1$ is performed assuming a 3 kGy radiation dose of the scintillator and a Gaussian distributed 10 kGy irradiation in its middle (corresponding to $y = 73$ mm) with a standard deviation of 21 mm.

## 9.4 Effects due to radiation damage

The most severe radiation damage effects occurred to the BPC module north during the running period 1995. The loss of light yield for scintillator fingers close to the beam pipe edge have been observed as well towards the end of the 1995 run in data using a kinematic peak (KP) sample. The final reconstructed energy $E_x$ as a function of the position $y$ within the fiducial volume showed as well a similar shape as the one shown in Figure 9.4, [SU98]. After the relative section-to-section calibration, the uniformity of the energy response across the whole fiducial volume for this running period is within $\pm 0.5\%$. For 1997 the uniformity of the energy response was improved to 0.3% [FR99]. A study of the linearity of the BPC is required in the evaluation of the systematic uncertainties in the analysis of the 1997 BPC data. In order to determine the radiation effects on linearity the degradation of the scintillators have been incorporated into an EGS4 Monte Carlo simulation by weighting the energy deposition of each shower particle inside the scintillator with the position dependent calorimeter response. This has been done for the BPC module north with respect to the running period of 1995 and 1997 implementing measured and simulated scintillator responses into an EGS4 simulation. This will be briefly summarized below:

### 9.4.1 Reconstruction of the calorimeter response

The precondition for the evaluation of radiation damage effects on the BPC is the determination of the calorimeter response. The attenuation curves of the scintillators have been determined from electron scans of individual scintillator fingers (see section 9.3.2) and from the light simulation (see section 9.3.3) with regard to the running period 1995 and 1997.

#### BPC response after the running period 1995

Due to the disassembling of the BPC after the running period 1995 it was possible to investigate systematically individual scintillators. Individual $^{106}$Ru scans have been performed on 40 % of all BPC scintillator fingers. Figure 9.16 presents the measured scintillator fingers (grey pads) of the BPC after the running period 1995. The attenuation curves of the scintillators which have not been measured are linearly interpolated by the curves of measured scintillator fingers from adjacent sections. The attenuation curves of the scintillators have been normalized using the information of the $^{60}$Co comparison (see section 9.3.2). Some measurements allow a cross check comparing the measured attenuation curves with the interpolated ones.

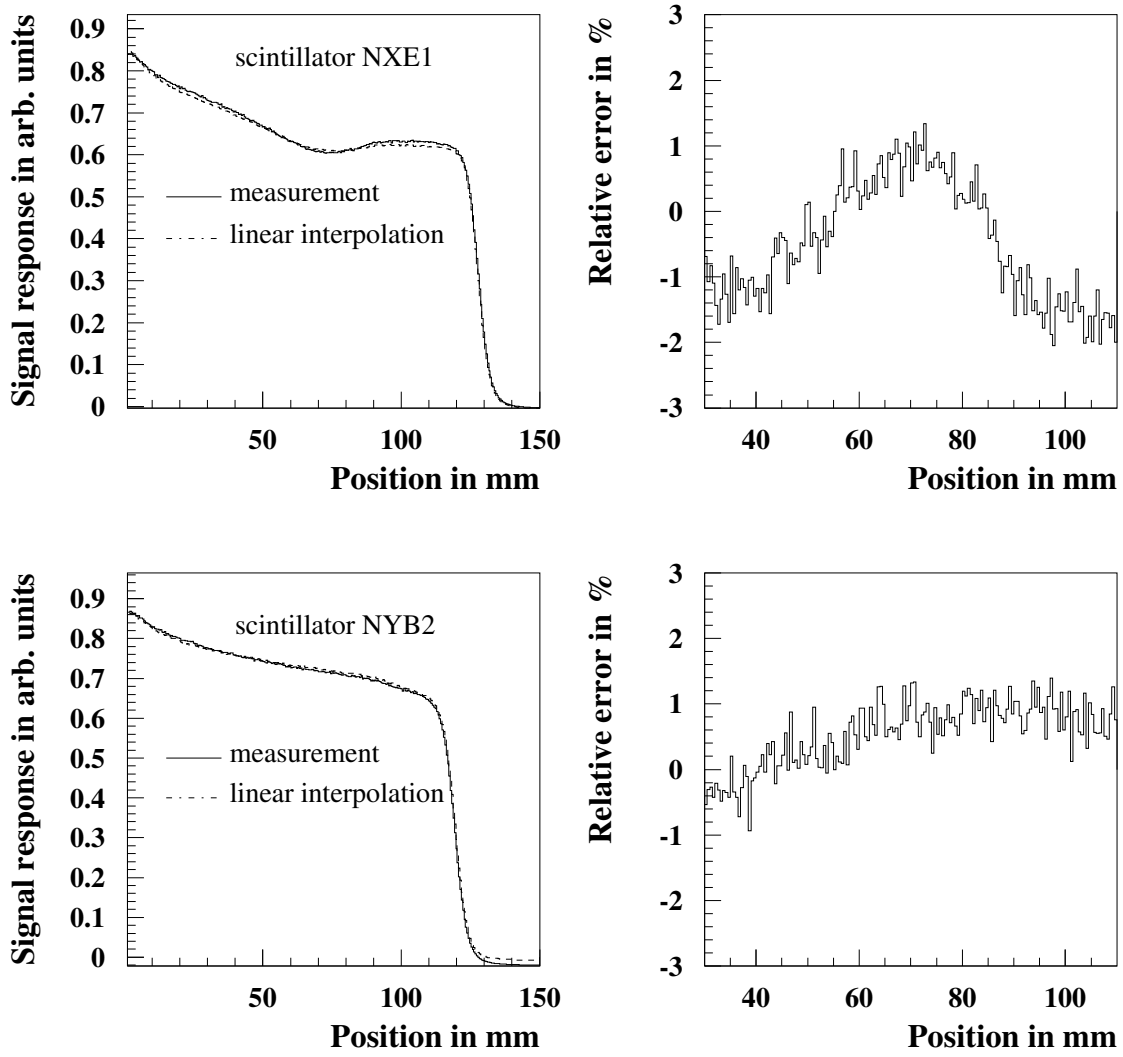


Figure 9.19: *Comparison of measured attenuation curves with linear interpolated ones determined from measurements of adjacent scintillators fingers (left diagrams). The curves refer to the scintillator NXE1 (top) and NYB2 (bottom) of the BPC module north after the running period 1995. The relative errors are in the order of maximal* $\pm 1\%$ *(right diagrams).*

The left diagrams in Figure 9.19 display the measured attenuation curves of a x-finger (top) and a y-finger (bottom) in comparison with the linear interpolated ones from adjacent scintillator fingers. The relative error between the measurements and the interpolation is found to be in the order of $\pm 1\%$ (right diagrams).

### BPC response after the running period 1997

After the running period 1997 the irradiation dose of the BPC was in the order of a few kGy. No further reinstallation was performed, so that no individual scans on scintillators were possible. However, an evaluation of the BPC response after the running period 1997 was of vital interest, especially with regard to the decision about usages in the future. Therefore the attenuation curves of the BPC scintillators have been simulated with respect to the running period 1997 based on the results of the $^{60}$Co data. The numerical simulation program lightsim calculates the

attenuation curves of the scintilliators using the irradiation of each scintillator determined by the comparison of $^{60}$Co data before and after the running period. The assumption is a similar Gaussian distributed irradiation profile of the BPC as measured after the running period 1995. The position dependent radiation dose $D(x,y,z) \approx D_{ij}(s)$ for each scintillator finger along the longitudinal direction was determined from the ratio $Q_{ij}(^{60}\mathrm{Co})$ of the scintillator responses. $Q_{ij}(^{60}\mathrm{Co})$ can be obtained in a first approximation by integrating the measured signal response of the $^{60}$Co scan around the maximum of the scintillator, or in a more specified procedure by the ratio of the weight factors resulting from the unfolding. The ratio of the scintillator responses is related with the radiation dose deposited inside the scintillator by equation 9.8 and 9.9. The evaluation of the radiation dose for a certain ratio of the scintillator responses is based on the comparison of measured and simulated attenuation curves of the running period 1995. For the ratio $Q_{ij}(^{60}\mathrm{Co}) = 0.7$ of the vertical scintillators the maximal radiation dose $D_{ij} = 10\,\mathrm{kGy}$ was found. For the horizontal scintillators the same radiation dose was found for the ratio $Q_{ij}(^{60}\mathrm{Co}) = 0.8$. Then a linear relation between radiation dose $D_{ij}$ and the ratio $Q_{ij}(^{60}\mathrm{Co})$ of a certain scintillator finger $i$ of the section $j$ is assumed by:

$$D_{ij} = \frac{10\,\mathrm{kGy} \cdot (1 - Q_{ij}(^{60}\mathrm{Co}))}{1 - Q_{10kGy}}. \tag{9.10}$$

$$Q_{10kGy} = \begin{cases} 0.7 & : \text{ in case of x-finger.} \\ 0.8 & : \text{ in case of y-finger.} \end{cases} \tag{9.11}$$

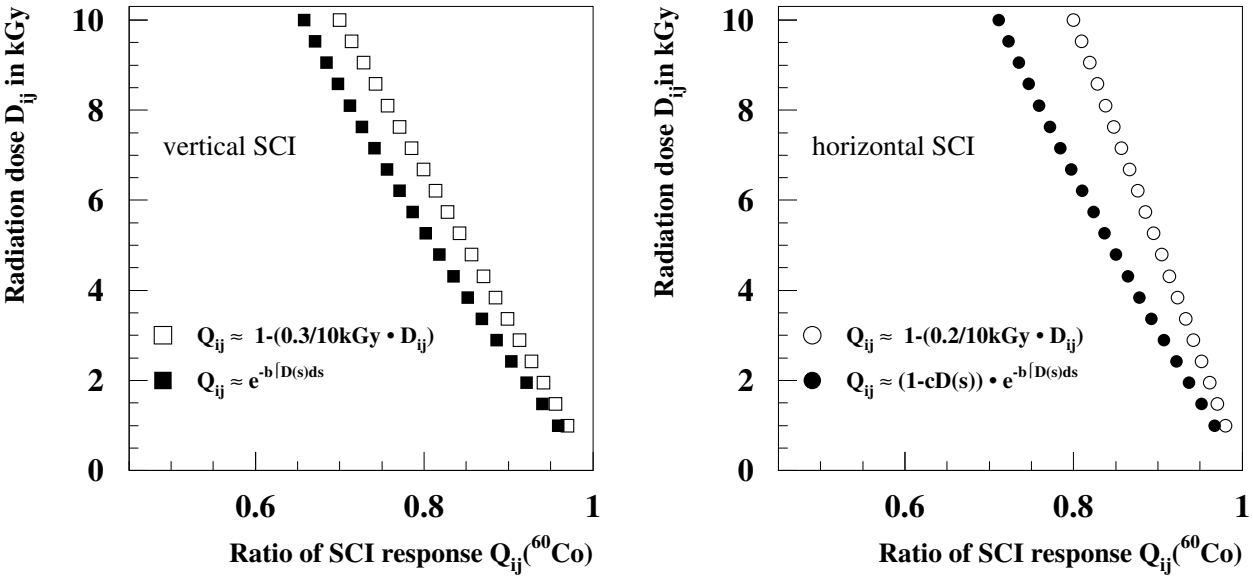


Figure 9.20: *The radiation dose as a function of the ratio of the scintillator responses for the x-fingers (squares) and the x-fingers (circles) based on the linear ansatz (empty symbols) and the exponetial ansatz (filled symbols).*

Figure 9.20 demonstrates the relation between the ratio $Q_{ij}(^{60}\mathrm{Co})$ and the radiation dose $D_{ij}$ for x-fingers (left diagram) and y-fingers (right diagram) based on equation 9.8, 9.9 and 9.10.

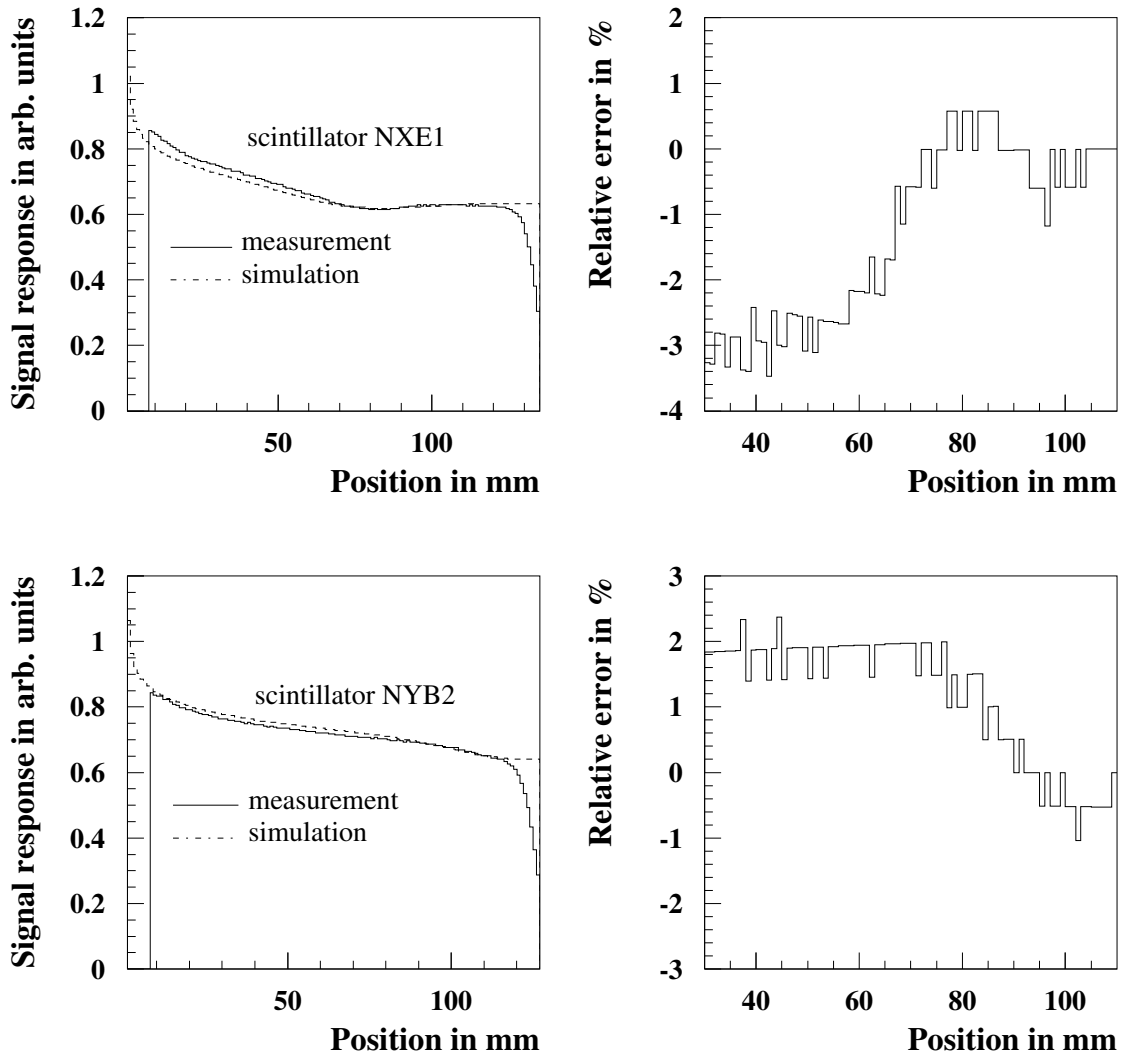


Figure 9.21: *Comparison of measured attenuation curves with simulated ones from the exclusive $^{60}Co$ comparison (left diagrams) of the scintillator NXE1 (top) and NYB2 (bottom) of the BPC module north after the running period 1995. The relative errors are in the order of maximal 3% (right diagrams).*

In order test the validity of the linear relation between the radiation dose $D_{ij}$ and the ratio of scintillator responses $Q_{ij}(^{60}\mathrm{Co})$ all the measured attenuation curves of the running period 1995 were compared with simulated ones. The simulation of the attenuation curves were determined from the numerical calculation based on the exclusive knowledge of the radiation dose resulting from equation 9.10. The curves were normalized with respect to the $^{60}$Co comparison. Figure 9.21 displays individual measured attenuation curves (left diagrams) of the running period 1995 and the simulated ones. The relative error (right diagrams) within the fiducial volume is found to be at most $\pm 2\%$. This confirms as well as the attenuation curves in Figure 9.18 that the assumption of a linear relation from equation 9.10 is valid.
Moreover the ratio of $^{60}$Co signal responses before and after the BPC running period 1997 was found to be greater than 0.9, which suggests less radiation damage than after the running period 1995. Therefore it is sufficient for the running period 1997 to assume the linear relation. In addition to the non-uniform irradiation a uniform radiation dose of 3 kGy is assumed for

the section $NX1$ closest to the HERA beams[9]. The linear ansatz will clearly overestimate the radiation damage effects with respect to the running period 1997 and thus result in an upper limit for the non-linearity effects on the BPC energy calibration.
Figure 9.22 shows the radiation dose in kGy of all x-fingers (left diagram) and y-fingers (right diagram) in the BPC North module after the running period 1997 calculated with equation 9.10. The amount of radiation damage is in the order of less than 2 kGy with a maximum of 5 kGy and varies in the order of 1-2 kGy from finger to finger which denotes the error of the radiation dose determination. These results clearly overestimate the expectations from the dose profile measurements. The knowledge of the radiation dose distribution allows to simulate the

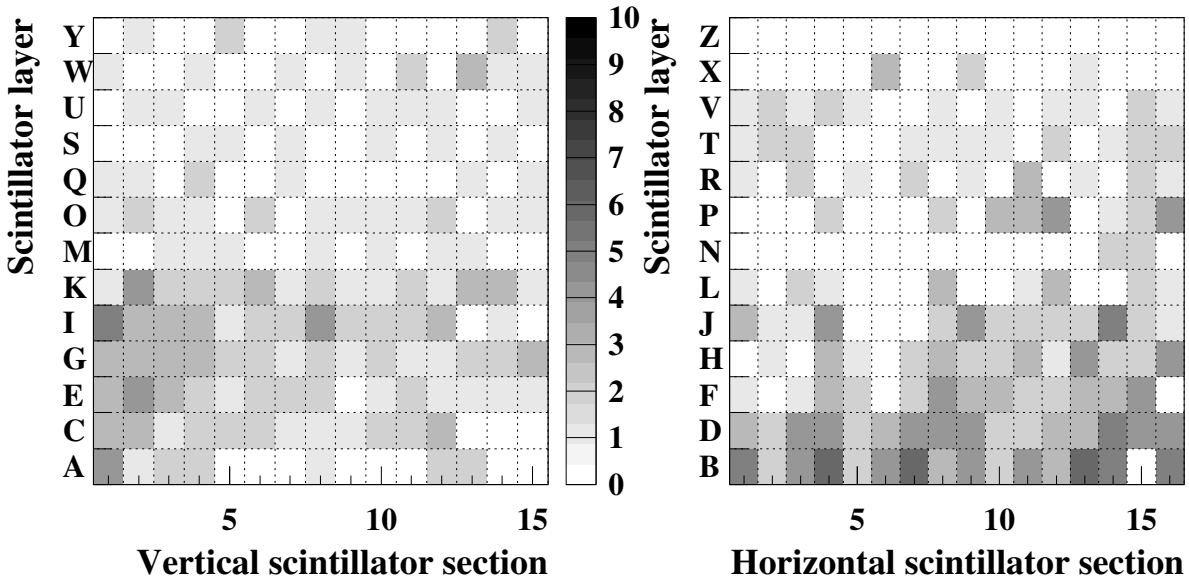


Figure 9.22: *Radiation dose in kGy of individual x-fingers (left) and y-fingers (right) in the BPC North module after the HERA running period 1997 based on the comparison of $^{60}Co$ signal responses.*

attenuation curves for each scintillator fingers. Figure 9.23 presents results of the simulated attenuation curves of the x-fingers (top) between the 1st and 9th scintillator layer from the 1st section which is closest to the HERA beams (left) and the 5th section (right). The bottom diagrams of Figure 9.23 displays the case for y-fingers between the 2th and 10th scintillator layer from the 8th section which is closest to the HERA beams (right) and the 4th section (left), see also Figure 9.17.

### 9.4.2 Linearity of energy calibration

The EGS4 simulation of the BPC was used to estimate the effects of the irradiation on the linearity of the BPC after the running period 1995 and 1997. In Figure 9.24 is shown the reconstructed energy in the BPC module north for energies of 5, 10, 15, 20, and 27.5 kGeV from the simulation for the running period 1997. Figure 9.24 displays the linearities from EGS4-MC-simulations with respect to the BPC module north after the running periods 1995 and 1997

[9]It has been found, that the simulated $NX1$ scintillator responses of 1995 show the best agreement with the measured ones assuming both an uniform 3 kGy radiation dose and a Gaussian distributed irradiation with a standard deviation of 21 mm.

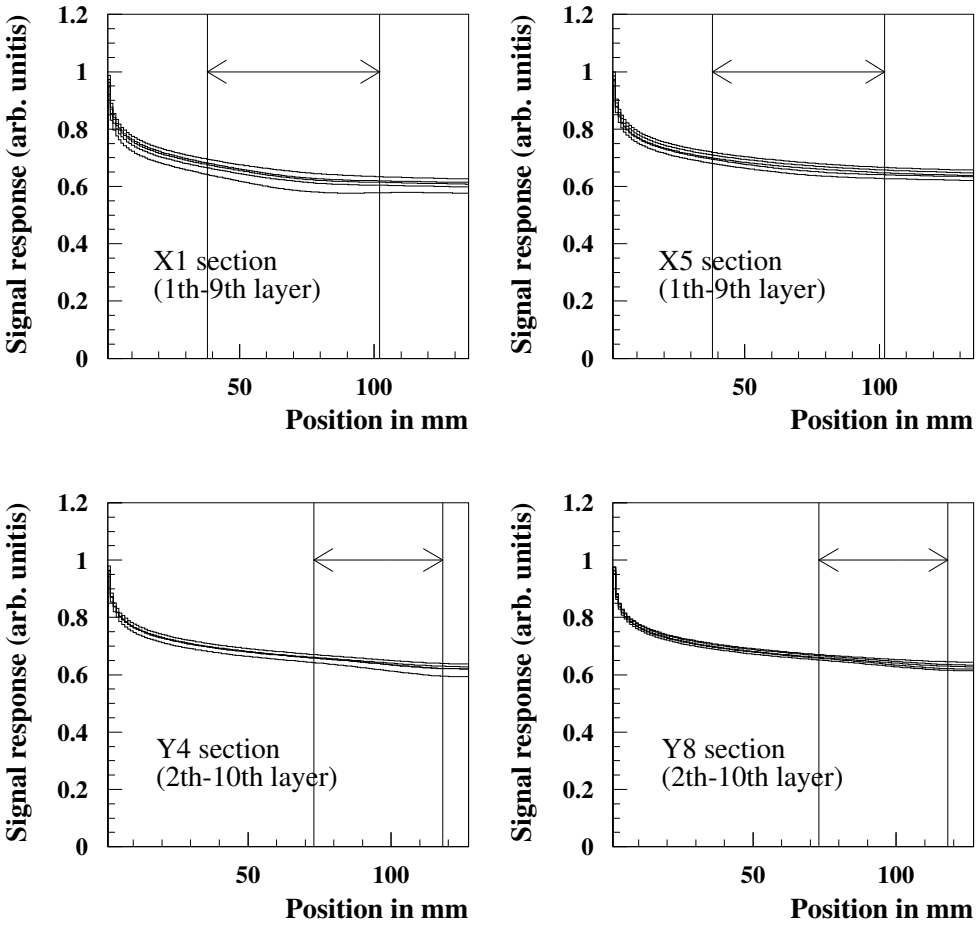


Figure 9.23: *Simulated attenuation curves of individual scintillator fingers from the BPC North module after the HERA run in 1997.*

in comparison with an undamaged reference module. For the latter the reference attenuation curves as determined from unirradiated scintillators are used for each x-finger and y-finger. The straight line in Figure 9.25 (left) is drawn through the reconstructed energy at 27.5 GeV and the origin. This refers to the actual energy scale calibration using kinematic peak events. Figure 9.25 (right) shows the deviation from this straight line as a function of the impact energy which in case of an undamaged BPC module north is less than 0.5 %. This is in good agreement with testbeam measurements at DESY of the BPC before installation in 1994 [MO98]. The worst case is given by the irradiation of the BPC module north after the running period 1995. For this case two MC-simulations have been done. The optimistical ansatz uses the simple ratio of integrated scintillator response values of the $^{60}$Co scans (blank triangle), while the more severe assumption uses the ratio of the weight factors of the scintillators determined from the unfolded $^{60}$Co signal responses. This yields a deviation less than 1% from linearity for energies above 8 GeV and 14 GeV. In case of the running period 1997 the deviation is less than 1% for energies above 4 GeV (filled circles). This is in good agreement with an estimate of the non-linearity at 16 GeV using QED Compton events [Mo98a]. A fit of the form $\propto \ln(E)$, indicated by the solid lines in Figure 9.25 (right), provides a good description of the deviation from linearity.

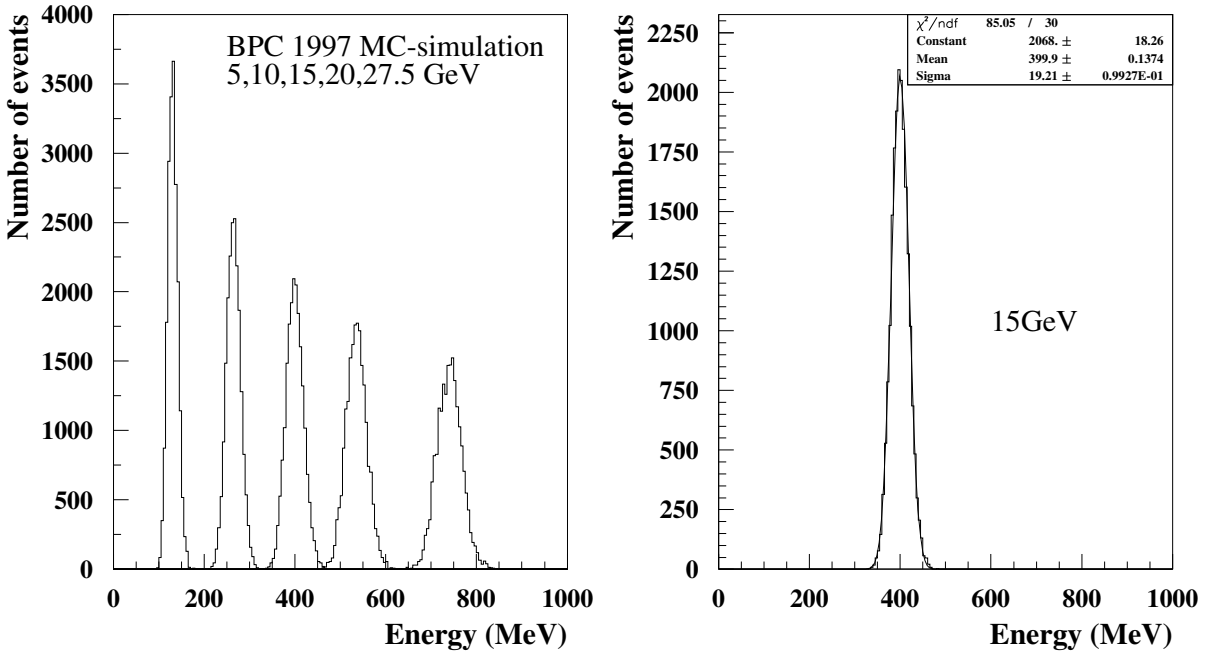


Figure 9.24: *Reconstructed energy of the BPC module north from an* EGS4 *MC-simulation using simulated attenuations curves with respect to the irradiation of scintillators after the running period 1997.*

## 9.5 Conclusions

The installation of the BPC within the existing ZEUS detector as a new component in 1995 required a radiation monitor system using active and passive radiation monitors since the BPC modules are installed very close to the HERA beams. During the 1995 HERA run, an accumulated dose of approximately 12 kGy had been observed at the closest distance of the BPC of approximately 4.3 cm to the beams. The accumulated radiation dose dropped to 10 kGy and 2.5 kGy for the HERA running periods 1996 and 1997.
The effect of this radiation on the scintillator fingers has been estimated using the results from $^{60}$Co scans before and after the 1995 and 1997 HERA run. Scans on individual scintillator fingers with UV-light clearly showed the change of the absorption coefficient due to the radiation. Scans with a $^{90}$Sr source showed the loss of primary light yield of the damaged scintillators. The attenuation curves of damaged/undamaged scintillators were measured with electrons from $^{106}$Ru and the results were well reproduced by a numeric simulation program.
An EGS4 MC simulation has been used to determine the effects on the linearity on the BPC energy response. In case of the running period 1995 the attenuation curves were measured from individual scintillator scans in connection with $^{60}$Co measurements. Whereas in case of the running period 1997 an numerical simulation of the attenuation curves and the $^{60}$Co scans were used. A linear relation between the $^{60}$Co results and the radiation dose was assumed to estimate the effects of the irradiation for the reconstruction of the calorimeter response. These results were incorporated into the MC simulation to determine the effects on the energy linearity. This was found to be about $1-2\%$ above the off-line positron energy cut of 7 GeV

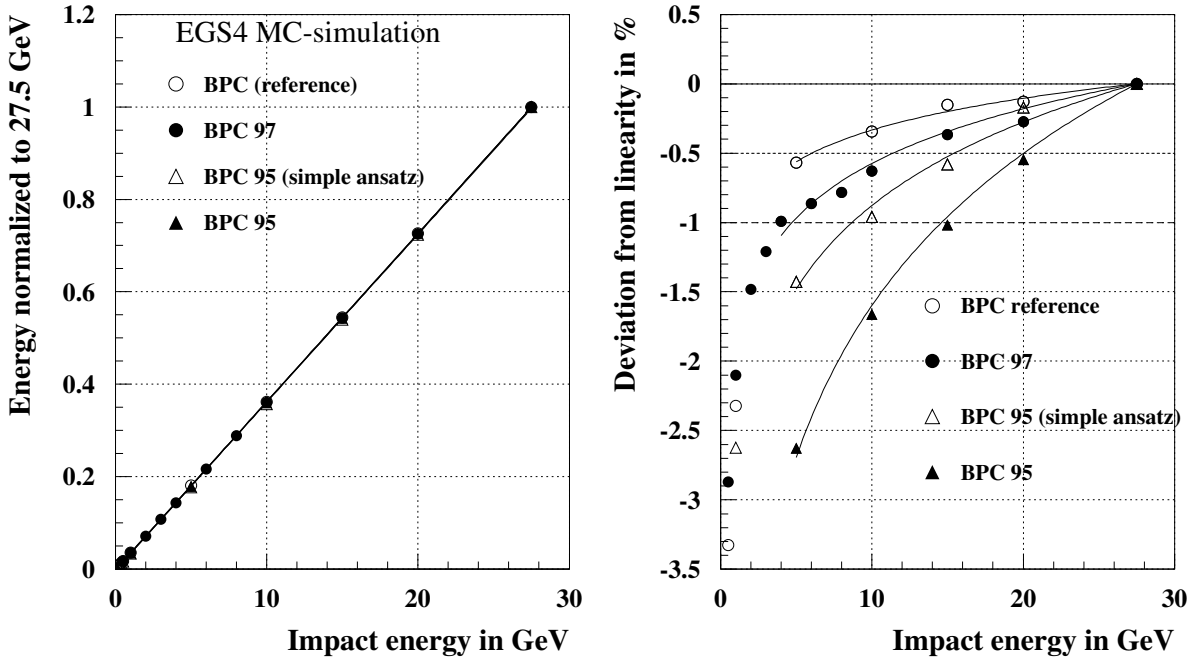


Figure 9.25: *Linearity of energy (left) and deviation from linearity in percent (right) from* EGS4-*MC-simulations with respect to the BPC module north after the running periods 1995 and 1997 in comparison with an undamaged reference module.*

of the BPC in 1995. The non-linearity decreased to be less then 1% above the off-line positron energy cut of 4 GeV of the BPC in 1997. The functional form has been used to determine the systematic error on the extracted proton structure function $F_2$ due to the observed non-linearity. The changes in $F_2$ are in the order of 2% [SU98] with respect to the running period 1995 decreasing significantly in 1997 in the order of 1% [FR99].

# Chapter 10

# Conclusions

The ZEUS calorimeter provides highly precise energy measurements which require both linearity and uniformity of the energy calibration at the level of 1%. The stability and the radiation resistance of the scintillators and wavelength shifters of the calorimeter are of fundamental importance. Theoretical as well as experimental aspects in the field of calorimetry, uniformity and radiation resistance of plastic scintillators and wavelength shifters have been described in this thesis. They were applied to the ZEUS calorimeter and to special components of the latter; the most important experimental basis is the $^{60}$Co off-line monitor system.
Testbeam measurements at DESY in June 1998 in connection with the $^{60}$Co monitor system were performed using a uniformly irradiated lead/scintillator test calorimeter similar to a FCAL EMC tower. The aim of these investigations was to study the influence of irradiated optical components on calorimetry and its monitoring capabilities. Measurements on single scintillators of the test calorimeter before and after irradiation using a scanning bench in connection with a radioactive source indicated the radiation damage. Two irradiated EMC sections and two reference sections were tested with regard to effects on linearity and uniformity with 1 to 6 GeV electrons.

- The irradiated scintillators exposed to doses of 5 and 10 kGy, respectively do not have a significant influence on the energy resolution, in contrast to the 1 kGy irradiated wavelength shifter.
- No significant influence of irradiation is visible on the linearity of the test calorimeter within the used range of electron energies.
- The uniformity of the calorimeter response of the irradiated sections is within $\pm 1\%$ in a region of $\pm 60$ mm around the centre of the scintillators and obviously better than the uniformity of the reference sections.
- It is demonstrated that the $^{60}$Co monitor system is well suited to determine the status of the optical components.

During the maintenance periods from 1996 to 1999 $^{60}$Co measurements were taken on several FCAL and RCAL sections controlling the quality with respect to possible variations of the longitudinal uniformity and the optical parameters, especially the transmission of the scintillators. The result of these measurements can be summarized as follows:

- The $^{60}$Co monitor system indicates no significant variation in the longitudinal structure of the calorimeter, therefore no evidence for effects due to radiation damage of the wavelength shifters or scintillators has been found.

- Yet a systematic reduction of the transmission of the scintillators of the whole ZEUS calorimeter is visible between the present data and the references from 1990. The change is in the order of 3 to 5 %.

This ageing effect corresponds to a change of the attenuation length of scintillators resulting from a uniform 3 kGy irradiation. The theoretical effects of irradiation on the ZEUS calibration have been well studied and can be quoted to estimate the measured ones from ageing:

- The change of the transversal uniformity of the light collection of the scintillators is expected to be smaller than 1%.
- The variation of the electromagnetic and hadronic energy resolution is expected to be about 0.5% and 0.1%, respectively.
- These effects are small in comparison to other systematic errors of measurements and overestimate the real effects of the ZEUS calorimeter.

In 1995 and 1997 two similar accidents of the HES water cooling system occurred to the ZEUS calorimeter which affected the electromagnetic sections of the RCAL module 17 and the FCAL module 8. The UNO signal in the electromagnetic sections decreased by up to 40%. In 1997 within the following 10 months 4 $^{60}$Co measurements were performed on the FCAL module 8 with the aim to study the influence of the water damage on the optical components and on the longitudinal uniformity of the calorimeter response. Similar measurements were performed once in 1997 on the RCAL module 17 in order to compare the water damage effects of both modules. A qualitative understanding of the water damage with regard to the wavelength shifters and the scintillator tiles was performed via two test calorimeter set-ups. The $^{60}$Co and UNO measurements showed that no influence of the water damage on the hadronic sections could be detected, whereas the electromagnatic sections showed a significant reduction of the transmission of the scintillators immediately after the accident.

- Yet in case of the FCAL module 8 the uniformity of the transmission as well as the ratio of scintillator responses was still in a range of $\pm$ 5%, the non-uniformities of the wavelength shifters were in a range of $\pm$10%.
- A strong recovery effect of the optical parameters was observed on the FCAL module 8 with approximately nominal values at the end.
- The effect on energy calibration was estimated to be in the order of 3% in case of the worst damaged sections. The investigation on the RCAL module 17 showed a similar result.

The installation of the BPC within the existing ZEUS detector as a new component in 1995 required a radiation monitor system using active and passive radiation monitors, since the BPC modules are installed very close to the HERA beams.

- During the 1995 HERA run, an accumulated dose of up to 12 kGy had been observed. The accumulated radiation dose dropped to 10 kGy and 2.5 kGy for the HERA running periods 1996 and 1997, respectively with no significant change in the following years.

The effect of this radiation on the scintillator fingers has been estimated using the results from $^{60}$Co scans before and after the 1995 and 1997 HERA run. Scans on individual scintillators

using radioactive sources and a UV-light system led to a detailed understanding about the effects of the irradiation on the scintillators. In case of the running period 1995 the attenuation curves of the scintillators were directly measured, whereas in case of the running period 1997 a numerical simulation of the attenuation curves was used. Both investigations were based on the $^{60}$Co measurements. A linear relation between the $^{60}$Co results and the radiation dose was assumed to estimate the effects of the irradiation for the reconstruction of the calorimeter response. These results were incorporated into an EGS4 MC simulation to determine the effects on the energy linearity.

- This was found to be about then $1-2\%$ above the off-line positron energy cut of 7 GeV of the BPC in 1995.
- The non-linearity decreased to be less then 1% above the off-line positron energy cut of 4 GeV of the BPC in 1997.

The results have been used to determine the systematic error on the extracted proton structure function $F_2$ due to the observed non-linearity.

- The changes in $F_2$ are in the order of 2% with respect to the running period 1995 decreasing significantly in 1997 to the order of 1%.

# Appendix A

# Simulation of light propagation

In the following chapter the calculation of light propagation through non-uniformly damaged rectlinear light guides will be briefly deduced. The basic idea of the numerical calculation is described in detail in chapter 4.4:

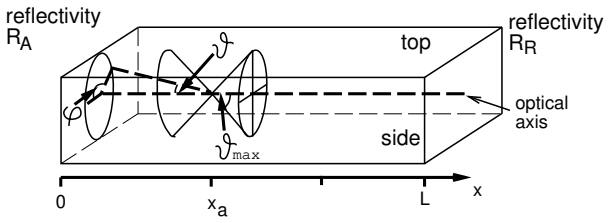


Figure A.1: *Sketch of a rectlinear light guide.*

Fluorescense light of the intensity $I(\lambda, x)$ within a rectlinear light guide will be emitted isotropically over the whole solid angle. Only light which is emitted within two light cones restricted by the angle of total inner reflection can leave the light guide at the open end contributing a measurable intensity. Figure A.1 illustrates the light propagation within a light guide from the position $x$ of the light production in dependence of the polar angle $\vartheta$ and the azimuth angle $\phi$ of emission with respect to the optical axis. The light guide is assumed to be irradiated along the longitudinal direction $x$ by Gaussian distributed radiation dose $D(x)$. The measurable intensity at the open end is decreased due to the reduction of the primary light yield and the attenuation of the light and reflection losses $R$ on the surfaces of the light guide. The reduction of intensity due to reflection on the side and top surfaces is computed by the material dependent factors $R_{side}$ and $R_{top}$. The reflections rate $N$ after light propagation of the length $x/cos(\vartheta)$ can be estimated by a simple geometrical ansatz:

$$N_{side}(x,\varphi,\vartheta) = \left( \left| \frac{x \tan\vartheta \cos\varphi}{l_{side}} \right| + \frac{1}{2} \right), \qquad N_{top}(x,\varphi,\vartheta) = \left( \left| \frac{x \tan\vartheta \sin\varphi}{l_{top}} \right| + \frac{1}{2} \right).$$

The calculation of the reflection rate considers only the whole-numbered results. $l_{side}$ and $l_{top}$ are the distances of the side and top surfaces of the light guide. In the following it is used $x = a + b$ assuming $N_{top}(a+b,\varphi,\vartheta) \approx N_{top}(a,\varphi,\vartheta) + N_{top}(b,\varphi,\vartheta)$.
The light within the first light cone propagates directly to the open end, whereas the light within the second light cone propagates first to the opposite side. The following equation describes the intensity $I_{d0}(x,\lambda,\varphi,\vartheta)$ of the light beam which hits the open end directly and transmits the light guide immediately:

$$I_{d0}(\lambda,x,\varphi,\vartheta) \;=\; I(\lambda,x) \cdot R_{side}^{N_{side}(x,\varphi,\vartheta)} \cdot R_{top}^{N_{top}(x,\varphi,\vartheta)} \cdot T_A(\vartheta) \cdot T_{dir}(\lambda,x,\vartheta). \qquad \text{(A.1)}$$

The transmission $T_{dir}(\lambda,x,\vartheta) = e^{-\frac{\mu(\lambda)\cdot x}{\cos\vartheta}} \cdot e^{-\frac{b(\lambda)}{\cos\vartheta}\int_0^x D(x')dx'}$ considers the light attenuation during the propagation from the position of light production to the open end of the light guide

over the path $x/cos\theta$. The attenuation depends on the position dependent absorption coefficient $\mu'(\lambda, x) = \mu(\lambda) + \Delta\mu(\lambda, x)$. The part of light $T_A(\vartheta)$ which transmits the end of the light guide immediately depends on the relative refraction index $n$ of the light guide assuming unpolarized light. It is given by Fresnel [BE73]:

$$T_A(\vartheta) = 1 - \frac{1}{2}\left(\left(\frac{(\sqrt{n^2 - \sin^2\vartheta} - \cos\vartheta)^2}{n^2 - 1}\right)^2 + \left(\frac{n^2\cos\vartheta - \sqrt{n^2 - \sin^2\vartheta}}{n^2\cos\vartheta + \sqrt{n^2 - \sin^2\vartheta}}\right)^2\right). \quad (A.2)$$

The part $R_A(\vartheta) = 1 - T_A(\vartheta)$ of light propagates through the whole light guide again. A part $R_R(\vartheta)$ of the remaining light reflects at the opposite side and propagates back to the open end, where again a part $T_A(\theta)$ of light transmits. The detected intensity $I_{d1}(x, \lambda, \varphi, \vartheta)$ of this part is then:

$$\begin{aligned} I_{d1}(\lambda, x, \varphi, \vartheta) &= I_{d0}(\lambda, x, \varphi, \vartheta) \cdot R_{side}^{N_{side}(2L,\varphi,\vartheta)} \cdot R_{top}^{N_{top}(2L,\varphi,\vartheta)} \\ &\quad \cdot R_A(\theta) \cdot R_R(\theta) \cdot T_{dir}(\lambda, L, \vartheta)^2. \end{aligned} \quad (A.3)$$

The transmission $T_{dir}(\lambda, L, \vartheta) = e^{-\frac{\mu(\lambda)\cdot L}{\cos\vartheta}} \cdot e^{-\frac{b(\lambda)}{\cos\vartheta}\int_0^L D(x')dx'}$ considers the attenuation during the light propagation through the whole length $L/cos\theta$ of the light guide. The square of $T_{dir}(\lambda, L)$ considers the light path $(2 \cdot L)/cos\theta$ from the open end to the opposite side of the light guide and back again. After $n$ reflections at the ends of the light guide the detected intensity yields:

$$\begin{aligned} I_{dn}(\lambda, x, \varphi, \vartheta) &= I_{d0}(\lambda, x, \varphi, \vartheta) \cdot R_{side}^{N_{side}(n\cdot 2L,\varphi,\vartheta)} \cdot R_{top}^{N_{top}(n\cdot 2L,\varphi,\vartheta)} \\ &\quad \cdot R_A(\theta)^n \cdot R_R(\theta)^n \cdot T_{dir}(\lambda, L, \vartheta)^{2\cdot n}. \end{aligned} \quad (A.4)$$

The total intensity of light which is observable at the open end is the sum of infinite light reflections $\sum_{i=0}^{\infty} I_{di}(\lambda, x, \varphi, \vartheta)$. It is a geometrical series converging to:

$$I_d(\lambda, x, \varphi, \vartheta) = \frac{I(\lambda, x) \cdot R_{side}^{N_{side}(x,\varphi,\vartheta)} \cdot R_{top}^{N_{top}(x,\varphi,\vartheta)} \cdot T_A(\vartheta) \cdot T_{dir}(\lambda, x)}{1 - R_{side}^{N_{side}(2L,\varphi,\vartheta)} \cdot R_{top}^{N_{top}(2L,\varphi,\vartheta)} \cdot R_A(\vartheta) \cdot R_R(\vartheta) \cdot T_{dir}(\lambda, L, \vartheta)^2}. \quad (A.5)$$

The light within the second light cone propagates to the opposite side, where a part $R_R(\theta)$ is reflected and propagates back to the open end of the light guide. Yet the whole path length of the light propagation is $(2L - x)/cos\theta$. Then the light which transmits the light guide yields the following intensity:

$$\begin{aligned} I_{i0}(x, \lambda, \varphi, \vartheta) &= I(\lambda) \cdot T_{dir}(\lambda, L, \vartheta) \cdot T_{ind}(\lambda, L - x, \vartheta) \\ &\quad \cdot R_{side}^{N_{side}(2L-x,\varphi,\vartheta)} \cdot R_{top}^{N_{top}(2L-x,\varphi,\vartheta)} \cdot R_R(\vartheta) \cdot T_A(\vartheta), \end{aligned} \quad (A.6)$$

where $T_{ind}(\lambda, L - x, \vartheta) = e^{-\frac{\mu(\lambda)\cdot(L-x)}{\cos\vartheta}} \cdot e^{-\frac{b(\lambda)}{\cos\vartheta}\int_x^L D(x')dx'}$ considers the attenuation during the light propagation over the length $(L - x)/cos\theta$ from the position of light production to the opposite side. The reflected light traverses during the propagation back to the open end the integrated dose $\int_o^L D(x')dx'$. Similar to equation A.5 the observable intensity $I_i(x, \lambda, \varphi, \vartheta)$ of the indirect light beam converges after infinite reflections to:

$$\begin{aligned} I_i(\lambda, x, \varphi, \vartheta) &= \frac{I(\lambda, x) \cdot R_R(\vartheta) \cdot T_A(\vartheta)}{1 - R_{side}^{N_{side}(2L,\varphi,\vartheta)} \cdot R_{top}^{N_{top}(2L,\varphi,\vartheta)} \cdot R_A(\vartheta) \cdot R_R(\vartheta) \cdot T_{dir}(\lambda, L, \vartheta)^2} \\ &\quad \cdot R_{side}^{N_{side}(2L-x,\varphi,\vartheta)} \cdot R_{top}^{N_{top}(2L-x,\varphi,\vartheta)} \cdot T_{dir}(\lambda, L, \vartheta) \cdot T_{ind}(\lambda, L - x, \vartheta). \end{aligned} \quad (A.7)$$

Under the presumption of an isotropic emission of fluorescense light overall directions two light beams with same angles $\varphi$ and $\vartheta$ can be added to $I_{total} = I_d + I_i$. The integration of equation 4.30 over all possible solid angles and wavelengths of the emission spectrum $[\lambda_a, \lambda_e]$ allows to calculate the measurable intensity $I_{meas}$ of the light which is emitted the light guide at the open end. The transformation of the equation 4.31 into a numerical summation yields:

$$I_{meas}(x) = \left( \sum_{l=1}^{l=l_n} \sum_{t=1}^{t=t_n} \sin\vartheta_t \sum_{p=1}^{p=p_n} I_{total}(x, \lambda_l, \varphi_p, \vartheta_t) \right) \Big/ \left( l_n \cdot p_n \cdot \sum_{t=1}^{t=t_n} \sin\vartheta_t \right), \tag{A.8}$$

$$I_{total}(\lambda_l, x, \varphi_p, \vartheta_t) = \frac{I_0(\lambda_l, x) \cdot (1 - c \cdot D(x)) \cdot T_A(\vartheta_t) \cdot (I_{direct}(\lambda_l, x, \varphi_p, \vartheta_t) + I_{indirect}(\lambda_l, x, \varphi_p, \vartheta_t))}{1 - T_{dir}(\lambda_l, 2L, \vartheta_t) \cdot R_{side}^{N_{side}(2L, \varphi_p, \vartheta_t)} \cdot R_{top}^{N_{top}(2L, \varphi_p, \vartheta_t)} \cdot R_A(\vartheta_t) \cdot R_R(\vartheta_t)},$$

$$I_{direct}(x, \lambda_l, \varphi_p, \vartheta_t) = T_{dir}(\lambda_l, x, \vartheta_t) \cdot R_{side}^{N_{side}(x, \varphi_p, \vartheta_t)} \cdot R_{top}^{N_{top}(x, \varphi_p, \vartheta_t)},$$

$$I_{indirect}(x, \lambda_l, \varphi_p, \vartheta_t) = R_R(\vartheta_t) \cdot T_{ind}(\lambda_l, L - x, \vartheta_t) \cdot T_{dir}(\lambda_l, L, \vartheta_t) \cdot R_{side}^{N_{side}(2L - x, \varphi_p, \vartheta_t)} \cdot R_{top}^{N_{top}(2L - x, \varphi_p, \vartheta_t)},$$

$$T_{dir}(\lambda_l, L, \vartheta_t) = e^{-\frac{\mu(\lambda_l) \cdot L}{\cos\vartheta_t}} \cdot e^{-\frac{b(\lambda_l)}{\cos\vartheta_t} \sum_0^L D(x')},$$

$$T_{ind}(\lambda_l, L - x, \vartheta_t) = e^{-\frac{\mu(\lambda_l) \cdot (L - x)}{\cos\vartheta_t}} \cdot e^{-\frac{b(\lambda_l)}{\cos\vartheta_t} \sum_x^L D(x')},$$

$$\sum_x^L D(x') = \sum_{x'=x}^{L} D_0 \cdot e^{-\frac{1}{2} \frac{(x' - x_D)^2}{{R_D}^2}},$$

with:

| | | |
|---|---|---|
| $x$ | : | position of light production, |
| $\lambda_n$ | : | wavelengths $l_n$ in discrete levels within the intervall $[\lambda_a, \lambda_e]$, |
| $\varphi_n$ | : | polar angle in $p_n$ in discrete levels with the intervall $[0, 2\pi]$, |
| $\vartheta_n$ | : | steradian $t_n$ in discrete levels within the intervall $[0, \vartheta_{max}]$, |
| $I_0(\lambda_n)$ | : | wavelength dependent intensity of light at the position of production, |
| $R_{side}$ | : | reflection coefficient at the side face of the light guide, |
| $R_{top}$ | : | reflection coefficient at the top face of the light guide, |
| $N$ | : | number of reflections using the indices: |
| $top$ | : | top face of the light guide, |
| $side$ | : | side face of the light guide, |
| $L$ | : | longitudinal distance of the light guide, |
| $R_A(\vartheta)$ | : | reflection coefficient at the open end, |
| $R_R(\vartheta)$ | : | reflection coefficient at the opposite side, |
| $T_A(\vartheta)$ | : | part of the light which transmits the open end, |
| $\mu(\lambda)$ | : | wavelength dependent absorption coefficient, |
| $x'$ | : | position in mm, |
| $x_D$ | : | position of maximum irradiation, |
| $D_0$ | : | maximum radiation dose, |
| $R_D$ | : | width of radiation dose distribution, |
| $c$ | : | reduction of light yield per radiation dose, |
| $b(\lambda)$ | : | permanent damage per radiation dose. |

Figure A.2: *The following presents the transformation of the numerical calculation A.8 of light propagation within a light guide into the computer code* LIGHTSIM *based on the programming language* C*:*

```
/*********************************************************************
 * lightsim.c:     Programm zur Simulation von Fluoreszenzlichtausbrei-  *
 *                 tung in quaderfoermigen Proben basierend auf dem      *
 *                 Programm quaderatten.c . Liefert ortsabhaengige       *
 *                 Intensitaeten. Beruecksichtigt nichtideale (R<>1)     *
 *                 Reflexionen an Seiten- und Deckflaechen und exponen-  *
 *                 tielle Abschwaechung im Medium sowie eine ortsab-     *
 *                 haengige, gaussfoermige Dosisverteilung mit Einfluss  *
 *                 auf Primaerlichtausbeute und Abschwaechlaengen        *
 *                                                                       *
 * Ein-/Ausgabe :  Alle Ein-/Ausgabedateien werden im Quelltext festge-  *
 *                 legt. Die Liste der einstellbaren Parameter wird in   *
 *                 den Kopf des Ergebnisdatenfiles geschrieben.          *
 *                                                                       *
 * notwendige Dateien: Zur Ausfuehrung des Programmes werden dieser      *
 *                 Quelltext (lightsim.c) und die Liste der wellen-      *
 *                 abhaengigen Mue Fluoreszenzintensitaeten und Dosis-   *
 *                 korrelationsparameter b (s.VECFILE_I_MUE") benoetigt. *
 *                                                                       *
 * JEDE GEWUENSCHTE PARAMETERAENDERUNG ERFORDERT NEUES KOMPILIEREN, etwa *
 *           durch:   "cc -o lightsim lightsim.c  -lm"                   *
 *                                                                       *
 * letzte Aend.:   22.Aug.1998, ib                                       *
 *                                                                       *
 * Copyright '98:  Andreas Dannemann und Ilja Bohnet                     *
 *********************************************************************/

#include <stdio.h>
#include <stdlib.h>
#include <math.h>
#include <string.h>

/*    Beginn der Protokollzeilen ### DIESE ZEILE NICHT AENDERN !!! ###    */
/*#########################################################################
  #                                                                       #
  # Definitionen der einstellbaren Parameter (lightsim.c)                 #
  #                                                                       #
  #########################################################################*/

#define VECFILE_I_MUE "lam_mue_iy7_b_scsn38.vec"
                                        /*   Lambda,Mue,I,b - Vektorenfile */

#define ERGEBNIS_VECFILE "yfinger10.vec"             /* PAW-Vektorenfile */

                                                /*   alle Laengen in mm:  */
#define PROBENLG       126.0                    /*      Probenlaenge      */
#define PROBENBR_HORI    2.5                    /* horizont. Probenbreite */
```

```
#define PROBENBR_VERT    8.0                    /* vertikal. Probenbreite */
#define ANREG_SCHRITT   1.0          /* Schrittweite zur Anregung         */
#define ANREG_START     0.0          /* Startpunkt der ortsabh. Anregung  */
#define ANREG_END      126.0         /* Endpunkt der ortsabh. Anregung    */

#define REFL_SEIT       0.99      /* Reflexionskoeffizient Seitenflaechen */
#define REFL_DECK       1.0       /* Reflexionskoeffizient Deckflaechen   */

#define N_BRECH         1.6       /*    Materialbrechungsindex            */

#define REFL_ANF        r_fresnel(theta)
                                  /* Reflexionskoefizient Ausleseflaeche  */
                                  /* eigentl.: r_fresnel(N_BRECH,theta)   */
#define REFL_ENDE       0.85      /* Reflexionskoefizient Endflaeche      */
#define INT_LO_PHI      0.0       /* untere Integrationsgrenze fuer Phi   */
#define INT_HI_PHI      M_PI/2    /* obere Integrationsgrenze fuer Phi    */
#define INT_LO_THETA    0.0       /* untere Integrationsgrenze fuer Theta */
#define INT_HI_THETA    asin(1/N_BRECH)
                                  /* obere Integrationsgrenze fuer Theta  */
                                  /* = Grenzwinkel der Totalreflexion     */

#define N_LAMBDA        100       /* Anzahl der Wellenlaengenpositionen   */
#define I_LAMBDA_START  1         /* No. der ersten Wellenlaengenposition */
#define N_THETA         50        /* Anzahl der Azimutwinkelunterteilungen*/
#define N_PHI           50        /* Anzahl der Polarwinkelunterteilungen */
#define C_GAMMA         9E-6      /* Dosisparameter  in 1/Gy              */
#define SCHADENS_ORT    121       /* Ort max. Schaedigung                 */
#define SCHADENS_BREIT  21        /* Breite der Schaedigung               */
#define SCHADEN         10000     /* Dosismaximum  in Gy                  */
#define ART_DER_AUSGABE 2         /* Ergebnisvektoren als
                                       (x,I_integral)-Spalten (2) oder als
                                       (x,I(lambda_1),.. ,I(lambda_n)) (1)
                                       Spalten ausgeben.
                                       1 fuer I_von_lambda oder
                                       2 fuer I_integral eintragen.       */
/*************************************************************************/
/*      Ende der Protokollzeilen ### DIESE ZEILE NICHT AENDERN !!! ###   */

/*************************************************************************
  #                                                                      #
  #                   H A U P T P R O G R A M M                          #
  #                                                                      #
  *************************************************************************/

main()
{
  double r_fresnel(double alpha);
```

```
double f_seit(double theta, double phi, double x);
double f_deck(double theta, double phi, double x);
double i_primaerlicht(double x);
double i_dosis(double anf, double end);
double i_kern(double theta, double x, double mue, double integrand_dos, double b);
FILE  *out_file,*c_quelltext;
double lambda[N_LAMBDA+1]={0},mue[N_LAMBDA+1]={0},i_fluo[N_LAMBDA+1]={0},
       b[N_LAMBDA+1]={0};
double anreg_ort,anreg_start=(double)ANREG_START,anreg_end=(double)ANREG_END,
       anreg_schritt=(double)ANREG_SCHRITT;
double phi,phi_start=(double)INT_LO_PHI,phi_end=(double)INT_HI_PHI,
       phi_schritt=(double)(INT_HI_PHI-INT_LO_PHI)/N_PHI;
double theta,theta_start=(double)INT_LO_THETA,theta_end=(double)INT_HI_THETA,
       theta_schritt=(double)(INT_HI_THETA-INT_LO_THETA)/N_THETA;
double kugelflaeche=(double)0.0,integrand_phi=(double)0.0;
double integrand_lambda=(double)0.0,integrand_theta=(double)0.0,
       intens_lambda=(double)0.0,intens_von_lambda[N_LAMBDA+1]={0},
       summen_normierung=(double)0.0;
double intensitaet_gesamt;
double int_phi_dir,int_phi_ind,refl_korr,i_prim,int_dosis_dir,int_dosis_ind,
       int_dosis_kom;
int    i_lambda,i_phi,i_theta,i_dos,
       parameter_geschrieben=0,line_no=0;
char   beginn_protokollzeilen[33]="/*    Beginn der Protokollzeilen",
       ende_protokollzeilen[33]="/*      Ende der Protokollzeilen",
       c_quell_zeile[80];

/*------------------------------------------------------------------------*/
/*    Einlesen der wellenlaengenabhaengigen mue und Fluoreszenzintens.    */
/*------------------------------------------------------------------------*/

(void) read_lam_mue_i_file(lambda,mue,i_fluo,b);


/*------------------------------------------------------------------------*/
/*    Einlesen der Programmeinstellungen und Schreiben in Ausgabefile     */
/*------------------------------------------------------------------------*/

if((c_quelltext = fopen("lightsim.c","r")) == NULL )
  { /*Datei futsch*/
  fprintf(stderr,
    "Ich kann meinen Quelltext lightsim.c nicht lesen...\n");
  exit(8);
}
else {   /* C-Quelltext vorhanden */
  if((out_file = fopen(ERGEBNIS_VECFILE,"w")) == NULL ) { /*Datei futsch*/
    fprintf(stderr,"Ich kann meine Ergebnisdatei %s nicht schreiben...\n",
```

```
            ERGEBNIS_VECFILE);
    exit(8);
  }
  else { /* Ergebnisdatei erfolgreich zum Schreiben geoeffnet */

    while ( feof(c_quelltext) == 0 ) { /* solange Fileende nicht erreicht */
      fgets(c_quell_zeile,sizeof(c_quell_zeile),c_quelltext);
      if (strncmp(c_quell_zeile, beginn_protokollzeilen,32)==0) {
        /* Beginn der Parameterabschrift */
        fgets(c_quell_zeile,sizeof(c_quell_zeile),c_quelltext);
        while ((strncmp(c_quell_zeile, ende_protokollzeilen,32)!=0)
               && ( feof(c_quelltext) == 0 )) {
          /* Schreibe mit bis zum Ende der Parameter */
          parameter_geschrieben=1;
          fprintf(out_file,"%s",c_quell_zeile);
          fgets(c_quell_zeile,sizeof(c_quell_zeile),c_quelltext);
        } /* Ende der Parameter zum Mitschreiben */
      } /* Ende der Parameterabschrift */
    } /* Ende des c-Quelltextes erreicht */
  } /* Ende Ergebnisdatei-Schreibtest */
} /* Ende c-Quelltext-Lesetest */
(void) fclose(c_quelltext);
if(parameter_geschrieben!=1) {
  fprintf(stderr,"Keine Parameter aus lightsim.c in %s geschrieben...\n",
          ERGEBNIS_VECFILE);
  exit(8);
}

/*-------------------------------------------------------------------------*/
/*               Ortschleife: Aenderung des Anregungsortes                 */
/*-------------------------------------------------------------------------*/

for (anreg_ort = anreg_start; anreg_ort <= anreg_end; anreg_ort = anreg_ort
     + anreg_schritt) {
  i_prim        = i_primaerlicht(anreg_ort);  /* Primaerlichtausbeute */;
  int_dosis_dir = i_dosis(0.0,anreg_ort);
  int_dosis_ind = i_dosis(anreg_ort,PROBENLG);
  int_dosis_kom = i_dosis(0.0,PROBENLG);
  /* printf("Die integrierte Dosis ist : %f\n", int_dosis_kom); */

  /*+++++++++++++++++++++++++++++++++++++++++++++++++++++++++++++++++++++++
    +                                                                      +
    +                  Beginn der Summation des Lichts                     +
    +                                                                      +
    ++++++++++++++++++++++++++++++++++++++++++++++++++++++++++++++++++++++*/

  integrand_lambda=(double)0.0;
```

```
/*------------------------------------------------------------------------*/
/*       Wellenlaengenschleife: Aenderung der Fluoreszenzwellenlaenge     */
/*------------------------------------------------------------------------*/
for (i_lambda = I_LAMBDA_START; i_lambda <= N_LAMBDA; i_lambda++) {
  integrand_theta=(double)0.0;

  /*----------------------------------------------------------------------*/
  /*            Thetaschleife: Aenderung des Azimutwinkels                */
  /*----------------------------------------------------------------------*/

  for (i_theta = 1; i_theta <= N_THETA; i_theta++) {
    theta=theta_start+(i_theta-0.5)*theta_schritt;
    integrand_phi=(double)0.0;

    /*--------------------------------------------------------------------*/
    /*               Phischleife: Aenderung des Polarwinkels              */
    /*--------------------------------------------------------------------*/

    for (i_phi = 1; i_phi <= N_PHI; i_phi++) {
      phi=phi_start+(i_phi-0.5)*phi_schritt;
      int_phi_dir =  f_seit(theta,phi,anreg_ort) * f_deck(theta,phi,anreg_ort)
      * i_kern(theta,anreg_ort,mue[i_lambda],int_dosis_dir,b[i_lambda]);
      int_phi_ind = REFL_ENDE * f_seit(theta,phi,2*PROBENLG-anreg_ort)
      * f_deck(theta,phi,2*PROBENLG-anreg_ort)
      * i_kern(theta,PROBENLG-anreg_ort,mue[i_lambda],int_dosis_ind,b[i_lambda])
      * i_kern(theta,PROBENLG,mue[i_lambda],int_dosis_kom,b[i_lambda]);
      refl_korr   =
      1 / ( 1 - pow(i_kern(theta,PROBENLG,mue[i_lambda],int_dosis_kom,b[i_lambda])
      * f_seit(theta,phi,PROBENLG) * f_deck(theta,phi,PROBENLG),2)
      * REFL_ANF * REFL_ENDE);
      integrand_phi = integrand_phi + i_prim * (int_phi_dir + int_phi_ind)
      * refl_korr;
    }
    /*--------------------------------------------------------------------*/
    /*   ENDE     Phischleife: Aenderung des Polarwinkels                 */
    /*--------------------------------------------------------------------*/

    integrand_theta = integrand_theta + sin(theta) * pow((1-REFL_ANF),2) *
      integrand_phi;
  }
  /*----------------------------------------------------------------------*/
  /*     ENDE      Thetaschleife: Aenderung des Azimutwinkels             */
  /*----------------------------------------------------------------------*/

  intens_lambda = i_fluo[i_lambda] * integrand_theta;
  intens_von_lambda[i_lambda] = intens_lambda;  /* monochr. Intensitaet*/
```

```
    integrand_lambda = integrand_lambda + intens_lambda;
  }
  /*-------------------------------------------------------------------------*/
  /* ENDE  Wellenlaengenschleife: Aenderung der Fluoreszenzwellenlaenge    */
  /*-------------------------------------------------------------------------*/

  integrand_theta=(double)0.0;

  /*-------------------------------------------------------------------------*/
  /*              Thetaschleife: Zur Normierung der Summe                    */
  /*-------------------------------------------------------------------------*/
  for (i_theta = 1; i_theta <= N_THETA; i_theta++) {
    theta = theta_start+(i_theta-0.5)*theta_schritt;
    integrand_theta = integrand_theta + sin(theta);
  }
  /*-------------------------------------------------------------------------*/
  /*     ENDE      Thetaschleife: Zur Normierung der Summe                   */
  /*-------------------------------------------------------------------------*/

  summen_normierung = N_LAMBDA * N_PHI * integrand_theta;
  integrand_lambda = integrand_lambda / summen_normierung;

  /*+++++++++++++++++++++++++++++++++++++++++++++++++++++++++++++++++++++++++
    +                                                                       +
    +                   Ende der Summation des Lichts                       +
    +                                                                       +
    +++++++++++++++++++++++++++++++++++++++++++++++++++++++++++++++++++++++++*/

  switch (ART_DER_AUSGABE)
    {
    case 1:
      for (i_lambda = I_LAMBDA_START; i_lambda <= (N_LAMBDA); i_lambda++) {
        (void) fprintf(out_file,"%6d %11.5lf %11.5lf %11.5lf %11.5lf\n",
                       ++line_no,anreg_ort,lambda[i_lambda],
                       intens_von_lambda[i_lambda],integrand_lambda);
      }
      break;
    case 2:
      (void) fprintf(out_file,"%5.1lf\t%11.5e\n",anreg_ort,integrand_lambda);
      break;
    default:
      fprintf(stderr,"Ich habe keine zuverlaessige Angabe ueber die ");
      fprintf(stderr,"ART_DER_AUSGABE in %s ...\n", ERGEBNIS_VECFILE);
      break;
    }
}
/*-------------------------------------------------------------------------*/
```

```
  /*   ENDE        Ortschleife: Aenderung des Anregungsortes                */
  /*-------------------------------------------------------------------------*/

  (void) fclose(out_file);
  return (0);
}


/*#########################################################################
  #                                                                       #
  # Unterprogramme und Funktionen                                         #
  #                                                                       #
  #########################################################################*/

/*+++++++++++++++++++++++++++++++++++++++++++++++++++++++++++++++++++++++++
  + Einlesen der 93 lambda-, mue-, Fluoreszenzintensitaetswerte         +
  +++++++++++++++++++++++++++++++++++++++++++++++++++++++++++++++++++++++++*/

int read_lam_mue_i_file(double *lambda,double *mue,double *i_fluo,double *b)
{
  FILE *i_mue_vecfile;
  int i_lambda;

  if((i_mue_vecfile = fopen(VECFILE_I_MUE,"r")) == NULL ) { /* Datei futsch */
    fprintf(stderr,"Ich kann die Datei %s nicht lesen...\n",VECFILE_I_MUE);
    exit(8);
  }
  else {   /* Alles ok */
    for (i_lambda = 1; i_lambda<=N_LAMBDA; i_lambda++) {
      (void) fscanf(i_mue_vecfile,"%lf%lf%lf%lf\n",&lambda[i_lambda],
                    &mue[i_lambda],&i_fluo[i_lambda],&b[i_lambda]);
      mue[i_lambda]=mue[i_lambda]/10.0; /* Normierung auf mm */
      b[i_lambda]  =b[i_lambda]/10.0;   /* Normierung auf mm */

    }
  }
  (void) fclose(i_mue_vecfile);
  return(0);
}
/*+++++++++++++++++++++++++++++++++++++++++++++++++++++++++++++++++++++++++
  + Berechnung der Seitenwandgesamtreflektivitaet aus phi, theta und x  +
  +++++++++++++++++++++++++++++++++++++++++++++++++++++++++++++++++++++++++*/

double f_seit(double theta, double phi, double x)
{
  double ergebnis;
  double b_seit=(double)PROBENBR_HORI;
```

```
  ergebnis=pow(REFL_SEIT,floor(x*tan(theta)*fabs(cos(phi))/b_seit+0.5));

  return (ergebnis);
}
/*++++++++++++++++++++++++++++++++++++++++++++++++++++++++++++++++++++++
  +   Berechnung der Deckwandgesamtreflektivitaet aus phi, theta und x  +
  ++++++++++++++++++++++++++++++++++++++++++++++++++++++++++++++++++++++*/

double f_deck(double theta, double phi, double x)
{
  double ergebnis;
  double b_deck=(double)PROBENBR_VERT;

  ergebnis=pow(REFL_DECK,floor(x*tan(theta)*fabs(-sin(phi))/b_deck+0.5));

  return (ergebnis);
}
/*++++++++++++++++++++++++++++++++++++++++++++++++++++++++++++++++++++++
  +   Berechnung der Primaerlichtausbeute im Quader                     +
  ++++++++++++++++++++++++++++++++++++++++++++++++++++++++++++++++++++++*/

double i_primaerlicht(double x){
  double ergebnis;
  double dosis;
  dosis =  SCHADEN * exp(-0.5*pow((x-SCHADENS_ORT)/SCHADENS_BREIT,2));
  ergebnis= (1- C_GAMMA * dosis);
  return (ergebnis);
}
/*++++++++++++++++++++++++++++++++++++++++++++++++++++++++++++++++++++++
  +   Berechnung der integrierten Dosis im Quader                       +
  ++++++++++++++++++++++++++++++++++++++++++++++++++++++++++++++++++++++*/

double i_dosis(double anf, double end){
  double i_dos;
  double integrand_dos;
  integrand_dos = 0;
  for (i_dos = anf; i_dos <= end-1; i_dos=i_dos+1){
  integrand_dos = integrand_dos +
  SCHADEN * exp(-0.5*pow((i_dos-SCHADENS_ORT)/SCHADENS_BREIT,2));
  };
  return (integrand_dos);
}
/*++++++++++++++++++++++++++++++++++++++++++++++++++++++++++++++++++++++
  +   Berechnung des Kerntermes zur Lichtabschwaechung im Quader        +
  ++++++++++++++++++++++++++++++++++++++++++++++++++++++++++++++++++++++*/
```

```
double i_kern(double theta, double x, double mue, double integrand_dos, double b){
  double ergebnis;
  ergebnis= exp(-mue*x/cos(theta)) * exp(-(b/cos(theta)) * integrand_dos);
  /* printf("schaden: %f\n", schadens_vert); */
  return (ergebnis);
}
/*++++++++++++++++++++++++++++++++++++++++++++++++++++++++++++++++++++++
  + Berechnung der Fresnelschen Reflexion an Grenzfl<E4>che bei Einfalls-  +
  + winkel alpha und Brechungsindex n_brech                                +
  ++++++++++++++++++++++++++++++++++++++++++++++++++++++++++++++++++++++*/

double r_fresnel(double alpha)
{
  double wurzel,rho_p,rho_s,refl,n_relativ;

  n_relativ=1/N_BRECH;
  wurzel = sqrt( pow(n_relativ,2) - pow(sin(alpha),2));
  rho_s  = - pow((wurzel - cos(alpha)) , 2)/(pow(n_relativ,2)-1);
  rho_p  = (pow(n_relativ,2)*cos(alpha) - wurzel) /
           (pow(n_relativ,2)*cos(alpha) + wurzel);
  refl   =  0.5*(pow(rho_s,2)+pow(rho_p,2));

  return(refl);
}

/*##########################################################################
  #                                                                        #
  # Ende der Unterprogramme und Funktionen                                 #
  #                                                                        #
  ##########################################################################*/
```

Table A.1: *Database for SCSN-38 from [DA96]: Wavelength $\lambda$, absorption coefficient $\mu$, primary light yield of an ideal detector $I_{0,ideal}$ and with respect to the absorption of the dyes Y7 of the wavelength shifter $I_{0,real}$, and the permanent damage per radiation dose $b(\lambda)$.*

| $\lambda$ (nm) | $\mu$ ($cm^{-1}$) | $I_{0,ideal}$ | $I_{0,Y7}$ | $b(\lambda) \cdot 10^4$ $(Gy \cdot cm)^{-1}$ | $\lambda$ (nm) | $\mu$ ($cm^{-1}$) | $I_{0,ideal}$ | $I_{0,Y7}$ | $b(\lambda) \cdot 10^4$ $(Gy \cdot cm)^{-1}$ |
|---|---|---|---|---|---|---|---|---|---|
| 352 | 24.017 | 0.704 | 0.045 | -0.586 | 452 | 0.006 | 0.390 | 0.569 | 0.008 |
| 354 | 24.494 | 0.717 | 0.038 | -0.586 | 454 | 0.006 | 0.374 | 0.553 | 0.008 |
| 356 | 27.214 | 0.762 | 0.036 | -0.586 | 456 | 0.006 | 0.358 | 0.537 | 0.007 |
| 358 | 23.693 | 0.820 | 0.040 | -0.586 | 458 | 0.005 | 0.342 | 0.520 | 0.007 |
| 360 | 25.607 | 0.879 | 0.037 | -0.586 | 460 | 0.005 | 0.325 | 0.499 | 0.007 |
| 362 | 25.108 | 0.924 | 0.042 | -0.586 | 462 | 0.005 | 0.308 | 0.473 | 0.006 |
| 364 | 25.546 | 0.942 | 0.045 | -0.586 | 464 | 0.005 | 0.289 | 0.441 | 0.006 |
| 366 | 25.504 | 0.942 | 0.050 | -0.586 | 466 | 0.004 | 0.268 | 0.402 | 0.006 |
| 368 | 24.550 | 0.910 | 0.058 | -0.586 | 468 | 0.004 | 0.247 | 0.361 | 0.006 |
| 370 | 24.396 | 0.870 | 0.065 | -0.586 | 470 | 0.004 | 0.227 | 0.317 | 0.006 |
| 372 | 24.169 | 0.828 | 0.081 | -0.586 | 472 | 0.004 | 0.208 | 0.271 | 0.006 |
| 374 | 24.325 | 0.795 | 0.097 | -0.536 | 474 | 0.004 | 0.189 | 0.225 | 0.006 |
| 376 | 23.746 | 0.778 | 0.117 | -0.586 | 476 | 0.004 | 0.173 | 0.183 | 0.006 |
| 378 | 22.025 | 0.770 | 0.142 | -0.627 | 478 | 0.004 | 0.158 | 0.148 | 0.005 |
| 380 | 20.568 | 0.772 | 0.174 | -0.768 | 480 | 0.004 | 0.146 | 0.115 | 0.005 |
| 382 | 19.222 | 0.776 | 0.209 | -0.801 | 482 | 0.004 | 0.136 | 0.087 | 0.005 |
| 384 | 17.211 | 0.780 | 0.247 | -0.787 | 484 | 0.003 | 0.127 | 0.064 | 0.005 |
| 386 | 15.220 | 0.783 | 0.282 | -0.749 | 486 | 0.003 | 0.118 | 0.046 | 0.005 |
| 388 | 13.385 | 0.785 | 0.318 | -0.667 | 488 | 0.003 | 0.111 | 0.033 | 0.005 |
| 390 | 11.457 | 0.790 | 0.354 | -0.588 | 490 | 0.003 | 0.105 | 0.023 | 0.004 |
| 392 | 9.609 | 0.801 | 0.398 | -0.488 | 492 | 0.003 | 0.099 | 0.015 | 0.004 |
| 394 | 7.899 | 0.822 | 0.442 | -0.396 | 494 | 0.003 | 0.093 | 0.010 | 0.004 |
| 396 | 6.433 | 0.849 | 0.491 | -0.314 | 496 | 0.003 | 0.087 | 0.006 | 0.004 |
| 398 | 5.159 | 0.886 | 0.555 | -0.242 | 498 | 0.003 | 0.081 | 0.004 | 0.004 |
| 400 | 3.867 | 0.925 | 0.626 | -0.175 | 500 | 0.003 | 0.076 | 0.003 | 0.004 |
| 402 | 2.820 | 0.962 | 0.702 | -0.118 | 502 | 0.003 | 0.071 | 0.002 | 0.004 |
| 404 | 1.985 | 0.991 | 0.775 | -0.069 | 504 | 0.003 | 0.066 | 0.001 | 0.004 |
| 406 | 1.379 | 1.000 | 0.831 | -0.035 | 506 | 0.003 | 0.060 | 0.000 | 0.004 |
| 408 | 0.910 | 0.996 | 0.876 | 0.011 | 508 | 0.003 | 0.056 | 0.000 | 0.004 |
| 410 | 0.554 | 0.970 | 0.897 | 0.016 | 510 | 0.003 | 0.051 | 0.000 | 0.004 |
| 412 | 0.339 | 0.934 | 0.901 | 0.019 | 512 | 0.003 | 0.047 | 0.000 | 0.004 |
| 414 | 0.196 | 0.893 | 0.894 | 0.020 | 514 | 0.003 | 0.043 | 0.000 | 0.003 |
| 416 | 0.121 | 0.854 | 0.884 | 0.020 | 516 | 0.003 | 0.039 | 0.000 | 0.003 |
| 418 | 0.074 | 0.825 | 0.883 | 0.019 | 518 | 0.003 | 0.035 | 0.000 | 0.003 |
| 420 | 0.039 | 0.804 | 0.886 | 0.019 | 520 | 0.003 | 0.032 | 0.000 | 0.003 |
| 422 | 0.028 | 0.795 | 0.911 | 0.017 | 522 | 0.003 | 0.029 | 0.000 | 0.003 |
| 424 | 0.023 | 0.788 | 0.938 | 0.016 | 524 | 0.003 | 0.026 | 0.000 | 0.003 |
| 426 | 0.019 | 0.782 | 0.965 | 0.015 | 526 | 0.003 | 0.023 | 0.000 | 0.003 |
| 428 | 0.017 | 0.773 | 0.987 | 0.015 | 528 | 0.003 | 0.020 | 0.000 | 0.003 |
| 430 | 0.015 | 0.756 | 0.999 | 0.014 | 530 | 0.003 | 0.018 | 0.000 | 0.003 |
| 432 | 0.013 | 0.733 | 1.000 | 0.013 | 532 | 0.003 | 0.016 | 0.000 | 0.003 |
| 434 | 0.012 | 0.699 | 0.976 | 0.012 | 534 | 0.003 | 0.015 | 0.000 | 0.003 |
| 436 | 0.011 | 0.659 | 0.933 | 0.011 | 536 | 0.003 | 0.013 | 0.000 | 0.003 |
| 438 | 0.010 | 0.615 | 0.879 | 0.010 | 538 | 0.003 | 0.012 | 0.000 | 0.003 |
| 440 | 0.009 | 0.572 | 0.820 | 0.010 | 540 | 0.003 | 0.010 | 0.000 | 0.003 |
| 442 | 0.009 | 0.530 | 0.761 | 0.009 | 542 | 0.003 | 0.009 | 0.000 | 0.003 |
| 444 | 0.008 | 0.490 | 0.703 | 0.009 | 544 | 0.003 | 0.008 | 0.000 | 0.003 |
| 446 | 0.008 | 0.456 | 0.655 | 0.009 | 546 | 0.003 | 0.007 | 0.000 | 0.003 |
| 448 | 0.007 | 0.430 | 0.618 | 0.008 | 548 | 0.003 | 0.006 | 0.000 | 0.003 |
| 450 | 0.007 | 0.407 | 0.589 | 0.008 | 550 | 0.003 | 0.005 | 0.000 | 0.003 |

Table A.2: *Database for PMMA (30 ppm Y7) from [DA96]: Wavelength $\lambda$, absorption coefficient $\mu$, primary light yield of an ideal detector $I_{0,ideal}$ and with respect to the detection of the photomultplier Valvo XP 2011, and the permanent damage per radiation dose $b(\lambda)$.*

| $\lambda$ (nm) | $\mu$ ($cm^{-1}$) | $I_{0,ideal}$ | $I_{0,real}$ | $b(\lambda) \cdot 10^5$ $(Gy \cdot cm)^{-1}$ | $\lambda$ (nm) | $\mu$ ($cm^{-1}$) | $I_{0,ideal}$ | $I_{0,real}$ | $b(\lambda) \cdot 10^5$ $(Gy \cdot cm)^{-1}$ |
|---|---|---|---|---|---|---|---|---|---|
| 426 | 3.720 | 0.004 | 0.003 | 0.500 | 520 | 0.004 | 0.545 | 0.729 | 0.048 |
| 428 | 3.930 | 0.004 | 0.003 | 0.600 | 522 | 0.004 | 0.496 | 0.678 | 0.047 |
| 430 | 4.140 | 0.005 | 0.004 | 0.500 | 524 | 0.004 | 0.446 | 0.625 | 0.046 |
| 432 | 4.310 | 0.005 | 0.004 | 0.500 | 526 | 0.003 | 0.406 | 0.583 | 0.045 |
| 434 | 4.420 | 0.006 | 0.005 | 0.500 | 528 | 0.003 | 0.371 | 0.545 | 0.043 |
| 436 | 4.480 | 0.009 | 0.007 | 0.400 | 530 | 0.003 | 0.335 | 0.505 | 0.042 |
| 438 | 4.470 | 0.012 | 0.010 | 0.400 | 532 | 0.003 | 0.308 | 0.477 | 0.043 |
| 440 | 4.420 | 0.016 | 0.013 | 0.400 | 534 | 0.003 | 0.285 | 0.452 | 0.042 |
| 442 | 4.340 | 0.026 | 0.021 | 0.400 | 536 | 0.003 | 0.261 | 0.426 | 0.041 |
| 444 | 4.270 | 0.040 | 0.033 | 0.300 | 538 | 0.003 | 0.243 | 0.408 | 0.041 |
| 446 | 4.200 | 0.053 | 0.044 | 0.400 | 540 | 0.003 | 0.227 | 0.393 | 0.040 |
| 448 | 4.180 | 0.083 | 0.069 | 0.300 | 542 | 0.003 | 0.211 | 0.376 | 0.039 |
| 450 | 4.180 | 0.119 | 0.100 | 0.400 | 544 | 0.003 | 0.197 | 0.361 | 0.039 |
| 452 | 4.220 | 0.156 | 0.132 | 0.300 | 546 | 0.003 | 0.184 | 0.347 | 0.039 |
| 454 | 4.280 | 0.216 | 0.184 | 0.200 | 548 | 0.003 | 0.170 | 0.331 | 0.038 |
| 456 | 4.320 | 0.287 | 0.245 | 0.300 | 550 | 0.003 | 0.158 | 0.317 | 0.038 |
| 458 | 4.340 | 0.357 | 0.308 | 0.200 | 552 | 0.003 | 0.146 | 0.303 | 0.036 |
| 460 | 4.320 | 0.441 | 0.383 | 0.100 | 554 | 0.002 | 0.134 | 0.288 | 0.035 |
| 462 | 4.200 | 0.531 | 0.465 | 0.200 | 556 | 0.002 | 0.123 | 0.274 | 0.035 |
| 464 | 4.020 | 0.622 | 0.549 | 0.100 | 558 | 0.002 | 0.113 | 0.261 | 0.034 |
| 466 | 3.780 | 0.704 | 0.627 | 0.100 | 560 | 0.002 | 0.103 | 0.245 | 0.034 |
| 468 | 3.490 | 0.784 | 0.705 | 0.100 | 562 | 0.002 | 0.094 | 0.232 | 0.034 |
| 470 | 3.090 | 0.863 | 0.784 | 0.000 | 564 | 0.002 | 0.086 | 0.220 | 0.033 |
| 472 | 2.630 | 0.914 | 0.838 | 0.000 | 566 | 0.002 | 0.077 | 0.206 | 0.032 |
| 474 | 2.210 | 0.953 | 0.882 | 0.000 | 568 | 0.002 | 0.070 | 0.195 | 0.031 |
| 476 | 1.820 | 0.992 | 0.928 | 0.100 | 570 | 0.002 | 0.064 | 0.185 | 0.031 |
| 478 | 1.550 | 1.000 | 0.946 | 0.100 | 572 | 0.002 | 0.058 | 0.175 | 0.030 |
| 480 | 1.220 | 0.995 | 0.953 | 0.100 | 574 | 0.002 | 0.053 | 0.166 | 0.029 |
| 482 | 0.917 | 0.990 | 0.960 | 0.110 | 576 | 0.002 | 0.049 | 0.158 | 0.029 |
| 484 | 0.687 | 0.977 | 0.958 | 0.130 | 578 | 0.002 | 0.044 | 0.149 | 0.028 |
| 486 | 0.510 | 0.959 | 0.953 | 0.120 | 580 | 0.002 | 0.040 | 0.142 | 0.026 |
| 488 | 0.372 | 0.942 | 0.948 | 0.110 | 582 | 0.002 | 0.037 | 0.135 | 0.027 |
| 490 | 0.262 | 0.932 | 0.951 | 0.140 | 584 | 0.002 | 0.033 | 0.128 | 0.026 |
| 492 | 0.185 | 0.925 | 0.957 | 0.120 | 586 | 0.002 | 0.030 | 0.122 | 0.023 |
| 494 | 0.132 | 0.918 | 0.965 | 0.100 | 588 | 0.002 | 0.027 | 0.116 | 0.026 |
| 496 | 0.087 | 0.914 | 0.975 | 0.087 | 590 | 0.002 | 0.026 | 0.116 | 0.027 |
| 498 | 0.064 | 0.910 | 0.986 | 0.077 | 592 | 0.002 | 0.023 | 0.104 | 0.022 |
| 500 | 0.043 | 0.906 | 0.998 | 0.071 | 594 | 0.002 | 0.020 | 0.098 | 0.017 |
| 502 | 0.025 | 0.893 | 1.000 | 0.068 | 596 | 0.002 | 0.018 | 0.092 | 0.013 |
| 504 | 0.019 | 0.875 | 0.997 | 0.064 | 598 | 0.003 | 0.016 | 0.087 | 0.013 |
| 506 | 0.014 | 0.857 | 0.994 | 0.060 | 600 | 0.002 | 0.014 | 0.081 | 0.011 |
| 508 | 0.011 | 0.825 | 0.975 | 0.059 | 602 | 0.002 | 0.013 | 0.075 | 0.009 |
| 510 | 0.009 | 0.787 | 0.948 | 0.056 | 604 | 0.003 | 0.011 | 0.070 | 0.008 |
| 512 | 0.007 | 0.748 | 0.920 | 0.054 | 606 | 0.003 | 0.010 | 0.065 | 0.005 |
| 514 | 0.006 | 0.701 | 0.878 | 0.053 | 608 | 0.003 | 0.009 | 0.059 | 0.002 |
| 516 | 0.005 | 0.648 | 0.830 | 0.051 | 610 | 0.003 | 0.007 | 0.055 | 0.000 |
| 518 | 0.005 | 0.595 | 0.778 | 0.049 | | | | | |

Table A.3: *Database for $PbWO_4$ from [TH99]: Wavelength $\lambda$, absorption coefficient $\mu$, primary light yield $I_{0,real}$ with respect to the detection of the photomultplier Hamamatsu R5900.*

| $\lambda$ (nm) | $\mu$ ($cm^{-1}$) | $I_{0,real}$ | $\lambda$ (nm) | $\mu$ ($cm^{-1}$) | $I_{0,real}$ | $\lambda$ (nm) | $\mu$ ($cm^{-1}$) | $I_{0,real}$ |
|---|---|---|---|---|---|---|---|---|
| 360 | 0.002 | 0.000 | 476 | 0.000 | 0.881 | 592 | 0.000 | 0.508 |
| 364 | 0.002 | 0.006 | 480 | 0.000 | 0.927 | 596 | 0.000 | 0.482 |
| 368 | 0.001 | 0.013 | 484 | 0.000 | 0.948 | 600 | 0.000 | 0.456 |
| 372 | 0.001 | 0.019 | 488 | 0.000 | 0.969 | 604 | 0.000 | 0.433 |
| 376 | 0.001 | 0.025 | 492 | 0.000 | 0.984 | 608 | 0.000 | 0.409 |
| 380 | 0.001 | 0.031 | 496 | 0.000 | 1.000 | 612 | 0.000 | 0.386 |
| 384 | 0.001 | 0.048 | 500 | 0.000 | 1.000 | 616 | 0.000 | 0.363 |
| 388 | 0.001 | 0.065 | 504 | 0.000 | 0.995 | 620 | 0.000 | 0.340 |
| 392 | 0.001 | 0.082 | 508 | 0.000 | 0.989 | 624 | 0.000 | 0.322 |
| 396 | 0.001 | 0.098 | 512 | 0.000 | 0.984 | 628 | 0.000 | 0.305 |
| 400 | 0.000 | 0.115 | 516 | 0.000 | 0.969 | 632 | 0.000 | 0.287 |
| 404 | 0.000 | 0.148 | 520 | 0.000 | 0.953 | 636 | 0.000 | 0.269 |
| 408 | 0.000 | 0.180 | 524 | 0.000 | 0.935 | 640 | 0.000 | 0.251 |
| 412 | 0.000 | 0.213 | 528 | 0.000 | 0.917 | 644 | 0.000 | 0.234 |
| 416 | 0.000 | 0.245 | 532 | 0.000 | 0.900 | 648 | 0.000 | 0.216 |
| 420 | 0.000 | 0.278 | 536 | 0.000 | 0.882 | 652 | 0.000 | 0.198 |
| 424 | 0.000 | 0.319 | 540 | 0.000 | 0.864 | 656 | 0.000 | 0.180 |
| 428 | 0.000 | 0.361 | 544 | 0.000 | 0.836 | 660 | 0.000 | 0.162 |
| 432 | 0.000 | 0.403 | 548 | 0.000 | 0.807 | 664 | 0.000 | 0.154 |
| 436 | 0.000 | 0.445 | 552 | 0.000 | 0.779 | 668 | 0.000 | 0.146 |
| 440 | 0.000 | 0.487 | 556 | 0.000 | 0.751 | 672 | 0.000 | 0.137 |
| 444 | 0.000 | 0.529 | 560 | 0.000 | 0.723 | 676 | 0.000 | 0.129 |
| 448 | 0.000 | 0.571 | 564 | 0.000 | 0.695 | 680 | 0.000 | 0.120 |
| 452 | 0.000 | 0.613 | 568 | 0.000 | 0.668 | 684 | 0.000 | 0.118 |
| 456 | 0.000 | 0.655 | 572 | 0.000 | 0.641 | 688 | 0.000 | 0.116 |
| 460 | 0.000 | 0.696 | 576 | 0.000 | 0.614 | 692 | 0.000 | 0.114 |
| 464 | 0.000 | 0.742 | 580 | 0.000 | 0.586 | 696 | 0.000 | 0.112 |
| 468 | 0.000 | 0.789 | 584 | 0.000 | 0.560 | 700 | 0.000 | 0.110 |
| 472 | 0.000 | 0.835 | 588 | 0.000 | 0.534 | | | |

# Appendix B

# Quality monitoring

The following tables present the results from $^{60}$Co outside and inside scans on the FCAL/RCAL between 1995 and 1999 in comparison with the references (see Chapter 7).

| **Results of $^{60}$Co outside scanning on the FCAL in 1994 to 1996** | | | | | | | |
|---|---|---|---|---|---|---|---|
| *module* | *tower* | *section* | $R/L_{94}$ | $R/L_{95}$ | $R_{d,95}$ | $R/L_{96}$ | $R_{d,96}$ |
| 11 | 11 | EMC1R | 0.67 | 0.66 | 0.67 | 0.66 | 1.44 |
| | | EMC1L | | | 0.61 | | 1.55 |
| | | EMC2R | 0.7 | 0.69 | 0.75 | 0.67 | 0.67 |
| | | EMC2L | | | 0.85 | | 0.61 |
| | | EMC3R | – | – | – | – | – |
| | | EMC3L | | | 3.11 | | 1.17 |
| | | EMC4R | 0.68 | 0.66 | 1.53 | 0.67 | 1.24 |
| | | EMC4L | | | 1.39 | | 1.35 |
| | | HAC1R | 0.68 | 0.69 | 0.99 | 0.67 | 0.77 |
| | | HAC1L | | | 0.71 | | 0.65 |
| | | HAC2R | 0.7 | 0.7 | 1.7 | 0.7 | 1.66 |
| | | HAC2L | | | 1.47 | | 1.53 |
| | 12 | EMC1R | 0.67 | 0.67 | 1.19 | – | – |
| | | EMC1L | | | 1.2 | | – |
| | | EMC2R | 0.68 | 0.68 | 1.06 | 0.69 | 1.38 |
| | | EMC2L | | | 1.14 | | 1.37 |
| | | EMC3R | 0.69 | 0.69 | 1.58 | 0.7 | 0.97 |
| | | EMC3L | | | 1.68 | | 1.12 |
| | | EMC4R | 0.67 | 0.65 | 1.17 | 0.68 | 1.59 |
| | | EMC4L | | | 1.48 | | 1.98 |
| | | HAC1R | 0.68 | 0.67 | 0.81 | 0.64 | 0.63 |
| | | HAC1L | | | 0.62 | | 0.5 |
| | | HAC2R | 0.68 | 0.68 | 1.05 | 0.70 | 0.84 |
| | | HAC2L | | | 0.85 | | 0.62 |

Table B.1: *R/L ratio and deviation from reproducibility $R_d$ of the $^{60}$Co signal responses from outside scans on the FCAL in 1995, 1996 in comparison to 1994.*

| **Results of $^{60}$Co outside scanning on the FCAL in 1994 to 1996** | | | | | | | |
|---|---|---|---|---|---|---|---|
| *module* | *tower* | *section* | $R/L_{94}$ | $R/L_{95}$ | $R_{d,95}$ | $R/L_{96}$ | $R_{d,96}$ |
| 12 | 11 | EMC1R | 0.65 | 0.67 | 1.9 | 0.64 | 1.14 |
| | | EMC1L | | | 1.66 | | 1.18 |
| | | EMC2R | 0.69 | 0.71 | 2.38 | 0.65 | 1.64 |
| | | EMC2L | | | 2.68 | | 2.07 |
| | | EMC3R | 0.67 | 0.66 | 2.6 | 0.69 | 2.08 |
| | | EMC3L | | | 2.46 | | 2.00 |
| | | EMC4R | 0.65 | 0.65 | 2.25 | 0.62 | 1.14 |
| | | EMC4L | | | 1.92 | | 1.48 |
| | | HAC1R | 0.67 | 0.69 | 1.45 | 0.67 | 0.62 |
| | | HAC1L | | | 1.76 | | 0.63 |
| | | HAC2R | 0.67 | – | – | – | – |
| | | HAC2L | | | 1.49 | | 1.53 |
| 12 | 13 | EMC1R | 0.61 | 0.61 | 1.92 | 0.58 | 1.44 |
| | | EMC1L | | | 2.16 | | 1.31 |
| | | EMC2R | 0.68 | 0.70 | 1.17 | 0.64 | 1.47 |
| | | EMC2L | | | 1.22 | | 0.98 |
| | | EMC3R | 0.66 | 0.66 | 2.43 | 0.66 | 0.93 |
| | | EMC3L | | | 2.06 | | 0.88 |
| | | EMC4R | 0.77 | 0.68 | 2.54 | 0.87 | 2.04 |
| | | EMC4L | | | 2.42 | | 1.58 |
| | | HAC1R | 0.69 | 0.69 | 1.17 | 0.66 | 0.83 |
| | | HAC1L | | | 1.12 | | 0.68 |
| | | HAC2R | 0.70 | 0.73 | 1.69 | 0.70 | 1.40 |
| | | HAC2L | | | 1.93 | | 1.49 |
| 13 | 12 | EMC1R | 0.66 | 0.68 | 1.14 | 0.68 | 1.97 |
| | | EMC1L | | | 1.18 | | 1.89 |
| | | EMC2R | 0.67 | 0.7 | 0.93 | 0.70 | 0.65 |
| | | EMC2L | | | 0.99 | | 1.03 |
| | | EMC3R | 0.69 | 0.70 | 1.00 | 0.70 | 0.96 |
| | | EMC3L | | | 0.95 | | 0.89 |
| | | EMC4R | 0.68 | 0.69 | 0.91 | 0.67 | 1.54 |
| | | EMC4L | | | 0.89 | | 1.36 |
| | | HAC1R | 0.67 | 0.67 | 1.31 | 0.67 | 0.63 |
| | | HAC1L | | | 1.52 | | 0.77 |
| | | HAC2R | 0.71 | 0.70 | 0.79 | 0.70 | 0.83 |
| | | HAC2L | | | 0.93 | | 0.96 |

Table B.2: *R/L ratio and deviation from reproducibility $R_d$ of the $^{60}$Co signal responses from outside scans on the FCAL in 1995, 1996 in comparison to 1994.*

| **Results of $^{60}$Co outside scanning on the RCAL in 1991 to 1998** | | | | | | | | | | | |
|---|---|---|---|---|---|---|---|---|---|---|---|
| *module* | *tower* | *section* | $R/L_{91}$ | $R/L_{95}$ | $R_{d,95}$ | $R/L_{96}$ | $R_{d,96}$ | $R/L_{97}$ | $R_{d,97}$ | $R/L_{98}$ | $R_{d,98}$ |
| 11 | 12 | EMC1R | 0.69 | 0.69 | 2.72 | 0.65 | 2.12 | 0.69 | 2.66 | 0.69 | 2.5 |
| | | EMC1L | | | 2.92 | | 1.25 | | 2.26 | | 2.06 |
| | | EMC2R | 0.69 | 0.68 | 1.74 | 0.65 | 1.81 | 0.66 | 1.64 | 0.66 | 1.36 |
| | | EMC2L | | | 2.04 | | 2.37 | | 1.97 | | 1.56 |
| | | HAC1R | 0.63 | 0.64 | 1.24 | 0.64 | 1.55 | 0.67 | 2.26 | 0.61 | 1.33 |
| | | HAC1L | | | 1.73 | | 2.24 | | 2.12 | | 2.35 |
| 12 | 11 | EMC1R | 0.67 | 0.67 | 1.75 | 0.66 | 1.43 | 0.66 | 1.47 | 0.66 | 1.52 |
| | | EMC1L | | | 1.37 | | 1.27 | | 1.33 | | 0.94 |
| | | EMC2R | 0.67 | 0.67 | 0.89 | 0.67 | 0.83 | 0.66 | 1.27 | 0.65 | 1.42 |
| | | EMC2L | | | 0.98 | | 0.70 | | 1.06 | | 1.26 |
| | | HAC1R | 0.69 | 0.68 | 1.41 | 0.68 | 1.45 | 0.67 | 1.45 | 0.65 | 1.82 |
| | | HAC1L | | | 1.16 | | 1.20 | | 1.14 | | 1.5 |
| | 13 | EMC1R | 0.69 | 0.66 | 1.28 | 0.62 | 1.88 | 0.67 | 1.56 | 0.63 | 1.18 |
| | | EMC1L | | | 1.38 | | 1.12 | | 1.93 | | 1.49 |
| | | EMC2R | 0.68 | 0.67 | 0.78 | 0.68 | 1.88 | 0.66 | 1.29 | – | – |
| | | EMC2L | | | 0.75 | | 0.70 | | 1.21 | | – |
| | | HAC1R | 0.69 | 0.67 | 1.67 | 0.69 | 1.43 | 0.67 | 1.75 | 0.65 | 1.99 |
| | | HAC1L | | | 1.91 | | 1.95 | | 2.30 | | 2.22 |
| 13 | 12 | EMC1R | 0.70 | – | – | 0.70 | 4.39 | 0.68 | 4.63 | 0.68 | 3.09 |
| | | EMC1L | | | – | | 4.37 | | 4.22 | | 2.37 |
| | | EMC2R | 0.68 | 0.67 | 2.27 | 0.65 | 1.59 | 0.65 | 1.99 | 0.65 | 1.34 |
| | | EMC2L | | | 2.77 | | 2.89 | | 2.85 | | 2.34 |
| | | HAC1R | 0.69 | 0.71 | 1.05 | 0.69 | 1.03 | 0.67 | 1.55 | – | 2.35 |
| | | HAC1L | | | 1.1 | | 0.81 | | 1.5 | | 1.69 |

Table B.3: *R/L ratio and deviation from reproducibility $R_d$ of the $^{60}$Co signal responses from outside scans on the RCAL in 1995, 1996, 1997, and 1998 in comparison to 1994.*

| **Results of $^{60}$Co outside scanning on the FCAL module 12 in 1991/1998** | | | | | |
|---|---|---|---|---|---|
| *module* | *tower* | *section* | $R/L_{91}$ | $R/L_{98}$ | $R_{d,98}$ |
| 12 | 3 | EMC1R | 0.68 | 0.65 | 1.81 |
| | | EMC1L | | | 1.7 |
| | | EMC2R | 0.73 | 0.68 | 1.81 |
| | | EMC2L | | | 2.32 |
| | | EMC3R | 0.72 | 0.69 | – |
| | | EMC3L | | | – |
| | | EMC4R | 0.69 | 0.65 | 1.36 |
| | | EMC4L | | | 1.35 |
| | | HAC1R | 0.62 | 0.58 | 2.61 |
| | | HAC1L | | | 2.65 |
| | | HAC2R | 0.72 | 0.69 | 0.94 |
| | | HAC2L | | | 1.28 |
| | 11 | EMC1/2R | 0.87 | 0.71 | 2.11 |
| | | EMC1/2L | | | 2.02 |
| | | EMC3/4R | 0.95 | 0.70 | 1.82 |
| | | EMC3/4L | | | 1.86 |
| | | HAC1/2R | 0.67 | 0.63 | 1.88 |
| | | HAC1/2L | | | 2.27 |

Table B.4: *R/L ratio and deviation from reproducibility $R_d$ of the $^{60}$Co signal responses from outside scans on the FCAL in 1998 in comparison to 1991.*

| **Results of $^{60}$Co inside scanning on the FCAL module 17 in 1990 to 1999** | | | | | |
|---|---|---|---|---|---|
| *module* | *tower* | *section* | $T_{90}$ | $T_{99}$ | $R_{d,99}$ |
| 17 | 8 | EMC3R | 0.717 | 0.688 | 0.747 |
| | | EMC3L | | | 1.186 |
| | | EMC4R | 0.688 | 0.638 | 1.271 |
| | | EMC4L | | | 1.157 |
| | | HAC1R | 0.664 | 0.625 | 1.109 |
| | | HAC1L | | | 1.110 |
| | | HAC2R | 0.677 | 0.638 | 0.649 |
| | | HAC2L | | | 0.580 |
| | 13 | EMC3R | 0.674 | 0.637 | 1.623 |
| | | EMC3L | | | 2.094 |
| | | EMC4R | 0.708 | 0.666 | 1.111 |
| | | EMC4L | | | 2.394 |
| | | HAC1R | 0.676 | 0.638 | 1.886 |
| | | HAC1L | | | 1.053 |
| | 16 | EMC3R | 0.680 | 0.644 | 1.508 |
| | | EMC3L | | | 1.896 |
| | | EMC4R | 0.714 | 0.671 | 1.643 |
| | | EMC4L | | | 2.002 |
| | | HAC1R | 0.666 | 0.631 | 1.281 |
| | | HAC1L | | | 2.805 |
| | | HAC2R | 0.678 | 0.639 | 0.996 |
| | | HAC2L | | | 1.653 |
| | 21 | HAC0R | 0.667 | 0.638 | 0.862 |
| | | HAC0L | | | 1.948 |
| | | HAC1R | 0.669 | 0.638 | 1.780 |
| | | HAC1L | | | 1.658 |
| | | HAC2R | 0.673 | — | 1.373 |
| | | HAC2L | | | 1.071 |
| | 22 | HAC0R | 0.662 | 0.633 | 0.937 |
| | | HAC0L | | | 1.334 |
| | | HAC1R | 0.675 | 0.650 | 1.152 |
| | | HAC1L | | | 1.538 |
| | | HAC2R | 0.673 | 0.646 | 1.437 |
| | | HAC2L | | | 1.474 |

Table B.5: *Transmission $T$ and deviation from reproducibility $R_d$ of the $^{60}$Co signal responses from inside scans on the FCAL module 17 in 1999 in comparison to 1990.*

# Bibliography


[AB98] H.Abramaowicz, A.Caldwell, *HERA Collider Physics*, DESY report (1998), DESY-REPORT-98-192.

[AN91] V.B.Anykeyev, A.A.Spiridonov, V.P.Zhigunov, *Comparative Investigation of Unfolding Methods*, Nuclear Instruments and Methods in Physics Research A303 (1991) 350-369.

[BE73] J.Eichler et al., *Optik III*, Bergmann-Schaefer, Lehrbuch der Experimentalphysik, Berlin 1973.

[BE87] E.Bernardi et al., *Performance of a Compensating Lead-Scintillator Hadronic Calorimeter*, Nuclear Instruments and Methods in Physics Research A262 (1987) 229-242.

[BE92a] U. Behrens et al., *Quality control and calibration of ZEUS forward and rear calorimeters with $^{60}Co$ sources*, Nucl. Instr. and Meth. A323 (1992) 611-625.

[BH97] S.Bhadra et al., *Design and Test of a Forward Neutron Calorimeter for the ZEUS Experiment*, Nuclear Instruments and Methods A394 (1997) 121-135.

[BI90] B.Bicken et al., *Radiation Damage of Plastic scintillators at Different Dose Rates,* Proc. 5th Int. Conf. on Instrumentation for Colliding Beam Physics, ed. E.P. Solodov, Novosibirsk, USSR, March 1990, pp. 348-354.

[BO93] B. Böhnert, *Untersuchung des Antwortverhaltens der optischen Komponenten des ZEUS-Kalorimeters durch ein $^{60}Co$-Präparat mit Hilfe eines Blei-Szintillator-Kalorimeters*, Diplomarbeit, Univ. of Hamburg (1993)

[BO96] I.Bohnet, *Experimentelle Untersuchung an den optischen Komponenten des ZEUS-Kalorimeters und Modifikation des $^{60}Co$-Meßsystems*, Diplomarbeit, Universität Hamburg (1996)

[BO97] B.Bodmann, *Vergleichende Alanin-Dosimetrie und Untersuchung strahleninduzierter Schden an SCSN38 mit Hilfe der Elektronen-Spin-Resonanz-Spektroskopie 1997*, Diplom-Arbeit, Univ. of Hamburg 1997.

[BO98a] I.Bohnet, B. Surrow, K. Wick, *Radiation Damage Effects in the Beam Pipe Calorimeter at ZEUS.* ZEUS-note, 98-026

[BO98b] I.Bohnet, A. Henkel, N. Gendner, K. Wick, R. Yoshida, *Uniformity measurements of the ZEUS Forward Calorimeter Module 8 with the $^{60}Co$ method*, ZEUS-note, 98-027

[BO98c] I.Bohnet, U.Fricke, B. Surrow, K. Wick, *Radiation Damage Effects in the Beam Pipe Calorimeter at ZEUS.* in Proceedings of the 6.International Conference on Advanced Technology and Particle Physics Villa Olmo, Italy October 1998, Nuclear Physics B (Proc. Suppl.) 78 (1999) 713-718, Elsevier Science B.V..

[BO99a] I.Bohnet, N.Krumnack, T.Neumann, K. Wick, R. Yoshida, *Investigations on Ageing effects of the optical components of ZEUS Calorimeter using the $^{60}Co$ monitor system.* ZEUS-note 99-58.

[BO99b] I.Bohnet, U.Fricke, *Investigations on Radiation Damage Effects in the Beam Pipe Calorimeter 1997 at ZEUS.* ZEUS-note 99-57.

[BO99c] I.Bohnet, N.Gendner, F.Goebel, T.Neumann, K. Wick, *Radiation Hardness of different calorimeters studied with a movable $^{60}Co$ source at the ZEUS detector.* in Proceedings of the 8.International Conference on Calorimetry in High Energy Physics, Lisbon, Portugal 1999, to be published in World Scintific Publishing Co.Pte.Ltd. .

[BO99d] I.Bohnet, N.Krumnack, *Primer zur $^{60}Co$-Analyse.* Internal Report, Univ. of Hamburg (1999).

[BR86] H.Brückmann, U.Behrens, B.Anders, *Hadron Sampling Calorimetry – A Puzzle of Physics*, DESY 86-155.

[BR97] J.Breitweg et al., ZEUS Collaboration, *Measurement of the proton structure function $F_2$ and $\sigma_{tot}^{\gamma^* p}$ at low $Q^2$ and very low $x$ at HERA*, Physics Letters B 407 (1997) 432-448.

[BU88] W.A.Burkhard, *C for Programmers*, Wadsworth Publishing Company, Belmont, California 1988

[BU93] G.Buß, W.Busjan, A.Dannemann, U.Holm, K.Wick, *Dose Rate Investigations of Scintillator and Wave Length Shifters*, Proc. 4th Int. Conf. on Calorimetry in High Energy Physics, La Biodola, Italy, Sept. 19-25, 1993, p. 568 .

[BU97] W.Busjan, *Strahlungsresistenz szintillierender Kunststoffasern in der Hochenergiephysik: Entstehung und Zerfall kurzlebiger Absorptionszentren*, Ph.D.thesis, Univ. of Hamburg (1997), DESY-THESIS-1996-09.

[CA98] C.Catterall, Y.Iga, *Improved Simulation of Hadronic Cascades in the Uranium Calorimeter*, ZEUS-note 98-077.

[DA90] A.Dannemann, U.Holm, T.Marckmann, K.Wick, *High and Low Dose Rate Irradiations of Scintillators and Wavelength Shifters*, in Proceedings of Large Hadron Collider Workshop, CERN 90-10 ECFA 90-133 VOL.3, Aachen October 1990.

[DA91] G.D.d'Agostini, *Unfolding Methods based on the Bayes Theorem*, ZEUS-note, 93-128.

[DA96] A. Dannemann, *Untersuchungen zur Strahlenresistenz polymerer Materialen für den Einsatz in Experimenten der Hochenergiephysik*, Ph.D. thesis, Univ. of Hamburg, internal report, DESY F35D-96-06.

[DR98] A.De Roeck, A.Wagner, *Lepton-Photon Interactions*, World Scientific Publishing Co. Pte. Ltd, 1997.

[FR99] U.Fricke, *Precision Measurement of the Proton Structure Function $F_2$ at Low $Q^2$ and Very Low x at HERA*, Ph.D.thesis, Univ. of Hamburg, in preparation.

[FU93] A.Fürtjes, *Kalibration des ZEUS Vorwärts- und Rückwärtskalorimeters*, Ph.D.thesis, Univ. of Hamburg (1992), DESY-THESIS-93-03.

[GI89] I.Gialas, A.C.Caldwell, S.M.Ritz, F.J.Sciulli, *Effect of light output nonuniformity on the ZEUS barrel calorimeter calibration*, ZEUS-note, 89-109

[HA91] T.Hasegawa et al., *Tests of new polysterene-based scintillators*, Nuclear Instruments and Methods A311 (1992) 498-504.

[HA97] D.Hasell, private communications.

[HB94] HERA-B Collaboration, *Technical Design Resport*, DESY-PRC 95-01 (1995).

[HE87] HERA Workshop, *Proceedings of the HERA Workshop, Vol.1+2*, edited by R.D.Peccei, DESY, Hamburg, 1987.

[HE93] HERMES Collaboration, *Technical Design Report*, DESY (1993).

[HE95] M.Herrmann, *Experimentelle Prüfung der Langzeitstabilität des ZEUS-Kalorimeters*, Diplomarbeit, Universität Hamburg (1995)

[HE97] W.Hein, private communications.

[HE98] A.Henkel, *Experimentelle Untersuchungen an optischen Komponenten des ZEUS-Detektors und Konfiguration eines Hochspannungs-Systems*, Diplomarbeit, Univ. of Hamburg (1998)

[HE99] A.Henkel, U.Holm, N.Gendner, R.P.Feller, A.Meyer-Larsen, *A PC based Readout System for fast CAMAC Electronics*, Zeus-note in preparation.

[HO93] ZEUS collaboration, *The ZEUS Detector*, Status Report 1993, edited by U.Holm.

[HO97] D.Horstmann, *Aufbau, Kalibrierung und Anwendung des ZEUS-Presampler-Detektors*, Ph.D.thesis, Univ. of Hamburg (1998), DESY F35D-97-07.

[HO99] U.Holm, I.Bohnet, K.Wick, T.Zoufal, *Radiation Damage of Plastic Scintillators and Consequences for Calorimetry*, in Proceedings of the 8.International Conference on Calorimetry in High Energy Physics, Lisbon, Portugal 1999, to be published in World Scintific Publishing Co.Pte.Ltd. .

[IG97] Y.Iga, S.Schlenstedt, *Status and Improvement of the ZEUS Calorimeter Simulation*, ZEUS-note 97-019.

[JA98] E.Janata, private communications.

[KC99] Dorian Kcira, *Photoproduction of jets in electron proton collisions bei HERA*, Ph.D.thesis, Univ. of Hamburg, in preparation.

[KL88] R.Klanner, *Test Program for the ZEUS Calorimeter*, Nuclear Instruments and Methods in Physics Research A265 (1988) 200-209, Elsevier Science Publishers B.V. .

[KL97] R.Klanner, private communications.

[KO95] U.Koetz, ZEUS Meeting, DESY, April, 1995.

[KR92] B.Krebs, *Experimentelle und theoretische Untersuchungen zur longitudinalen Uniformität des ZEUS-Kalorimeters mit punktförmigen Präparaten*, Dissertation, Universität Hamburg (1992)

[KR93] B.Krebs, *Primer zum $^{60}$Co-Scannen*, Internal Report, Univ. of Hamburg, 1993

[LE97] W.R.Leo, *Techniques for Nuclear and Particle Physics Experiments*, Springer-Verlag, New York (1997).

[LO90] E.Lohrmann, *Hochenergiephysik*, Teubner (1990).

[LO96] M.Löwe, *Measurement of Positron-Proton Scattering at $Q^2 = 0.25\ GeV^2$*, Ph.D.thesis, Univ. of Hamburg (1995), DESY-THESIS-1996-03.

[LO97] B.Loehr, private communication.

[MA91] T.Mayer-Kuckuck, *Kernphysik*, Teubner (1991).

[ME98] N.Meyners, private communications.

[ME96] A.Meyer-Larsen, *Neutroneninduzierte Strahlenschden an Plastikszintillatoren 1996*, Diplom-Arbeit, Univ. of Hamburg 1996.

[ME99] A.Meyer-Larsen, *Konstruktion, Aufbau und Kalibration eines strahlrohrnahen Bleiwolframatkalorimeters zur Verwendung im ZEUS-Experiment*, Ph.D.thesis, Univ. of Hamburg, in preparation.

[MO98] T.Monteiro, *Study of Exclusive Electroproduction of $\rho^0$ Mesons at Low $Q^2$ and Very Low $x$ using the ZEUS Beam Pipe Calorimeter at HERA*, Ph.D. thesis, Univ. of Hamburg, DESY-THESIS-1998-027.

[Mo98a] V. Monaco, *Measurement of the Proton Structure Function $F_2$ at Low $Q^2$ and Low $x$ with the beam Pipe Tracker and Beam Pipe Calorimeter of ZEUS at HERA*,, Ph.D.thesis, Univ. of Turin, 1998.

[NE85] W.R.Nelson et al., *The EGS4 Code System*, SLAC-265, Stanford, 1985.

[NE96] T.Neumann, Ph.D.thesis, Univ. of Hamburg, in preparation

[NE97] N.Gendner, Ph.D.thesis, Univ. of Hamburg, in preparation

[GE98] N.Gendner et al. *A $PbWO_4$ Beampipe Calorimeter for ZEUS (I)*, ZEUS-note 98-072.

[PA95] *paw-Physics Analysis Workstation, An Introductory Tutorial*, CERN, Genf 1995.

[PE82] D.H.Perkins, *Introduction to High Energy Phsics*, Addison-Wesley (1982).

[PO96] B.Povh, K.Rith, C.Scholz, F.Zetsche, *Teilchen und Kerne*, Springer-Verlag, Berlin-Heidelber-New York (1996).

[PR99] H.Prause, private communications.

[QU98] A.Quadt, *Measurement and QCD Analysis of the Proton Structure Function $F_2$ from the 1994 HERA Data Using the ZEUS Detector*, Ph.D.thesis, Univ. of Oxford (1998), DESY-THESIS-1998-007.

[RO83] A.Rost, *Grundlagen der Elektronik*, Springer-Verlag Wien New York, 1983.

[RO87] M.Rohde, *A Test of the Scintillator Material SCSN-38 for Radiation Damage from Depleted Uranium*, ZEUS-note 87-55.

[RO99] M.Rohde, private communication.

[RU95] B.Ruhm, *Akzeptanzberechnungen für das ZEUS-Strahlrohrkalorimeter*, Diplomarbeit, Univ. of Hamburg (1995), DESY-THESIS-1995-03.

[RU11] E.Rutherford, Philosophical Magazine 21, 1911.

[SC86] H.U.Schmidt, *Meßelectronik in der Kernphysik*, Teubner,1986

[SC93] W.Schott, U.Holm, E.Lohrmann, M.Nakahata, M.Rohde, F.Turkot, *The ZEUS Background Radiation Monitor (BRM)*, ZEUS-note 93-002.

[SC94] C.Schroeter, *Linux-GPIB User's Guide*, Fachhochschule Berlin 1994.

[SC95] I.Schatz, *Analyse der mit dem $^{60}$Co-Scanner am ZEUS-Kalorimeter gemessenen Signalantworten*, Diplomarbeit, Universität Hamburg (1995)

[SK98] U.Schneekloth, *Recent HERA Results and Future Prospects*, DESY 98-060,1998

[SP85] M.R.Spiegel, *Statistik*, McGraw-Hill Book Company, Weinheim, 1985.

[SU97] B.Surrow, *Proceedings of the Workshop on Deep Inelastic Scattering and QCD (DIS 97)*, J.Repond (AIP, Chicago, 1997).

[SU98] B.Surrow, *Measurement of the Proton Structure Function $F_2$ at Low $Q^2$ and Very Low $x$ with the ZEUS Beam Pipe Calorimeter at HERA*, Ph.D. thesis, Univ. of Hamburg, DESY-THESIS-1998-004

[SU98a] L. Suszycki, *Synchrotron Radiation at the HERA Upgrade*, ZEUS-note 98-039.

[TA88] J.R.Taylor, *Fehleranalyse*, VCH Verlagsgesellschaft, Weinheim 1988.

[TH99] S.Thies, *Untersuchungen an Komponenten eines kompakten elektromagnetischen Kalorimeters aus $PbWO_4$-Kristallen*, Diplomarbeit, Univ. of Hamburg (1999), in preparation.

[WI98] K.Wick, private communications.

[WOE91] T.Woeniger, *Influence of Calorimeter Calibration Errors on the Measurement of Deep Inelastic Scattering*, Ph.D.thesis, Univ. of Hamburg (1991).

[WU95] B.Wulkop, K.Wick, W.Busjan, A.Dannemann, U.Holm *Investigation of the Radiation Damage Process in Scintillators During Irradiation*, Symposium on Radiation Effects on Polymers, Washington D. C. (USA), 23.-25.8.94, and Polymer Preprints 35 (1994) 924

[YO97] R.Yoshida, private communications.

[ZE85] ZEUS Collaboration, *ZEUS a Detector for HERA*, Letter of Intent, June 1985.

[ZE91] ZEUS Collaboration, *Construction and Beam Test of the ZEUS Forward and Rear Calorimeter*, Nuclear Instruments and Methods in Physics Research A309 (1991) 101-142

[ZE98] W.Zeuner, private communication.

# Acknowledgement

This thesis was carried out within the ZEUS experiment at the I. Institute of Experimental Physics at the University of Hamburg. During the last three years I got in touch with a huge number of people due to the work within the international ZEUS Collaboration at DESY consisting of technicians, workers and scientists. It has been a wonderful experience to be a member of this physics community to see the teamwork of all my colleagues.
First of all, I want to thank Prof. Dr. Klaus Wick for enabling me to start with this thesis, his continuous support and guidance all the time I was working on it, and his enormous patience.
I am also very grateful to Prof. Dr. Robert Klanner for his strong support, useful discussions and comments on my reports, notes and this thesis, and his advice.
I want to thank all the members of the $^{60}$Co group for their help and cooperation, especially R. Feller, N. Gendner, A. Hacker, A. Henkel, N. Krumnack, E. A. Möller and H. Prause.
I want to thank Dr. W. Hain, Dr. B. Loehr, Dr. R. Yoshida, Dr. W. Zeuner and the other members of the ZEUS calorimeter group, who's teamwork contributed to the success of my work.
A Special thank goes to Rik Yoshida for inspiring me to continue my life as a scientist, also to Wolfram Zeuner for his advice and for reading the whole draft.
It is also a pleasure to thank the members of HH1 for the lively discussions and the nice atmosphere, especially B. Bodmann, Dr. W. Busjan, M. Herrmann (for his linguistical comments), Dr. U. Holm, A. Meyer-Larsen (in particular for his help in computer questions), and T. Zoufal (also for reading the whole draft) and other colleagues and students of our institute.
Special thanks to my friends Ulli Fricke, Thomas Neumann and last but not least to Dr. Bernd Surrow, who always helped in all aspects of physics and beyond.
I want to thank my parents Mönchen, Ulrich, Folker and Alexander, and all my other friends for their support and presence, especially Philipp and Vessna (also for reading the whole draft), Lena, Floh, Ulf, Martin, Gela, Christian, Barnie, Kris and Corinna, Carmen and Henrieke.
I am glad to have met all these people.